

NORTHWESTERN UNIVERSITY

Peripheral Neural Representations of Naturalistic Tactile
Stimuli in the Vibrissal-Trigeminal System

A DISSERTATION

SUBMITTED TO THE GRADUATE SCHOOL
IN PARTIAL FULFILMENT OF THE REQUIREMENTS

for the degree

DOCTOR OF PHILOSOPHY

Field of Neuroscience

By

Nicholas Edward Bush

EVANSTON, ILLINOIS

September 2019

© Copyright by Nicholas Edward Bush 2019

All Rights Reserved

Abstract

Many species of rodents rely on the set of exquisitely sensitive facial vibrissae (whiskers) to guide rich behaviors in which other senses are inadequate. Although whiskers are, like all hairs, inert strands of keratin, they provide the animal with a rich landscape of tactile information which is used to guide complex behaviors. This behavioral importance is complimented by striking anatomical and neural structure to make the rodent whisker system one of the most widely studied model systems across many disciplines of neuroscience.

However, the vibrissal research field lacks a detailed understanding of how the set of primary sensory neurons responsible for the initial translation of environmental information into the neural code parses together the complex landscape of tactile interactions with the world. Although much work has been done to dissect the coding properties of these primary sensory neurons (found in the trigeminal ganglion – Vg), individual reductionist experiments offer only a snapshot of the response properties of these neurons. It is still unclear how the coding properties of Vg neurons interpret external information in terms of the fundamental drivers of whisker-object interactions: the mechanical deformations experienced in the follicle. Although the relationship between primary sensory neuron encoding and mechanical deformations has long been expected, the ability to quantify the mechanics governing whisker contact has been impractical. In addition, the whisker system evolved to parse mechanical information from a variety of mechanical contexts in which the features present in the stimuli are complex and covary. Previous work averages over this variability and can only provide glimpses at how the entire range and complexity of natural stimuli are represented.

The work described here focuses on how complex and naturalistic mechanical information might be acquired and represented in primary sensory neurons of the vibrissal-trigeminal system. In doing so, we underscore the computational complexity required of the system. We first quantify the mechanical drivers of whisker-object interactions in restricted 2D motions in both anesthetized and awake rats to show that primary sensory neurons do indeed directly represent mechanical stimulus properties. We then describe how a natural stimulus – wind – affects the motion of the whisker, and demonstrate that Vg neuron responses correlate with feature parameters of such complex and natural stimuli.

A major short-coming of much work describing the whisker system, not just studies of Vg neurons, is that they neglect motion of the whiskers in 3D space. To address this shortcoming, we first describe formal coordinate systems for describing 3D whisker motions which underscore the complexity of the 3D information available to the system. We culminate the work with recordings from Vg neurons during naturalistic and variable 3D deflections while quantifying 3D mechanical information. This work allows us to describe the broader tuning characteristics of Vg neurons to the large space of possible tactile stimuli, and makes predictions about how the population of Vg neurons may afford flexible and complete representations of the tactile world.

Taken together, we hope this work will encourage the whisker field to account for and to appreciate the richness of the sensory, motor, and behavioral capabilities of the rodent whisker system.

Supplemental videos are included in this work. Detailed descriptions of these videos can be found in the supplemental figures section. Briefly: supplemental video 2.1 illustrates the qualitative difference between awake and passive whisker contacts; supplemental videos 2.2A-D provide examples of the stimulus space structure explored in a number of active and passive stimulation

experiments; supplemental video 2.3 gives a qualitative example of the difference between distal and proximal passive whisker stimulations; supplemental videos 5.1-5.3 give example whisker reconstructions, mechanical consequences of contact, and neural activity for 3 example neurons during the 3D stimulation protocol described in chapter 5.

Acknowledgements

This work was funded by the following sources: NIH F31-NS092335 and NIH T32-HD057845 to NEB, and NIH R01-NS093585 to MJZH and SAS.

My advisor Mitra will often remind us that science is a human endeavor. The work in this thesis is a culmination of many years of scientific work, and as such, represents more than just a series of experiments and analyses. It is a culmination of the support, emotional and professional, of everyone who has been a part of my life these past years, and to all of you I owe thanks.

I would first and foremost like to thank my parents, Edward and Carolyn Bush, to whom I owe everything. At every step of the way you have been there to support me in anything I pursued. You gave me the freedom to make my own choices, and to learn that those choices have consequences. You let me take things apart to see how they worked even when I (invariably) couldn't put them back together-- but you taught me that with little hard work you can fix anything (except a broken heart). You taught me to put all of myself into the things that matter to me; this work is a culmination of that persistence. All of these lessons have helped me become the person and scientist I am today, and I will never be able to thank you enough for that gift.

To my sister, who is a source of constant inspiration, happiness, and strength. Erica, you work harder than anyone I know in pursuit of your dreams, and I am proud of you every day. Thank you for making every day a bit brighter.

To my partner, Ally Mohr, you bring out the parts of me of which I am most proud. Thank you for your endless patience in this process, for your unwavering support and belief in me, and for making me face my fears head-on when I would rather hide from them. You remind me what's important when I am lost so that I may find my way back.

To the friends and colleagues in NUIN – James Ellis, Dominic Frank, Natalie Frederick, Josh Glaser, Tom Harmon, Carmen Lin, Dan Ohm, Dan O’Young, Nelly Papalambros, Brad Radvansky, Eanna Ryan, Laura Shanahan, and the partners and friends that supported us – your friendship has been the defining and brightest feature of this journey. Long after the trials of our PhD work has faded we will recall the good times we have shared.

I would especially like to thank Evan Fazio for your consistent friendship and support every day these past several years. There is no difficulty or triumph I would not (and did not) share. Thank you for being there, always.

My scientific pursuits could not have been possible without lessons I have learned from music. I want to thank my music teachers: Pat Hooper, Ken Stein, and Scott Burns for teaching me to practice intentionally, to listen carefully, and that there are no wrong notes-just creative dissonance.

I have been lucky to have had many excellent teachers throughout my life. I would like to thank Janet Kagan, Cathy Hoffman, and Dr. John Carleton for stoking an early interest in science and math, and for teaching me the joy of applying myself to the most difficult problems presented to me.

I want to thank my undergraduate research mentor, Dr. Louis Lucas, for introducing me to the joys and challenges of performing and refining experiments, and giving me the opportunity to engage with research early in my scientific career. Thank you to Dr. William Rochlin, for teaching me the important lesson that science is not memorized from a textbook, but uncovered through the long line of successes and failures of experiments.

I have been very fortunate to have been guided by a supportive committee that have taught me important lessons not only in science, but in all aspects of my academic career. Thank you to Dr. Robert Linsenmeier, Dr. Greg Schwartz, and Dr. Sliman Bensmaia as much for the discussions and criticisms that have strengthened my work as for the encouraging words that have made me proud of it. Thank you for the professional guidance and inclusion that you have offered that guides my development as a contributor to the future of scientific research.

I would especially like to thank Dr. Sara Solla for her mentorship throughout the course of my PhD. You have acted as second advisor to me in all aspects of the projects in this thesis, and your consistent guidance in computational techniques has shaped the way I think about neuroscientific problems. You have been a thorough and patient teacher and collaborator, and you have been encouraging in the face of difficult challenges. Some of my greatest joy in my PhD has been the process of working through challenging problems with you in great detail, and I will miss those discussions as I go on to pursue other work.

None of this work could have been possible without the scientific help, support, and friendship of the members of the Hartmann Lab, past and present, whose diversity in expertise as well as personal experience made for an environment of constant learning and collaboration: Ian Abraham, Trevor Alston, Hannah Emnett, Sean Finn-Samuels, Dr. Matt Graff, Chase Gunderud, Dr. Jennifer Hobbs, Thomas Janssen, Kevin Kleczka, Yifo Luo, Yan Man, Dr. Brian Quist, Annieruth Sawyer, Dr. Chris Schroeder, Sanjana Sharma, Tor Shepherd, Dr. Joe Solomon, Dr. Blythe Towal, and Yingfen Yi. I would like to especially thank Admir Resulaj, Nadina Zweifel, Dr. Yan Yu, Dr. Hayley Belli, Dr. Anne Yang, Dr. Lucie Huet, and Pravin Kumarappan for their close friendship and collaboration on the work in this thesis. Lastly, I would like to thank my friend, peer mentor,

and colleague in the lab, Dr. Chris Bresee. You were by my side every day teaching me the ropes and guiding me through projects; I owe so much to your constant mentorship.

Lastly, I want to especially thank my advisor, Dr. Mitra Hartmann, whose guidance for the past 6 years has, and will forever be, excellent and defining. Thank you for knowing exactly when to let me struggle with a problem, and when to step in to move me forward. Thank you for helping me to grow into someone who is confident enough in myself to hold fast to my opinions and arguments, and secure enough to admit when I am wrong; for supporting and encouraging balance between my work and my pursuits outside the lab; for making time for me, and all your students, especially when it was difficult. Thank you for helping me feel like a colleague and not just a student; in this way I am proud of the work I have done and the growth I have made.

List of Abbreviations

AI – Adaptation index

CPG – Central pattern generator

DRG – Dorsal root ganglion

DSI – Direction selectivity index

GLM – Generalized Linear Model

L4 – Layer 4

PrV – Principle nucleus of the trigeminus

RA – Rapidly adapting

S1 – Primary somatosensory cortex

SA – Slowly adapting

SpV – Trigeminal Nucleus

STA – Spike triggered average

Vg – Trigeminal ganglion

VPL – Ventroposterior lateral region of the thalamus

VPM – Ventroposterior medial region of the thalamus

Table of Contents

CHAPTER 1: INTRODUCTION.....	20
<i>1.1 SENSING IS A FUNDAMENTAL FUNCTION OF NERVOUS SYSTEMS.....</i>	<i>20</i>
<i>1.2 THE RODENT WHISKER SYSTEM AS A MODEL FOR SENSORY PROCESSING.....</i>	<i>20</i>
<i>1.3 ACTIVE SENSING IN THE WHISKER SYSTEM – MOTOR COMPONENTS.....</i>	<i>22</i>
<i>1.4 THE VARIETY OF TACTILE SENSATION.....</i>	<i>25</i>
<i>1.5 PRIMARY SENSORY NEURONS OF VIBRISSAL TACTILE SENSING: THE TRIGEMINAL GANGLION.....</i>	<i>26</i>
<i>1.6 THE MORPHOLOGY AND ANATOMY OF WHISKERS, FOLLICLES, AND MECHANORECEPTORS.....</i>	<i>28</i>
<i>1.7 CODING PROPERTIES OF TRIGEMINAL GANGLION NEURONS.....</i>	<i>29</i>
1.7.1 Adaptation properties.....	30
1.7.2 Direction tuning.....	31
1.7.3 Speed and amplitude coding.....	32
1.7.4 Temporal precision.....	33
1.7.5 Texture coding.....	34
1.7.6 Active sensation coding.....	35
<i>1.8 MECHANICAL CODING: AN ALTERNATE STIMULUS CORRELATE.....</i>	<i>38</i>
<i>1.9 MY EXPERIMENTS: COMPLEX AND NATURALISTIC MECHANICAL STIMULATION.....</i>	<i>40</i>
 CHAPTER 2: DECOUPLING KINEMATICS AND MECHANICS REVEALS CODING PROPERTIES OF TRIGEMINAL GANGLION NEURONS IN THE RAT VIBRISSAL SYSTEM.....	 43
2.1 ABSTRACT.....	43
2.2 INTRODUCTION.....	43
2.3 RESULTS.....	46
2.3.1 Quantifying the kinematic and mechanical variables of contact.....	46
2.3.2 Manual stimulation decouples kinematic and mechanical variables of contact.....	50

	12
2.3.3 Follicle state in the awake and anesthetized animal	52
2.3.4. Generalized linear models.....	53
2.3.5 Relative importance of predictor variables	57
2.4 <i>DISCUSSION</i>	63
2.4.1 Kinematic and mechanical signals are coupled in standard passive stimulation experiments	63
2.4.2 Decoupling mechanical and kinematic signals during contact reveals that Vg responses are better predicted by mechanics than kinematics	64
2.4.3 Kinematic and mechanical variables as explanatory variables for Vg firing	65
2.4.4 A mechanical framework for interpreting primary sensory signals during both contact and non-contact whisking.....	67
2.4.5 Limitations of the current approach	69
2.5 <i>MATERIALS AND METHODS</i>	72
2.5.1 Surgical Procedures	72
2.5.1.1 Anesthetized recordings	73
2.5.1.2 Awake recordings.....	74
2.5.2 Calculation of kinematic and mechanical variables	75
2.5.3 Generalized Linear Models:.....	76

CHAPTER 3: WHISKER VIBRATIONS AND THE ACTIVITY OF TRIGEMINAL

PRIMARY AFFERENTS IN RESPONSE TO AIRFLOW 80

3.1 <i>ABSTRACT</i>	80
3.2 <i>INTRODUCTION</i>	80
3.3 <i>MATERIALS AND METHODS</i>	82
3.3.4 Mechanical experiments	82
3.3.5 Quantifying vibration magnitude	83
3.3.6 Quantifying vibration direction.....	84
3.3.7 Quantifying whisker resonance.....	85

	13
3.3.8 Neural recordings during airflow stimulation	88
3.3.8.1 Surgical procedures	88
3.3.8.2 Airflow delivery	89
3.3.8.3 Airflow stimulus calibration	90
3.3.9 Experimental design and statistical analysis	91
3.4 RESULTS	93
3.4.1 Vibration magnitude increases along the whisker length and depends on airflow speed and the ratio of the whisker's arc length to its base diameter	93
3.4.2 Vibration magnitude scales linearly with bending magnitude, except at extreme values of airspeed.....	97
3.4.3 At low airspeed, whiskers vibrate parallel to the airflow direction, transitioning to perpendicular vibration at high airspeed.	99
3.4.4 Recording the activity of Vg neurons in response to sustained airflow stimulation	102
3.4.5 Vg neurons respond continuously to sustained airflow stimulation while exhibiting some adaptation over the duration of the stimulus.....	103
3.4.6 All Vg neurons increase firing rate with airspeed.....	105
3.4.7 Vg firing rate depends on airflow direction, and a neuron's preferred airflow direction can change with airspeed	108
3.4.8 The firing periodicities of Vg neurons are close to whiskers' resonances	110
3.4.9 Implications for Vg coding of airflow speed and direction.....	114
3.5 DISCUSSION	117
3.5.1 Mechanical basis driving whisker vibrations	117
3.5.2 Average airflow and the local flow profile	118
3.5.3 Airflow versus touch stimuli.....	119
3.5.4 Characterization of Vg neuron responses to airflow stimuli compared to touch	121
CHAPTER 4: WHISKING MECHANICS AND ACTIVE SENSING	123
4.1 ABSTRACT	123
4.2 INTRODUCTION	123

	14
<i>4.3 THE GEOMETRY OF WHISKING</i>	126
<i>4.4 THE MECHANICS OF QUASI-STATIC CONTACT</i>	130
<i>4.5 THE LOCATION OF WHISKER-OBJECT CONTACT POINTS FROM DIFFERENT REFERENCE FRAMES</i>	133
<i>4.6 WHERE VS. WHAT: DETERMINING OBJECT LOCATION AND CONTOUR</i>	135
<i>4.7 CONCLUSIONS</i>	140
CHAPTER 5: CONTINUOUS, MULTIDIMENSIONAL CODING OF COMPLEX TACTILE STIMULI BY PRIMARY SENSORY NEURONS OF THE VIBRISSAL SYSTEM	142
<i>5.1 ABSTRACT</i>	142
<i>5.2 INTRODUCTION</i>	142
<i>5.3 RESULTS</i>	144
5.3.1 Acquisition of 3D stimulus information	144
5.3.2 Most neurons are jointly tuned to direction and location of stimulation along the whisker arclength	147
5.3.3 Temporal patterns of spikes during contact are complex and direction dependent	150
5.3.4 Neural responses are correlated with many components of the stimulus, but many components of the stimulus are themselves tightly correlated	154
5.3.5 GLMs reveal strong encoding of rotation and distributed tiling of explored stimulus space	157
<i>5.4 DISCUSSION</i>	164
5.4.1 Classical Vg tuning curves are “slices” of possible neural responses to complex stimuli	165
5.4.2 Vg neural responses tile the mechanical space	166
5.4.3 Adaptation characteristics of Vg neurons lie along a continuum	168
5.4.4 On the plausibility of a dense code	170
<i>5.5 METHODS</i>	172
5.5.1 Surgical procedures and electrophysiological recordings	172
5.5.2 3D whisker reconstruction	174
5.5.3 3D contact point estimation	176

	15
5.5.4 Contact determination	177
5.5.5 3D mechanical models	178
5.5.6 2D mechanical models	179
5.5.7 Smoothing, alignment, and upsampling	180
5.5.8 Contact removal	181
5.5.9 Derivative calculations	182
5.5.10 Identification of direction and arclength groups	182
5.5.11 Direction Selectivity Index (DSI)	184
5.5.12 Adaptation Index (AI)	184
5.5.13 Low-dimensional tuning maps	185
5.5.14 Generalized linear models (GLMs)	185
5.5.15 Pearson Correlations	187
5.5.16 Canonical angles	188
5.5.17 Participation ratios	189
CHAPTER 6: DISCUSSION	191
6.1 TOWARD A MORE COMPLETE DESCRIPTION OF PRIMARY SENSORY REPRESENTATIONS	191
6.2 NATURAL, MULTIDIMENSIONAL STIMULI ARE REQUIRED FOR COMPLETE SENSORY REPRESENTATIONS	193
6.3 PERCEPTUAL TASKS MAY OVERLAP DURING SENSING	195
6.4 A LITTLE SLOW; MISSING THE TEMPORAL CODE	197
6.5 WHAT DEFINES A CELL CLASS?	198
6.6 3D WHISKER MOTION AND MECHANICAL RESPONSE INVARIANCE: FUTURE DIRECTIONS	201
6.7 SIMULATION OF VG POPULATIONS	202
7: SUPPLEMENTAL INFORMATION	205
7.1 SUPPLEMENTAL FIGURES	205
7.2 SUPPLEMENTARY VIDEOS	213

REFERENCES..... 215

List of Figures and Tables

Figure 1.1 Whisker array layout and ascending sensory pathways	27
Figure 2.1: Example Vg recordings from both anesthetized and awake rats.....	45
Figure 2.2 Mechanical and kinematic variables associated with contact.	47
Figure 2.3: Manual stimulation reliably decouples mechanical and kinematic variables.	52
Figure 2.4: Optimal linear filters indicate that moment is the most important predictor of Vg neural firing.	56
Figure 2.5: Comparison between full and subset models.	58
Figure 2.6: Mechanical models outperform kinematic models for manual deflections.	61
Table 3.1. Whisker length, tip diameter, and base diameter, and values of the coefficient λ_n used to compute theoretical resonant frequencies	88
Figure 3.1. Airflow stimulus calibration.....	92
Figure 3.2 Vibration magnitude varies with airspeed and whisker geometry.	96
Figure 3.3 Vibration magnitude scales with bending magnitude.	98
Figure 3.4 Vibration direction tends to be parallel with the airflow direction at low airspeed, and perpendicular to the airflow direction at high airspeed.	101
Figure 3.5 Activity of Vg neurons in response to a sustained airflow stimulus	104
Figure 3.6 The firing rate of Vg neurons increases with airspeed	107
Figure 3.7 Firing rate changes with airflow direction.....	109
Figure 3.8 The firing periodicities of Vg neurons are related to the whiskers' first mode resonances.....	113
Figure 3.9 Idealized forces generated by airflow acting on the whisker	115

Figure 4.1 Arrangement of the whiskers on the mystacial pad and reference frames relevant to whisking mechanics.....	125
Figure 4.2 Object coordinates in the head-centered, resting-whisker, and whisker-centered reference frames	128
Figure 4.3 Mechanical signals in the whisker-centered reference frame.....	131
Figure 4.4 The geometry of contact.....	136
Figure 5.1: Acquisition of 3D stimulus information.....	147
Figure 5.2: Most neurons have firing rates that correlate both with arclength of contact and deflection direction	149
Figure 5.3: The temporal structure of the V_g responses can be complex and direction dependent	151
Figure 5.4: State spaces for each whisker fall in a lower dimensional subspace.....	156
Figure 5.5: Statistical modeling of V_g neurons	161
Figure 5.6: Neural tuning is well distributed across the population and covers the full input space	163
Supplemental Figure 2.1: Spike triggered averages.	205
Supplemental Figure 5.1: Relationship between bending magnitude and rotation magnitude...	206
Supplemental Figure 5.2: PCA descriptions of the input space.....	209
Supplemental Figure 5.3: Neural representations of the input space.....	211
Supplemental Figure 5.4: Performance of the neural model as a function of the number of neural vectors.....	212
Video 2.1: Comparison of active whisking with passive, manual deflection.	213

Videos 2.2A – 2.2D: 3D visualization of mechanical and kinematic relationships in awake and anesthetized animals.....	213
Video 2.3: Comparison of distal and proximal contact in the anesthetized rat.	213
Video 5.1: Reconstruction of three-dimensional whisker motion with neural recording-Example Cell 1.....	213
Video 5.2: Reconstruction of three-dimensional whisker motion with neural recording-Example Cell 2.....	214
Video 5.3: Reconstruction of three-dimensional whisker motion with neural recording-Example Cell 3.....	214

Chapter 1: Introduction

1.1 Sensing is a fundamental function of nervous systems

Extracting actable information from the environment is a fundamental role of sensory systems. Sensory systems must first transduce energy from interactions with the environment into a representation in the population of primary neurons that consist of spike trains (Flock, 1971; Lumpkin et al., 2007). From there, sensory processing pathways transform that representation of the external environment into features that can shape and guide motor behaviors. That transformation can be so simple as to be almost non-existent, as is the case of monosynaptic reflexes in which primary sensory neurons synapse directly on to motor neurons to elicit a movement (Liddell et al., 1924). In this case, the information required to guide the behavior is crude enough that simple anatomical specificity of the sensory transduction leads to a fast and simple movement. In other cases, the sensory information required to guide a behavior is more complicated, and more processing must accompany the raw sensory information for it to be actable. Often that information must be integrated with the animal's state and history of past experiences. One way of achieving such a rich representation is via hierarchical cascades of feature extraction. This often occurs through parallel anatomical streams in which different categories of features are extracted through different streams and sent to different cortical targets and transformed into a motor response (Desimone et al., 1984; Enroth-Cugell et al., 1966; Hubel et al., 1962; Newsome et al., 1988). The study of how sensory processing pathways receive, transform, and transmit those features is a major branch of the study of nervous systems.

1.2 The rodent whisker system as a model for sensory processing

One particularly common model system for investigating sensory processing is the rodent vibrissal-trigeminal (whisker) system, rats and mice being the most frequently studied, with some of the first investigations of the function of the rodent whisker system dating to 1912 (Vincent, 1912). This preponderance has been driven in large part by the regular grid-like arrangement of whiskers in the animal's mystacial pad (cheek), that is mirrored in layer 4 of the primary somatosensory cortex (S1) in striking cytoarchitectural structures termed "barrels" (Welker et al., 1974; Woolsey et al., 1970). The arrangement of the whiskers, and subsequent barrels, is conserved across individuals in the species, such that each whisker can be given an identity, defined by the row and column of the array in which that whisker resides (Fig. 1.1A-D). Across animals, a given whisker will have similar morphological properties (Belli et al., 2017). The barrels are somatotopically arranged cortical regions that primarily represent sensory information from single whiskers. They occupy a disproportionate amount of cortical surface area when compared to the whisker's anatomical size, as well as retain single whisker resolution in the cortex, indicating their role as preeminent sensor in the rodent's somatosensory representation (Welker, 1971; Welker et al., 1974). This over representation, coupled with the experimental advantages afforded by both the single whisker somatotopy and the anatomical accessibility of the primary somatosensory cortex at the surface of the dorsal aspect of the brain, makes for a system that is easy to access and interrogate.

Sensory systems, however, include more than the layer 4 cortical representation of the external world. In addition to the striking and enlarged "barrels", single whisker somatotopically organized structures were observed in the Ventral Posterior Medial (VPM) nucleus of the thalamus – termed barreloids (Land et al., 1995; van der Loos et al., 1973) and the principal Nucleus of the Trigeminal

(PrV) – termed “barettes” (Ma et al., 1984). These regions were shown to be anatomically connected such that sensory information from primary sensory neurons in the Trigeminal Ganglion (Vg) synapse onto PrV, which decussates and projects to VPM, which in turn projects to layer 4 (L4) of S1 (Erzurumlu et al., 1980; Hayashi, 1980; Jacquin et al., 1986; Veinante et al., 2000; Williams et al., 1994). This comprises the so-called lemniscal pathway that is thought to be the primary pathway for processing tactile sensory information (Fig 1.1E). The vibrissal sensory pathway anatomy resembles that of cutaneous primate somatosensation where the peripheral neurons of the Dorsal Root Ganglion (DRG) ascend the spinal cord to synapse onto brainstem neurons of the gracile or cuneate nucleus, decussate and continue to the Ventro-Posterior Lateral portion of the thalamus (VPL), and then to L4 of S1. In addition to the lemniscal pathway, there exist additional ascending parallel pathways. The number, function, and organization of these pathways is still a subject of research, but it is well accepted that all these pathways branch off from the trigeminal nucleus (SpV) at the level of the brainstem (Jacquin et al., 1986; Yu et al., 2006). Each pathway is thought to mediate the extraction of different types of information as does the what/where-ventral/dorsal streams in the visual system (Diamond et al., 2008; Yu et al., 2006). A schematic of the ascending pathways of the vibrissal sensory system is shown in Figure 1.1 E.

1.3 Active sensing in the whisker system – motor components

For some animals, including those that are the focus of neuroscience research, the whiskers are not simply passive sensory organs. Rather, the position of each whisker can be controlled by musculature in and around the mystacial pad (Dorfl, 1985). This control makes the whisker system a rich sensorimotor apparatus. The species of mice and rats that are the focus of much research exhibit a back and forth rhythmic motor pattern termed “whisking”. This pattern is stereotypical,

but is capable of rich variability (Bermejo et al., 2005; Bermejo et al., 2002; Deutsch et al., 2012; Grant et al., 2009; Hartmann, 2009; P. M. Knutsen et al., 2008; Mitchinson et al., 2007; Towal et al., 2008). The animal protracts its whiskers forward (rostrally) until the whiskers extend far in front of the face, and the whiskers are returned back to rest position during retraction. The retraction phase is generally faster than the protraction phase. One cycle of this behavior is called a “whisk”. Protraction and retraction are actuated by separate groups of muscles (protractors and retractors).

These muscles are classified as either “intrinsic” or “extrinsic” (Dorfl, 1985; Haidarliu et al., 2015). Intrinsic muscles are fully contained within the mystacial pad; these muscles are small and attach at either end to a follicle. An intrinsic muscle attaches to the apical portion of the follicle (near the skin) and wraps around the root of the follicle of the whisker caudal to it, within a given row. These intrinsic muscles allow, theoretically, for actuation of individual whiskers. Intrinsic muscles play a large role in the protraction phase. On the other hand, extrinsic muscles have an attachment point outside the mystacial pad, and generally affect the entire array of whiskers on the ipsilateral side of the face. They are more often involved in retraction of the whiskers. (Dan N. Hill et al., 2008) Proprioceptors are thought to not exist in these muscles, and the question of how rodents monitor the position of their whisker array is an area of continuing research.

Whisking has been shown to be under the control of a central pattern generator (CPG) located in a nucleus of the brainstem called the vibrissal zone of the intermediate band of the reticular formation (vIRT). This region has been shown to receive input from the pre-Bötzinger complex (preBötC) which governs breathing rhythm generation. Whisking rhythm has been shown to synchronize with breathing (Moore et al., 2013). This is not to say that whisking motion is always

identical and driven exclusively by rhythmic patterns. A number of more complex whisking patterns have been observed in behavioral experiments (Arkley et al., 2014; Grant et al., 2009; Hobbs et al., 2015, 2016; Mitchinson et al., 2007; Towal et al., 2008). Animals will tend to unilaterally and reflexively retract their whiskers when contacting an unknown object. Such situations will often be followed by orienting the head towards the unexpected object. The animal may also perform a behavior called foveal whisking in which the animal executes a sequence of small whisker motions around this novel object (Mitchinson et al., 2007).

Whisking behavior can be drastically influenced by body and head motions. It has been shown that animals will whisk asymmetrically during head turns in a manner that shifts the bilateral center of the whiskers towards the future head direction, offering a “look-ahead” into the space the head is about to move (Towal et al., 2008). During locomotion through dark and narrow corridors, animals tend to hold their whiskers protracted rather than performing rhythmic whisking. They do so in a manner that maintains light contact with the wall at the tips of the whiskers. This allows the animal to move quickly through the corridor while avoiding collisions (Arkley et al., 2014).

Although the main component of whisking is in the rostro-caudal direction, whisking is not a two-dimensional behavior (Bermejo et al., 2005; Bermejo et al., 2002; Knutsen et al., 2008). The whisker array extends significantly in the dorsoventral plane due to the dorsoventral spread of the emergence points of the whisker, the angles with which the whiskers emerge from the skin, and the intrinsic curvature of the whisker itself (Belli et al., 2018; Huet et al., 2014). During protraction, the whiskers move in the dorsoventral direction (called elevation change, often denoted ϕ), although to a lesser extent than in the rostrocaudal direction. The whiskers also rotate about the

main axis of the follicle (called roll, denoted ψ). Both roll and elevation change are tightly correlated with the protraction angle (denoted θ) (Knutsen et al., 2008).

The whisker system is thus a sensorimotor system in that the sensory information that is acquired through exploration can be directly driven from the motor output of the system, and the ability to interpret sensory information relies on accurate estimation and accountability of the motor state of the system. Body, head, and intrinsic whisker motion all compound to move the whisker with respect to the environment, affecting the resultant interactions between the whisker and the environment. Interactions with a particular object during different behavioral situations can result in the acquisition of disparate sensory signals, but effective sensation requires that the animal be capable of accounting for the context of the motion that acquired a given sensation.

1.4 The variety of tactile sensation

The ubiquity of whiskers across most mammalian species speaks to their versatility as sensory organs (Muchlinski, 2010). In rodents alone, the whiskers have been shown to mediate many different behaviors. In order to do so, the animal must be able to parse many different features present in the tactile environment. The animal must be able to interpret physical features such as coarse and fine object shape, texture, and compliance to be able to locate, identify, and determine how to interact with objects in the environment. Whiskers have been shown to be involved in behaviors including: texture discrimination, object localization, object discrimination, gap crossing, social touch, and wind following (Celikel et al., 2007; Knutsen et al., 2006; Morita et al., 2011; Rao et al., 2014; Yu et al., 2016a). The question of how this variety of behaviors and the variety of information important to serve those behaviors could be represented in a single sensory representation is the primary aim of this thesis.

1.5 Primary sensory neurons of vibrissal tactile sensing: The Trigeminal Ganglion

Ultimately, the variety of behaviors, the types of information extracted, and the diversity of computations executed in the multiple parallel streams of the ascending tactile system are all served by a single representation of the tactile stimulus space. This representation exists in the whisker responsive primary sensory neurons in the trigeminal ganglion (Vg) (Zucker et al., 1969). The trigeminal ganglion conveys tactile information from the entire orofacial region, not just the whiskers. This thesis will only be concerned with whisker responsive trigeminal ganglion neurons that form part of the maxillary branch of the trigeminal nerve.

The peripheral axons of these neurons (that extend to the follicle) synapse onto or terminate in a variety of specialized endings called mechanoreceptors that contain the molecular machinery to transduce physical deformations into electrical potentials (see details below). Importantly, these peripheral axons only innervate one vibrissa (Kerr et al., 1964; Zucker et al., 1969), and approximately 200-400 Vg neurons innervate one whisker (Rice, 1993; Rice et al., 1986). These neurons are silent when the vibrissa are untouched. The central branch of the axon ramifies profusely to form collaterals that synapse onto many targets in the brainstem (Hayashi, 1980; Jacquin et al., 1986). This ramification is important in that most or every parallel ascending pathway receives an identical copy of the sensory representation present in the Vg neurons. No part of the Vg neuron has been shown to receive synapses from other cells, and so there is no known mechanism by which top-down or lateral modulation could occur. Understanding how Vg neurons represent tactile information is thus crucial for interpreting responses and functions of structures in central regions, and the manner in which these neurons represent the space of external information available to the system is the focus of this thesis.

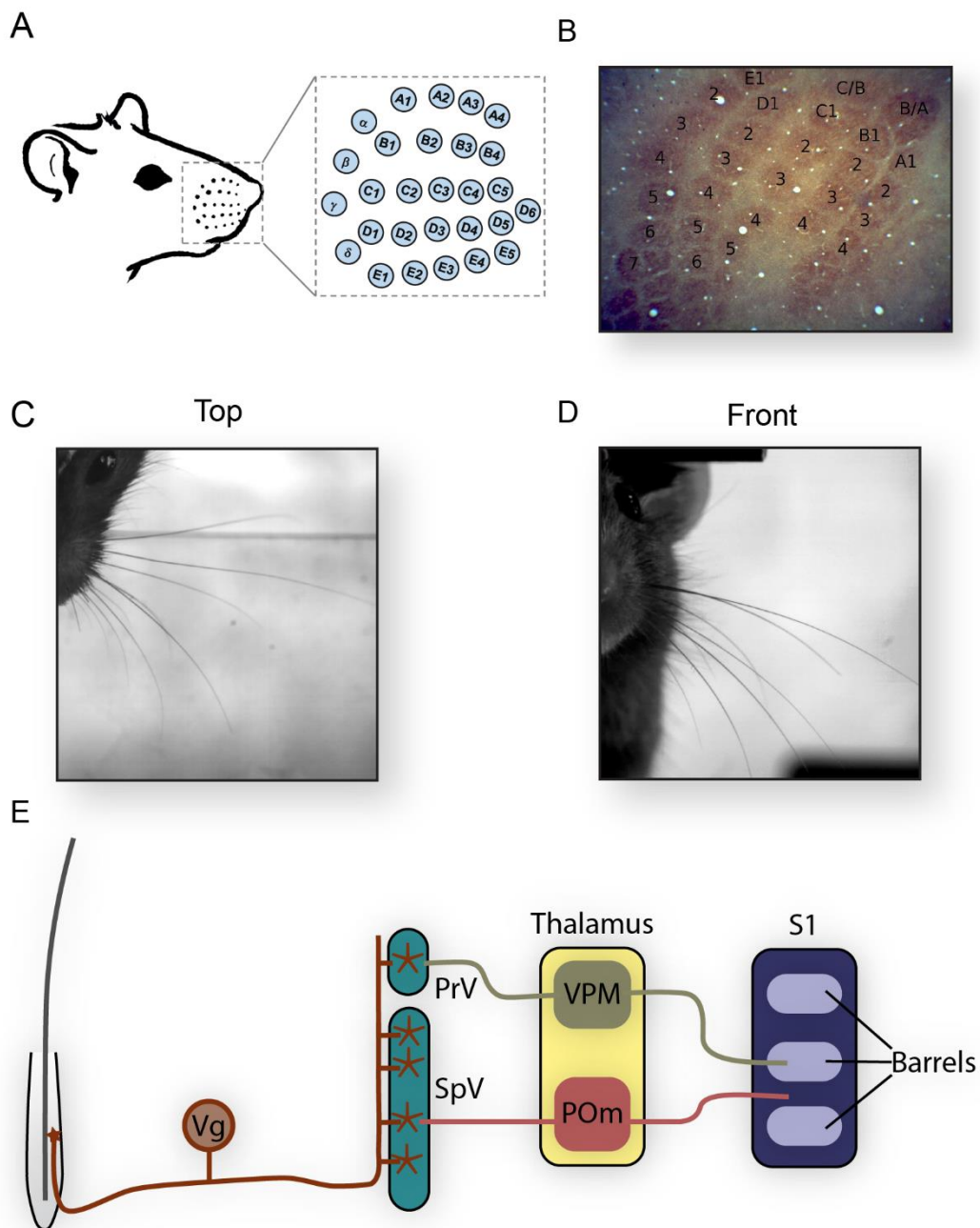


Figure 1.1 Whisker array layout and ascending sensory pathways: (A) Adapted from figure 3.2 left: Schematic of the rodent face with whisker basepoints indicated. *Right:* Arrangement and identities of whiskers as they appear on the mystacial pad. (B) Cytochrome oxidase staining of L4 S1 showing barrels. Row and column ID are shown superimposed. (C) Top down image of the whisker array during whisking. Mouse face appears in upper-left of image.

(D) Front on image of whisker array during whisking. Mouse face appears on left of image.
 (E) Schematic of ascending sensory information from the whisker. Whisker follicle complex is shown left in gray. Mechanoreceptor (brown star) is innervated by neurons of the Vg (Brown). Vg axon collaterals terminate (brown) in the PrV and SpV of the brainstem (teal). Projection neurons from brainstem ascend to the thalamus (yellow). Lemniscal (green) and paralemniscal (pink) pathways are shown. These pathways subsequently project to barrels (light purple) in S1 (dark purple).

1.6 The morphology and anatomy of whiskers, follicles, and mechanoreceptors

In order to make sense of the way in which trigeminal ganglion neurons represent tactile information, it is crucial to appreciate the sensing apparatus itself: the vibrissa. Vibrissae are inert hairs with no sensors along their length. In many animals they are enlarged with respect to pelagic fur (Ebara et al., 2002; Rice, 1993; Rice et al., 1986). In the rat and mouse (as well as many animals not the focus of this thesis), the number and arrangement of vibrissae is conserved across individuals. This arrangement allows for vibrissae to have identities based on their arrangement in the array of vibrissae, and they are named based on the row and column in which they are found (Fig 1.1A). A whisker of a given identity has physical and mechanical properties that are similar across individuals (e.g., length, curvature, base diameter) (Belli et al., 2017).

Each vibrissa is embedded in an enlarged follicle that exhibits a complex structure of blood filled sinuses, tissues of varying stiffness, and multiple physiological types of mechanoreceptors distributed both around the circumference, and longitudinally along the axis of the follicle (Ebara et al., 2002; Rice, 1993; Rice et al., 1986). While the anatomical and functional diversity of mechanoreceptors is still a focus of study, four major types seem to account for most of the mechanoreceptors in the follicle: Merkel cells, Lanceolate endings, reticular endings, and club-like endings (Abraira et al., 2013; Takatoh et al., 2018). Of these, the Merkel cell is perhaps the

best understood. The mechanically gated ion channel *Piezo2* is necessary for the mechanical sensitive capabilities(Woo et al., 2014), the Merkel cell proper and the Vg neuron axon both contribute to the Vg stimulus response properties(Woo et al., 2015), and the merkel cell releases norepinephrine(Hoffman et al., 2018). Axons of Vg neurons integrate over a small population of mechanoreceptors in the follicle, but the innervation of a given Vg neuron is always over only one mechanoreceptor type in one vibrissa, and generally from a spatially localized region of that vibrissa's follicle(Ebara et al., 2002; Rice, 1993; Rice et al., 1986).

Currently, the complexity of the tissue mechanics and anatomy of the follicle, as well as the genetic and anatomical inaccessibility of the mechanoreceptor sub-types limits our ability to analyze the physical consequences of vibrissal-environment interactions within the follicle(Whiteley et al., 2015). However, the relative simplicity of the whisker itself has allowed us to develop mechanical models which quantify the forces and moments (torques) experienced at the base of the vibrissa (where the vibrissa enters the follicle) that results from the bending of the whisker in response to a force applied along its length (Huet et al., 2016; Huet et al., 2015; Quist et al., 2014). The majority of analyses in this thesis will consider these forces and moments as a complete description of physical interactions with the environment.

1.7 Coding properties of trigeminal ganglion neurons

The analysis and quantification of Vg neuron responses to tactile stimuli had its start as early as 1969 with the seminal study by Zucker and Welker (Zucker et al., 1969). This first study pioneered a method by which many quantitative properties of Vg neurons are inferred. First, Vg neurons are isolated via extracellular sharp tungsten electrode recordings. In this early study, the ganglion was surgically exposed, but many later studies take advantage of the now known stereotactic location

of the Vg to simplify surgical procedures, and instead drive a tungsten electrode ventrally from the dorsal pial surface to the location of the Vg. Whisker responsive units were isolated via manual stroking of the entire vibrissal array. Zucker and Welker found that activity of whisker responsive Vg neurons was driven by manual stimulation of one and only one vibrissa, and whisker responsive neurons were spatially localized in the Vg. After isolating a whisker responsive Vg neuron, the investigators made a series of qualitative descriptions of neural responses to manual (i.e., hand-held) stimulation of that neuron's receptive field (whisker). Many of these descriptions are still prevalent for the interpretation of quantitative results today. Importantly, they then quantified neural responses to electrically controlled stimulation now termed "ramp and hold". They placed a probe on the whisker 5mm from its emergence from the follicle and used a galvanometer to deflect the whisker from its rest position to a second "deflected" position. They surveyed through a set of prescribed stimulation parameters in which the amplitude and velocity of whisker deflection could be varied independently. This stimulation design has been mimicked and expanded on to the present day (Bale et al., 2015; Campagner et al., 2016; Lichtenstein et al., 1990; Ramirez et al., 2014; Shoykhet et al., 2000) to investigate the stimulus response profiles of whisker responsive neurons from Vg to cortex. Zucker and Welker's pioneering work foreshadowed many results that would be later quantified in great detail.

1.7.1 Adaptation properties

A common drive across disciplines of neuroscience is to classify neurons into subpopulations that share anatomical, molecular, or functional characteristics—often requiring combinations of these features to distinguish among neural subpopulations (Zeng et al., 2017). A classical example of this is seen in cutaneous skin mechanoreceptors in which rapidly adapting (RA) and slowly adapting

(SA) properties are seen in anatomically distinct populations of mechanoreceptors in primate skin. In this framework, RA mechanoreceptors respond to the onset and offset of cutaneous deformation, and SA receptors respond strongly during onset, but continue responding during the duration of the stimulus (Johnson, 2001). This classification was described early in investigations of Vg neurons through the use of the ramp and hold stimulus described previously. When deflected, some neurons tended to respond to the onset only, onset and offset, or throughout the duration of the stimulus (Gibson et al., 1983a). This distinction continues to be used as a tool to describe responses in most investigations of Vg coding, including some that suggest parallel processing streams based on these response categories (Chagas et al., 2013; Jones et al., 2004a; Lottem et al., 2015; Severson et al., 2017; Stuttgen et al., 2006; Takatoh et al., 2018).

It would be a mistake, however, to think that the literature is in agreement that Vg neurons fall into categorical adaptation groups. Although many studies take advantage of apparent categorization based on response type to simplify analyses, it is well documented that “between the rapidly adapting (phasic) and slowly adapting (tonic) extremes... [are] touch receptors that differ in their degree of responsiveness to static deformation” (Gibson et al., 1983a). The claim that adaption properties vary smoothly from one extreme to another is supported by data in (Gibson et al., 1983a; Jones et al., 2004b; Lichtenstein et al., 1990), and is a major conclusion of Chapter 5.

1.7.2 Direction tuning

Perhaps the most immediate feature which could be intuited as an important for driving Vg neuron activity is the direction with which the whisker is stimulated. Indeed, the number of spikes, spike rates, thresholds, and adaptation properties of Vg neurons have all been shown to be modulated by the direction with which a whisker has been stimulated (Jones et al., 2004b; Lichtenstein et al.,

1990). Frequently, a neuron's preferred direction will be determined aurally via audio amplification of neural responses during manual deflection of the neuron's innervated whisker, and subsequent experiments or analyses will be performed only considering the neuron's preferred direction (Bale et al., 2013; Chagas et al., 2013; Jones et al., 2004a). It is important to appreciate that active protraction of whiskers during natural exploration is primarily in the rostro-caudal direction (Bermejo et al., 2002). Directional tuning may arise as a result of mechanoreceptor location in the follicle (unpublished data).

It is not, however, adequate to restrict consideration of Vg neuron's representation of the tactile space to only this motion, as there is significant motion out of the rostro-caudal (Knutsen et al., 2008). In addition, motion of objects in the external environment as well as motion of the head with respect to the environment will cause deflection of the whiskers out of this plane. It is known that as whiskers protract, the follicle rotates about its own axis, changing the relative orientation of the whisker with respect to the head (Knutsen et al., 2008). Since the mechanoreceptors are rigidly linked to this follicle, one would expect the Vg representation – and subsequently its preferred direction – to rotate with the follicle. The impact of this rotation on neural coding has not yet been shown, but a discussion of the implications of this rotation is detailed in Chapter 4, and is the subject of future work implied by this thesis.

1.7.3 Speed and amplitude coding

A second intuition for Vg coding properties is that firing properties are modulated by stimulus magnitude. By employing a ramp and hold stimulation, several studies have varied only the deflection amplitude or the deflection velocity and shown that Vg neurons will increase the probability of spiking as a monotonic function of either of these parameters (Gibson et al., 1983a,

1983b; Shoykhet et al., 2000; Zucker et al., 1969). In addition, neurons exhibit differing non-linear properties including thresholding and saturation(Gibson et al., 1983b). A neuron's threshold is the minimum amplitude or velocity that will elicit a spike during the ramp and hold stimulus. The thresholds have been shown to be continuously distributed across the population of neurons recorded(Gibson et al., 1983b), and the dynamic range of these thresholds varies from angular deflections as small as .01 degrees to 10 degrees(Gibson et al., 1983b).

1.7.4 Temporal precision

Although the ramp and hold stimulation paradigm offers substantial experimental control, the temporal pattern of the stimulus lacks complexity and offers little in understanding the information in the temporal patterning of spike trains. A group of studies definitively show that Vg neurons exhibit an impressive degree of temporal precision and response invariance when presented identical stimuli(Bale et al., 2015; Bale et al., 2013; Gibson et al., 1983b; Jones et al., 2004a; Jones et al., 2004b). The first two studies in this group isolated single Vg neurons and attached a piezo-electric stimulator to that neuron's associated whisker(Jones et al., 2004a; Jones et al., 2004b). They stimulated the whisker with a sequence of predetermined "frozen" bandpassed noise motions. This stimulus has the advantage of incorporating a wide band of frequency components, therefore sampling a variety of velocities and amplitudes simultaneously. The investigators could then repeat the identical "noise" trajectory of the whisker deflection many times. In doing so, they observed that individual spike trains recorded for different trials –but the same stimulus trace—were close to identical (Jones et al., 2004b). They were then able to compute a spike triggered average to determine the feature of the stimulus trace that drove that particular neuron. Later, another group performed a similar analysis while employing a more powerful statistical technique called a

“Generalized Linear Model” which can account for the neurons recent spiking activity to inform the features being represented (Bale et al., 2013). Both groups were able to show robust and repeatable temporal responses in Vg neurons that suggest that the response function from which Vg neurons map interactions in the environment to spiking activity is invariant and temporally precise. Recently, this latter group carefully measured the variance in latency between whisker-object contact onset and Vg firing to show that an individual Vg neuron can spike with trial to trial variability in spike timing well less than 1 ms (Bale et al., 2015). This suggests an extreme fidelity and determinism of this system to represent the physical features of the environment. That is to say, there is little to no appreciable probabilistic influence on these neurons’ activity; if one were to perfectly know the stimulus, and the stimulus response-function, then one could predict the exact firing pattern of these neurons.

1.7.5 Texture coding

Texture can be very informative about the identity of an object, and how best to interact with it. Texture is the subject of much research in the primate and cutaneous literature (Darian-Smith et al., 1982; DiCarlo et al., 2000; DiCarlo et al., 1998; Sinclair et al., 1991), although there is comparatively less known about how texture information is acquired in the whisker system. Moreover, it is difficult to define at what scale shape ends and texture begins. Despite it being a difficult stimulus to quantify, rats have been shown to be able to discriminate very similar textures (Morita et al., 2011), and so Vg neurons must be able to represent features about texture that can be extracted in some part of the tactile processing pathway. Presumably the precise temporal response properties described above aid in representing features important for texture discrimination. Importantly, a number of mechanical studies have quantified whisker behavior

during both artificial experiments in which an isolated whisker is swept along different textures, as well as during natural exploration (Oladazimi et al., 2018; Ritt et al., 2008; Wolfe et al., 2008). A major finding is that whiskers experience so-called “stick-slip” events in which the whisker will be stuck along the surface of the texture, and release suddenly to evoke a high velocity “slip” event. These stick slip events have been shown to cause robust responses of Vg neurons (Arabzadeh et al., 2005). Presumably, the frequency of these stick-slip events can inform the animal of an object’s texture.

An alternative hypothesis suggests that as a whisker interacts with textures, vibrations that are close to that whisker’s resonant frequency (as determined by the whisker’s length and stiffness) are amplified, and others attenuated (Andermann et al., 2004; Neimark et al., 2003). This would result in an increase in Vg response to tactile features that elicit whisker vibrations near that whisker’s intrinsic resonance, with smaller (rostral) whiskers having a higher resonance frequency than those larger (caudal).

It is still unclear which of these texture decoding hypothesis is more appropriate. It seems that Vg neurons directly encode the explicit motion and micro-motion of the whisker during texture interactions, and thus relay information about the underlying texture features as they are filtered through the biomechanical properties of the whisker/follicle. Subsequent extraction of relevant features from this high-fidelity representation is thought to occur in more central regions (Isett et al., 2018). This decoding scheme would likely rely heavily on the identity of the whisker from which the Vg response was obtained.

1.7.6 Active sensation coding

During natural exploration, whiskers are palpated in the rostro-caudal direction at an average frequency of 8Hz(Carvell et al., 1990). This self-motion will not only affect the sensory signals that are elicited during contacts, but also cause above threshold deformations of the follicle during non-contact whisking as a result of both the inertia of the whisker itself and the deformation of the cheek during mystacial muscle contractions(Curtis et al., 2009; Leiser et al., 2007; Severson et al., 2017; Szwed et al., 2003). These “reafferent” signals will be acquired in conjunction with the sensory signals that occur during contact with the environment. Presumably, the reafferent signal can be used to monitor whisker position(Szwed et al., 2003). However, it must be accounted for to allow for accurate readout of externally driven sensory information.

To investigate how Vg neurons encode sensory signals during active contact with objects, a group employed a method called “artificial whisking” (Szwed et al., 2003; Szwed et al., 2006b; Zucker et al., 1969). In this method, the facial motor nucleus (7n) is stimulated with a train of electrical stimulus pulses. This causes contraction of the extrinsic and intrinsic muscles of the mystacial pad and protraction like movements in which all the whiskers sweep forward. It is important to note that although this method does elicit movements of the whiskers, these motions are unnatural for multiple reasons. First, electrical stimulation has the problem of reverse recruitment in that large diameter motor neurons are recruited before small diameter motor neurons due to the decreased resistance of these larger fibers. This opposes the Hennemen size principle in which small motor units are recruited first. Second, co-contraction of the muscles involved in both protraction and retraction occurs, evoking unnatural strains on the mystacial pad. Lastly, normal retraction is executed by activation of the extrinsic retractors and is faster than the protraction phase(Dan N. Hill et al., 2008; Knutsen et al., 2005), but artificial whisking relies on passive relaxation to return

the whiskers to rest. This all serves to alter the kinematic trajectory of whisking. In addition, the artificial whisking trajectory is ballistic. During natural whisking, protraction is halted upon contact with an object (Mitchinson et al., 2007), but during electrical whisking protraction continues until cessation of stimulation or maximum contraction of the muscles. This causes an unnatural profile of post-contact stimulation.

Despite these caveats, the understanding of how Vg neurons encode contacts during active touch are strongly influenced by these studies. In this work, the authors describe 4 main categories of Vg neurons: whisking, touch, whisking/touch, and high threshold. “Whisking” neurons respond similarly to free air protractions (no contact) as to contact; “touch” neurons are active during contact but not during free air whisking; “whisking/touch” neurons respond during free air whisking and increase their firing during touch; and “high threshold” neurons did not respond to contacts during artificial whisking. They further classify the touch cells by the profile of their touch response: contact cells respond at the onset of contact, detach cells at the offset, contact/detach cells at both onset and offset, and pressure cells throughout the contact. One can imagine these categories overlapping with the RA/SA profiles described previously. Given that the electrical stimulation of this work was restricted to rostral-caudal motion, preferred directions could account for distinctions between contact and detach like responses. Further, it is possible that the “high threshold” cells had preferred directions not driven under these experimental protocols. The authors show that objects presented more proximal to the cheek evoke higher spike rates in “pressure” cells, and that the delay between onset of whisking and the firing of “contact” cells correlates with the angular (i.e., azimuthal) location of an object. They then suggest a population code in which the radial distance of an object can be encoded in the absolute firing rate of the

pressure cells, and the azimuthal location by the delay between a cell that fires during the onset of whisking (whisking cell) and the firing of a contact cell. The vertical component of object location can be determined by the identity of the whisker that contacted an object (Ahissar et al., 2008).

This view of object localization has prevailed in the literature, but seems fundamentally too fragile to allow for robust representation of the environment in situations in which the head is moving, or when whisking does not follow the same ballistic trajectory, e.g., when there are changes in motor patterns driven by sensory information.

More recently, experiments have been performed in the awake, head fixed animal which allows for natural whisking kinematics and object interactions (Campagner et al., 2016; Severson et al., 2017). This has been made possible by more accurate videography and image processing/whisker tracking. During behavior in awake animals, the state of the whiskers during a whisk seem to be encoded by “phase” neurons that are driven by the dynamic inertial forces experienced by the whisker, rather than in a temporal code from whisking onset (Severson et al., 2017; Wallach et al., 2016). Moreover, these phase neurons are shown to modulate their firing rate during touch, and so a phase signal must be able to be robustly extracted despite contact signals that may occur if this proposed code is to be viable.

1.8 Mechanical coding: an alternate stimulus correlate

Even in early work on Vg neurons, it was appreciated that the mechanical correlates of whisker contact ought to represent the fundamental drivers of Vg neuron activity. Kinematic parameters such as deflection amplitude and velocity are definable for rigid body motions of the whisker (which happens when stimulation occurs near the base), but become ambiguous if stimulation moves distally where the whisker will experience significant bending for the same applied force.

The definition of velocity and amplitude thus become unclear. For example, velocity must be defined as the motion of a given point with respect to another; when the whisker bends, each point will have a different velocity with respect to the whisker base, and so the definition of velocity is unclear.

With the adoption of high resolution high speed videography, accurate tracking of the entire whisker shape has become commonplace(Clack et al., 2012). This has allowed for estimates of the forces and moments experienced at the follicle to be computed. Work in our lab has developed two dimensional (top-down only) and more recently, three dimensional, numerical mechanical models that can account for the material properties of the whisker to estimate the forces and moments experienced at the base of the follicle(Huet et al., 2015; Quist et al., 2012a). Other groups measure the curvature of the whisker as a proxy for moment experienced(Campagner et al., 2016; Hires et al., 2015; Severson et al., 2017).

Our group's full mechanical model has the benefit of being able to calculate the forces and moments with appropriate units and scale, is more accurate, and is robust to tracking errors. However, this approach is computationally intensive. The curvature metric is practical in that the curvature can be calculated directly from the shape of the whisker, and the point of contact does not need to be robustly tracked. It suffers in that curvature can only be calculated at a given point on the whisker, and as such, does not account for the variation in stiffness along the whisker.

The more behaviorally relevant stimulus features investigated previously – direction, radial distance of contact, and velocity among others – can be mapped nonlinearly to combinations of forces and moments(Huet et al., 2017; Yang et al., 2016). A major hypothesis of this work (and other work published concurrently) is that Vg neurons more directly represent physical

information in the force-moment framework as compared to the behaviorally relevant quantities. As stated previously, phase in the whisk cycle is thought to be coded for by neurons sensitive to the inertial moments caused by dynamic motion of the whisker.

Behavioral experiments in which the mechanical properties of a whisker are altered show that animals judge object position based on the resultant mechanics at the base of the follicle (Pammer et al., 2013), and mechanical simulations have shown that the 3D contact point can be unambiguously determined from combinations of mechanical components (Huet et al., 2017). It is clear that a transformation from mechanical properties to object location occurs at some point in the tactile processing pathway.

1.9 My experiments: complex and naturalistic mechanical stimulation

Much of the work detailed above describes Vg neuron response properties as varying with a small number of parameters. This is largely due to the experimental paradigms in which Vg neural response are described; stimulus sets are generally small in amplitude (<1mm), vary in only one or two dimensions of the stimulus (velocity, amplitude, direction), or are restricted to motion in one spatial dimension. In each of these separate experiments, Vg neuron response properties have been shown to vary with any of the varied parameters, suggesting that the underlying response of the neuron can be excited by many features along many of the dimensions of the available stimulus space (Bale et al., 2013; Campagner et al., 2016; Gibson et al., 1983b; Jones et al., 2004a; Jones et al., 2006; Leiser et al., 2007; Lichtenstein et al., 1990; Lottem et al., 2011; Severson et al., 2017; Shoykhet et al., 2000; Stuttgen et al., 2008; Szwed et al., 2003; Szwed et al., 2006b).

During natural exploration, the stimuli encountered will be larger in amplitude than most of the stimuli presented in previous experiments. In addition, the stimuli will be complex in that many

features will covary simultaneously, and stimuli will occur with non-stereotyped temporal structure. In order to understand the functional role of these neurons in representing the physical environment, it is crucial to understand how these neurons respond to complex and naturally varying stimuli drawn from a multivariate space of features. This need is well appreciated in the visual field where the study of the statistics of natural scenes and the neural representations of those complex stimuli has a comparatively long history (Field, 1999; Geisler, 2008; Vinje et al., 2000).

In this work we investigate the responses of Vg neurons to complex, natural, and naturalistic stimulation, with the end goal of understanding the primary drivers of sensory representation at the first stage of tactile processing in the vibrissal system.

In chapter 2, we implement a novel mechanical model of whisker bending accompanied with a manual stimulation protocol in which stimulations are of large amplitude and continuously vary across stimulus features. We employ statistical models of neurons to show that Vg neurons more linearly represent the physical forces and moments present as the whisker bends, rather than performing a transformation to object position at this first level.

In chapter 3, we investigate a novel ethological role for vibrissal encoding of wind, a complex, but behaviorally relevant stimulus not considered until now. Building on behavioral and mechanical work from other members of the lab which describe how whiskers react under airflow stimulation that resembles wind (Yu et al., 2016a; Yu et al., 2016b). We stimulate the whisker with a naturalistic wind stimulus and quantify how the Vg neurons respond to features of the wind stimulus, including airspeed and direction.

In chapter 4, we address the shortcoming that 3D spatial information is often neglected in vibrissal research. We introduce and formalize a set of coordinate systems in 3D that mathematically describe the behavior of whiskers during exploration, and discuss the implications of accounting for 3D motion on neural representations.

In chapter 5 we implement a number of technical advances to investigate the neural coding of complex 3D stimuli. By carefully reconstructing the 3D whisker during complex manual stimulation and applying advanced statistical techniques, we call to question the longstanding idea of a presence of functional information streams at the level of the ganglion. We present evidence against segregating Vg neurons into categories on the basis of adaptation properties or firing rate correlations with single stimulus parameters. Instead we propose that the population of Vg neurons form an overlapping tiling of the available stimulus space. This describes a general computational principle governing sensory stimulus representation in the vibrissal system that is in line with computational principles described in other sensory systems.

Chapter 2: Decoupling kinematics and mechanics reveals coding properties of trigeminal ganglion neurons in the rat vibrissal system

2.1 Abstract

Tactile information available to the rat vibrissal system begins as external forces that cause whisker deformations, which in turn excite mechanoreceptors in the follicle. Despite the fundamental mechanical origin of tactile information, primary sensory neurons in the trigeminal ganglion (Vg) have often been described as encoding the kinematics (geometry) of object contact. Here we aimed to determine the extent to which Vg neurons encode the kinematics vs. mechanics of contact. We used models of whisker bending to quantify mechanical signals (forces and moments) at the whisker base while simultaneously monitoring whisker kinematics and recording single Vg units in both anesthetized rats and awake, body restrained rats. We employed a novel manual stimulation technique to deflect whiskers in a way that decouples kinematics from mechanics, and used Generalized Linear Models (GLMs) to show that Vg neurons more directly encode mechanical signals when the whisker is deflected in this decoupled stimulus space.

2.2 Introduction

Rats, like many rodents, rely heavily on tactile information from their vibrissae (whiskers) to explore their world. Tactile signals are generated both during active whisker movement – when the rat brushes and taps its whiskers against objects – and during passive contact. Deformations of the vibrissae are transduced by mechanoreceptors in the follicle (Ebara et al., 2002), and the resulting electrical signals are integrated by primary sensory neurons in the trigeminal ganglion (Vg). From the Vg, signals are relayed to the brainstem trigeminal nuclei, thalamus, and primary

somatosensory cortex. Neurons in the Vg are thus the “gatekeepers” of tactile information for the vibrissal trigeminal system (Jones et al., 2004b; Leiser et al., 2006, 2007).

Several studies have demonstrated that rodents can use their vibrissae to localize objects with high precision (Kleinfeld et al., 2011; Knutsen et al., 2009; Knutsen et al., 2006; Krupa et al., 2001; Mehta et al., 2007; O'Connor et al., 2010; Pammer et al., 2013). Accordingly, previous work has focused on quantifying the response of Vg neurons in terms of kinematic (geometric) variables of contact, including radial distance to an object, angular position, and angular velocity (Gibson et al., 1983a, 1983b; Jones et al., 2004a; Jones et al., 2004b; Leiser et al., 2007; Lichtenstein et al., 1990; Lottem et al., 2009, 2011; Lottem et al., 2015; Shoykhet et al., 2000; Shoykhet et al., 2003; Szwed et al., 2003; Szwed et al., 2006b).

An alternative possibility is that Vg neurons relay a high fidelity encoding of whisker mechanics – forces and moments at the base of the whisker – to be processed at later stages of the trigeminal pathway. If Vg neurons were to encode kinematic variables, a transformation from mechanical variables at the base of the whisker into kinematic variables would have to occur within the follicle (Whiteley et al., 2015) and/or through the primary afferent integration of mechanoreceptor responses.

Here we directly address the question of whether Vg neurons represent mechanical or kinematic variables. It is challenging to disentangle these alternatives because the kinematics and mechanics of contact are tightly coupled under most standard experimental protocols; this coupling is especially strong during small angle deflections and when deflections occur near the whisker base. To date, this intrinsic coupling and the absence of mechanical modeling have prevented a quantitative evaluation of the extent to which Vg neurons respond to kinematic vs. mechanical

inputs.

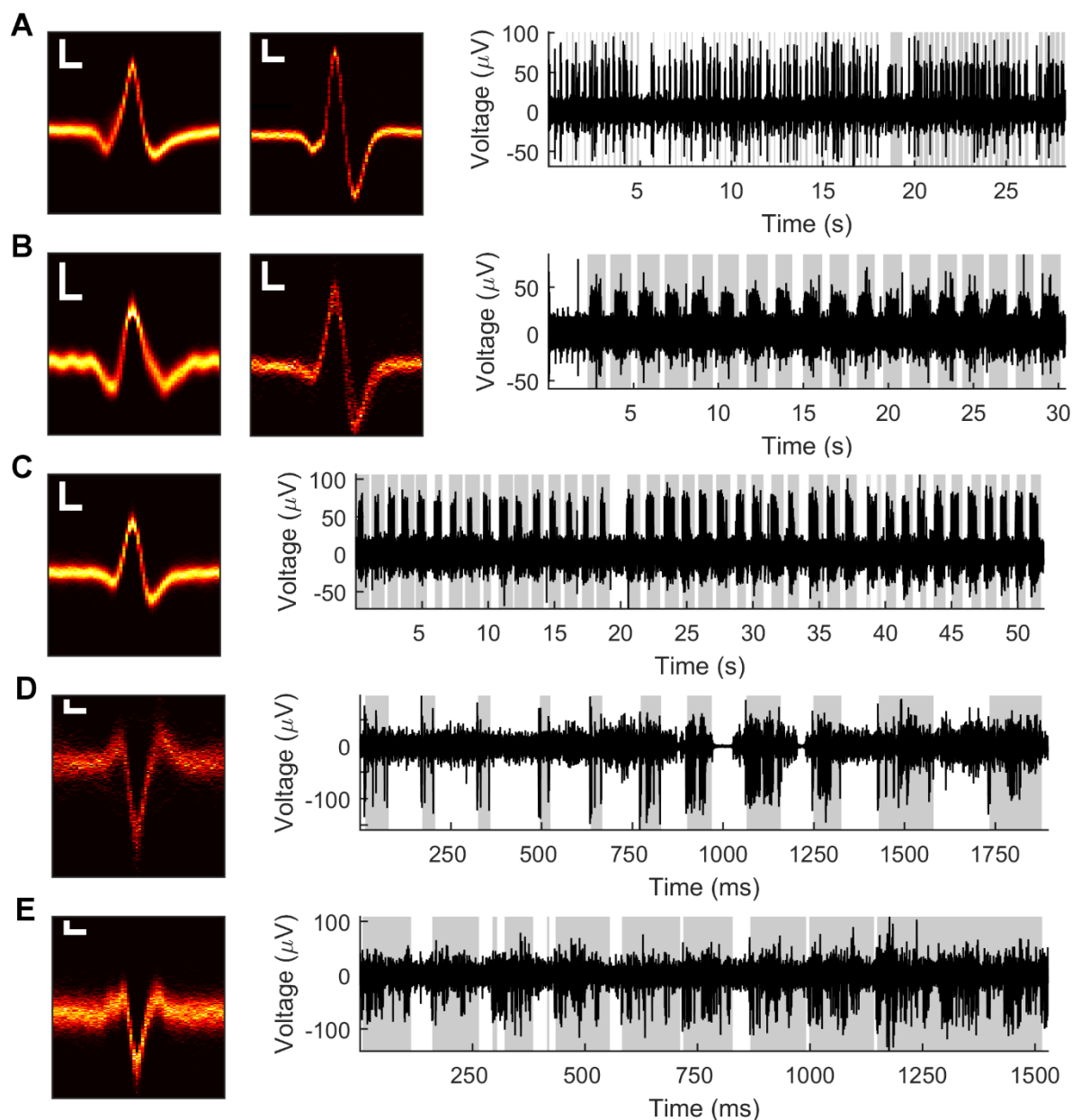


Figure 2.1: Example Vg recordings from both anesthetized and awake rats. Data from five neurons in the anesthetized animal (A-C) and two neurons in the awake animal (D-E). **Left:** Heatmaps of isolated spike waveforms over all recordings of each neuron. Two waveforms in A and B indicate simultaneously recorded neurons. Scale bars are $200\mu\text{V}$, $200\mu\text{s}$; width of waveforms is 1.5 ms . **Right:** Segments of bandpass filtered ($300\text{-}6,000\text{ Hz}$) raw neural traces during periods of passive

deflection in the anesthetized animal (**A-C**) or active contact in the awake animal (**D-E**). Gray shading indicates periods of contact

In the present study we developed a novel manual stimulation technique that allowed us to impose large angle deflections far from the whisker base, and thereby to systematically explore large regions of the tactile input space in which mechanics and kinematics decouple. We recorded from single Vg neurons in both anesthetized and awake animals, extracted the kinematics of contact from high-speed video, and computed the mechanics of contact using a quasi-static model of whisker bending. We then used Generalized Linear Models (GLMs) to quantify Vg responses in terms of both sets of variables and investigate which description more accurately predicts Vg firing rate. We found that only when the input space is large and kinematics are decoupled from mechanics does mechanical information better predict firing activity for a majority of Vg neurons.

2.3 Results

2.3.1 Quantifying the kinematic and mechanical variables of contact

We recorded high-speed video (300 fps) during manual deflection of 18 single whiskers in anesthetized rats while simultaneously recording neural responses from 22 Vg neurons. Example neural data are shown in Fig. 2.1A-C. Whiskers were deflected with a hand-held graphite probe in two directions (rostro-caudal and caudo-rostral), with amplitudes up to several mm. Stimulation was delivered at variable radial distances that ranged up to ~90% of the whisker length, and at two speeds, “fast” and “slow.” Note that manual stimulation caused radial distance of contact, velocity, and deflection amplitude to vary across deflections. The two dimensional (2D) whisker shape was tracked in each video frame to quantify the kinematic and mechanical variables of contact.

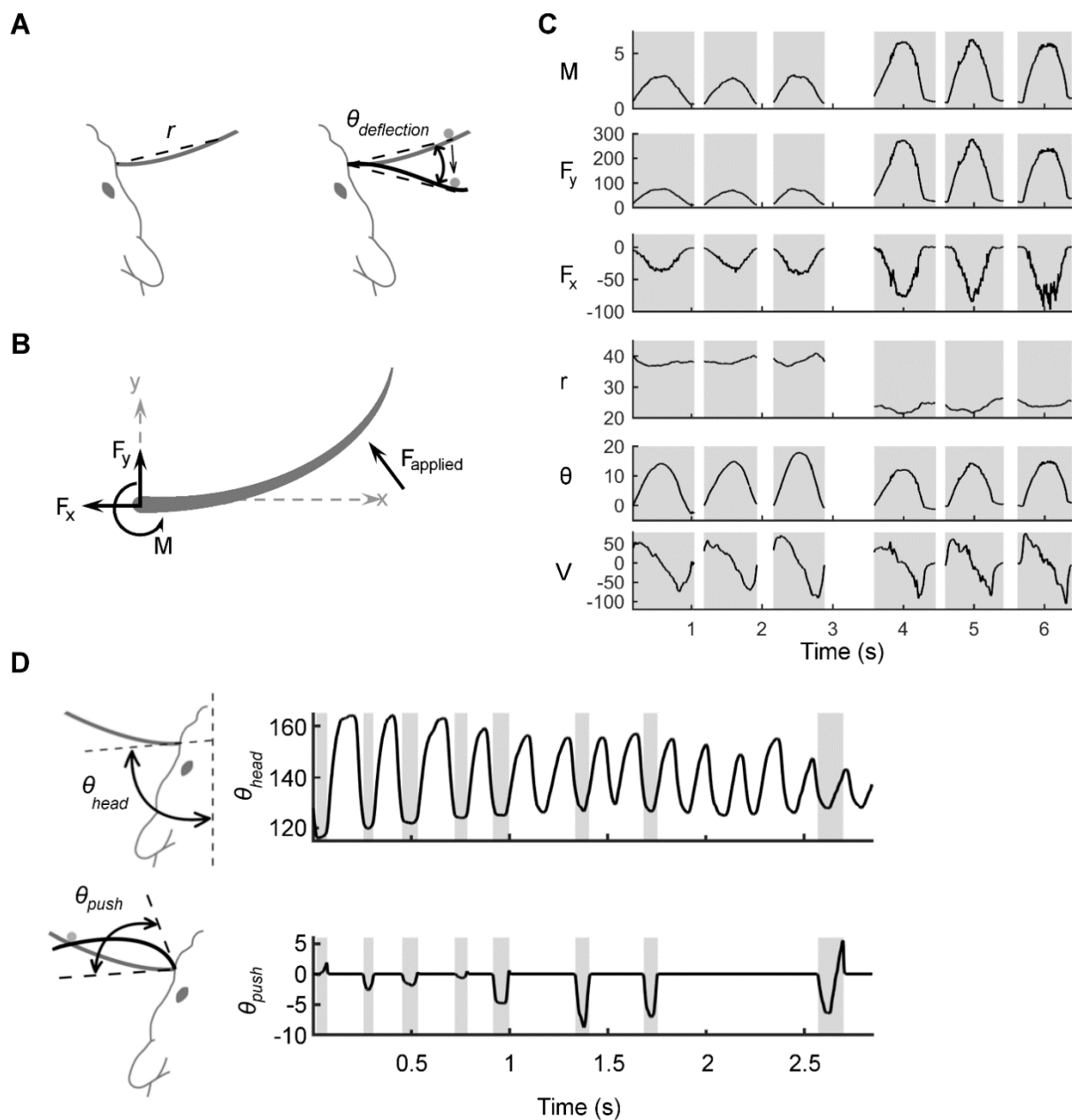


Figure 2.2 Mechanical and kinematic variables associated with contact. (A) Schematic of the kinematic variables of contact. The shape and position of the whisker when at rest is in gray. The variable r indicates the straight-line distance from the basepoint to the contact point. During passive deflections, the relevant angle is $\theta_{\text{deflection}}$, the angle between the line segment that connects the basepoint to the current point of contact and the line segment that connects the basepoint to the initial contact point. The velocity (V), not shown, is the temporal derivative of $\theta_{\text{deflection}}$. (B) Schematic of the mechanical variables of contact: bending moment (M), and the transverse (F_y) and axial (F_x) components of the applied force (F_{applied}). All variables are

computed at the whisker base. **(C)** Examples of mechanical and kinematic variables during six manually delivered passive deflections in the anesthetized rat. Shading denotes contact episodes. The stimulations are similar but not identical to each other; this imparts a naturalistic variability to the tactile inputs. Units for F_x and F_y are μN ; M is in $\mu\text{N}\cdot\text{m}$; r is in mm, θ is in degrees, and V is in degrees/sec. **(D)** In the awake rat, $\theta_{\text{deflection}}$ is no longer well defined, and the relevant angle is θ_{push} , the angle swept out by the tangent to the whisker at its base as the whisker deflects against an object. The velocity V is the temporal derivative of θ_{push} . The figure illustrates that θ_{head} , the angle between the tangent to the whisker at its base and the midsagittal plane, is not a valid kinematic variable to explain neural responses because it varies independently of contact.

Kinematic variables are illustrated in Fig. 2.2A and consist of the radial distance of contact (r), the angular displacement ($\theta_{\text{deflection}}$), and the velocity of deflection (V , the temporal derivative of $\theta_{\text{deflection}}$, not shown). Kinematic variables were extracted directly from the shape of the whisker, as detailed in *Materials and Methods*. During non-contact times, all kinematic variables are undefined.

The mechanical variables of contact were computed numerically based on the full tracked whisker shape using a quasi-static, frictionless model of elastic beam bending (see *Materials and Methods*; (Birdwell et al., 2007; Quist et al., 2012a; Solomon et al., 2008; Solomon et al., 2010)). As illustrated in Fig. 2.2B, in 2D the three mechanical signals at the base of the whisker are bending moment (M), transverse force (F_y), and axial force (F_x). Because the mechanical model is quasi-static, all mechanical signals are exactly zero during periods of non-contact.

Examples of both mechanical and kinematic variables are shown in Fig. 2.2C, which shows the signals evoked during six passive deflections of the whisker at two different radial distances.

Shaded regions indicate contact episodes. Notice that each deflection varies slightly from every other deflection, reflecting the naturalistic variability of manual stimulation.

In a separate group of animals we recorded high-speed video (1,000 fps) while rats explored a vertical pole (seven whiskers, nine neurons). Examples of neural data recorded in the awake animal are shown in Fig. 2.1D-E. Whisker shape was tracked and the kinematic and mechanical variables of contact were calculated. Supplementary Video 2.1 compares examples of manually delivered deflections and active whisking behavior.

The variables that describe active whisking are the same as those for passive contact, except that the calculation of the angular position of contact must change. In the awake animal, the contact point does not move with respect to the whisker basepoint, so $\theta_{\text{deflection}}$ is not well defined. Instead the relevant angle is θ_{push} (Fig. 2.2D, bottom left), the angle swept out by the tangent of the whisker base from the time of contact onset to the current time (Bagdasarian et al., 2013; Kaneko et al., 1998; Mehta et al., 2007; Quist et al., 2012b; Solomon et al., 2006; Solomon et al., 2011).

Given that the present work aims to compare the relative ability of mechanical and kinematic variables to describe Vg responses, which are strongly affected by contact, it is not appropriate to use the angle of the whisker with respect to the midsagittal plane (θ_{head}) as a kinematic variable. The angle θ_{head} contains no information about contact; note in Fig. 2.2D that θ_{head} varies significantly throughout the trial, while θ_{push} varies only during contact. If the variable θ_{head} were used as an input, it would unfairly favor a mechanical explanation for Vg firing because it would add a variable with no contact information to the kinematic hypothesis.

We have not included whisking phase (i.e. the relative value of θ_{head} within each whisking cycle) as a potential explanatory variable for the response of Vg neurons. Although this variable is represented in Vg responses during non-contact whisking (Wallach et al., 2016) and is of clear importance in central trigeminal structures (Curtis et al., 2009; Fee et al., 1997), the present study is limited to an analysis of contact whisking, during which kinematic and mechanical coding can be directly compared.

2.3.2 Manual stimulation decouples kinematic and mechanical variables of contact

To determine the extent to which Vg neurons encode the mechanics or kinematics of contact, it is essential to observe contact conditions under which these two sets of input variables are decoupled. Fig. 2.3 compares kinematic and mechanical variables computed for two whiskers during active exploration (Fig. 2.3A,B) to those observed during passive, manual deflection (Fig. 2.3C,D).

Mechanical and kinematic variables are often tightly coupled during awake behavior (Fig. 2.3A). Although some degree of decoupling is possible in the actively whisking animal (Fig. 2.3B), the explored regions in input space depend on the animal's behavior. It is challenging to reliably sample a large, decoupled input space with the awake animal.

In contrast, manual stimulation offers a simple and reliable method to explore a large, decoupled region of the input space (Fig. 2.3C,D). Manual stimulation can involve large angle deflections (up to 60°) at large radial distances (up to 45 mm) more consistently than in the actively behaving animal. Exploring these large regions decouples the kinematic and mechanical inputs, allowing us to address the question of whether Vg neurons encode mechanics or kinematics.

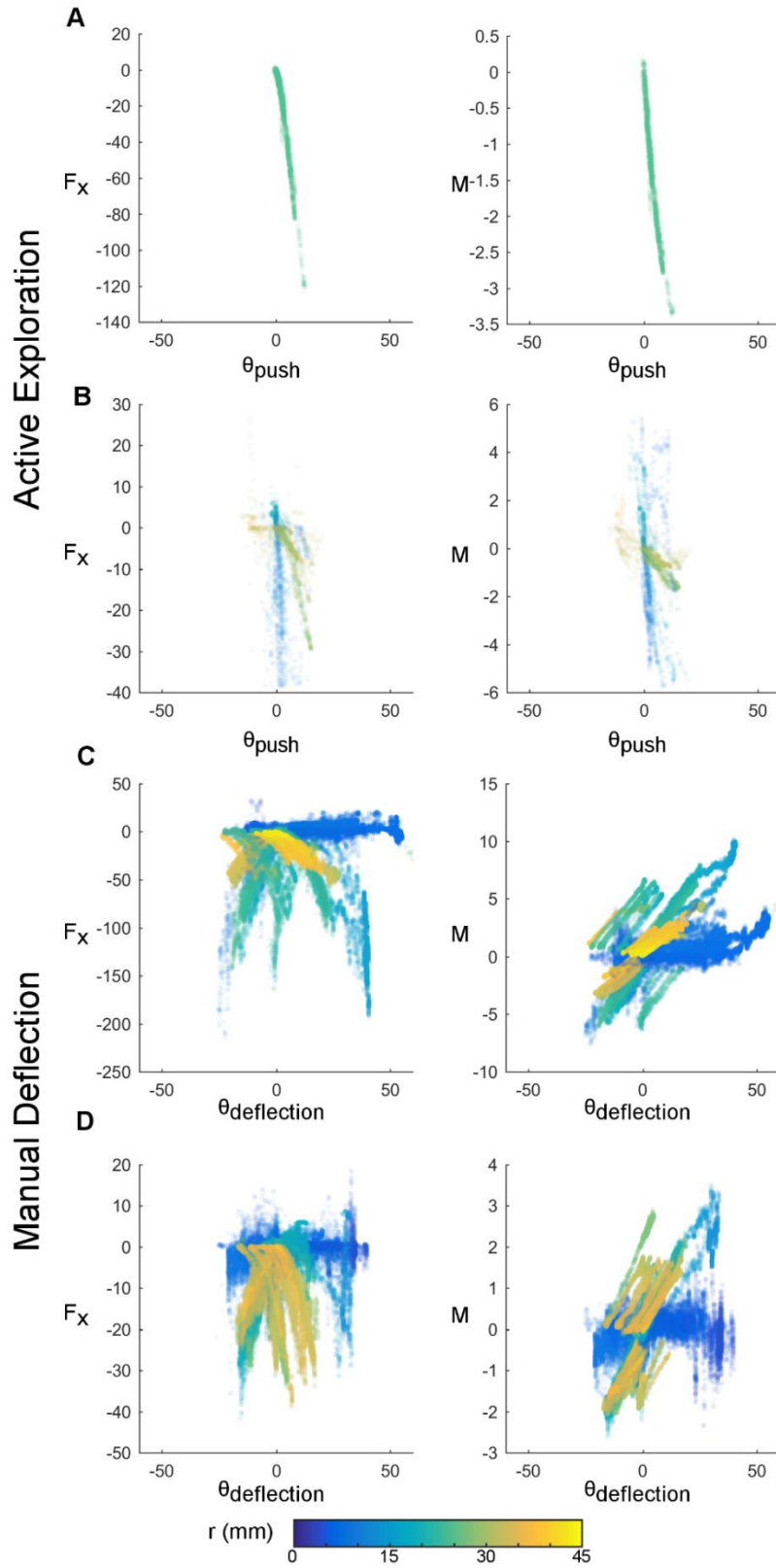


Figure 2.3: Manual stimulation reliably decouples mechanical and kinematic variables.

Mechanical and kinematic variables of contact are shown across trials of active whisking (rows A and B, whiskers C1 and Gamma respectively) and passive manual stimulation (rows C and D, whiskers B1 and D1 respectively). Awake trials were 3.02 sec (A) and 12.9 sec (B) duration; passive trials were 64.67 sec (C) and 114.53 sec (D) in duration. Each point represents the observed mechanical and kinematic inputs for a 1 ms time bin. The x-axis depicts the angular coordinate of contact in degrees, the y-axis either the axial force (F_x , units of μN) or moment (M , units of $\mu\text{N}\cdot\text{m}$). Color represents the radial distance of contact in mm. During manual deflection, a larger input space is sampled. The actual range spanned by the mechanical variables depends on whisker identity.

Supplementary Videos 2.2A-2.2D show rotating views of three dimensional versions of the plots in Figure 2.3, now including the radial distance of contact r as a third axis.

2.3.3 Follicle state in the awake and anesthetized animal

It is possible that the rigidity with which the whisker base is held during contact differs between the awake and anesthetized animal. In the awake animal, capillaries at the level of the cavernous sinus could increase hydrostatic pressure and thereby the rigidity of the whisker-follicle junction (Rice, 1993). In addition, the activation of muscles surrounding the whiskers could increase the rigidity of the follicle with respect to the mystacial pad. Either or both of these changes near the whisker base could alter the whisker's deformation in response to an applied force. Given that the follicle-whisker junction has been shown to be rigid in the anesthetized animal (Bagdasarian et al., 2013), blood-based hydrostatic changes are unlikely to be responsible for differences in rigidity between awake and anesthetized states. Changes in muscle activation, however, are a potentially significant effect that remains to be fully investigated.

In the anesthetized animal, we observed large translations and rotations of the follicle in the skin when a force is applied to the stiff, proximal portion of the whisker (Supplementary Video 2.3).

Translations and rotations were not observed during contacts at the more flexible, distal portion of the whisker; this rigidity is similarly observed in the awake animal, where mystacial muscles prevent movement of the follicle during contact.

We therefore restricted our analyses in the anesthetized animal to distal contacts ($\geq 40\%$ of the whisker length), where the apparent rigidity of the whisker-follicle-skin interface is significantly greater than the rigidity of the whisker at contact and the follicle does not move appreciably during contact.

2.3.4. Generalized linear models

We employed generalized linear models (GLMs) to determine the relative importance of kinematic and mechanical variables in predicting neural firing. GLMs include linear combinations of the history of various input variables, as well as the non-linear characteristic of biological neurons, to predict the firing rate of a neuron given previously observed stimulus inputs and the resultant spiking patterns (Pillow et al., 2008). The GLM approach lends itself to the analysis of both active and passive deflections. “Full model” GLMs were constructed using the three mechanical and the three kinematic variables ($F_y, F_x, M, r, \theta, V$) as input variables (predictors) for the observed spike train at 1 ms resolution.

We invoke a formulation of the GLM in which the predictors are convolved with a set of nonlinear basis functions (“raised cosine bumps”) that cover a desired temporal window into the past over which to consider the stimulus history (Pillow et al., 2008). Here we choose the five dimensional basis shown in Fig. 2.4A. Each predictor thus gives rise to five “convolved predictors”, each with the temporal structure of the corresponding basis function. The basis functions extended 75 ms

into the past, to match the temporal extent of the cross-correlations between the observed spikes and the various predictors while not being longer than the shortest inter-stimulus interval.

This procedure gives us a total of 30 “convolved predictors” (6 predictors * 5 basis functions) that are the inputs to the model. The GLM then fits optimal coefficients (β_{lj} , $1 \leq l \leq 5$, $1 \leq j \leq 6$) for each of the 30 convolved predictors, where l is the index of the basis function and j is the index of the predictor. The model includes one additional coefficient β_0 for a constant term. These 31

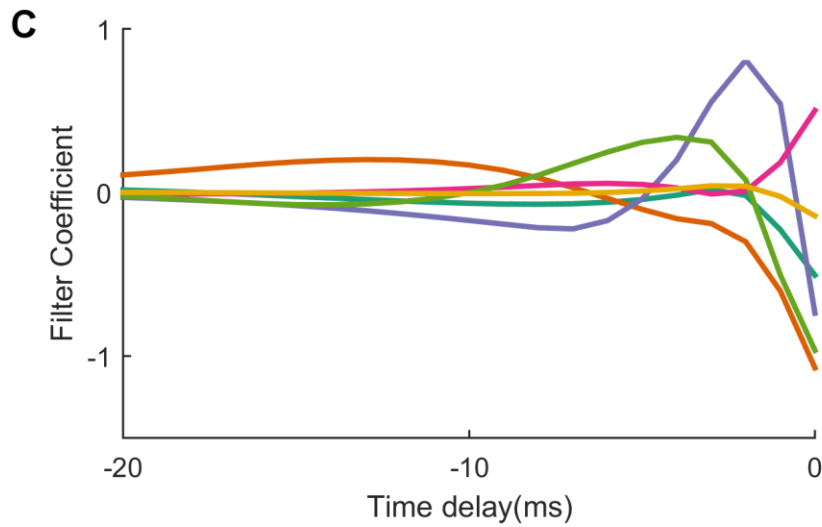
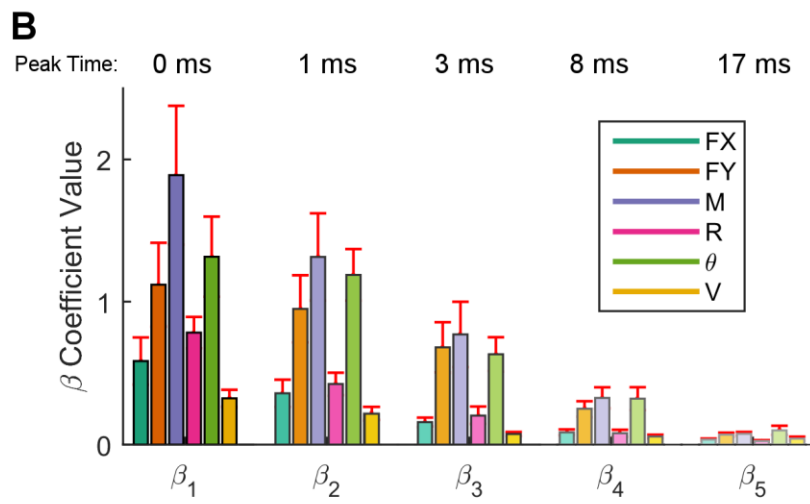
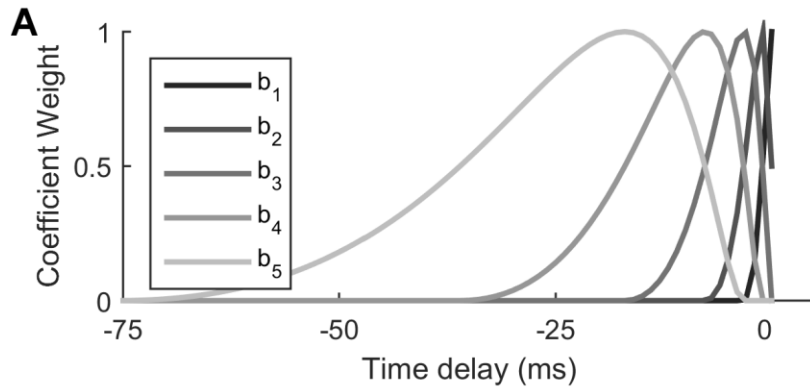


Figure 2.4: Optimal linear filters indicate that moment is the most important predictor of Vg neural firing. (A) The non-linear basis of “raised cosine bumps.” (B) Average absolute value of the GLM fit coefficients (β) across all neurons. β_1 refers to the coefficient of l_{th} cosine basis function, with l_1 being the most recent and precise, and β_5 being the most delayed and diffuse. Shading corresponds to the basis function plotted in (A). Two neurons have been omitted from this aggregate analysis because their outlying coefficients β (order 10^{13}) distorted the averages reported here. (C) The linear combination of the basis functions b_l plotted in (A) with the coefficients β_{lj} obtained from the GLM fit allows us to obtain predictor specific filters α_j , shown here as a function of time (truncated at 20 ms for visualization) for an example neuron. These filters quickly decay to zero, indicating that the majority of the information important to the cell is contained in the preceding few milliseconds. For the cell shown here, moment, transverse force, and angular displacement are important input signals, with moment being the most important.

coefficients are used to construct a linear combination of the 30 convolved predictors; this linear combination is the argument to a sigmoidal nonlinearity that outputs the instantaneous probability of firing at every 1 ms time bin.

Before convolving with the basis set, the predictors are whitened to have zero mean and unit standard deviation. This allows us to compare β coefficients for different predictors that would otherwise be on different scales. Fig. 2.4B shows the mean absolute value of the β_{lj} coefficients across all neurons. Each set in this figure refers to a particular basis function; the coefficients labeled as β_1 actually comprise all six coefficients β_{1j} , $1 \leq j \leq 6$, where the index j labels the predictors ($F_y, F_x, M, r, \theta, V$). The six coefficients labeled as β_1 represent the weight of the most temporally recent and precise time period as specified by the basis function b_1 ; this period covers 0 to 4 ms into the past with a peak time at 0 ms. The most recent time period is clearly the most important in predicting spikes for all six predictors. Subsequent sets of coefficients represent the importance of more distant past times, as specified by the corresponding basis functions shown in Fig. 2.4A. The very small values of the coefficients β_5 associated with the basis function b_5 indicate

that there is no need to look much further than 25 ms into the past. Among all predictors, moment M has the largest coefficient β for the first four basis functions; this indicates that on average, moment is the most important predictor of firing activity.

As detailed in *Materials and Methods*, it is useful to obtain predictor specific filters β_j , $1 \leq j \leq 6$, as a linear combination of the basis functions b_l , $1 \leq l \leq 5$, with the coefficients β_{lj} , $1 \leq l \leq 5$, $1 \leq j \leq 6$ obtained from the GLM fit. These predictor specific filters, shown in Fig. 2.4C for an example neuron, illustrate the impact of each predictor on the neuron's firing. Note that the filters shown in Fig. 2.4C decay to zero after about 15 ms, and that for this neuron, a change in moment from negative to positive, a negative θ , and a negative F_y are the inputs that drive the cell to fire. An alternative characterization of inputs relevant to Vg firing follows from calculating spike-triggered averages (STA) for each of the input variables. The STAs for the neuron depicted in Fig. 2.4C are shown in Supplemental Figure 2.1.

2.3.5 Relative importance of predictor variables

Bending moment is not only the most important input to the example neuron in Fig. 2.4C, but also emerges as the most important input across all neurons in Fig. 2.4B. However, all input variables contribute to the GLM fits. Different neurons might respond strongly to different combinations of input variables. To quantify whether kinematic or mechanical variables provide better predictions of firing activity, we constructed separate GLMs that had access to only the kinematic variables or only the mechanical variables. We refer to these models as “subset models.” We calculated the coefficient of determination (R^2) between the predicted spiking probability given by these subset models and the predicted spiking probability of the full model. Note that this metric is not a

measure of how well the models predict the neuron's firing, but rather of how much of the information captured by the full model can be accounted for by either of the two subset models.

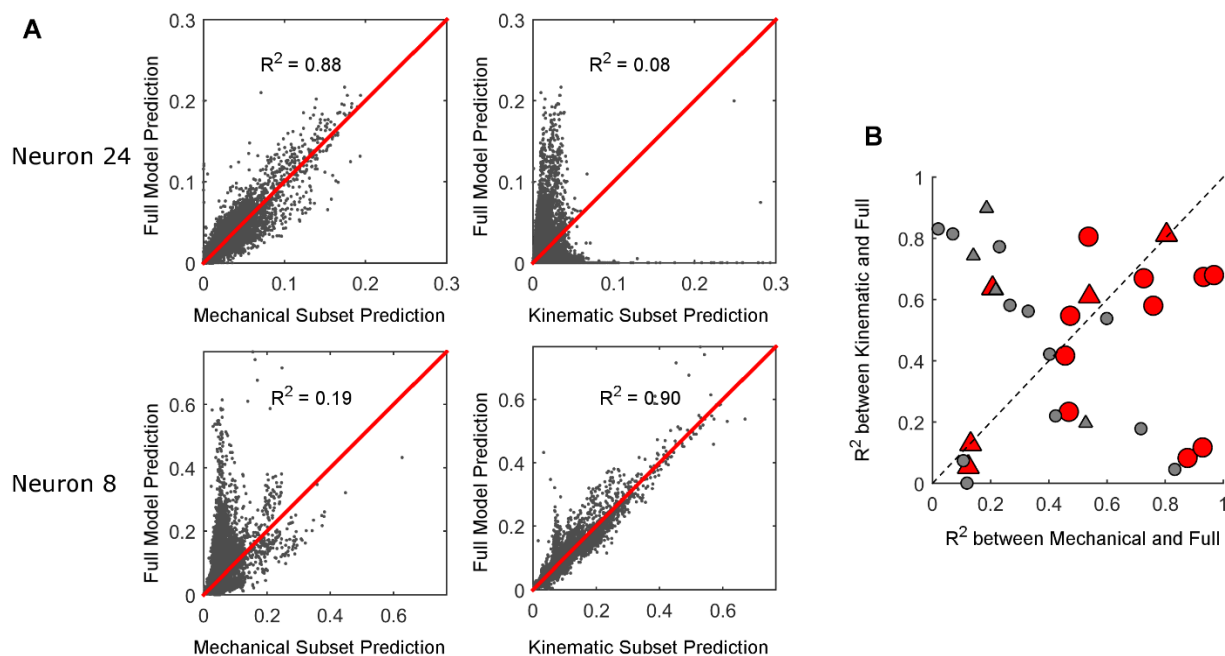


Figure 2.5: Comparison between full and subset models. (A) The firing rate prediction of each subset model is plotted against the prediction of the full model. The predictions are probability of a spike in each 1 ms time bin. For neuron 24 in the first row, the mechanical model is well correlated with the full model and the kinematic model is not; the opposite is true for neuron 8 in the second row. (B) The R^2 between the firing rate predicted by the full model and the firing rate predicted by each subset model (mechanical on the x-axis; kinematic on the y-axis). Each data point represents one neuron. Triangles represent cells recorded during active contact; circles represent neurons recorded during manual deflections. Red markers correspond to models that predict the cell's spike rate better than the median accuracy ($R > 0.30$). Gray markers indicate poor prediction accuracy ($R \leq 0.30$).

Examples of the relationship between the subset model predictions and the full model predictions are shown in Fig. 2.5A. For neuron 24, the predictions of the mechanical subset model correspond well to those of the full model ($R^2 = 0.88$), while the predictions of the kinematic subset model do not ($R^2 = 0.08$). This result indicates that the information present in the mechanical variables

accounts for most of the information that the full model uses to predict spike rates. The opposite is true for neuron 8: the information present in the kinematic variables better accounts for the information that the full model uses to predict spike rates.

The quality of the subset models is quantified over all neurons in Fig. 2.5B, which plots the R^2 values between the predictions of the mechanical subset model and those of the full model against the R^2 values between the predictions of the kinematic subset model and those of the full model. An inverse relationship is apparent, indicating that if the predictions of one subset model account well for the predictions of the full model, the predictions of the other subset model do not.

So far, our analysis has not addressed the quality of the full model predictions. To quantify the accuracy of the full model, we computed the Pearson Correlation Coefficient (R) between the GLM predicted rate and the observed spike rate, obtained by smoothing the spike train with a Gaussian kernel ($\sigma = 15$ ms; see *Materials and Methods*). In Fig. 2.5B, data points are shaded red if their R is above the median R value (0.3), and grey if their R is equal to or below the median R value. A majority of the red markers (10/15) fall below the diagonal, suggesting that when the full model relies on the information provided by the mechanical subset of input variables, the model performs better.

We next asked how well the full model and the subset models could predict the spike rate of each neuron. The distribution of R values for the full model is shown in Fig. 2.6A. The median R value across all neurons is 0.30. There was no significant difference between active contact and passive deflections (Wilcoxon rank-sum test $p = 0.18$).

We then asked how the accuracy of the subset models compares to that of the full model for both active contacts and manual deflections. In Fig. 2.6B we plot the distribution of the percent error between the full model and each of the subset models. Percent errors near zero indicate that the subset model performed as well as the full model; values below zero indicate that the subset model performed better than the full model. The data shown in Fig. 2.6B omits two points for which the full model performs worse than both subset models. These points also exhibited the worst full model performance, with R values smaller than 0.05. All subsequent analyses omit these two points.

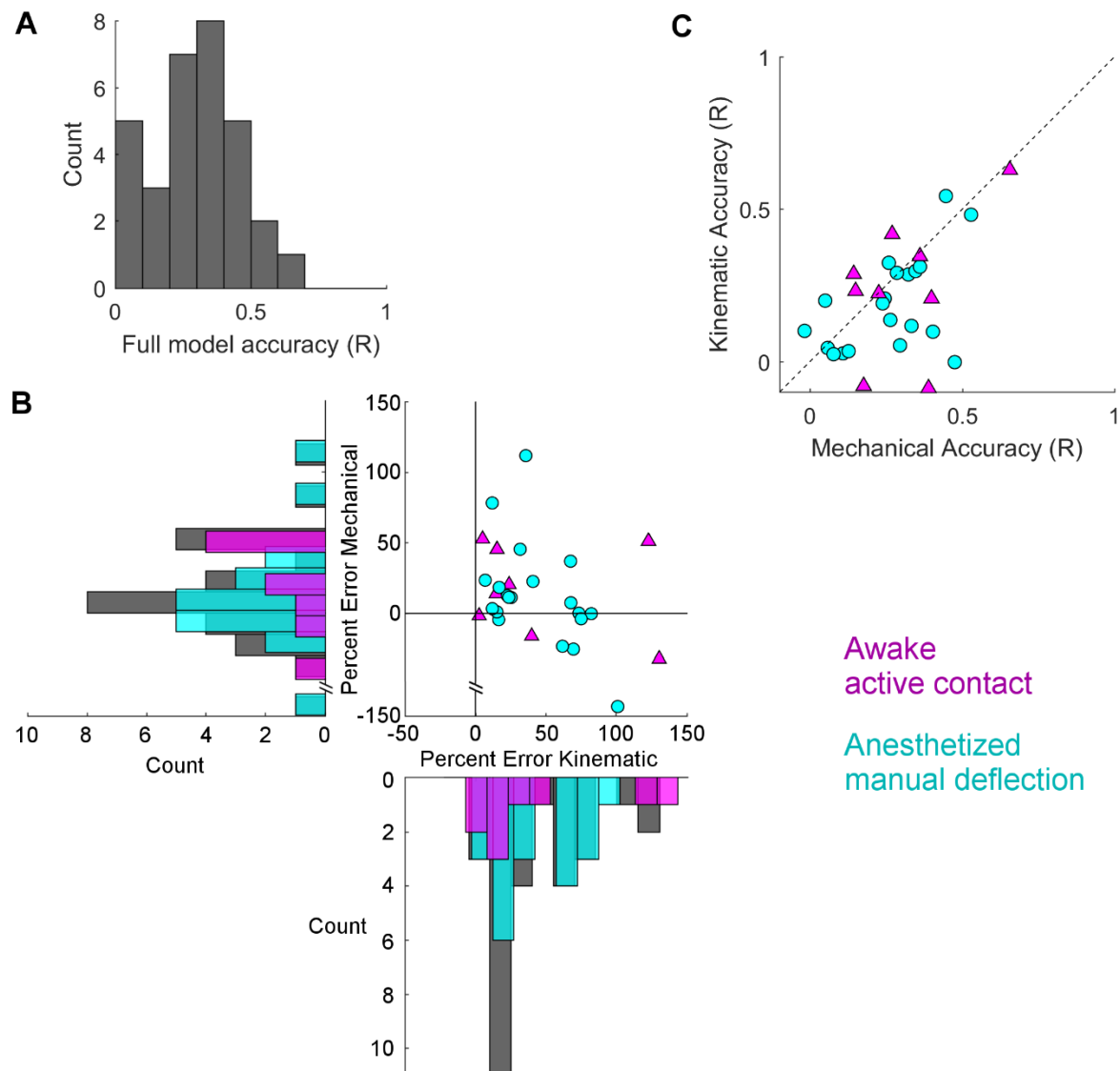


Figure 2.6: Mechanical models outperform kinematic models for manual deflections.

Pearson correlation coefficients (R) between GLM predictions and observed spike rate smoothed at 15 ms are compared between the full model and the subset models. **(A)** Histogram of Pearson correlations between the spike rates predicted by the full model and the observed spike rates, for all neurons. **(B)** Percent error between the R value for the full model and for each of the subset models is plotted for each neuron. Active contact responses are plotted as magenta triangles, manual deflections as cyan circles. Values close to zero indicate that the subset model performed almost as well as the full model; values less than zero indicate that the subset model performed better than the full model. Histograms indicate the distributions of the percent differences of each subset model for active contacts (magenta), manual deflections (cyan), and the whole population (gray). For the data shown here (see text), results for the

subset model trained on mechanical data are significantly closer to zero for manual deflections but not for active contacts. (C) The R values for the two subset models are plotted against each other. Points that lie below the diagonal indicate that the mechanical model better predicted the spike rate than the kinematic model. Color and marker scheme same as in (B).

For the manual stimulation data, the median percent error for the mechanical subset models tend to lie closer to zero than the median percent error for the kinematic models (Wilcoxon signed rank test $p < 0.05$); in contrast, there is no such trend for the active contact data (Wilcoxon signed rank test $p = 0.43$).

Finally, in Fig. 2.6C, we compared the accuracy of the mechanical subset model versus that of the kinematic subset model for both active contacts and passive, manual deflections. We found that 75% (15/20) of neurons recorded with passive stimulation lie below the diagonal (linear model slope 95% CI = [0.20 0.96], paired t-test $p < 0.05$), while those neurons recorded with active touch lie closer to the diagonal (6/9 above, 3/9 below; linear model slope 95% CI = [-0.42, 1.73], paired t-test $p = 0.37$). These results indicate that although the mechanical model better predicts firing during manual stimulation, there is no evident preference for kinematic or mechanical models during active touch.

The input space characterization in Fig. 2.3 explains why it is not possible to distinguish between subset models during active contact: in this scenario, the input space is relatively small and the kinematics and mechanics tend to be more tightly coupled than under manual, passive stimulation. If the inputs to the two subset models are highly coupled – as they are in the active case – then these models receive similar input information and neither can be expected to predict V_g activity better than the other.

2.4 Discussion

Neurons of the trigeminal ganglion are the gatekeepers of all available tactile information in the rodent vibrissal system. The manner in which these neurons represent tactile information places direct constraints on the processing performed by more central trigeminal structures, including thalamus and cortex. Understanding how information is encoded and transformed in Vg neurons is thus essential to obtaining an understanding of vibrissal related responses in these central structures.

2.4.1 Kinematic and mechanical signals are coupled in standard passive stimulation experiments

Historically, responses of neurons in the vibrissotrigeminal system have been described in terms of whisker kinematics (Gibson et al., 1983b; Jones et al., 2004a; Jones et al., 2004b; Leiser et al., 2007; Lottem et al., 2015; Moore et al., 2015; Shoykhet et al., 2000; Simons, 1978; Szwed et al., 2003; Szwed et al., 2006b; Zucker et al., 1969). More recently, however, studies have suggested that mechanics offer an alternative explanation for firing properties of neurons at multiple levels of the trigeminal pathway (Campagner et al., 2016; Chen et al., 2015; Hires et al., 2015; Xu et al., 2012).

The possibility that Vg neurons encode the mechanics of touch is not inconsistent with the body of literature describing kinematic encoding, because mechanical and kinematic variables are often inherently coupled. It is common to stimulate whiskers through small angles close to the base, so that almost no bending of the whisker occurs (Gibson et al., 1983b; Jones et al., 2004a; Jones et al., 2004b; Lichtenstein et al., 1990; Zucker et al., 1969). Under these stimulation conditions there is no room for mechanics and kinematics to decouple, making it impossible to distinguish between these two coding possibilities. Campagner et al. (2016) elegantly demonstrate this coupling during

passive stimulation with a piezoelectric (piezo) bender. They show that during piezo stimulation, curvature change and angle are tightly correlated; GLMs based on either of these variables therefore produce indistinguishable predictions. They further show that in the awake animal, in contrast, curvature change and angle are decorrelated; they attribute this decorrelation to the awake condition.

The novel manual stimulation paradigm of the present work demonstrates that kinematics and mechanics are not necessarily coupled during passive stimulation, nor necessarily decoupled during active contact (Fig 2.3). Decoupling is essential to distinguish between the two possible coding schemes in the trigeminal ganglion.

2.4.2 Decoupling mechanical and kinematic signals during contact reveals that Vg responses are better predicted by mechanics than kinematics

The novel manual whisker stimulation protocol employed in the present work allows us to reliably explore larger regions of input space in which the strong coupling between mechanics and kinematics breaks down (Fig. 2.3). By working in this decoupled regime, the present study demonstrates that Vg neurons more closely represent mechanical rather than kinematic variables during contact. The optimal filters produced by the GLM more heavily weight the mechanics of contact; on average, bending moment is the most important predictor in models that have access to both mechanical and kinematic inputs (Fig. 2.4B).

Furthermore, in cases where mechanics (rather than kinematics) account for most of the predictive ability of the full model, the full model better predicts the spiking behavior of the neuron. The predictive accuracy of models with access to only mechanical inputs is frequently as good as that of models with access to all inputs; this is less frequently the case for models with access to only

kinematic inputs (Fig. 2.6B). Finally, models with access to only mechanical inputs perform better than those with access to only kinematic inputs (Fig. 2.6C).

Importantly, the improved predictive accuracy attributed to mechanical variables is seen only for experiments in which the kinematics and mechanics are decoupled and thus carry distinct information. In our experiments, body-restrained awake animals only infrequently exhibited the type of whisking behavior that would be required to sample a large input space and decouple kinematics and mechanics. Accordingly, models of Vg responses in the awake animal based on mechanical variables rarely outperformed those based on kinematic variables, practically mirroring the null result observed by Campagner et al. (2016) during passive stimulation when mechanical and kinematic information were coupled.

It is worth emphasizing that our conclusions, as well as those of Campagner et al. (2016), regarding the comparative ability of kinematic and mechanical variables to predict the firing of Vg neurons, are based on a simple model of neural encoding: that Vg neurons respond to a linear combination of relevant features of the stimulus, followed by a global static nonlinearity that accounts for the Poisson statistics of the spike generation process. This is the conceptual framework that underlies the choice of GLM models, whose ability to predict the firing of Vg neurons in response to passive stimulation was first established by Bale et al. (2013). In asking which set of variables, kinematic vs mechanical, are better predictors of Vg activity when used as inputs to a GLM model, we ask which set of variables is more informative within the hypothesis of linear-non-linear (LNL) encoding.

2.4.3 Kinematic and mechanical variables as explanatory variables for Vg firing

At first glance, some results of the present work may appear to contradict those of Campagner et al. (2016). Our results show that mechanical models perform better than kinematic models in anesthetized experiments but show little distinction in the awake animal. In direct contrast, Campagner et al. (2016) find similar performance of mechanical and kinematic models in the anesthetized animal but that mechanical models perform better than kinematic models in the awake preparation.

The fundamental reason for the apparent discrepancy is that in the awake animal Campagner et al. (2016) use a kinematic variable (θ_{head}) that varies independently of object contact, but a mechanical variable (change in curvature) that varies only with contact. Given that the response of Vg neurons is strongly correlated with contact (Leiser et al., 2007; Zucker et al., 1969), the mechanical variable will necessarily have a higher predictive value, especially at 100 ms time scales that match the duration of a whisk.

The reason θ_{head} is independent of contact is that this angle is measured with respect to the midline of the animal's head. In contrast, change in curvature at the base (a proxy for bending moment) is measured independently of the whisker's position relative to the head. The angle θ_{head} and curvature change will be decoupled in the awake experiments because contact with an object can occur at different positions relative to the head. For example, a whisker can exhibit very similar curvature changes regardless of whether it makes contact with a peg at $\theta_{\text{head}} = 70^\circ$ or at $\theta_{\text{head}} = 110^\circ$.

In Campagner et al. (2016) figure 2.4G it is clear that if one were to account for the value of θ_{head} at the initial contact with the pole, curvature change would be strongly correlated with an angle that would not be θ_{head} but θ_{push} – the angle used in the present work and in other studies of

mechanical coding of object location (Bagdasarian et al., 2013; Birdwell et al., 2007; Kaneko et al., 1998; Pammer et al., 2013; Solomon et al., 2011). Campagner et al. (2016) briefly address this point. Their results from the awake animal show smaller differences in performance between models based on kinematic or mechanical inputs when θ_{push} is used as the kinematic variable, consistent with the present findings.

In the anesthetized rat experiments of Campagner et al. (2016), θ_{head} and curvature are always strongly correlated because the whisker is trimmed (to 5 mm), angles of deflection are relatively small (10°), and the deflection is always applied at the same value of θ_{head} . Had these experiments used large amplitude deflections and/or deflections further from the whisker base, θ_{head} would presumably have decoupled from curvature changes.

More subtly, the quantification of mechanical inputs differs between the present work and that of Campagner et al. (2016). Forces and moments at the whisker base cannot be measured directly because any sensor placed at the whisker base would interfere with the whisker's mechanics. Campagner et al., (2016) use curvature change at the base as a proxy for bending moment, an approximation based on linear elastic beam theory (Beer et al., 2015). In contrast, we use a validated quasi-static model of whisker bending to compute forces and moments at the base during contact (Birdwell et al., 2007; Huet et al., 2016; Huet et al., 2015; Solomon et al., 2008; Solomon et al., 2010). This model accounts for the full shape of the whisker, not just the base segment, and offers the advantage of computing the axial and transverse forces in addition to bending moment.

2.4.4 A mechanical framework for interpreting primary sensory signals during both contact and non-contact whisking

Our work and that of Campagner et al. (2016) agree that Vg neurons encode mechanical variables more robustly than kinematic variables; we suggest that the consistency of this result across studies helps interpret recent data demonstrating phase coding in Vg neurons during free air whisking (Wallach et al., 2016). The work of Campagner et al. (2016) shows that during non-contact whisking, a GLM with access to angular acceleration can account for much of the Vg firing. With the assumption that Vg neurons are mechanically sensitive, our analyses suggest that the phase encoding described by Wallach et al., 2016 and the angular acceleration tuning described by Campagner et al. (2016) both result from inertial forces on the follicle that occur during periods of high angular acceleration (Boubenec et al., 2012; Quist et al., 2014).

Many Vg neurons are known to respond during both non-contact and contact whisking (Leiser et al., 2007; Szwed et al., 2003). Here we propose that the encoding of mechanical signals provides a unified explanation for both phase tuning during non-contact whisking and responses during contact. Ultimately, a dynamic model that describes inertial forces during non-contact whisking will be required to verify this hypothesis. It remains unknown how downstream neurons might distinguish Vg spikes that encode phase and hypothetically represent inertial forces from Vg spikes that represent contact forces.

In this light, the results of all four recent studies (Campagner et al., 2016; Quist et al., 2014; Wallach et al., 2016), including work in this thesis, provide strong support to the view that Vg neural responses more generally represent the mechanical deformations that occur at the level of the follicle, and that apparent correlations between Vg firing and kinematics are a result of inherent correlations between kinematics and mechanics. This line of evidence suggests that previous results describing the encoding of kinematic variables in the Vg correspond to scenarios

characterized by strong correlations between kinematic and mechanical variables. It remains possible that central brain regions take advantage of this inherent correlation to extract behaviorally relevant information about object location or features; there is support from both simulation (Solomon et al., 2011) and behavioral (Bagdasarian et al., 2013; Pammer et al., 2013) studies indicating that rodents could use a combination of F_x and M to determine the 2D location of a contact point.

2.4.5 Limitations of the current approach

Our models were unable to reach very high prediction accuracies (median R value = 0.30, max = 0.65); this performance is not as good as might be expected in view of previous evidence that Vg neuron responses are highly precise and repeatable given identical stimuli (Bale et al., 2015; Jones et al., 2004a; Jones et al., 2004b).

We offer four explanations for these seemingly low correlation values.

First, we note that in the present study, R value is only computed during contact, in order to avoid inflation of this statistic due to periods of non-contact when spiking is absent (anesthetized) or sparse (awake). When correlation coefficients were computed to include both periods of contact and non-contact in the awake animal, median R-values increased from 0.27 to 0.47 for kinematic models and 0.26 to 0.38 for mechanical models. Including periods of non-contact in model evaluation will tend to inflate model performance; any variable that captures transitions between contact and non-contact will easily predict the associated changes in Vg firing rate.

Second, the present work, as well as the majority of reports of Vg neuron firing activity in both awake and anesthetized experiments, is based entirely on a 2D analysis, even though there is ample evidence that the whisker moves in 3D (Hobbs et al., 2015, 2016; Huet et al., 2014, 2016; Huet et

al., 2015; Knutsen et al., 2008; Yang et al., 2016) and that Vg neurons are directionally tuned in three dimensions (Jones et al., 2004a; Lichtenstein et al., 1990; Minnery et al., 2003).

Third, the quasi-static models used to compute forces and moments at the base of the whisker omit the effects of friction and whisker dynamics, including collisions and vibrations (Boubenec et al., 2012; Shantanu P Jadhav et al., 2009; Quist et al., 2014; Ritt et al., 2008; Wolfe et al., 2008; Yan et al., 2013). To predict spikes at high temporal resolution would require the use of a dynamic model and the ability to track the whisker at spatiotemporal resolutions beyond the capability of the videographic approaches used here.

Lastly, our models are based on linear combinations of stimuli that vary over wide ranges. The only nonlinearity in the model, a static nonlinearity applied to the linear combination as a whole, accounts for the Poisson nature of spiking statistics. This type of simplified Linear-Nonlinear (LNL) model offers strong mathematical advantages; in the case of a GLM, a guarantee that the fitting function that determines the coefficients of the model is convex and has a unique solution easily reachable by gradient methods. However, these models do not allow for linear combinations or nonlinearities that could be specific to some regions in the space of inputs. As our experimental methods sample wider regions of input space, it seems reasonable to expect that a single linearized assumption over the full space followed by a single, global nonlinear transformation will prove to be too simplistic. The relatively low quality of prediction achieved here thus might signal the limitations of this type of GLM.

Another limitation of our approach is a time resolution of 15 ms, considerably less than the ms or even sub-ms resolution exhibited by Vg neurons (Bale et al., 2015; Jones et al., 2004a). Temporal resolution was similarly limited the study of Campagner et al. (2016), who employed a 100 ms

window in contrast to our 15 ms Gaussian kernel. This limit is due in part to experimental constraints in the temporal resolution of the kinematic and mechanical variables chosen as explanatory variables for Vg activity and used as GLM inputs, as addressed in both *Results* and *Experimental Procedures*. As discussed above, the quasi-static models used to compute forces and moments at the base of the whisker further limit the achievable time resolution.

In addition, both our work and that of Campagner et al. (2016) use a similar single-trial modeling approach. Trial averaging would have allowed us to predict spike timing with higher accuracy (Bale et al., 2013), but would have required precise duplication of motor command across trials. The variability of whisking behavior in awake animals prevents this duplication. As for the deflection experiments in anesthetized animals, precise duplication could only be achieved by sampling within a narrow region of stimulus space, an approach deliberately avoided here in order to achieve kinematic and mechanical decoupling.

Our work thus offers predictive accuracies as high as can be achieved within these experimental and modeling limitations. The results point towards the conclusion that mechanics more accurately predict primary sensory neuron firing than kinematics, within the hypothesis of linear-non-linear (LNL) encoding, and when the two sets of variables are decoupled. A more stringent test of this hypothesis would require a full 3D characterization of both kinematic and mechanical signals at higher spatiotemporal resolution, a full dynamic model of the whisker for computing forces and moments at its base, and possibly an increased level of modeling sophistication beyond GLMs.

Ultimately, access to a large, decoupled input space is likely to be critical in understanding the coding properties of Vg neurons during natural behavior. Body or head restrained animals tend to generate relatively stereotyped, small angle whisking motions (Deutsch et al., 2012) that sample

the input space within the coupled regime (Fig. 2.3). However, tactile information acquired through whisking during exploratory behavior is varied and complex (Arkley et al., 2014; Carvell et al., 1990; Grant et al., 2009; Hobbs et al., 2016; Mitchinson et al., 2007; Saraf-Sinik et al., 2015; Schroeder et al., 2016; Sellien et al., 2005; Towal et al., 2008; Voigts et al., 2015). Neurons of the Vg must be able to encode the signals associated with the full range of potential stimuli, including large angle deflections and very distal contacts. By adopting a mechanical characterization of tactile information, we can quantify the large input space available during tactile sensation in a manner that incorporates the true shape and deformability of the whisker.

2.5 Materials and Methods

All procedures involving animals were approved in advance by the Northwestern University Animal Care and Use Committee. A total of fourteen female Long Evans rats (age 2-6 months) were used.

2.5.1 Surgical Procedures

Animals were anesthetized with a ketamine-xylazine hydrochloride combination delivered intraperitoneally (60 mg/kg ketamine, 3.0 mg/kg xylazine, and 0.6 mg/kg acepromazine maleate). Four or five stainless steel screws were placed in the skull over neocortical areas and covered in dental acrylic. For anesthetized recordings this structure was affixed to the surgical bed; for chronic (awake) recordings, it formed the base of the electrode implant.

A small (~1mm diameter) craniotomy was then performed in order to allow access to the trigeminal ganglion (Vg), at location ~2mm caudal relative to bregma and ~2mm lateral to the midline. A single tungsten electrode (FHC, Bowdoin, ME; typical impedance 2-5 M Ω) was lowered to a depth of ~10mm until multi-unit responses to whisker deflections could be heard. The

electrode was then lowered more slowly until isolated single neuron responses to tactile stimulation of a single vibrissa were obtained.

For chronic recordings, the electrode was then fixed in place using dental acrylic. In some animals, electrodes were bilaterally implanted in the Vg. Recordings from awake, chronically implanted animals were started no sooner than four days after surgery and continued for up to three weeks. All chronic implantation surgeries were performed in a sterile field.

2.5.1.1 Anesthetized recordings

Five animals were used to test the responses of Vg neurons to passive, manual deflection. After performing the craniotomy described above, single tungsten electrodes (FHC $\sim 1\text{M}\Omega$) were lowered to a depth of ~ 10 mm until a neuron that responded to the deflection of a single whisker was isolated. We recorded video from a top-down view at 300 fps with an exposure time of 1 ms (Teledyne Dalsa Genie HM640; Waterloo, Canada).

Neural signals were amplified on an A-M Systems (Sequim, WA) four channel amplifier (1,000x gain) with analog bandpass filtering between 10 Hz and 10 kHz before digital sampling at 40 kHz using Datawave SciWorks (Loveland, CO). After acquisition, traces were digitally bandpass filtered between 300 Hz and 6,000 Hz before spike sorting. Spikes were identified and sorted offline, and spike times were rounded to the nearest ms for comparison with video data. Examples of raw data are shown in Fig. 2.1A-C.

In order to robustly track the whisker in the high-speed video, the surrounding fur was removed with depilatory cream (Nair™; Church and Dwight, Ewing, NJ) and surrounding whiskers were either trimmed or held back against the fur. Care was taken not to deform the whisker or the mystacial pad during recordings.

Whiskers were deflected manually by pressing a 0.3 mm graphite rod against the whisker (Supplementary Video 2.1B). Between 20 and 40 deflections were applied at variable radial distances (up to 90% of the whisker length), at two velocities and two directions (rostral to caudal, and caudal to rostral) for a total of 80-160 deflections per whisker. Analyses were restricted to distal contacts (>40% of the whisker length), where the follicle does not move appreciably during contact. Whiskers were also held in a deflected position for periods of about 3 s to test adaptation characteristics. All deflections were on the order of several mm.

2.5.1.2 Awake recordings

Seven animals were gentled for 8-10 days prior to surgery. During gentling, rats were acclimated to restraint in a V-shaped fabric bag that prevented body movement but permitted head and neck movements.

Starting four days after surgery, on each day of testing we gently restrained the rat and again confirmed that each neuron responded to tactile stimulation of one and only one whisker. All other whiskers on that side of the rat's face were trimmed to the level of the fur. Rats were then placed in the fabric bag, and high-speed video (Photron FastCam, San Diego, CA; either 1024PCI or 512PCI) was used to record the top-down view of the rat's head as it whisked against a rigid vertical peg (3 mm diameter). Video was taken at 1,000 fps, with a shutter speed of 1/3,000 s to reduce motion blur.

Signals from Vg neurons were recorded with a Triangle Biosystems (Durham, NC) 8-channel preamplifier (2x gain) and a custom-built amplifier (500x gain). Signals were analog band-pass filtered between 0.33 Hz and 10 kHz before sampling at 40 kHz using Datawave SciWorks. Traces were then digitally bandpass filtered between 300 Hz and 8,000 Hz before spike sorting. Spikes

were identified and sorted offline, and spike times were rounded to the nearest ms for comparison with video data. Examples of raw data are shown in Fig. 2.1 D-E.

2.5.2 Calculation of kinematic and mechanical variables

For both anesthetized and awake experiments, whisker shape was extracted from each video frame using the software Whisk (Clack et al., 2012). The kinematic and mechanical variables of contact were computed from the whisker shape; see Fig. 2.2.

The kinematic variables of contact are: radial distance (r), angle of contact (θ_{push} or $\theta_{\text{deflection}}$), and angular velocity (V). The variable r is the linear distance between the basepoint and the contact point. The variable $\theta_{\text{deflection}}$ is valid for manual deflection; as illustrated in Fig. 2.2A, it is the angle between two line segments: one that connects the initial point of contact to the whisker basepoint and one that connects the current contact point to the whisker basepoint (Gibson et al., 1983a, 1983b; Lichtenstein et al., 1990; Lottem et al., 2009, 2011; Shoykhet et al., 2000; Shoykhet et al., 2003). The variable θ_{push} is valid for active whisking; as illustrated in Fig. 2.2D, it represents the angle swept out by the tangent to the whisker at its base from the time of contact onset to the current time (Bagdasarian et al., 2013; Quist et al., 2012b; Solomon et al., 2011). The velocity (V) is the temporal derivative of either $\theta_{\text{deflection}}$ or θ_{push} .

The mechanical variables of contact are the axial force (F_x), the force parallel to the whisker axis near its base, positive pointing out of the follicle; the transverse force (F_y), the force perpendicular to the whisker axis, directed in the rostral direction; and the bending moment (M), the moment about the vertical z-axis that passes through the whisker base. Mechanical variables were

computed using a quasi-static model of whisker bending (Birdwell et al., 2007; Quist et al., 2012b; Solomon et al., 2008; Solomon et al., 2010).

All mechanical and kinematic data were median filtered to eliminate point outliers. Variables computed from video acquired at 300 fps were linearly interpolated to 1,000 Hz for comparison with spike times on the 1 ms scale. Velocity was calculated using a central difference approximation of the angular component of contact and low pass filtered at 85 Hz.

The spike train was smoothed with a Gaussian kernel with standard deviation σ to find the rate $r(t)$:

$$r(t) = \frac{1}{\sqrt{2\pi\sigma^2}} \sum_{j=1}^N e^{-\frac{(t-t_j)^2}{2\sigma^2}}, \quad (\text{Equation 2.1})$$

where N is the total number of spikes, σ is the standard deviation of the kernel, and t_j is the time of spike j . The standard deviation σ of the Gaussian kernel was varied between 1 ms and 500 ms to observe the effect of temporal smoothing on the quality of predictions. An optimal kernel width of $\sigma = 15$ ms was chosen for all subsequent analyses. This was the smallest value of σ , below which we observed a sharp decrease in the quality of predictions.

2.5.3 Generalized Linear Models:

Each GLM is of the form:

$$p(t) = f\left(\sum_{j=1}^K \sum_{t'=0}^{\tau} \alpha_j(t') x_j(t-t')\right). \quad (\text{Equation 2.2})$$

Here $p(t)$ is the probability that the neuron emits a spike in the 1 ms time interval centered at time t , f is a logistic nonlinearity, and j sums over all the predictor variables. Each one of these variables x_j , $1 \leq j \leq K$, contributes to the argument of the logistic nonlinearity through its current value and its values in the preceding τ time bins, weighted by the filter parameters $\alpha_j(t')$, $0 \leq t' \leq \tau$. Full models used $(r, \theta, V, F_x, F_y, M)$ as predictor variables ($K = 6$), while subset models had access to either kinematic variables (r, θ, V) or mechanical variables (F_x, F_y, M) , so that $K = 3$.

Since the neural response is quantified as a spike either present or absent in each 1 ms time bin, the statistics process being modeled is Bernoulli and the nonlinearity is sigmoidal (McCullagh et al., 1989):

$$f(u) = \frac{1}{1+e^{-u}}. \quad (\text{Equation 2.3})$$

The GLM finds the filters $\{\alpha_j(t')\}$, $0 \leq t' \leq \tau$, $1 \leq j \leq K$ that maximize the likelihood of the observed spiking activity. To enforce continuity of the filters as a function of time and reduce the number of coefficients needed to specify the model, it is convenient to introduce a basis of “raised cosine bumps” $b_l(t)$, $1 \leq l \leq L$ (Pillow et al., 2008). Here we used the $L = 5$ basis shown in Fig. 2.4A. The functions peak at 0 ms ($l = 1$), 1 ms ($l = 2$), 3 ms ($l = 3$), 8 ms ($l = 4$), and 17 ms ($l = 5$); the basis covers 75 ms into the past.

The expansion of each filter in terms of this basis, namely

$$\alpha_j(t') = \sum_{l=1}^L b_l(t') \beta_{lj}, \quad (\text{Equation 2.4})$$

results in an interesting reformulation of the GLM:

$$p(t) = f\left(\sum_{j=1}^K \sum_{l=1}^L \beta_{lj} \tilde{x}_{lj}(t)\right), \quad (\text{Equation 2.5})$$

where the input variables to the model $\tilde{x}_{lj}(t)$ are now “convolved predictors”, the filtered versions of the original input variables, namely:

$$\tilde{x}_{lj}(t) = \sum_{t'=0}^{\tau} b_l(t') x_j(t-t'). \quad (\text{Equation 2.6})$$

In this formulation, the problem of fitting the parameters of the GLM is reduced from that of finding the filters $\alpha_j(t')$, $1 \leq j \leq K$, $0 \leq t' \leq \tau$, to that of fitting a smaller number of parameters: the coefficients β_{lj} , $1 \leq l \leq L$, $1 \leq j \leq K$.

To evaluate each GLM we implemented ten-fold cross-validation, using 90% of each neuron’s dataset to fit the coefficients β_{lj} . The fitted GLM was used to predict the spike rate on the remaining 10% of the data. This procedure was repeated ten times, so that the entire neural response was eventually predicted from a model whose coefficients were fit on independent data. This method prevents overfitting and allows the model to be evaluated based on how well it generalizes to new data.

The quality of each GLM was quantified through the correlation coefficient between the predicted rate $p(t)$ of Equation 5 and the rate $r(t)$ obtained from Equation 1.

Data for non-contact periods were omitted in calculations of correlation coefficients. Given that Vg neurons do not fire during non-contact, a precise prediction of no activity during these periods would have unduly inflated model performance. Predictions were tracked only during contact periods.

Percent difference between the subset models and the full model was calculated as $100 * \frac{(R_{full} - R_{subset})}{R_{full}}$, where R is the Pearson Correlation Coefficient between the observed spike rate $r(t)$ and the predicted spike rate $p(t)$ obtained with either the full model or one of the two subset models.

Chapter 3: Whisker vibrations and the activity of trigeminal primary afferents in response to airflow

3.1 Abstract

Rodents are the most commonly studied model system in neuroscience, but surprisingly few studies investigate the natural sensory stimuli that rodent nervous systems evolved to interpret. Even fewer studies examine neural responses to these natural stimuli. Decades of research have investigated the rat vibrissal (whisker) system in the context of direct touch and tactile stimulation, but recent work has shown that rats also use their whiskers to help detect and localize airflow. The present study investigates the neural basis for this ability as dictated by the mechanical response of whiskers to airflow. Mechanical experiments show that a whisker's vibration magnitude depends on airspeed and the intrinsic shape of the whisker. Surprisingly, the direction of the whisker's vibration changes as a function of airflow speed: vibrations transition from parallel to perpendicular with respect to the airflow as airspeed increases. Recordings from primary sensory trigeminal ganglion neurons (Vg) show that these neurons exhibit responses consistent with those that would be predicted from direct touch. Trigeminal neuron firing rate increases with airspeed, is modulated by the orientation of the whisker relative to the airflow, and is influenced by the whisker's resonant frequencies. We develop a simple model to describe how a population of neurons could leverage mechanical relationships to decode both airspeed and direction. These results open new avenues for studying vibrissotactile regions of the brain in the context of evolutionarily important airflow-sensing behaviors and olfactory search.

3.2 Introduction

Animal nervous systems, and the computations they perform, evolve to process and act on sensory information critical for survival. For rodents, the whiskers (vibrissae) are a particularly important sensory modality and the brain structures associated with the whiskers are correspondingly expanded (Welker et al., 1974; Woolsey et al., 1970). Although the rodent whisker system is a premier model for studying active touch (Chakrabarti et al., 2018; Hobbs et al., 2015; Kleinfeld et al., 2011; Knutsen et al., 2006; Maravall et al., 2014; O'Connor et al., 2013) we still lack a full understanding of the stimuli that guided the evolution of vibrissal-related neural structures.

We recently demonstrated that whiskers aid rats in localizing an airflow source, suggesting that somatosensory regions of the rodent brain may have evolved to process signals associated with airflow, in addition to direct touch (Yu et al., 2016a). Such processing is likely to be particularly important in the coordination of whisking and sniffing during olfactory search (Bhattacharyya et al., 2015; Kleinfeld et al., 2014; Moore et al., 2013; Ranade et al., 2013; Smear et al., 2011). These behavioral findings raise the question: how do the whiskers mechanically respond to airflow, and how do whisker-sensitive neurons of the trigeminal system represent airflow information?

Previous work has shown that a whisker both bends and vibrates in response to airflow stimulation (Yu et al., 2016b). Vibrissal-responsive neurons would be expected to respond to both of these mechanical components. In the present study we quantify the magnitude and direction of whisker vibration for a wide range of airflow stimulation parameters. We then record from a small number of vibrissal-responsive primary sensory neurons in the trigeminal ganglion (Vg) while delivering airflow stimuli to the whisker array.

Because the responses of Vg neurons to direct touch are well-characterized, we can confirm expectations for their responses to airflow using only a small set of neurons. We find that Vg firing rates adapt over the course of seconds; firing rates increase with airspeed and are affected by the orientation of the whisker relative to airflow; and spiking periodicity is related to the whiskers' resonant frequencies. We conclude with a synthetic model that hypothesizes how features of both bending and vibration may be coded simultaneously in whisker-responsive afferents, providing the animal cues about both airspeed and direction.

3.3 Materials and Methods

All procedures involving animals were approved in advance by Northwestern University's Animal Care and Use Committee.

3.3.4 Mechanical experiments

Mechanical experiments were performed on five vibrissae plucked from a single, adult (≥ 3 months old) female Long Evans rat. Each whisker was identified by its row and column position within the array (van der Loos et al., 1973): E2, α , A2, C2, and D5. To ensure that the whiskers were representative of typical rat whiskers, we confirmed that their geometric and mechanical parameters (length, base diameter, density) fell well within the range of the dataset described by Belli et al., 2017. This dataset includes parameters for 519 whiskers from both male and female rats, with whiskers obtained in seven different laboratories. We therefore expect all mechanical results to generalize to male rats. The geometry of each whisker was obtained by scanning it on a flatbed scanner (Epson Perfection 4180 Photo) and then manually tracing its shape in Photoshop. Detailed descriptions of the experimental setup, three-dimensional video tracking, and vibrissal morphology are provided in previous work (Yu et al., 2016b). Briefly, the base of each whisker

was mounted in a clamp and a hair dryer was used to deliver airflow through a long PVC tube at six different airspeeds (approximately 0.5, 1.4, 2.2, 3.4, 4.4 and 5.6 m/s) The vibrissae were positioned such that the intrinsic curvature was oriented at five angles relative to the airflow (0° , 45° , 90° , 135° , and 180°).

For each combination of orientation and airspeed, two orthogonally mounted video cameras (Photron, FASTCAM-1024PCI), each fitted with a macro lens, were used to capture the whisker's shape at 1,000 frames per second (fps). The two camera views were merged to reconstruct the whisker's 3D shape. To ensure we captured steady-state behavior of the whisker, video recording began at least 10 seconds after airflow was applied and lasted for 5 seconds (5,000 frames).

The airspeeds were selected based on meteorological studies of land-surface wind speeds, which typically range between 0-5 m/s (Monahan et al., 2011). We also used a hot-wire anemometer (Omega, model HHF42, resolution = 0.1m/s) to measure wind speed in locations where we had observed rats to live (bushes, dumpsters, fields, etc.). These measurements confirmed that the range 0.5-5.6 m/s bracketed the wind speeds that rats would typically encounter.

Reynolds number (Re) calculations were performed for all 519 whiskers in the dataset of Belli et al., 2017. Re was computed as $Re = uD/\nu$, where u is the airflow speed, D is the diameter of the whisker, and ν is the kinematic viscosity of air. For fixed values of u and ν , the maximum value for Re is always found at the whisker base, where the diameter is largest.

3.3.5 Quantifying vibration magnitude

Previous studies have shown that in response to an airflow stimulus a whisker will bend to a new position and then vibrate around that new deflected position (Yu et al., 2016b). Bending and

vibration can thus be thought of as the mean and fluctuations of the whisker's position in airflow. Vibration magnitude was therefore computed as the fluctuations of the whisker about its mean, as follows.

First, each whisker was discretized into nodes, spaced 2 mm apart. Second, we calculated the mean (x, y, z) position of each node in airflow (the temporal average of the position over all 5,000 frames). We found the vector connecting the whisker's basepoint to the mean position of that node ("vector 1"). Third, for each of the k video frames we found the vector connecting the whisker's basepoint to the instantaneous (x, y, z) position of that node ("vector 2"). For each node and each frame k , the instantaneous vibration magnitude ϕ_k was then computed as the angle between vector 1 and vector 2. Finally, for each node, the vibration magnitude ϕ_{vib} was found as the time average of the absolute value of all 5,000 instantaneous vibration magnitudes:

$$\phi_{vib} = \frac{1}{T} \sum_{k=1}^T |\phi_k| \quad (\text{Equation 3.1})$$

where k is the frame number, and T is the video duration (5,000 frames).

3.3.6 Quantifying vibration direction

To quantify vibration direction we used the following method. At each node along the whisker length, we imagined taking a cross-section of the whisker, perpendicular to its long axis. The position of the node in that cross-sectional plane was then plotted for each video frame. This procedure revealed how much the whisker vibrated at each point along its length. We defined the vibration direction index (*VDI*) to quantify the extent to which this vibration direction is parallel or orthogonal to airflow direction:

$$VDI = \frac{N_{\perp}}{N_{\parallel}} \text{ (Equation 3.2)}$$

where N_{\perp} denotes the number of frames in which the whisker nodal position fell in either the first or third quadrants, and N_{\parallel} is the count in either the second or fourth quadrants. Air is always taken to flow from the second quadrant to the fourth quadrant, at an angle -45° relative to the x-axis. Therefore, N_{\perp} quantifies the number of times that the node was displaced to a position perpendicular to the airflow direction, while N_{\parallel} quantifies the number of times that the node was displaced to a position parallel to the airflow direction. Note that the displacements used to compute the *VDI* contain both perpendicular and parallel (tangential) components. The *VDI* identifies whether the ratio of the perpendicular to parallel components is greater than or smaller than unity. As seen in Fig. 3.4A, $VDI < 1$ indicates an ellipse shape with its major axis in the second and the fourth quadrants, $VDI > 1$ indicates an ellipse shape with its major axis in the first and the third quadrants, and $VDI \approx 1$ indicates a circular shape.

3.3.7 Quantifying whisker resonance

The mass of each whisker was measured using a Mettler-Toledo UMX2 ultra microbalance with a resolution of $\pm 0.1 \mu\text{g}$. The whisker's base diameter (D) and tip diameter were measured at 10x magnification (Leica DM750). After measuring the diameter, the whiskers were scanned on a flatbed scanner (Epson Perfection 4180 Photo) and their shapes were traced in Matlab[®]. These traces were used to compute the whisker's arc length (S). The whisker was approximated as a truncated cone to compute its volume, and divided by its mass to compute its density (ρ). Equation 3, which describes the resonant modes for a fixed-free tapered cantilever beam, was used to calculate the theoretical resonant frequencies for each whisker (Georgian, 1965):

$$f_n = (\lambda_n D/4S^2)(E/\rho)^{1/2}/(2\pi) \quad (3)$$

All parameters on the right side of this equation, except Young's modulus (E) and the coefficient λ_n are either measured values or computed directly from measured ones. The coefficient λ_n , associated with resonant mode number (subscript n), was obtained from linear interpolation between tabulated values (Georgian, 1965), as shown in Table 3.1.-Young's modulus was set at either 3 GPa or 11 GPa (Birdwell et al., 2007; Hartmann et al., 2003; Kan et al., 2013; Neimark et al., 2003; Quist et al., 2011) to bracket the possible range of resonance frequencies.

Whisker identity	Length (mm)	Tip diameter (μm)	Base diameter (μm)	$(A_t/A_b)^{1/2}$	λ_n for Mode 1	λ_n for Mode 2	λ_n for Mode 3
				1.00	3.52	22.03	61.70
				0.50	4.63	19.55	48.50
				0.33	5.29	18.76	43.78
C3	17.7	29	105	0.27	5.70	18.58	42.00
				0.25	5.85	18.51	41.34
□	40.0	36	150	0.24	5.94	18.52	41.05
C4 (2 speeds)	12.8	16	82	0.19	6.39	18.59	39.65
B3	16.4	10	79	0.12	6.98	18.68	37.80
C2	33.8	13	123	0.10	7.16	18.70	37.23
				0.10	7.20	18.71	37.10
E3	23.8	13	139	0.09	7.31	18.89	37.20
C4 (3 speeds)	12.1	7	84	0.08	7.50	19.19	37.37
D3	17.7	5	98	0.05	7.95	19.92	37.77
				0	8.72	21.15	38.45

Table 3.1. Whisker length, tip diameter, and base diameter, and values of the coefficient λ_n used to compute theoretical resonant frequencies. This table shows the geometric parameters of the whiskers associated with the eight recorded neurons. The variables A_t and A_b denote the area of the tip and base of the conical cantilever beam, respectively. Rows that leave whisker parameters blank indicate values of λ_n adopted directly from Georgian (1965). The other rows contain values of λ_n computed by finding $(A_t/A_b)^{1/2}$ from whisker parameters and then linearly interpolating between the values from Georgian (1965).

3.3.8 Neural recordings during airflow stimulation

3.3.8.1 Surgical procedures

Five adult female Long Evans rats (age ~90 days) were anesthetized with an anesthetic cocktail delivered intraperitoneally (60 mg/kg ketamine, 3.0 mg/kg xylazine, and 0.6 mg/kg acepromazine maleate). Due to the limited number of animals, only one sex was used. We expect results to generalize to males, as both follicle structure (Ebara et al., 2002) and primary sensory neuron encoding properties appear consistent across sexes (Gibson et al., 1983b; Jones et al., 2004b; Leiser et al., 2007; Shoykhet et al., 2000; Stuttgen et al., 2006). For the duration of surgery and recording, adequate anesthetic depth was ensured by assessing the toe-pinch reflex every fifteen minutes and by carefully monitoring for any whisker twitches. Boosters were administered as necessary to maintain a deep plane of anesthesia. Body temperature was maintained at approximately 37°C using a water-regulated heat therapy pump (HTP – 1500, Adroit Medical Systems). With the animal placed in a custom head-fixation apparatus, an incision was made along the midline of the scalp and the skull exposed. Three or four stainless steel screws were placed in the skull over neocortical areas and covered in dental acrylic. This structure was affixed to the surgical bed to maintain head fixation while nose brace and the ear bars were removed, to allow full access to the left side of the whisker array.

A ~1 mm diameter craniotomy was performed ~2 mm caudal to bregma and ~2 mm lateral from midline above the trigeminal ganglion (Vg). A tungsten electrode (FHC, Metal Electrode; typical impedance 2–5 M Ω) was advanced to a depth of ~9 mm until multi-unit responses to manual whisker deflections were observed. The electrode was then advanced slowly until a single, whisker responsive, neuron was isolated. Neural signals were amplified through an A-M Systems Model 1700 amplifier with bandpass filtering between 1 Hz and 10 kHz before digital sampling and acquisition at 40 kHz in Datawave SciWorks. After isolation of a single vibrissal responsive unit, airflow stimuli were presented and neural responses were recorded. Recorded voltage signals were digitally bandpass filtered between 300 Hz and 8000 Hz before spike detection and sorting with the open-source software *Klusta* (Rossant et al., 2016).

3.3.8.2 Airflow delivery

As described above, anesthetized animals were placed in a custom head-fixation apparatus that allowed free access to all whiskers on the left side of the mystacial pad. A regulated compressed air source was connected to a custom airflow delivery apparatus, and airflow was supplied from three directions, -45° , 0° and 45° relative to the lambda-bregma plane, towards the center of the whisker array. The airflow delivery apparatus was carefully calibrated to direct airflow to the same point at the center of the array from all three directions, and varying the pressure of the compressed air allowed us to control the airspeed at the center of the vibrissal array as measured with the hot-wire anemometer.

Two protocols were used during experiments. In the first protocol, we measured the airspeed at the center of the array before each stimulus condition (speed/direction combination) and adjusted the pressure of the airflow source to obtain the expected airspeed at the center of the whisker array.

This protocol used two airspeed conditions: 1 m/s and 3 m/s. The second protocol was optimized to increase the amount of data collected by calibrating the airspeed from a fixed apparatus calibrated once before the collection of data. This protocol used 3 speeds (1 m/s, 3 m/s and 5 m/s). Four neurons were recorded using the first protocol and another four neurons were recorded based on the second protocol.

For each combination of airspeed and direction, we presented the airflow stimuli for 10 trials, with the following exceptions in which 9 trials were performed: whisker D3 at 0 deg, 5 m/s; whisker C3 at 45 deg, 5 m/s; whisker B3 at -45 deg, 1 m/s. A trial consisted of sustained airflow presentation for 15 seconds. A pause of 4 seconds between trials was included to allow the whisker to relax to rest.

3.3.8.3 Airflow stimulus calibration

All airspeeds were measured using the hot wire anemometer. To calibrate the airspeeds, the airflow apparatus was fixed in position and the anemometer was affixed to a 3-axis motorized manipulator (Sutter MP-285). Airspeed measurements were taken from the anemometer at a range of positions for all tested pressures and apparent directions.

The airflow map for each combination of speed and direction was obtained and is shown in Fig. 3.1. Each panel in the first column (Fig. 3.1 A-C) compares the measured airspeeds for the different directions, keeping supply pressure constant. The overlap at all positions and directions indicates that, for each pressure (intended airspeed) and location, the airspeed is consistent across directions. Each panel in the second column (Fig. 3.1 D-F) shows the measurements for a given direction across airspeeds. The airspeed drops off as the mediolateral distance increases. The airspeed drops off as rostrocaudal distance increases, but not so much so that the apparent speed at the anterior

region of the whisker array at one pressure is the same as the apparent speed at the posterior region of the array. The airspeed maps at different speed values are distinct from each other (Fig. 3.1 D-F), allowing us to investigate the effect on the neural response from different airflow directions and airspeeds.

3.3.9 Experimental design and statistical analysis

Five whiskers plucked from an adult female Long Evans rat were used in the mechanical experiment, each with different base diameters and arc lengths. Vibrations of each of the five whiskers were analyzed at six different airspeeds and at five different orientations relative to the airflow. For the neural experiment, responses from eight primary sensory trigeminal ganglion neurons (Vg) from five adult female Long Evans rats were recorded. Airflow was delivered to the whisker array from three directions relative to the rat's head, and at each direction either two or three airflow speeds were used.

Data are presented as either the mean and standard deviation (Figs 3.2 DEF) or as the mean and standard error of the mean (Figs 3.3B, 3.4B, 3.6, and 3.7). Statistical analyses were performed in Matlab™. A repeated measures one way ANOVA with Tukey's post hoc test was performed to examine the effect of orientation on the vibration magnitude. A two way ANOVA test with Tukey's post hoc test was performed to examine the effects of the airspeed and the airflow direction on the firing rate of the Vg neurons.

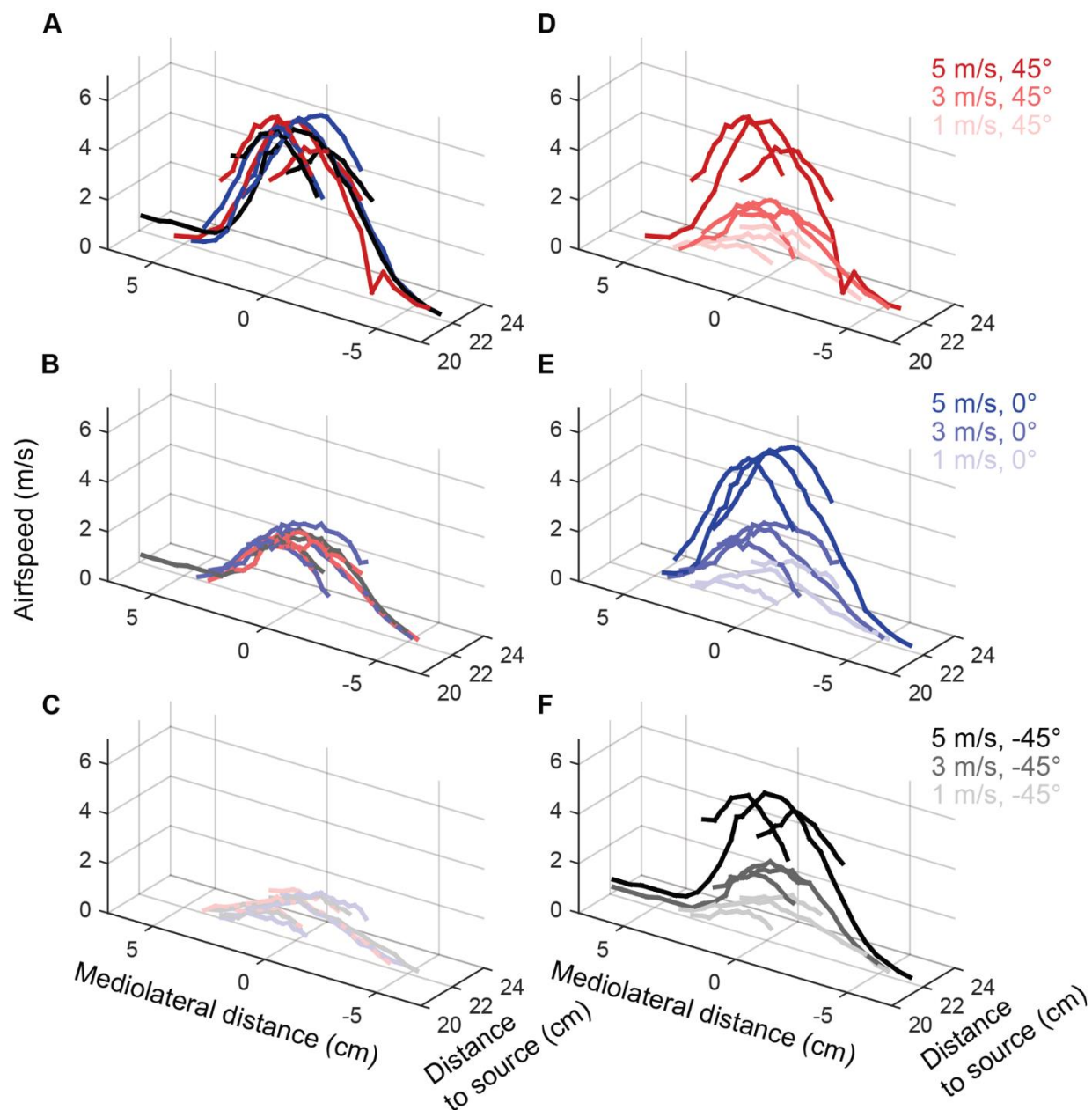


Figure 3.1. Airflow stimulus calibration. In all subplots, the origin (0,0) represents the location of the airflow source, the coordinate (0, 22) is close to the center of the whisker array, and all units are in cm. Red, blue and black indicate an airflow direction of 45°, 0°, and -45° respectively. The saturation of the color represents the magnitude of the airspeed. Dark, medium and light colors indicate 5 m/s, 3 m/s and 1 m/s, respectively. (A-C) Each panel compares the measured airspeeds for the different directions, keeping supply pressure constant. The overlap at all positions and directions indicates that for each pressure (intended airspeed)

there is no bias in airspeed across directions. **(D-F)** Each panel shows the measurements for a given direction across airspeeds. Although airspeed is not constant across all positions in the array, the airspeeds at each position within the array are distinct across pressures. Therefore, comparisons across pressure are equivalent to comparisons across airspeed.

3.4 Results

3.4.1 Vibration magnitude increases along the whisker length and depends on airflow speed and the ratio of the whisker's arc length to its base diameter

As described in *Materials and Methods*, we used high speed video (1,000 fps) to quantify the three dimensional (3D) mechanical behavior of whiskers in response to sustained airflow stimuli. Five whiskers were tested, each identified by their row and column position within the array (van der Loos et al., 1973): E2, α , A2, C2, and D5. The whiskers' shapes and geometric parameters (arc length S , base diameter D , and S/D ratio) are shown in Fig. 3.2 A. Airflow stimuli were delivered at six different speeds (approximately 0.5 m/s, 1.4 m/s, 2.2 m/s, 3.4 m/s, 4.4 m/s, and 5.6 m/s) and from five different directions (0° , 45° , 90° , 135° , and 180°). The airflow "direction" was defined as the orientation of the whisker's intrinsic curvature relative to the airflow, with 0° and 180° representing concave forwards and backwards relative to the airflow, respectively, and 90° representing concave upwards relative to the airflow. Discrete 3D positions ("nodes") along the whisker were tracked at intervals of 2 mm (Yu et al., 2016b). Linear interpolation between these nodes then yielded the complete shape of the whisker.

The whisker, as a non-rigid beam, both bends and vibrates in response to an airflow stimulus. At each point along the whisker, the bending magnitude (θ_{bend}) can be quantified as the angle between that point on the whisker at rest and the mean position of that point when the whisker is

in airflow. As schematized in Fig. 3.2B, previous work has shown that the bending magnitude increases along the whisker length, so that more distal portions of the whisker rotate through larger angles than more proximal regions (Yu et al., 2016b). This earlier work also showed that the bending magnitude at each node depends strongly on airflow speed, the ratio of the whisker's arc length to its base diameter (S/D ratio), and weakly on the whisker's orientation relative to airflow (Yu et al., 2016b).

We anticipated that similar relationships would be found for vibration magnitude, as schematized in Fig. 3.2B. To test this possibility, we quantified vibration magnitude at each node along the whisker by finding the average angular displacement of the node from its mean position (see *Methods* for details). Results showed that, like bending magnitude, vibration magnitude was greatest at distal rather than proximal locations along the whisker length. This result is illustrated for two example nodes on the α whisker in Fig. 3.2C. In this example the whisker was oriented concave forward into the airflow (orientation angle = 0°) and vibration magnitude is plotted as a function of airspeed for nodes at 40% and 80% out along the whisker length. Airspeed strongly drives the magnitude of vibrations at both nodes, but vibration magnitude is always larger at 80% of the whisker length than at 40% of the length. Similar results were found for all orientation angles and for all whiskers.

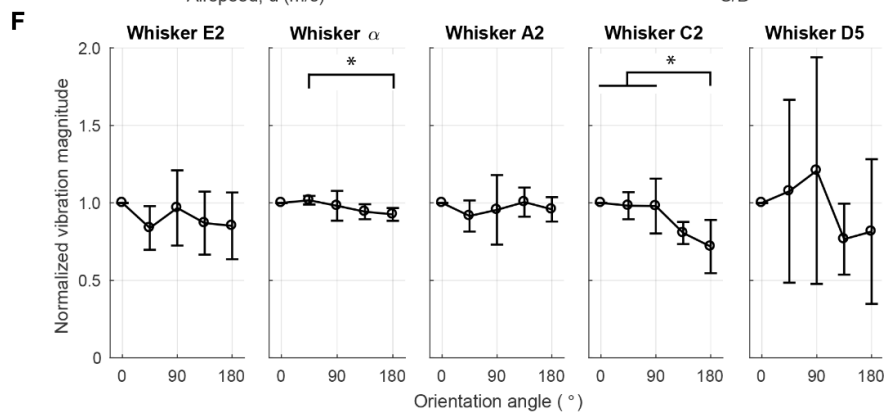
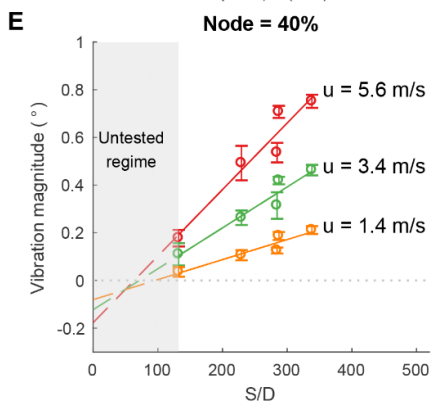
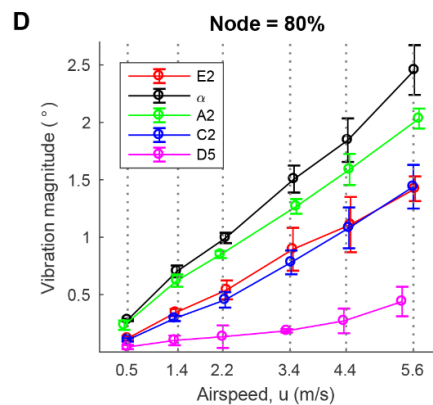
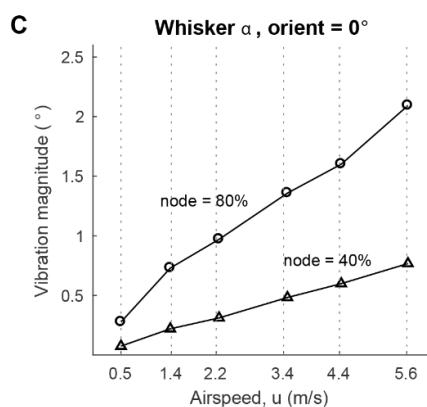
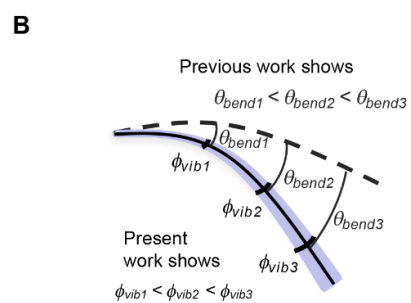
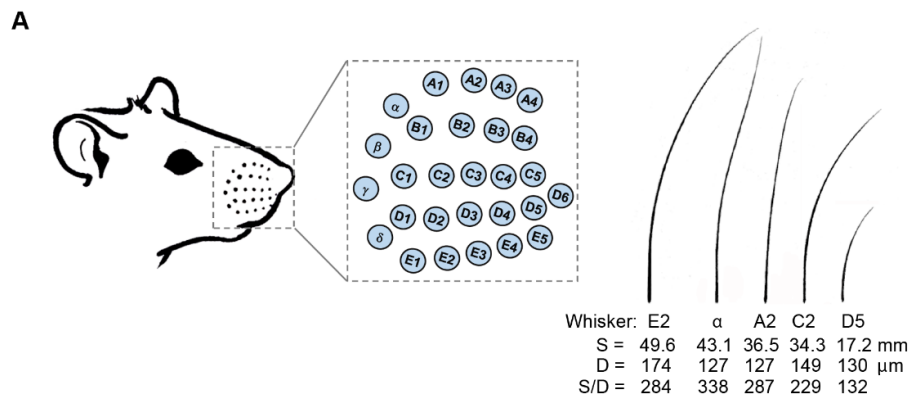


Figure 3.2 Vibration magnitude varies with airspeed and whisker geometry. (A) Left) A drawing of a rat and mystacial pad with whisker basepoints highlighted as cyan dots. Drawing adapted from Belli et al., 2018 (Belli et al., 2018). These whisker basepoints are expanded in the inset to show their identities. Right) five whiskers with different S/D ratios were used in the experiments. A lower S/D ratio means that the whisker is stiffer compared to a whisker of the same length with a higher S/D ratio. Manual tracings of the scanned whiskers are shown. (B) Schematic of bending and vibration magnitudes. Dashed curve indicates the position of the whisker at rest (no airflow). Solid curve indicates the mean position of the whisker in the presence of airflow. Blue transparent region schematizes vibration magnitude around the static bending. θ_{bend} and ϕ_{vib} indicate bending magnitude and vibration magnitude, respectively. For all whiskers in all conditions, we found that $\phi_{vib1} < \phi_{vib2} < \phi_{vib3}$. (C) Vibration magnitude is larger at more distal locations along the whisker. The plot shows the vibration magnitude of nodes located at 40% and 80% along the whisker α . In this example, the whisker was oriented concave forward into the airflow, but similar results held for all whiskers at all orientations. (D) Vibration magnitude increases linearly with airspeed. Results are shown for nodes 80% out along the whisker length and averaged over all orientation angles (mean \pm SD). (E) Vibration magnitude increases approximately linearly with the S/D ratio of the whisker. Along the x-axis, ordered from small to large S/D ratio, the whisker identities are D5, C2, E2, A2 and α . Results are shown for a node 40% out along each whisker and at airspeeds of 1.4, 3.4 and 5.6 m/s, mean \pm SD at five orientations. Linear fits between vibration magnitude and S/D ratio show increasing slopes with airspeed. Because airspeeds were not identical for all five whiskers, values of vibration magnitude have been interpolated between the airspeeds closest to the speed of interest. (F) The whisker's orientation relative to airflow did not strongly contribute to vibration magnitude. In each subplot the vibration magnitude has been normalized by that whisker's vibration magnitude at orientation angle 0° (concave forwards, toward the airflow). Only the α whisker ($F(4,25) = 3.12$, $p = 0.0329$) and C2 whisker ($F(4,25) = 6.63$, $p = 0.0009$) showed significant changes in vibration magnitude due to orientation (one way ANOVA with repeated measures). Tukey's post hoc testing indicates that only four (out of fifty) pairs of group comparisons show a significant difference – for α whisker, only the vibration magnitude at 180 deg is significantly lower than the one at 45 deg ($p = 0.0458$), and for C2 whisker, the vibration magnitude at 180 deg is significantly lower than the ones at 0 deg ($p = 0.0039$), 45 deg ($p = 0.0073$), and 90 deg ($p = 0.0079$). Asterisks indicate $p < 0.05$. Results show mean \pm SD at six airspeeds for a node 40% out along each whisker.

Vibration magnitude was found to increase with airspeed for all whiskers tested, as shown in Fig. 3.2D. The figure shows that vibration magnitude increases approximately linearly with airspeed, but that the slopes are different for the different whiskers. Again, based on analogy to results for bending magnitude (Yu et al., 2016b), we anticipated that the whisker's S/D ratio could have a

strong influence on vibration magnitude. This relationship is plotted in Fig. 3.2E, showing that vibration magnitude scales approximately linearly with the whisker's S/D ratio. For visual clarity, results are shown for only three airflow speeds, but the linear trend applies to all tested airflow speeds. It is unsurprising that a whisker with a low S/D ratio will vibrate less than a whisker with a large S/D ratio as the stiffness of a conical whisker scales as D to the fourth power.

The orientation of the whisker relative to airflow had only a weak effect on vibration magnitude, and the effect was not consistent across whiskers. Fig. 3.2F plots the vibration magnitude obtained at each orientation of the whisker normalized by the vibration magnitude obtained when the whisker was oriented at 0° . Only the α whisker ($F(4,25) = 3.12$, $p = 0.0329$) and C2 whisker ($F(4,25) = 6.63$, $p = 0.0009$) showed significant changes in vibration magnitude due to orientation (one way ANOVA with repeated measures). This result stands in contrast to results for bending magnitude, which was found to exhibit a weak but significant dependence on whisker orientation relative to airflow for all whiskers tested (Yu et al., 2016a). The effect of the whisker's orientation angle on vibration magnitude is even weaker and less consistent, with only four out of fifty pairs of group comparisons showing significant differences (Fig. 3.2F).

3.4.2 Vibration magnitude scales linearly with bending magnitude, except at extreme values of airspeed

As previously shown in Fig. 3.2BC, both bending magnitude (θ_{bend}) and vibration magnitude (ϕ_{vib}) increase along the whisker length. The bending magnitude defines the static component of whisker deflection in response to airflow. In contrast, the vibration magnitude quantifies the dynamic component. The bending and vibration magnitudes can be conceptualized as the mean and deviation of the deflection, respectively.

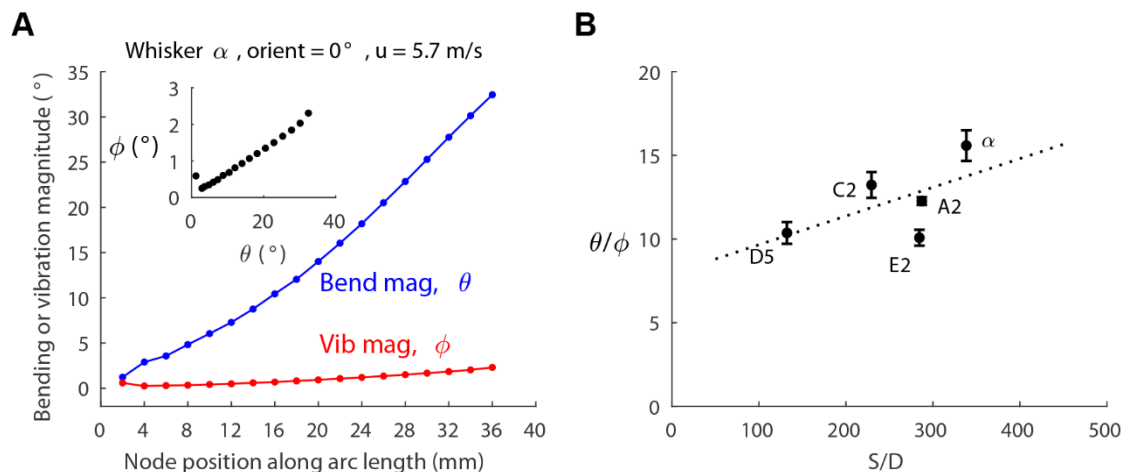


Figure 3.3 Vibration magnitude scales with bending magnitude. (A) Bending magnitude and vibration magnitude along the arc length of the α whisker with orientation angle 0° and airspeed 5.7 m/s. The inset shows vibration magnitude versus bending magnitude for all the nodes of the α whisker. (B) The ratios of bending magnitude to vibration magnitude ($\theta_{bend}/\theta_{vib}$) of all five whiskers fall within a range of 10-16, and slightly increase with the S/D ratio. The dashed line represents the line of linear regression over the five means. Data show mean \pm S.E.M. over all whisker nodes at all velocities and all orientation angles.

Unsurprisingly, we found that bending magnitude is always much larger than vibration magnitude. For a given whisker, however, their ratio remains approximately constant. An example of bending and vibration magnitudes of the \square whisker when stimulated at a single airspeed and orientation is shown in Fig. 3.3A. As shown in the inset, vibration magnitude scales linearly with bending magnitude along the whisker length.

Similar results were found for all other whiskers, orientation angles, and airspeeds, with one notable exception to the constant θ_{bend}/ϕ_{vib} ratio: at the highest airspeed, the vibration magnitude of the largest whiskers tended to saturate, while the bending magnitude continued to increase. Thus, their ratio decreased slightly (data not shown).

Regardless of whether cases of high airspeed were omitted or included, the ratio of bending magnitude to vibration magnitude was found to increase weakly with the S/D ratio. This effect is shown in Fig. 3.3B for all five whiskers. The θ_{bend}/ϕ_{vib} ratios of these five whiskers fall between 10 - 16, increasing slightly from D5 to α . As found in previous studies (Belli et al., 2017), the S/D ratio varies systematically as a function of both column and row, so we can expect the Greek arc of whiskers to exhibit the largest bending to vibration ratio, and the most rostral whiskers the smallest ratio.

3.4.3 At low airspeed, whiskers vibrate parallel to the airflow direction, transitioning to perpendicular vibration at high airspeed.

Previous work has demonstrated that whiskers always tend to bend in the direction of airflow, regardless of airspeed, whisker geometry, or orientation of the whisker relative to the airflow (Yu et al., 2016b). We quantified vibration direction for each whisker by tracking the position of a node located ~80% out along its length.

Results shown in Fig. 3.4, reveal that the whisker's vibration direction is more complex than its bending direction. The top row of Fig. 3.4A shows the whisker's vibrations during an airflow stimulus of 0.5 m/s. The position of the node, tracked over time, forms an ellipse with its major axis parallel to the airflow direction. This distribution becomes circular as the airspeed increases to 3.5 m/s (Fig. 3.4A, center row), and returns to an elliptical shape at a high airspeed of 5.6 m/s, but with the major axis perpendicular to the airflow direction (Fig. 3.4A, bottom row).

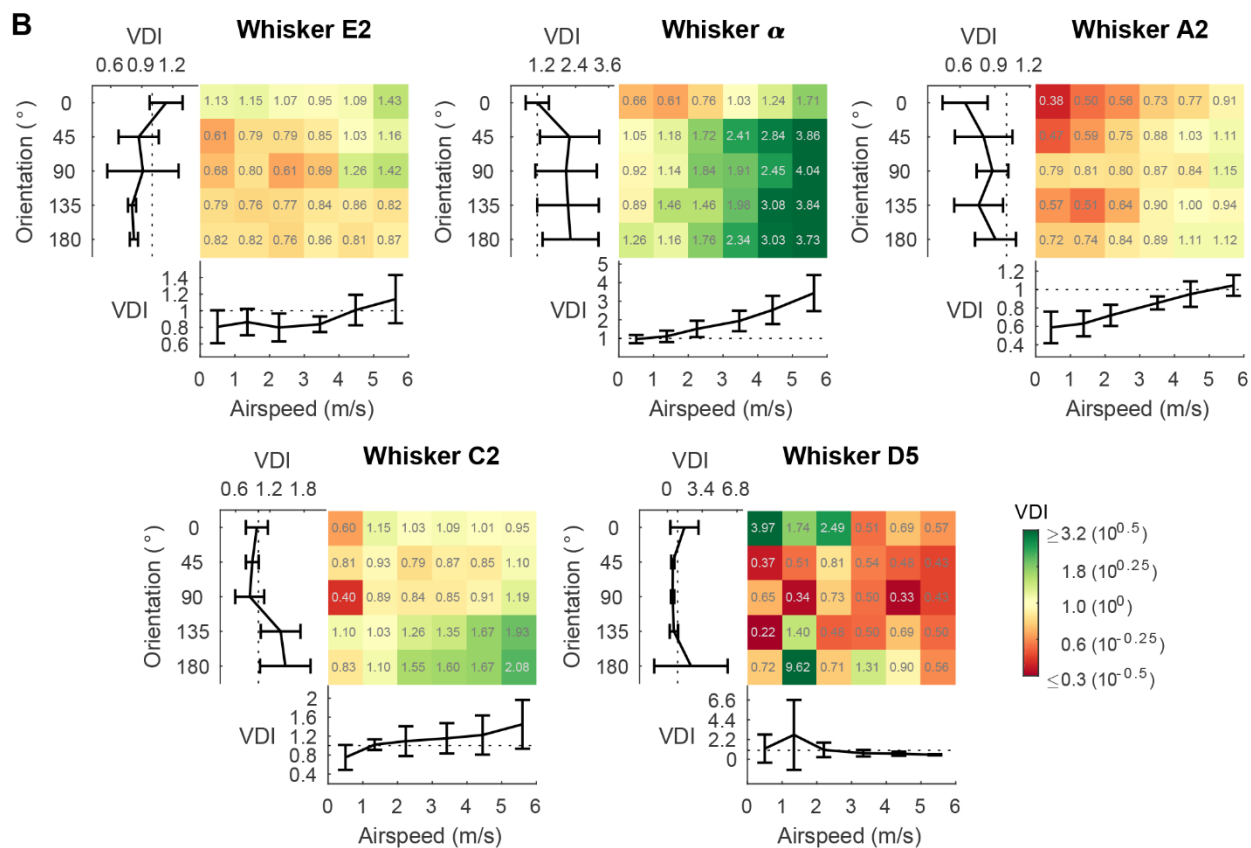
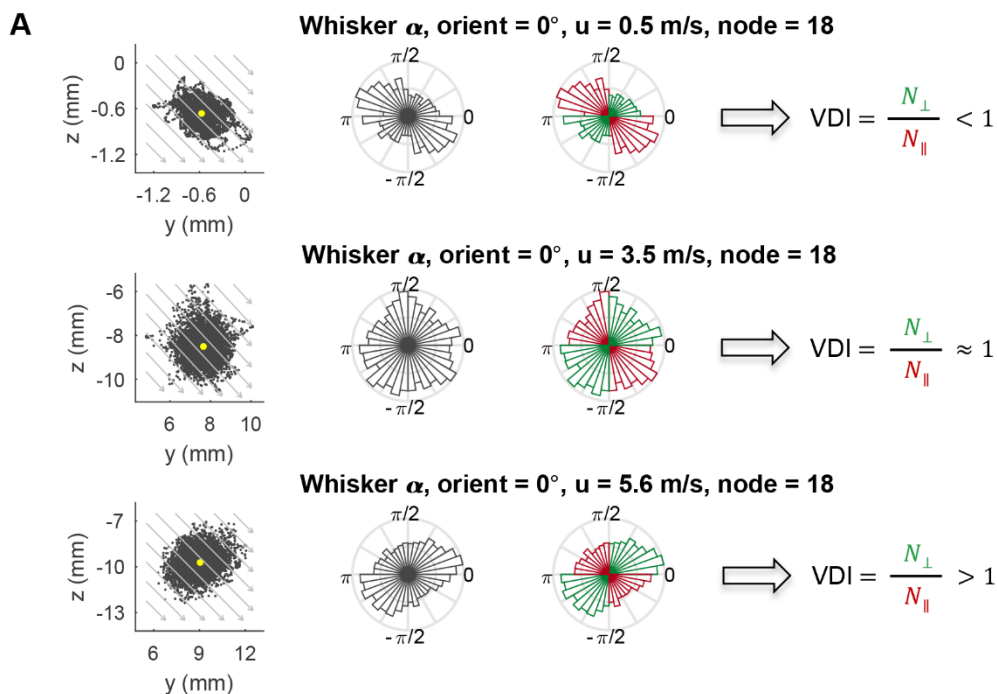


Figure 3.4 Vibration direction tends to be parallel with the airflow direction at low airspeed, and perpendicular to the airflow direction at high airspeed. (A) The airflow-evoked vibration of the α whisker at an orientation angle of 0° provides an example of the general finding that increases in airspeed are associated with transitions in vibration direction. The three rows of this figure show vibrations that occur for airspeeds of 0.5 m/s (vibration primarily parallel to airflow direction), 2.3 m/s (vibration equally likely in all directions), and 5.6 m/s (vibration primarily perpendicular to airflow direction). Each row contains three subplots. The first subplot in each row plots a point for the node position at every time point in the trial (5,000 samples). Gray arrows indicate airflow direction. The second subplot in each row shows the normalized polar histogram of the node positions. The third subplot in each row shows the same normalized polar histogram, but color codes the polar angles of the first and third quadrants in green, and the polar angles of the second and fourth quadrants in red. Vibration direction index is less than 1 in the top row, approximately equal to 1 in the center row, and greater than 1 in the bottom row. N_{\perp} is the number of perpendicular counts and N_{\parallel} is the number of parallel counts. (B) The vibration direction index VDI at each orientation angle and each airspeed for each whisker at a node around 80% out along the whisker length. The color grid plot indicates the VDI at each of the six airspeeds and each of the five orientation angles. Note that the colormap legend is log scaled and the value of the vibration direction index for each condition is labeled in each grid. For each whisker, the subplot underneath the color grid plot shows the VDI as a function of airspeed, and the subplot on the left shows VDI as a function of orientation angle. Data are shown as mean \pm S.E.M.

To quantify the degree to which vibrations were parallel or perpendicular to the direction of airflow, we define the vibration direction index (VDI) as the ratio of the count of time points in which the whisker node fell in the first and third quadrants, to the count in the second and fourth quadrants. A $VDI > 1$ indicates that a majority of the vibration direction is perpendicular to airflow, and a $VDI < 1$ indicates vibration direction is parallel with airflow direction.

We calculated the VDI for all orientations and airspeeds for all five whiskers, for a node 80% out along the whisker length, as shown in Fig. 3.4B. With the exception of the shortest whisker (D5) whose vibration displacements were mostly smaller than $100 \mu\text{m}$, the VDI increases with airspeed, indicating a shift from parallel vibration to perpendicular vibration as airspeed increases. Interestingly, whisker α , which has the largest S/D ratio (Fig. 3.2A), exhibits a distinct perpendicular vibration at all airspeeds greater than 2.2 m/s. Although the orientation of the

whisker relative to the airflow was found to have some influence on vibration direction, no clear trends were found across whiskers.

To investigate the origin of the vibrations, and the potential causes of the shift in direction, we computed the Reynolds number (Re) for a set of 519 whiskers with different geometries (Belli et al., 2017). Across all 519 whiskers, the maximum Re (always found at the whisker base, where the diameter is largest) ranged between 1.2 and 8.4 for the lowest airspeed of 0.5 m/s; between 8.3 and 57.1 for an airspeed of 3.4 m/s; and between 13.6 and 94.0 for the highest airspeed of 5.6 m/s. Flow mechanics around flexible and thin bodies is not well understood at these low Reynolds numbers, but we suggest that the observed whisker vibrations may be at least partially aeroelastic in nature (see *Discussion*).

3.4.4 Recording the activity of Vg neurons in response to sustained airflow stimulation

Decades of research have used the rodent vibrissal system as a model to study tactile coding and somatosensory processing, and numerous experiments have characterized the responses of primary sensory neurons in the trigeminal ganglion (Vg) neurons to direct touch (Arabzadeh et al., 2006; Arabzadeh et al., 2005; Bush et al., 2016a; Campagner et al., 2016; Chagas et al., 2013; Gibson et al., 1983a, 1983b; Jones et al., 2004a; Jones et al., 2004b; Kwegyir-Afful et al., 2008; Leiser et al., 2007; Lichtenstein et al., 1990; Lottem et al., 2009, 2011; Severson et al., 2017; Shoykhet et al., 2000; Stuttgen et al., 2008; Stuttgen et al., 2006; Szwed et al., 2003; Szwed et al., 2006b; Zucker et al., 1969). Evaluating the whisker's mechanical responses to airflow in the context of this wealth of neural data allows us to form a set of expectations for how Vg neurons should respond when stimulated by airflow. We collected a set of extracellular recordings from neurons of the Vg to

assess the extent to which they responded in a manner consistent with results from previous studies that have used direct tactile stimulation.

The responses of eight Vg neurons were recorded in response to airflow stimulation delivered at different speeds and from different directions. In these experiments, the head of the anesthetized animal was fixed in position, so airflow direction is defined relative to the animal's head rather than with respect to a single whisker (Fig. 3.5A). Airflow was directed at the whisker array from three different directions (-45° , 0° , and 45°) and at either two or three different speeds (1 m/s, 3 m/s, and sometimes 5 m/s). Ten trials were performed for each pairing of airspeed and direction, with care taken to align the center of airflow on the center of the whisker array (see Fig. 3.1 in *Materials and Methods*). On each trial, airflow was directed for 15 seconds toward the whisker array, and the whiskers were allowed to return to rest during a 4-second inter-trial interval.

3.4.5 Vg neurons respond continuously to sustained airflow stimulation while exhibiting some adaptation over the duration of the stimulus.

All studies of Vg neurons agree that these neurons have no background firing rate, and are excited only during whisker deflections or motion. In view of these previous studies, we would expect Vg neurons to respond sharply at the onset of airflow, and cease firing quickly after airflow ends.

It is more challenging to use studies of direct tactile stimulation to form expectations for how Vg neurons might adapt to sustained airflow stimulation. Numerous studies have used tactile stimulation to show that Vg neurons can be broadly classified into rapidly adapting (RA) and slowly adapting (SA) cell types given a ramp-and-hold (Gibson et al., 1983a, 1983b; Jones et al., 2004b; Lichtenstein et al., 1990; Lottem et al., 2009, 2011; Zucker et al., 1969).

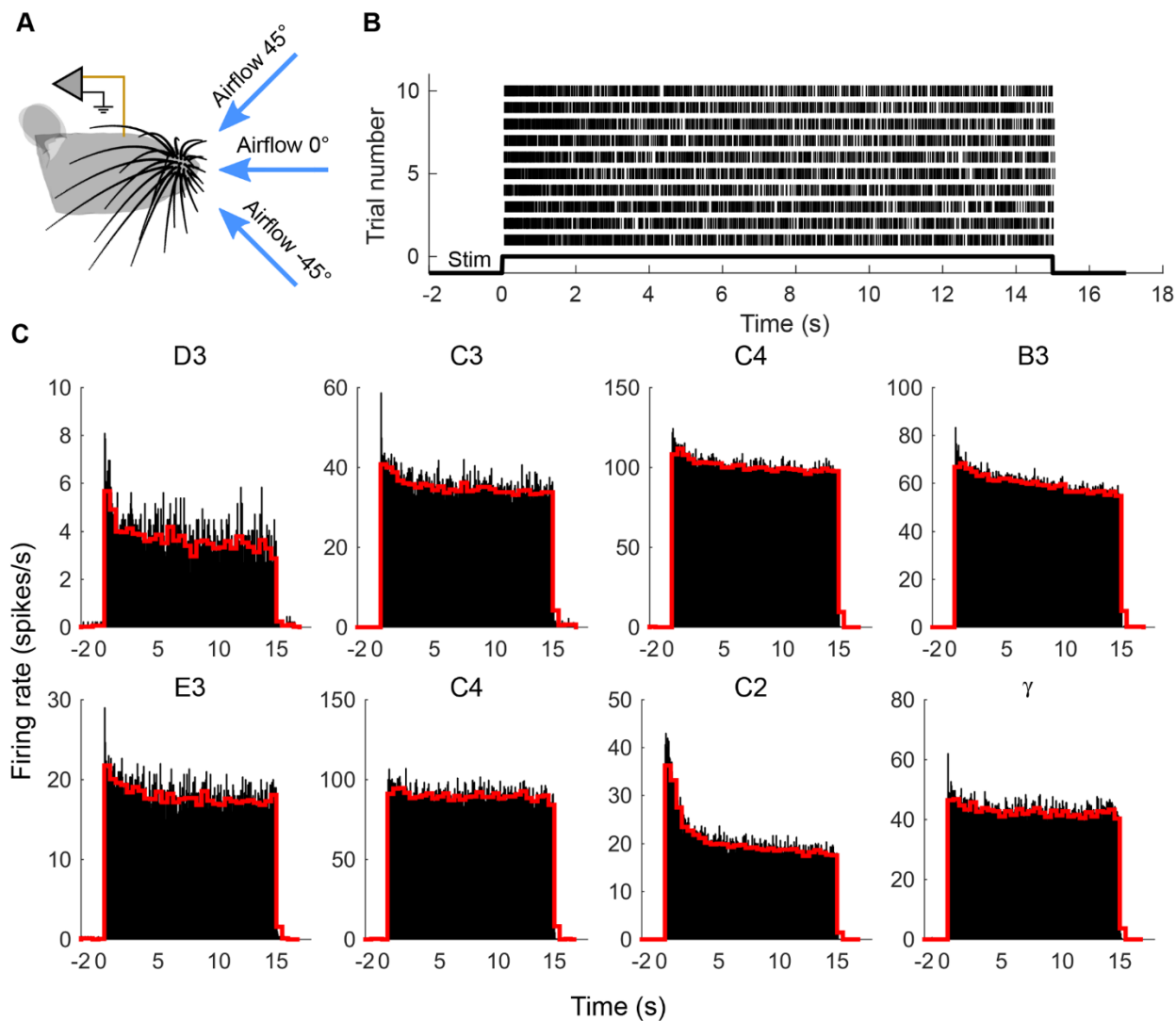


Figure 3.5 Activity of Vg neurons in response to a sustained airflow stimulus. (A) Airflow was directed at the center of the whisker array from three different directions. (B) Raster plot of action potentials from a neuron innervating the C2 whisker. Data are shown for all 10 trials obtained with an airspeed of 3 m/s and airflow direction of -45° . (C) Peri-stimulus time histograms (PSTHs) for all neurons collapsed across all trials and conditions. Airflow stimulus begins at time = 0 ms. Neurons are labeled by the row and column identity of the whisker that they innervate. Data for neurons in the top row have been averaged over 90 trials that included three orientations and three airspeeds (1 m/s, 3 m/s and 5 m/s), while data for neurons in the bottom row have been averaged over 60 trials that included three orientations but only two airspeeds (1 m/s and 3 m/s). Black histograms have a bin size of 50ms; red histograms have a bin size of 500ms. Whisker C2 is the same neuron shown in (B).

However, airflow consists of both slow, constant (bending) and fast, changing (vibration) components, so we would expect both RA and SA type neurons to respond throughout the entire duration of the airflow stimulation. The degree of adaptation will depend on complex interactions between the biophysics of the neuron and the variations in both bending and vibration.

An example of the spike train obtained from one neuron is shown in Fig. 3.5B, for a single air speed and direction (3 m/s, -45°). As expected, the neuron begins to respond at the onset of the airflow stimulus and continues until stimulus offset. A high firing rate is associated with stimulus onset. During the inter-trial interval, the neuron is silent.

These results were found for all eight neurons on all trials, as shown in the peri-stimulus time histograms (PSTHs) of Fig. 3.5C. For each neuron, two PSTHs are shown averaging data across all trials and all conditions: the first on a short time scale (black, bin size=50 ms), and a second on longer time scale (red, bin size=500 ms). All neurons exhibit a strong response to stimulus onset, fire continuously during airflow stimulation, and are silent in the absence of stimulation. No neuron ceases firing before the end of the stimulus.

Figure 3.5C further shows that Vg neuron exhibits a variety of adaptation characteristics in response to airflow stimulation. Some neurons adapted on a time scale less than 50 ms, as shown in the large peaks of the high-resolution histograms for neurons C3, E3, and γ . Other neurons exhibited a slower relaxation with a duration of many seconds, as evident in the low-resolution histograms for C4 (top row), B3, D3, and C2. Notably, some neurons do not reach a clear steady-state response even after 15 seconds of sustained stimulation.

3.4.6 All Vg neurons increase firing rate with airspeed

One characteristic feature of Vg responses is that firing rates increase with increased stimulus magnitude. This strong correlation has been found for both ramp-and-hold stimulation in the anesthetized animal as well as during object contact in electrical whisking and awake exploration (Bush et al., 2016a; Campagner et al., 2016; Gibson et al., 1983a, 1983b; Kwegyir-Afful et al., 2008; Leiser et al., 2007; Lottem et al., 2011; Severson et al., 2017; Shoykhet et al., 2000; Stuttgen et al., 2008; Szwed et al., 2003; Szwed et al., 2006b; Zucker et al., 1969). In addition, numerous studies have demonstrated that Vg neurons respond strongly to vibrational stimuli, both in the anesthetized and awake animal, with both presumptive SA and RA cells increasing their firing rate to increased vibration magnitude (Arabzadeh et al., 2006; Arabzadeh et al., 2005; Jones et al., 2004a; Lottem et al., 2009; Stuttgen et al., 2006).

Our studies of the whisker's mechanical response to airflow have indicated that the bending of each whisker increases linearly with airspeed (Yu et al., 2016b). In addition, Figs. 3.2 and 3.3 of the present work show that vibration amplitude generally increases linearly with airspeed, scaling directly with the bending magnitude. Thus, as airspeed increases, the whiskers will not only bend more, but also vibrate more. Based on studies of direct tactile stimulation, we would therefore expect Vg activity to increase monotonically in response to higher airspeeds.

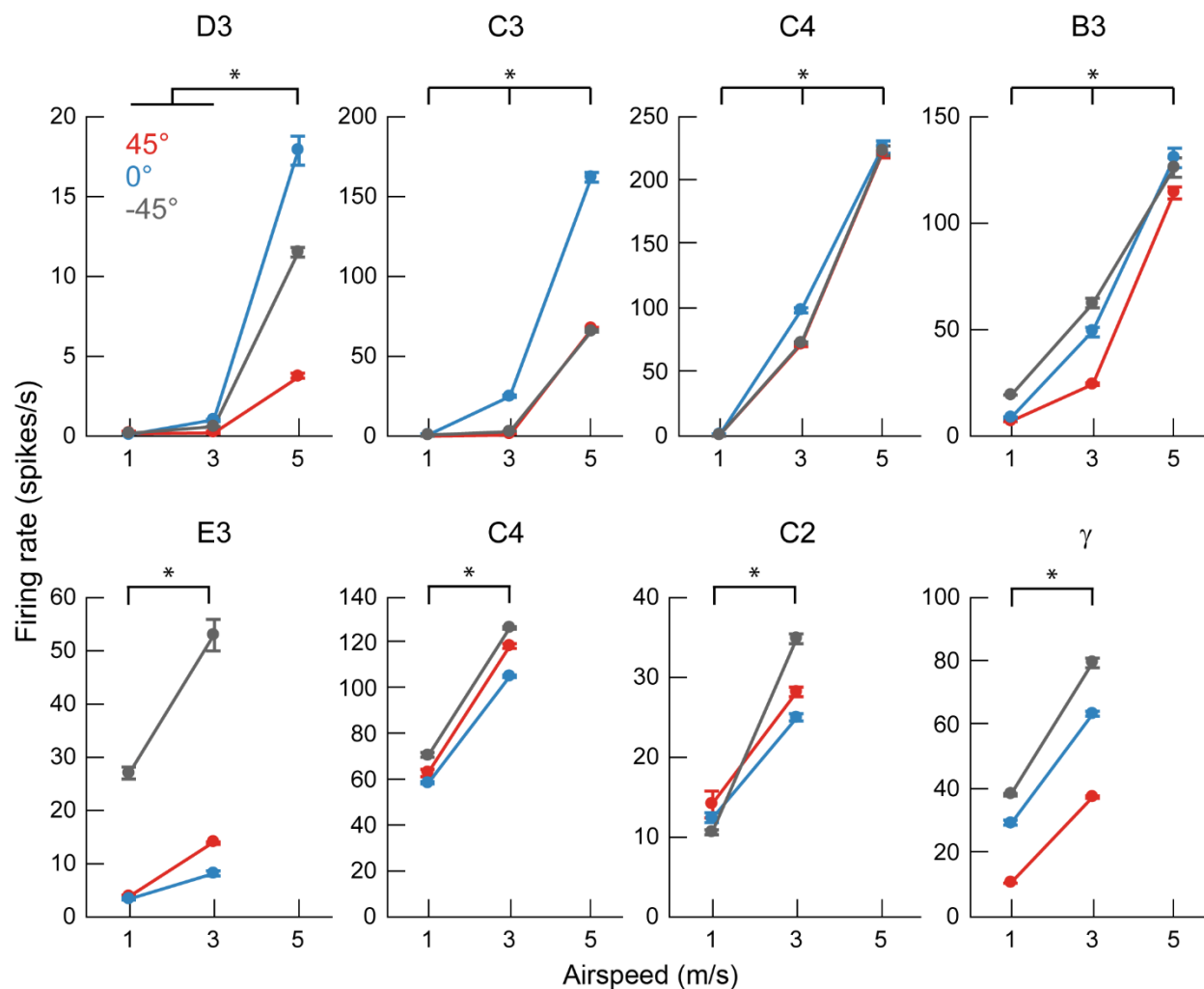


Figure 3.6 The firing rate of Vg neurons increases with airspeed. All eight neurons show an increase of firing rate with airspeed (Two-way ANOVA: main effect of airspeed, $p < 0.001$ for all neurons. Asterisks indicate $p < 0.05$ for Tukey's post-hoc test). Three airspeeds were used for neurons shown in the top row and two airspeeds used for neurons shown in the bottom row. Black, blue and red indicate airflow directions -45° , 0° , and 45° , respectively. Data show mean \pm S.E.M. over all tested trials at each condition.

We computed the average firing rates for each trial at each airflow condition, and results are plotted in Fig. 3.6. In line with expectations, all neurons increase firing rate with airspeed, for all orientations of the whisker (two way ANOVA: main effect of airspeed $p < 0.001$ for all neurons, D3: $F(2,80) = 1126$, $p = 2.6e-59$; C3: $F(2,80) = 8367$, $p = 1.2e-93$; C4: $F(2,81) = 4612$, $p = 3.6e-$

84; B3: $F(2,80) = 1530$, $p = 1.7e-64$; E3: $F(1,54) = 184$, $p = 4.9e-19$; C4: $F(1,54) = 4818$, $p = 1.7e-54$; C2: $F(1,54) = 594$, $p = 7.9e-31$; $\square\square F(1,54) = 2447$, $p = 1.2e-46$, group comparisons with Tukey's post-hoc test $p < 0.05$ were asterisked in Fig. 3.6). Firing rates are highly variable across neurons (note the y-axis scale differences), and the change in firing rate as airspeed increases also varies considerably. Figure 3.6 also shows that each neuron's firing rate depends on the airflow direction, an effect explored in more detail in the next section.

3.4.7 Vg firing rate depends on airflow direction, and a neuron's preferred airflow direction can change with airspeed

Vg neurons are well known to exhibit strong directional tuning (Jones et al., 2004a; Kwegyir-Afful et al., 2008; Lichtenstein et al., 1990; Zucker et al., 1969). During direct tactile stimulation, the direction in which the Vg neuron responds the most strongly is termed that neuron's "preferred direction." In analogy to direct tactile stimulation, we designated the airflow direction in which the neuron exhibited the highest firing rate that neuron's "preferred airflow direction."

To observe the effect of airflow direction on the neural response, we account for the effect of firing rate increases associated with higher airspeeds (as was shown in Fig. 3.6). Therefore, we normalize each neuron's firing rate by its maximum firing rate at each airspeed. Plotting these normalized firing rates as a function of airflow direction (Fig. 3.7) clearly shows that all neurons change their firing rate with airflow direction. This result was confirmed with a two way ANOVA: main effect of direction $p < 0.001$; interaction effect of speed*direction $p < 0.001$ for all neurons. (two way ANOVA: main effect of direction $p < 0.001$ for all neurons, D3: $F(2,80) = 183$, $p = 1.4e-30$; C3: $F(2,80) = 1518$, $p = 2.4e-64$; C4: $F(2,81) = 12.2$, $p = 2.3e-5$; B3: $F(2,80) = 51.5$, $p = 4.2e-15$; E3: $F(2,54) = 470$, $p = 7.0e-35$; C4: $F(2,54) = 161$, $p = 1.8e-23$; C2: $F(2,54) = 11.8$, $p = 5.5e-5$; $\square\square F(2,54) = 879$, $p = 6.4e-42$, group comparisons with Tukey's post-hoc test $p < 0.05$ were asterisked

in Fig. 3.7),(two way ANOVA: interaction effect of direction*airspeed $p < 0.001$ for all neurons, D3: $F(4,80) = 157$, $p = 4.6e-37$; C3: $F(4,80) = 806$, $p = 9.2e-64$; C4: $F(4,81) = 8.1$, $p = 1.6e-5$; B3: $F(4,80) = 11.9$, $p = 1.3e-7$; E3: $F(2,54) = 40.0$, $p = 2.4e-11$; C4: $F(2,54) = 15.5$, $p = 4.8e-6$; C2: $F(2,54) = 27.8$, $p = 4.9e-9$; γ : $F(2,54) = 36.3$, $p = 1.0e-10$).

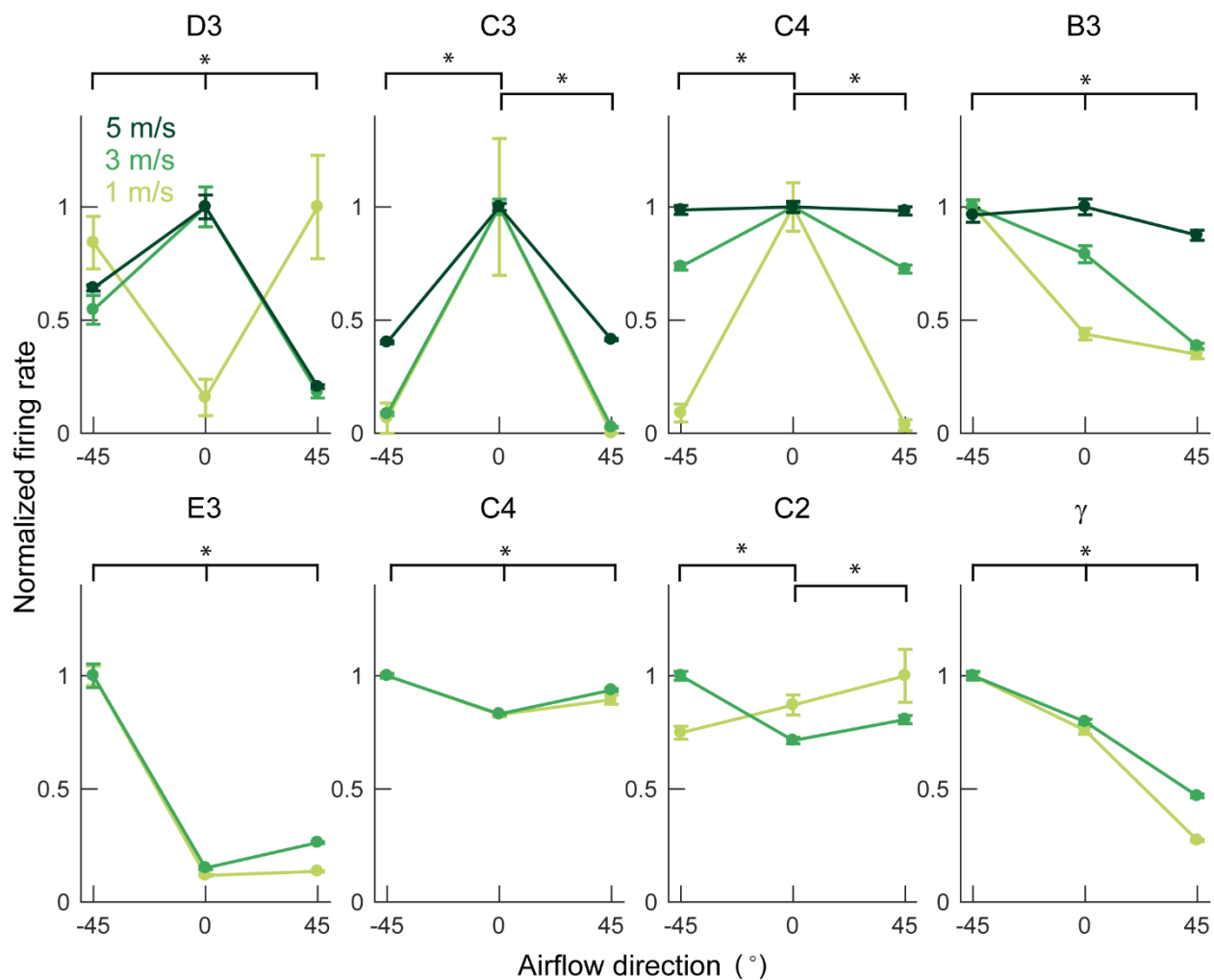


Figure 3.7 Firing rate changes with airflow direction. All eight neurons show variations in firing rate with airflow direction (Two-way ANOVA: main effect of direction, $p < 0.001$ for all neurons. Asterisks indicate $p < 0.05$ for Tukey's post-hoc test). Each neuron is labeled with the row and column identity of the whisker it innervates. Light, medium, and dark green curves indicate slow, medium, and fast airspeed (approximately 1, 3, and 5 m/s) as indicated by the legend in the first subplot. Three airspeeds were used for neurons shown in the top row and two

airspeeds used for neurons shown in the bottom row. Data show mean \pm S.E.M. over all trials at each condition. Firing rates are normalized to the maximum mean firing rate for a given airspeed. The absolute firing rates can be seen in Fig. 3.6.

More intriguingly, we found that a neuron's preferred airflow direction can change with airflow speed. For example, for airflow stimulation at 1 m/s, the neuron that innervates the D3 whisker prefers airflow directions of $\pm 45^\circ$, and responds only weakly to airflow delivered from a direction of 0° . This direction preference reverses for higher airspeeds at 3 m/s and 5 m/s. The neuron that innervates the C2 whisker exhibits a similar shift in preferred airflow direction with increased airspeed. Moreover, the modulation depth – the degree to which a neuron shows differential responses across directions – is often reduced as airspeed increases. In other words, the tuning of the cell's preferred airflow direction weakens as stimulus magnitude increases. This effect is seen clearly for the neurons that innervate whiskers C3, B3, γ , D3, and C4 (top).

In light of the present study's finding that vibration direction changes with airspeed (Fig. 3.4), we suggest that these changes in the neuron's preferred direction might be partially explained by shifts in the main axis of the whisker vibration. That is, as airspeed increases, the whisker vibrates in a different direction, altering the mechanical input to the follicle.

3.4.8 The firing periodicities of Vg neurons are close to whiskers' resonances

The whisker's intrinsic dynamics – which includes its resonant properties – are an essential component of any dynamic behavior that it exhibits, including non-contact whisking (Quist et al., 2014; Severson et al., 2017), collisions (Boubenec et al., 2012; Kan et al., 2013; Quist et al., 2014), and texture-induced vibrations (Arabzadeh et al., 2006; Arabzadeh et al., 2005; Ritt et al., 2008; Wolfe et al., 2008). Previous studies using direct tactile stimulation have found large increases in

Vg firing rates associated with the mechanical amplification of the whisker's vibrations near its resonance modes (Andermann et al., 2004).

Our previous work has indicated that airflow stimulation causes whiskers to vibrate near their resonance modes (Yu et al., 2016b), and Figs 3.2 and 3.3 of the present work further indicate that the magnitude of these vibrations depends on airspeed. Interpreting these mechanical results in light of the previous studies of Vg responses to vibrations (Andermann et al., 2004), we might expect Vg neurons to entrain to the whisker's resonant modes. A caveat, however, is that the resonance modes are extremely broad (Yu et al., 2016b), and the vibration direction changes with airspeed, which shifts the Vg neuron's preferred airflow direction (Figs 3.4 and 3.7). Therefore, we can form no strong expectations for the magnitude of this postulated entrainment.

To evaluate the degree to which Vg neurons entrain to the whisker's first resonant mode, we computed the autocorrelation of each spike train for each neuron as a measure of spiking periodicity. Fig. 3.8A shows the autocorrelations of the spike train for each neuron averaged over all conditions and trials. Peaks in the autocorrelation indicate periodicities in the spike pattern. These firing periodicities could result either from a neuron's intrinsic cellular dynamics (Hutcheon et al., 2000; Prescott et al., 2008), or from the periodicity of the mechanical stimuli (Fourcaud-Trocme et al., 2003; Salinas et al., 2000), or (most likely) from a complex interaction between neuronal biophysics and the mechanical stimulus.

To determine the extent to which the observed periodicities in the spike trains reflect the vibration of the whisker, we computed the theoretical resonances of the whiskers associated with each neuron (see *Methods*). As shown in Fig. 3.8A, the first, second, and third mode resonance ranges are superimposed on the autocorrelation curves, with uncertainty ranges established by varying

Young's Modulus between 3-11 GPa (Birdwell et al., 2007; Hartmann et al., 2003; Kan et al., 2013; Neimark et al., 2003; Quist et al., 2011). The first resonance range (yellow highlight) overlaps with the major peak of the autocorrelation curve for many, but not all, neurons.

We then compared the theoretically-predicted first mode resonant frequency of the whisker (based on the measured whisker shape and mass) with the peaks found from the autocorrelation curves of the neural spike trains. Major peaks in the autocorrelation curves are shown as red arrows for all neurons except for the neuron that innervated whisker C3. This particular neuron exhibited a unique autocorrelation profile, with the strongest peak close to the third resonance mode with a period of 1 ms (1,000 Hz). This large, high frequency response may indicate that the neuron is firing near its maximal firing rate, with 1 ms representing its refractory period. In order to appropriately compare this neuron's response with the first-mode whisker resonances predicted from mechanical analysis, we chose the maximum autocorrelation coefficient within the peak closest to the first mode resonance.

Results of this analysis are shown in Fig. 3.8B. In general, spiking periodicities are close to the theoretical whisker resonances, but responses of some neurons fall outside of the predicted range. These results indicate that the vibrational mechanical stimulus likely contributes to the temporal patterning of Vg neuron spiking but that Vg neurons do not strongly entrain to whisker resonances during airflow stimulation. The weak entrainment likely occurs for three reasons: the resonance modes induced by vibrations are broad (Yu et al., 2016b); the neuron could respond to features of the stimulus other than vibration (such as small variations in airflow structure); and the intrinsic properties of the neuron will influence spiking patterns.

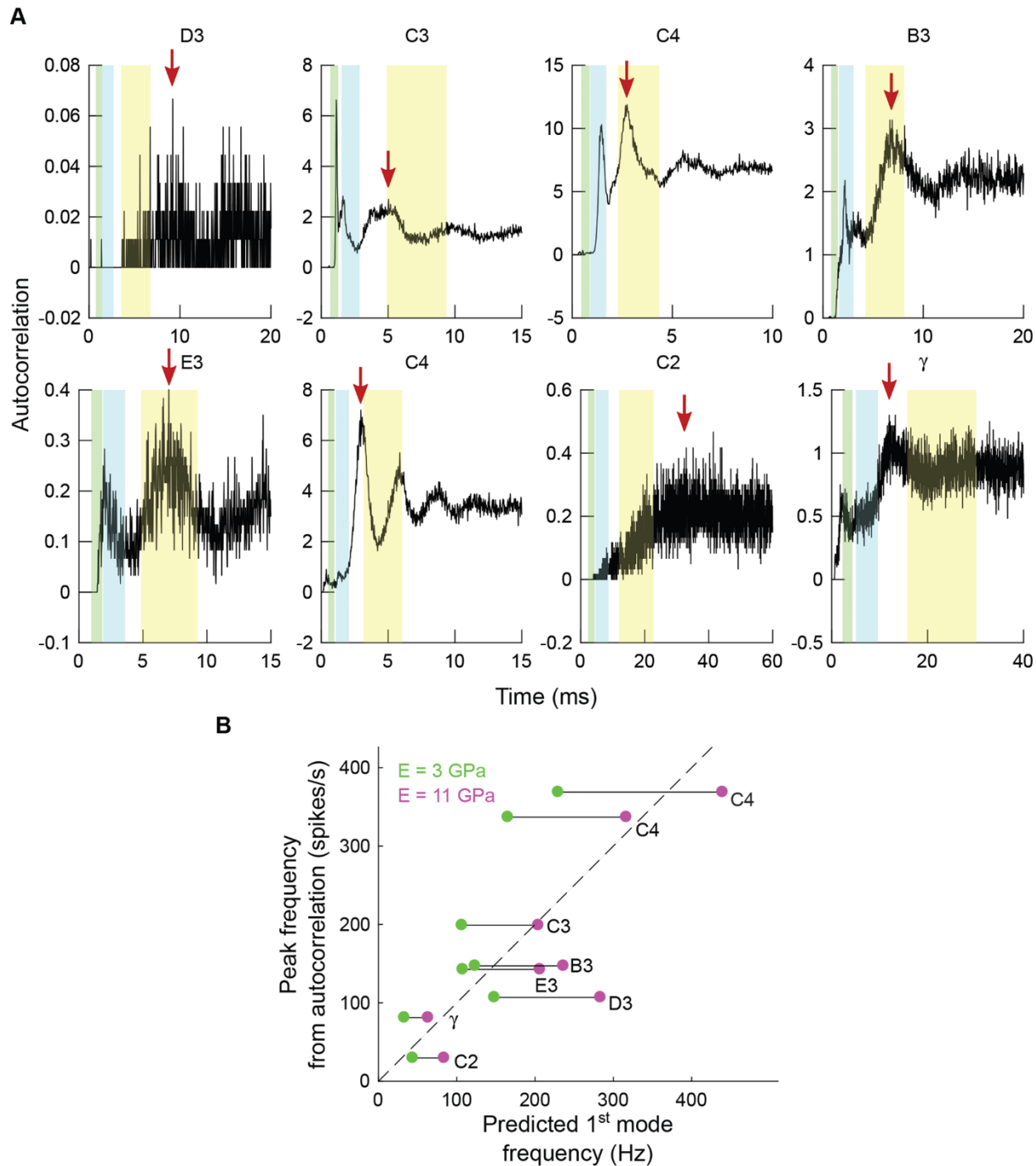


Figure 3.8 The firing periodicities of Vg neurons are related to the whiskers' first mode resonances. (A) Autocorrelation of the spike trains for each neuron across all conditions and trials. The peaks of the autocorrelation curves are indicated by red arrows. Shaded regions in yellow, cyan and green represent ranges for the 1st, 2nd and 3rd theoretical resonant modes of

the whiskers computed by varying Young's modulus between 3 GPa and 11 GPa. Note that the abscissa has units of time, so the theoretical resonant modes are computed in terms of period, not frequency. **(B)** Relationship between predicted first mode resonance of the whisker and the observed autocorrelation peak frequency. The dashed line represents the line of equality. Green and magenta dots indicate the predicted first mode frequency given Young's modulus at 3 GPa and 11 GPa, respectively, and the lines connecting these two dots are the predicted ranges for that neuron.

3.4.9 Implications for Vg coding of airflow speed and direction

As indicated previously, a whisker will tend to bend in the direction of the wind, regardless of airspeed (Yu et al., 2016b). However, the present study has shown that – in contrast to bending direction – the whisker's vibration direction varies significantly with airspeed (Fig. 3.4), and that the Vg neuronal response is in part due to this vibration (Figs 3.7 and 3.8). Thus vibration contaminates the airflow direction cue associated with whisker bending.

Figure 3.9 provides intuition for how airspeed-dependent variations in vibration direction would affect neural responses. The figure schematizes two idealized neurons, A and B, that prefer forces in two orthogonal directions, x and y. The three panels show the forces exerted on the whisker in response to low, medium, and high speed airflow. Assuming that the airflow is in the x-direction, the force due to bending (F_b) will drive neuron A, because the whisker always bends in the direction of the airflow. Although the magnitude of F_b increases with airspeed, it does not influence neuron B. In contrast, the force due to vibration (F_v) contains components that act in both x- and y-directions. As airspeed increases, the major axis of vibration direction gradually changes from parallel to the airflow to perpendicular. Thus, at low airspeed, the vibration force primarily affects neuron A, at medium airspeed both neurons are affected approximately equally, and at high airspeed, the vibration force more strongly drives neuron B. Just as for the bending force, the average magnitude of the vibration force increases with airspeed.

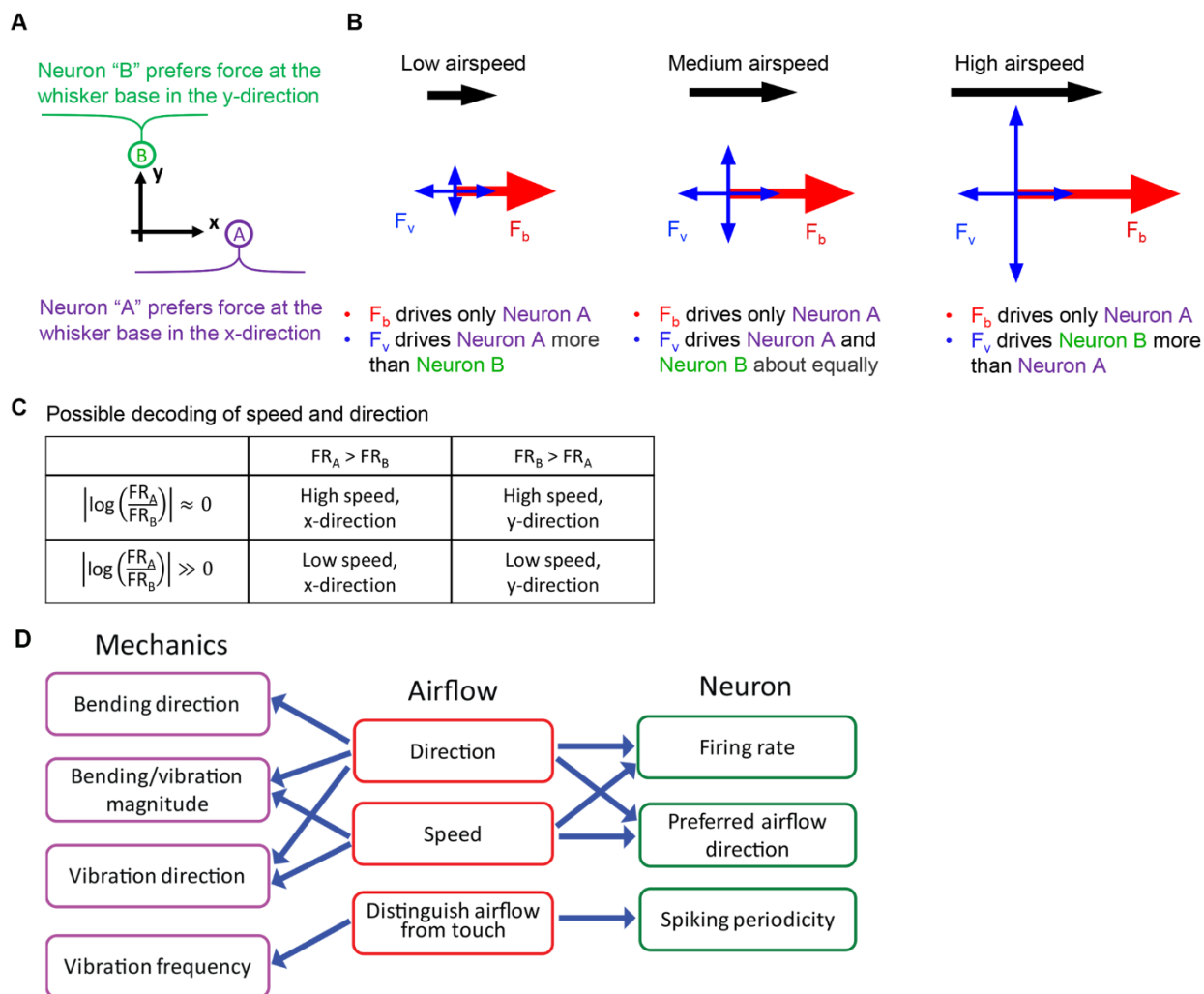


Figure 3.9 Idealized forces generated by airflow acting on the whisker. (A) Idealized neurons A and B prefer forces in the x- and y- directions, respectively. (B) In all panels, the whisker is imagined to come out of the page. F_b and F_v are the forces exerted by the airflow on the whisker, as they would be measured at the whisker base. These forces represent the combined effect of distributed airflow along the length of the whisker and the way that the whisker's intrinsic mechanical properties filter those forces. F_b represents force due to bending (a quasi-static force acting solely in the x-direction), and F_v represents force due to vibration (a dynamic term, containing components in both x- and y- directions). The magnitudes of F_b and F_v both increase with airspeed, but only F_v changes its direction of action. (C) A possible two-neuron readout scheme for airspeed and direction. If neurons A (x-direction tuned) and B (y-direction tuned) exhibit the same response patterns for a given force stimulus then airflow direction can be determined by comparing which neuron fires more, and speed can be inferred from the ratio of the firing rates. Specifically, with A and B now representing firing rates FR_A and FR_B : if $A > B$ and A/B is small, then airspeed is high in the x-direction. If $A > B$ and A/B

is large, then airspeed is low in the x-direction. If $B > A$ and B/A is small, then airspeed is high in the y-direction. If $B > A$ and B/A is large, then airspeed is low in the y-direction. If the neurons do not have the same response profile for a given force input, then this scheme still holds provided the mapping to firing rate is known. The absolute value of the log ensures that the ratio is symmetric with respect to neuron identity (A/B is equivalent to B/A). **(D)** Relationships between the whisker's mechanical response, the physical parameters of airflow, and the responses of primary sensory neurons in the trigeminal ganglion.

If the whisker's vibration in response to airflow were purely random (i.e., without any relationship to airspeed or direction), it would only add noise to the Vg response. However, the whisker's vibration, and thus the neural response, carries significant information about airspeed. Although a single neuron is insufficient to disambiguate direction from airspeed (it cannot be assumed to be able to distinguish the components of F_v from F_b) a population response may suffice. Specifically, as the F_v component perpendicular to airflow increases, the ratio of the forces in the x and y directions – and thus the ratio between the firing rates of neurons A and B – decreases. This ratio (Fig. 3.9C) could be coupled with knowledge of the absolute magnitude of both responses to infer both the speed and direction of the airflow (e.g., if neuron A is firing more than B, then airflow is in the positive x-direction, and the speed can be obtained from the ratio of firing rates).

Together with previous descriptions of the whisker's bending and frequency response to airflow (Yu et al., 2016b) the relationships between airflow information, whisker mechanics, and the Vg neural response can be summarized as shown in Fig. 3.9D. The left column of the figure lists the mechanical consequences of airflow. Bending magnitude, vibration magnitude, and vibration direction are related to both airflow direction and speed, while bending direction is only affected by airflow direction. Vibration frequency is not strongly affected by these parameters (Yu et al., 2016b).

The right half of Fig. 3.9D links airflow information to the Vg neural response. Both the direction and speed of the airflow influence a neuron's average firing rate. Given that the vibration direction changes with airspeed, a neuron might preferentially respond to one airflow direction at low speed and a different airflow direction at high speed. Airflow and touch could be distinguished based on neural response; firing will be sustained and quasi-periodic in response to airflow but would attenuate relatively quickly in response to discrete touch.

We can use the relationships outlined in Fig. 3.9D to link whisker mechanics with the neural response. Larger bending and/or vibration magnitudes in high speed airflow will tend to generate higher firing rates. Changes of vibration direction with airspeed will alter a neuron's preferred airflow direction, and vibration at a whisker's natural resonance frequency will help drive neural spiking periodicity.

3.5 Discussion

Fluid flow sensing in land mammals could aid in several important behaviors including olfactory search and predator avoidance. We have demonstrated that rats use their whiskers during anemotaxic behaviors (Yu et al., 2016a), and that a whisker's bending response correlates with airflow information (Yu et al., 2016b). The present work is the first characterization of the whiskers' vibrational response and the Vg neural response to airflow.

3.5.1 Mechanical basis driving whisker vibrations

If the whisker did not vibrate in response to airflow, its bending response could be used to uniquely determine airflow speed and direction. Increased airspeed would increase whisker bending, which would increase the firing rate of Vg neurons. The whisker would bend in the direction of airflow, maximally exciting a particular population of Vg neurons best tuned to that direction.

However, whiskers do vibrate in response to airflow, and further, the vibration direction changes from parallel to perpendicular as airspeed increases (Fig. 3.4). Two possible mechanisms could account for these vibrations. Vortex-induced vibrations are expected to occur for Reynolds numbers (Re) greater than ~ 40 , and will tend to cause the whisker to vibrate perpendicular to the flow direction (Billah et al., 1991; Taneda, 1956; C. Williamson et al., 2004). However, Re calculations indicate that at airspeeds up to ~ 3 m/s nearly all rat whiskers will be in a regime where $Re < 40$, suggesting that a second mechanism – aeroelastic flutter – may be primarily responsible for the parallel vibrations at low airspeeds (Billah et al., 1991; McKay, 2012; Taneda, 1956). Aeroelastic vibrations are as yet poorly understood, but result from positive feedback between the deflection of an object and the forces exerted by fluid flow: the object extracts energy from the airstream through its own motion (Abdelkefi, 2016; Billah et al., 1991). We therefore suggest that the observed change in vibration direction may represent a transition from a regime dominated by aeroelastic vibrations to one dominated by vortex-induced vibrations. The exact origin of the vibrations and the cause of their directional transition will require further mechanical studies.

Regardless of the physical mechanism, the result is that vibration will cause ambiguity in single unit Vg coding of speed and direction, which can be resolved when the response of the entire population of Vg neurons is considered (Fig. 3.9).

3.5.2 Average airflow and the local flow profile

Given that vibrations are a physical consequence of a cantilever exposed to airflow, it seems likely that biology would exploit the information available from vibrations. In contrast to bending, which reflects the low frequency, time-averaged flow profile, vibrations could provide information about high frequency changes in local flow structure. This type of spectral division resembles how quasi-

static bending information may be used to extract surface contours and shape, with vibrations providing information about texture.

One use for local flow structure is that an animal could potentially determine an object's size or shape based on the "bluff" around the object. Although vortices rapidly dissipate in air, flow past different objects will cause different flow profiles that could be sensed by rodents in a manner analogous to pinned wake-tracking (Dehnhardt et al., 1998; Dehnhardt et al., 2001). Given the close relationship between whisking and sniffing (Moore et al., 2013), local flow structure may also aid in refining olfactory search (Catania, 2013; Khan et al., 2012).

Fast vibrations could also help enable rapid escape responses, as do many arthropod flow-sensing hairs (Casas et al., 2010; Jacobs, 1995). An important difference, however, is that each arthropod hair tends to rotate at its base as a rigid body (Albert et al., 2001; Humphrey et al., 2007; Magal et al., 2006), rather than bend as does a rat whisker. In addition, because arthropod hairs are much shorter than whiskers, they are generally immersed within the boundary layer; the hairs therefore tend to couple mechanically and a hair's vibration frequency is not dominated by its intrinsic resonance (Humphrey et al., 2007). Equally important, arthropods often have distinct hair subtypes: tactile hairs, specialized for touch stimuli, are significantly longer than flow-sensing hairs (Albert et al., 2001; Barth et al., 2004). In contrast, rat whiskers serve a dual function as touch and flow sensors.

3.5.3 Airflow versus touch stimuli

Given that both airflow and touch cause whiskers to deform in a way that evokes Vg neural firing, an important question is how the animal might distinguish responses due to airflow from those due to touch. The two stimuli differ in several important ways.

During airflow stimulation, all whiskers in the array will bend in the same direction as the airflow. In contrast, a tactile stimulus will cause bending only for those whiskers that are touched, and their bending directions will not necessarily be the same as each other. Whisker curvature, the rat's whisking trajectory, as well as object shape and surface roughness will all jointly cause each whisker to bend and slip in slightly different directions (Hobbs et al., 2016; Huet et al., 2016; Huet et al., 2015; Solomon et al., 2008; Solomon et al., 2010).

In airflow, a distributed load is exerted along the whisker length, and its magnitude depends on the whisker's diameter and airflow parameters including Re and airspeed. In touch, however, only a small whisker segment touches an object, and contact is generally intermittent rather than continuous. These two different loading conditions will generate different mechanical signals at the whisker base.

In airflow, all whiskers will simultaneously vibrate near resonance. These vibrations are superimposed on bending and will continue without damping if airflow is sustained. In touch, however, only those touched whiskers will vibrate. A number of parameters including the whisker's intrinsic dynamics, the contact location along the whisker length, stick-slip, friction, and object surface texture, affect its vibration frequencies (Boubenec et al., 2012; Quist et al., 2014; Ritt et al., 2008; Vaxenburg et al., 2018; Wolfe et al., 2008). Additionally, as the whisker increasingly deflects against an object, these touch-induced vibrations will damp out (Boubenec et al., 2012; Hobbs et al., 2016; Quist et al., 2014). When deflecting past an object edge, whiskers will vibrate near their resonances (just as they do for airflow), but unlike in airflow, these post-touch vibrations will damp and are not superposed on bending. Lastly, airflow will generate a unique relationship between bending and vibration across the whisker array— longer whiskers will

bend and vibrate more than shorter whiskers, but will vibrate at lower frequencies. Touch stimuli will not generate this systematic relationship across the array.

3.5.4 Characterization of Vg neuron responses to airflow stimuli compared to touch

Neural encoding of vibration and bending has been well studied at many levels of the trigeminal pathway using direct tactile stimulation; vibrissal deformation induces mechanical signals that are encoded by primary sensory neurons of the Vg. Vg neurons have high temporal bandwidth and respond strongly to both bending and vibration (Arabzadeh et al., 2006; Arabzadeh et al., 2005; Chagas et al., 2013; Gibson et al., 1983a, 1983b; Jones et al., 2004a; Jones et al., 2004b; Kwegyir-Afful et al., 2008; Leiser et al., 2007; Lichtenstein et al., 1990; Lottem et al., 2009, 2011; Shoykhet et al., 2000; Stuttgen et al., 2008; Stuttgen et al., 2006; Szwed et al., 2006b).

Given that rats can and do rely on their whiskers to localize airflow sources, we expected Vg neurons to encode information about airflow stimulus features. We further expected responses to be analogous to those obtained during tactile stimulation, as the underlying driver of neural responses – mechanics at the whisker base – ought to be grossly comparable between touch and airflow stimulation.

This expectation was supported by a small set of Vg neural responses; all neurons responded robustly to airflow but had widely varying maximum firing rates (between 8 – 120 spikes/sec) and varying degrees of adaptation (Fig. 3.5). All neurons increase firing rate with airspeed, consistent with both the increased bending and vibration magnitude associated with higher airspeed. In addition, a neuron's preferred airflow direction can change with airspeed, possibly because the whisker vibrates in a different direction at different airspeeds. Finally, neurons exhibit periodicities in their firing rate related to the predicted resonance frequency for their associated whisker.

This small set of recordings describes the major stimulus-response relationships that lay the groundwork for understanding neural representations of airflow. Comprehensive descriptions of airflow encoding by Vg neurons will require precise (and currently impractical) quantification of 3D whisker motion during neural recording, in addition to a larger sample of neurons. High precision measurements of whisker motion will be required to distinguish small differences in response types across whiskers, and to investigate how the fast whisker dynamics relate to spiking. With the limited stimulus quantification available, we have characterized some primary response characteristics with a small sample; further investigation of this modality is better served when stimulus quantification is improved.

Chapter 4: Whisking mechanics and active sensing

4.1 Abstract

We describe recent advances in quantifying the three-dimensional (3D) geometry and mechanics of whisking. Careful delineation of relevant 3D reference frames reveals important geometric and mechanical distinctions between the localization problem (“where” is an object) and the feature extraction problem (“what” is an object). *Head-centered* and *resting-whisker* reference frames lend themselves to quantifying temporal and kinematic cues used for object localization. The *whisking-centered* reference frame lends itself to quantifying the contact mechanics likely associated with feature extraction. We offer the “windowed sampling” hypothesis for active sensing: that rats can estimate an object’s spatial features by integrating mechanical information across whiskers during brief (25 – 60 ms) windows of “haptic enclosure” with the whiskers, a motion that resembles a hand grasp.

4.2 Introduction

The rodent vibrissal-trigeminal system is one of the oldest models for the study of active sensing in the field of neuroscience (Richardson, 1909; Simons, 1978; Vincent, 1912; W. I. Welker, 1964; Wineski, 1985). The past five years have seen several breakthroughs in the field of vibrissal research, including the discovery of the central pattern generating circuits responsible for rhythmic whisking (Moore et al., 2013) and their close association with sniffing behavior (Moore et al., 2013; Ranade et al., 2013), as well as the elucidation of differential processing along parallel thalamocortical pathways (Moore et al., 2015; Yu et al., 2013). However, we still do not fully understand how to interpret the signals in these central structures, in part because we do not yet

fully understand the inputs: the tactile signals that drive the responses of primary sensory neurons in the trigeminal ganglion.

Recent advances in three-dimensional (3D) whisker mechanics (Huet et al., 2016; Huet et al., 2015; Knutsen et al., 2008; Yang et al., 2016) offer the opportunity to compute the complete set of tactile inputs transmitted by the vibrissae during active tactile exploration. The goal of the present paper is to review recent literature so as to establish a unified framework for describing the geometric and mechanical variables relevant to whisking behavior. Specifically, we develop formalisms for head-centered and whisker-centered reference frames and compare them with the more traditional resting-whisker reference frame. The whisker-centered reference-frame is well suited to describe mechanical information about the external world transmitted by the whisker, but it is geometrically unintuitive. The resting-whisker reference frame is well suited to describe the location of an object relative to a particular whisker, but is ill suited to describing mechanical variables and mechanoreceptor deformation.

By carefully distinguishing between these reference frames, we argue that a whisking rodent will face two separate problems during tactile exploration. The first is how to localize an object in head-centered coordinates based on tactile information that originates in whisker-centered coordinates (“where” is the object). The second is how to integrate information across multiple whiskers to estimate the object’s contour, independent of its location in head-centered coordinates (“what” is the object). In this review we focus on the rat whisker system, but the framework also applies to mice and other rodents.

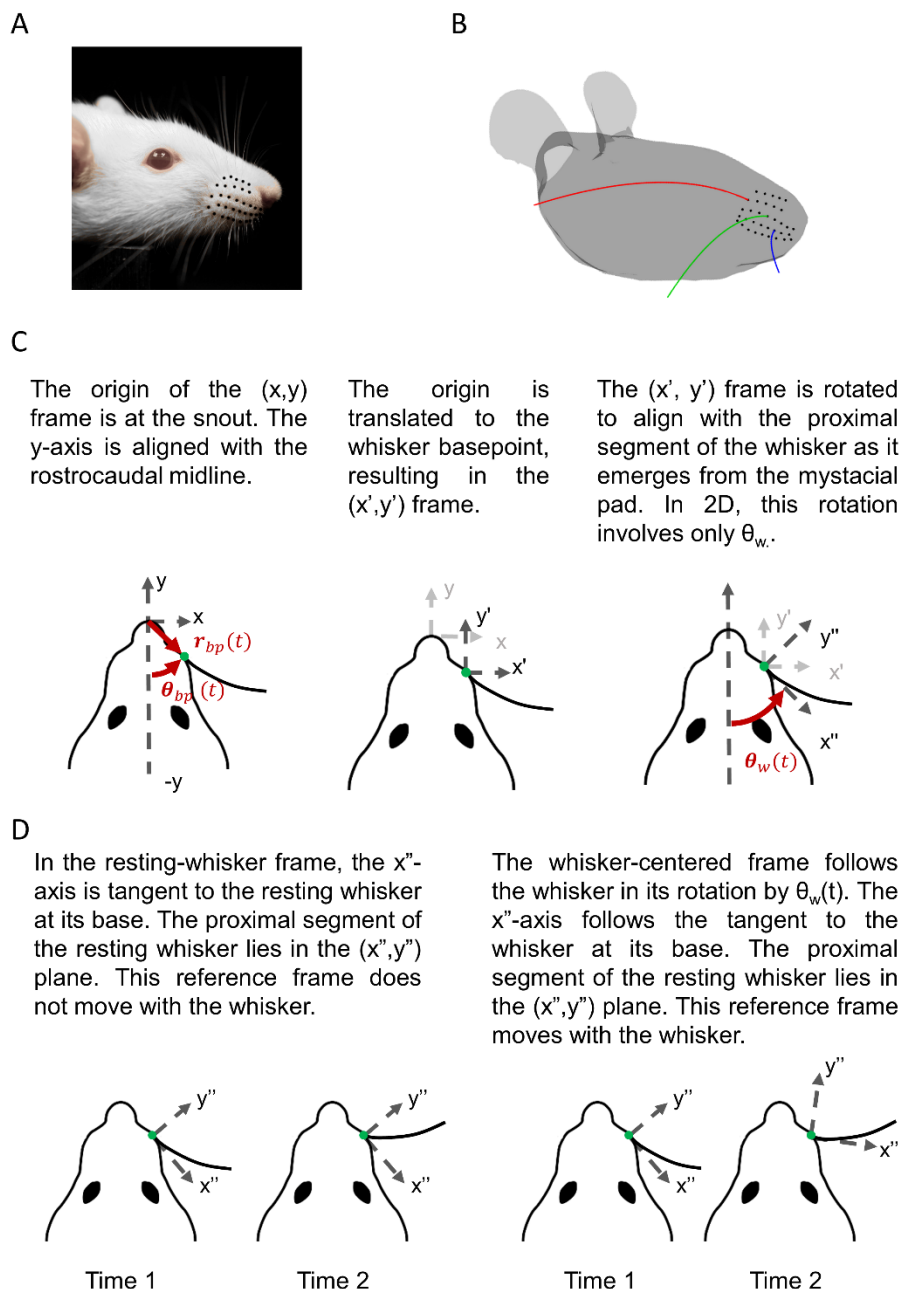


Figure 4.1 Arrangement of the whiskers on the mystacial pad and reference frames relevant to whisking mechanics. **A)** The whiskers of the rat mystacial pad are organized in rows and columns. **B)** Whisker length and curvature vary systematically across the array. **C)** Panels illustrate a two-step process to transform between head-centered, resting-whisker, and whisker-centered reference frames. The translation moves the origin from the snout to a whisker basepoint with polar coordinates (r_{bp}, θ_{bp}) in the head-centered reference frame; θ_{bp} is measured counterclockwise from the midline. The rotation results in a new reference frame

in which the proximal segment of the whisker lies in the x'' - y'' plane and is tangent to the x'' -axis at its base. The y'' -axis is perpendicular to the x'' -axis, with positive defined as the direction in which the tip curves concave forward. **D)** The resting-whisker reference frame does not rotate with the whisker. In contrast, the whisker-centered reference frame rotates with $\theta_w(t)$.

4.3 The geometry of whisking

Whiskers are arranged in a regular array (rows and columns) on the rat's face, and

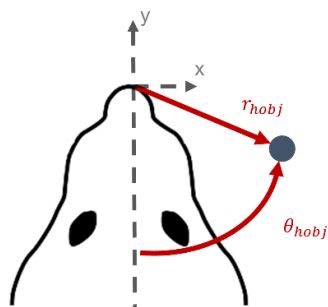
decrease in length from caudal to rostral (Fig 4.1AB). Each whisker has an intrinsic curvature that follows from approximating its proximal shape by a parabola (Knutsen et al., 2008; Towal et al., 2011). Intrinsic curvature varies systematically across the array (Fig 4.1B); shorter whiskers tend to have larger curvature than longer whiskers and also a more variable curvature across whiskers (Quist et al., 2012a).

Each whisker is held tightly within a follicle at its base (Bagdasarian et al., 2013; Ebara et al., 2002). Each follicle is packed with mechanoreceptors, and is actuated by both intrinsic and extrinsic muscles (Deschenes et al., 2015; Haidarliu et al., 2012; Haidarliu et al., 2015; Haidarliu et al., 2010; Kim et al., 2012; Simony et al., 2010). Whisking behavior allows rodents to move their whiskers independently of the head, and it is therefore important to distinguish between head-centered and whisker-centered reference frames.

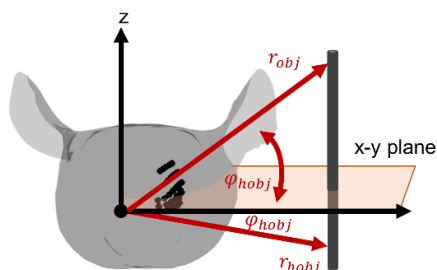
Because each whisker is held tightly by its follicle (Bagdasarian et al., 2013), and because the base of a whisker is relatively stiff (Hires et al., 2013; Quist et al., 2011; Quist et al., 2012a; Voges et al., 2012; M. Williams et al., 2010; Yan et al., 2013), the follicle and the proximal segment of the whisker move approximately as a single unit (a rigid body) relative to the head. Figure 4.1C describes the time-dependent position and orientation of this unit in a head-centered reference frame.

Head-centered reference frame

2D object coordinates are $(r_{hobj}, \theta_{hobj})$.



3D object coordinates are $(r_{hobj}, \theta_{hobj}, \phi_{hobj})$. The elevation angle ϕ relative to the (x,y) plane is shown for two different contact points.

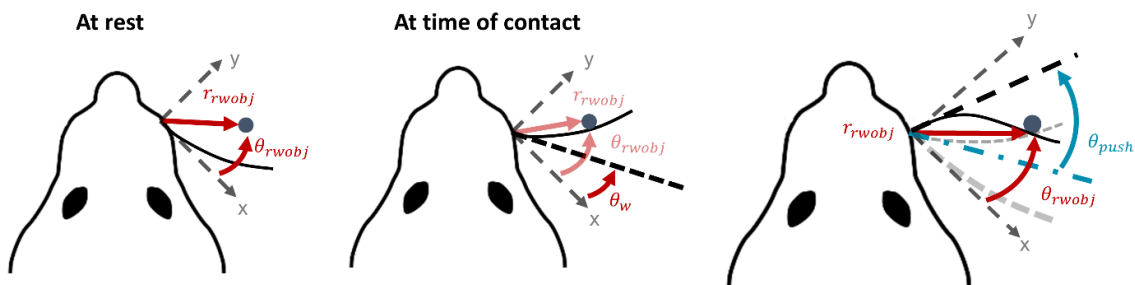


Resting-whisker reference frame

2D object coordinates are $(r_{rwobj}, \theta_{rwobj})$.

Radial distance is measured from the whisker basepoint to the location of the object. Angular object location does not change as the whisker rotates through θ_w .

As the whisker protracts against an object, the angle θ_{push} measures the change in θ_w from onset of contact.



Whisker-centered reference frame

2D object coordinates are $(r_{wobj}, \theta_{wobj})$.

Radial distance is measured from the whisker basepoint to the location of the object. Angular object location changes as the whisker rotates.

As the whisker protracts against an object and deforms, the x-axis continues to track the tangent to the proximal segment of the whisker. The angle θ_{push} measures the change in θ_w from onset of contact.

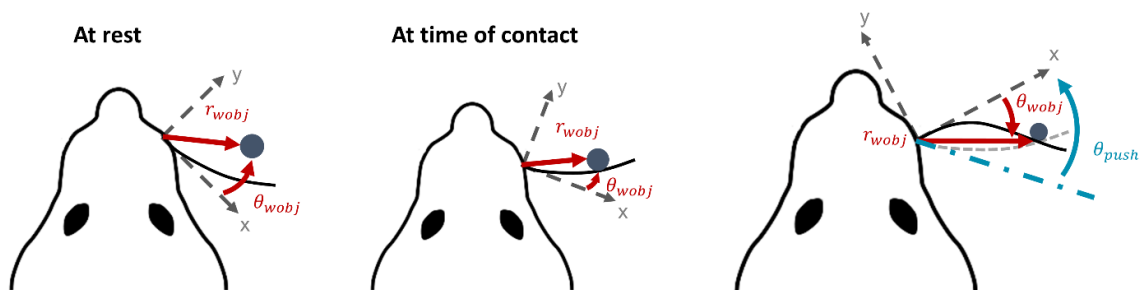


Figure 4.2 Object coordinates in the head-centered, resting-whisker, and whisker-centered reference frames. Here we drop the double prime notation used in Fig 4.1 to refer to the axes in the resting-whisker and whisker-centered reference frames. Object location in the *head-centered reference frame* (h) does not depend on the motions of the whisker. The *resting-whisker reference frame* (rw) stays fixed as the whisker rotates; object coordinates do not change during whisker motion. The angle θ_{push} measures the change in θ_w from the onset of contact. The *whisker-centered reference frame* (w) rotates with the whisker; the angular location of the object changes continuously, both before and during contact. As in the resting-whisker reference frame, θ_{push} measures the change in θ_{push} from the onset of contact. In both resting-whisker and whisker-centered reference frames, whisker position at rest is shown as a thick grey dashed line, whisker position at contact as a thin grey dashed line, and whisker position when protracting against the object as a thin black line.

The two-step process depicted in Figure 4.1C – namely, a translation of the head-centered reference frame to the location of the whisker basepoint and a rotation that aligns the translated reference frame to the proximal segment of the whisker – describes the location and orientation of the whisker with respect to a head-centered reference frame. This process results in the two new reference frames shown in Figure 4.1D: a resting-whisker reference frame and a whisker-centered reference frame.

For the resting-whisker reference frame, the rotation considers the whisker at biomechanical rest and aligns the x'' -axis with the proximal segment of the whisker as it emerges from the mystacial pad. The y'' -axis is perpendicular to the x'' -axis, with positive defined as the direction in which the tip curves concave forward. This reference frame is now fixed. In contrast, the whisker-centered reference frame moves with the whisker. In this frame, the whisker always lies in the x'' - y'' plane and is tangent to the x'' -axis at its base.

This approach can be extended to the full three-dimensional (3D) case. In 3D, the base point coordinates $(r_{bp}, \theta_{bp}, \phi_{bp})$ for the translation include an additional angle, the elevation angle ϕ_{bp} . In 3D, three angles $(\theta_w, \phi_w, \zeta_w)$ are needed to characterize the rotation, where θ_w is the horizontal

angle, ϕ_w is the elevation angle, and ζ_w is the roll of the whisker around its own tangent at the base (Knutsen, 2015; Knutsen et al., 2008; Towal et al., 2011).

The angle θ_w is measured in a horizontal plane and the angle ϕ_w in an elevation plane, both oriented relative to the plane that defines the pitch of the rat's head. In physiological experiments, zero head pitch is defined by aligning bregma with lambda. An alternative, appropriate in the context of some biomechanical and behavioral experiments, is to define zero pitch such that the basepoints of the whiskers lie in horizontal rows (Towal et al., 2011), or such that the two eyes and the nose lie in the horizontal plane (Knutsen et al., 2008). Each choice offers distinct advantages and disadvantages, depending on the experimental questions asked. Once the zero head pitch plane, and thus the horizontal plane, has been identified, the elevation plane can be computed from projecting the whisker onto the horizontal plane: the tangent to the real whisker at its base and the tangent to the projected whisker at its base define the elevation plane.

Finally, it is important to recall that all of these coordinates, $(r_{bp}, \theta_{bp}, \phi_{bp})$ and $(\theta_w, \phi_w, \zeta_w)$, are functions of time, as they describe the position and orientation of the whisker's base in the head-centered reference frame.

The position of an object relative to the rat can be described in any of the three coordinate systems of Fig 4.1CD: the head-centered, the resting-whisker, or the whisker-centered reference frame. Throughout the present work, we assume the object to be a vertical peg, as is often used in behavioral experiments (Knutsen et al., 2006; Mehta et al., 2007; O'Connor et al., 2010; Pammer et al., 2013). For simplicity, the peg is assumed to have infinitesimally small radius, as if it were a line segment.

Object coordinates in each of these three reference frames are illustrated in Fig 4.2. Object location in the head-centered reference frame is self-explanatory; the position of the object in this frame does not depend on how the whisker moves. The other two reference frames require a few additional notes.

First, if the basepoint location $(r_{bp}, \theta_{bp}, \phi_{bp})$ changed with time, the origin of these two reference frames and the object coordinates in these two reference frames would translate accordingly. For the pure rotational motion illustrated in the examples of Fig 4.2, basepoint translation can be neglected; 2D object coordinates in the resting-whisker reference frame $(r_{wobj}, \theta_{wobj})$ thus remain constant during the whisk. In contrast, while r_{wobj} also remains constant in the whisker-centered reference frame, θ_{wobj} changes continuously and becomes negative after significant deflection against an object. Note also that as the whisker makes contact with and deflects against the object, its 2D rotation from the onset of contact is measured by a new angle, θ_{push} . If the whisker were perfectly straight, θ_{push} would be equal and opposite to θ_{wobj} , but because the whisker has intrinsic curvature, their relationship is more complicated and depends on the radial distance r_{wobj} .

Finally, we note that the characterization of object location from any of the three reference frames is easily extended to the 3D case; this simply requires an additional angle for elevation relative to the corresponding horizontal plane, namely $(r_{hobj}, \theta_{hobj}, \phi_{hobj})$, $(r_{wobj}, \theta_{wobj}, \phi_{wobj})$, or $(r_{wobj}, \theta_{wobj}, \phi_{wobj})$. See Section 4 for a more detailed analysis of the unexpected subtleties of 3D object location.

4.4 The mechanics of quasi-static contact

When the whisker makes contact with an object, a mechanical transient is generated (a dynamic effect), and the whisker begins to bend. The quasistatic forces associated with bending are slower, but generally larger in magnitude than the transient forces associated with the collision (Boubenec et al., 2012; Hartmann, 2015; Quist et al., 2014). Fig 4.3AB provide 2D and 3D illustrations, respectively, of the mechanical signals at the base of the whisker generated by contact (Clements et al., 2006; Hires et al., 2013; Huet et al., 2015; Kaneko et al., 1998; Pammer et al., 2013; Scholz et al., 2004; Solomon et al., 2006; Solomon et al., 2010).

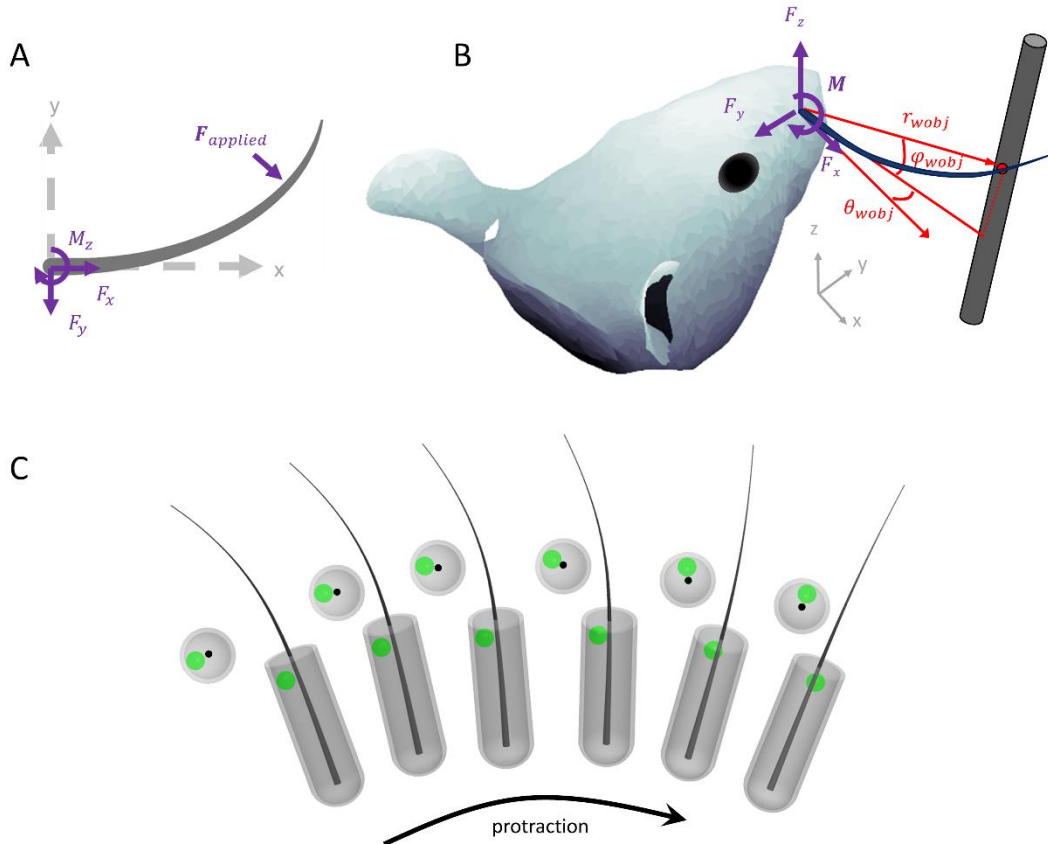


Figure 4.3 Mechanical signals in the whisker-centered reference frame. A) The 2D applied force F is decomposed into an axial component F_x along the whisker's axis and a transverse component F_y . The bending moment M_z at the whisker base has magnitude $|M_z|=r_{wobj} |F_y|$. **B)** The 3D applied force is F decomposed into an axial component F_x and two transverse

components F_y and F_z . The bending moment \mathbf{M} at the whisker base is $\mathbf{M} = \mathbf{r}_{wobj} \times \mathbf{F}$. Contact point coordinates in the whisker-centered frame are $(r_{wobj}, \theta_{wobj}, \phi_{wobj})$. **C**) During a protraction, the follicle and the whisker base rotate and roll as a single unit. The deformations on a mechanoreceptor (green dot) within the follicle are computed in the reference frame of the whisker. Whisker-centered coordinates maintain the geometric relationship between the whisker base and any given mechanoreceptor within the follicle at all times during a protraction. Resting-whisker coordinates cannot achieve this invariance because they are fixed in a single angular location, corresponding to the start of protraction.

Mechanical signals at the whisker base cannot be directly measured, because placing a sensor at the whisker base would interfere with its mechanics. Quantifying these contact variables requires either mechanical modeling (Bush et al., 2016a; Clements et al., 2006; Huet et al., 2016; Kaneko et al., 1998; Pammer et al., 2013; Quist et al., 2012a; Scholz et al., 2004; Solomon et al., 2008; Solomon et al., 2011; Yan et al., 2013) or the use of geometric proxies. For example, change in curvature near the whisker base during contact is sometimes an appropriate proxy for change in bending moment at the whisker base (Campagner et al., 2016; Chen et al., 2015). The quality of the proxy will depend on the exact method by which changes in curvature are computed (e.g., computing a spline vs. fitting a circle near the whisker base). Moreover, whenever the curvature is not computed precisely at the base, its actual value will depend on the somewhat subjective choice of a point “near the base” at which the curvature is computed.

As noted, the diagrams in Fig 4.3AB use the whisker-centered reference frame; it is in this coordinate system that mechanical signals are transmitted to the follicle. To clarify this point, consider the whisker’s location relative to mechanoreceptor endings within the follicle (Fig 4.3C). Mechanoreceptors respond to deformations caused by the motion of the whisker within the follicle. These deformations activate Vg neurons, the “gatekeepers” of all vibrissal-related information to

the trigeminal pathway (Arabzadeh et al., 2006; Bale et al., 2015; Bale et al., 2013; Bush et al., 2016a; Campagner et al., 2016; Jones et al., 2004a; Jones et al., 2004b; Leiser et al., 2006, 2007; Lichtenstein et al., 1990; Lottem et al., 2011; Whiteley et al., 2015). A meaningful physical description of how mechanoreceptors will deform, and thus how Vg neurons will respond, requires a reference frame in which the location of the mechanoreceptor relative to the whisker does not change as the whisker moves. Vg response to mechanical stimuli thus requires that these stimuli be characterized in the whisker-centered reference frame.

4.5 The location of whisker-object contact points from different reference frames

How might the rat localize an object in the context of reference frames and variables described above?

Consider a rat whisking against a peg situated at two different horizontal angles ($\theta_{hobj} = 51^\circ$ and $\theta_{hobj} = 79^\circ$) relative to its snout (Fig 4.4A and 4.4B, at time of initial contact). A 2D view from the top, further simplified by neglecting whisker curvature (see insets at top left), correctly indicates that all whiskers caudal to the peg will make contact with the peg at a single horizontal angular location in the head-centered reference frame (θ_{hobj}). However, the 2D view gives the misleading impression that there is a simple relationship between the angular location θ_{hobj} of the object in the head-centered reference frame and the angle θ_w through which the whisker must rotate in order to make contact with the object.

The 3D views reveal considerable more complexity. All three whiskers make initial contact with the object at different values of θ_w , ϕ_w and ζ_w , because the orientations of each of the whiskers are different in the head-centered reference frame. Note that although θ_{hobj} differs by exactly 28°

between Figs 4.4A and 4.4B, the θ_w values for the whiskers do not shift by 28° . The complex relationship between θ_w and θ_{hobj} is due to the intrinsic curvature of the whiskers.

In whisker-centered coordinates, all whiskers have different values of r_{wobj} and θ_{wobj} at the time of initial contact, while ϕ_{wobj} is identically zero because the whiskers have not deflected out of their individual x-y planes. Also note that in head-centered coordinates, the coordinates of the whisker-object contact point r_{hobj} and ϕ_{hobj} are different for each whisker, while θ_{hobj} stays constant because the peg is assumed to have infinitesimally small radius. If the peg had finite radius, then θ_{hobj} would change as the whisker slips along its length; this type of motion is termed “longitudinal slip” (Clements et al., 2006; Kaneko et al., 1998; Kim et al., 2012; Scholz et al., 2004; Solomon et al., 2008; Solomon et al., 2010).

Fig 4.4C and 4.4D depict the geometry of contact after all whiskers have protracted against the peg until θ_w has increased by 10° . Roll (ζ_w) and elevation (ϕ_w) change with θ_w according to the kinematic equations for whisking motions developed by Knutsen et al., 2008 (Knutsen et al., 2008). After this protraction, the coordinates $(\theta_w, \phi_w, \zeta_w)$ of whisker orientation relative to the head have changed, as have the coordinates $(r_{wobj}, \theta_{wobj}, \phi_{wobj})$ of the object in the whisker-centered reference frame. The value of ϕ_{wobj} is no longer zero, because the whiskers have now deflected out of their initial planes.

It is interesting to note that the location of the whisker-peg contact points have also changed in the head-centered reference frame, both from whisker to whisker and during the protraction. These changes may seem unintuitive, because the location of the peg does not change relative to the head. Nevertheless, the location of the whisker-peg contact points have changed because the whiskers

slip against the peg, both vertically and along their length. In this example, the peg is assumed to have vanishingly small radius, and the value of θ_{hobj} changes with protraction but not from whisker to whisker. In contrast, both r_{hobj} and θ_{hobj} change considerably from whisker to whisker but less so as a given whisker protracts against the peg. If the peg had finite radius, θ_{hobj} would also vary considerably from whisker to whisker.

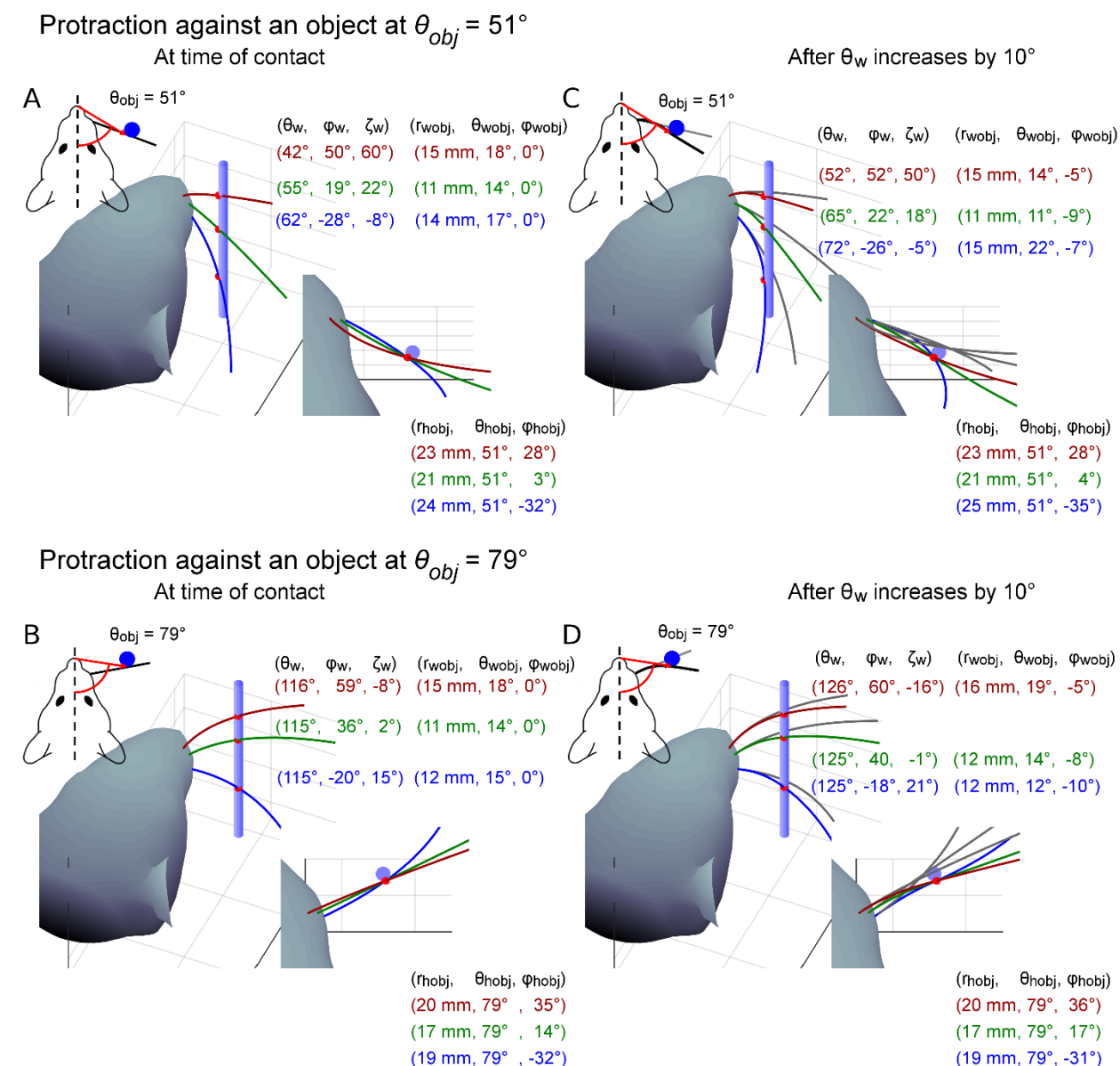
The panels of Fig 4.4 summarize the significant challenges of the 3D object localization problem for the rodent, and also implicitly reveal an important “where/what” distinction in the vibrissal system. In panels 4A and 4B, the animal must localize the peg at two different angular positions. In panels 4C and 4D, as the whiskers deflect against the object the animal should have the same perception of the contour of the peg, regardless of whether the whiskers made contact with the peg at 51° or 79° .

Our approach to this problem is based on the observation that object location (“where” is the object) is most easily expressed in the head-centered or resting-whisker reference frames. In contrast, it is the whisker-centered reference frame that provides an optimal and most natural frame for the calculation of the contact forces and moments that lend themselves to a description of object contour (“what” is the object). In the next section, we examine the sources of information available to the animal for determining object location as well as object contour.

4.6 Where vs. what: determining object location and contour

Consider first the problem of *localizing* the peg at either 51° or 79° (Fig 4.4AB). Both the resting-whisker and the head-centered reference frames lend themselves to an intuitive description of object location (Ahissar et al., 2011; Kleinfeld et al., 2011; Knutsen et al., 2009; Knutsen et al., 2006; Mehta et al., 2007; O'Connor et al., 2010; Pammer et al., 2013). To localize an object, the

rat must detect the mechanical transients generated by collision with an object, determine the location of its whisker at the instant of contact, and determine the location along the whisker at which contact was made.



coordinates in both whisker-centered and head-centered reference frames, are shown for three different whiskers (red, green, and blue). **C and D)** Whisker angular coordinates and contact point coordinates in the same reference frames and for the same three whiskers, after all three have protracted against the peg until θ_w has increased by 10° . The changes in roll (ζ_w) and elevation (ϕ_w) with θ_w were simulated according to the kinematic equations for whisking motions developed by Knutsen et al., 2008 (Knutsen et al., 2008).

However, determining the whisker's location at the instant of object contact is challenging because there are very few proprioceptors in the whisking muscles (Ebara et al., 2002; Moore et al., 2015). The rat has thus no direct access to $(\theta_w, \phi_w, \zeta_w)$, though some information may be available through the mesencephalic nuclei (Mameli et al., 2016; Mameli et al., 2010). Recent studies have suggested that reafferent signals reporting whisking phase could be combined with an efferent copy of whisking midpoint and amplitude to estimate angular whisker position θ_w (Fee et al., 1997; Hill et al., 2011; Kleinfeld et al., 2011; Wallach et al., 2016). Given that the elevation and roll of the whisker are tied closely to protraction angle (Knutsen, 2015; Knutsen et al., 2008), the full 3D angular position of the whisker $(\theta_w, \phi_w, \zeta_w)$ at the time of contact could in principle be determined.

Several excellent review articles have recently surveyed the neurophysiological basis for the implementation of this type of localization scheme (Ahissar et al., 2011; Diamond et al., 2008; Kleinfeld et al., 2006; Knutsen et al., 2009). From a purely mechanical standpoint, this localization approach is plausible because the whisker has very little mass, and its proximal region behaves like a rigid body during non-contact whisking (Knutsen, 2015; Knutsen et al., 2008). The rat would thus be able to monitor and control purely kinematic variables (i.e., phase, midpoint, amplitude) to obtain an estimate of whisker position during localization behaviors. However, this localization

scheme requires precise timing information to allow the computation of θ_w at time of contact. Moreover, values of θ_w must be monitored separately for each whisker.

A complementary hypothesis emerges from considering 3D geometric and mechanical effects. Because the whisker rolls as it protracts, the orientation of the whisker varies systematically through the whisking cycle (Knutsen, 2015; Knutsen et al., 2008). In turn, the whisker's orientation at the time of object contact will determine the direction in which it is deflected by the object (Huet et al., 2016; Huet et al., 2015; Solomon et al., 2008; Solomon et al., 2010; Yang et al., 2016). The direction of whisker bending could thus provide a mechanism for the rat to determine the horizontal angle at which the whisker has made contact with the object (Knutsen et al., 2008; Yang et al., 2016).

Consider next the problem of *extracting the contour* of the peg. In principle, the rat could determine object contour by computing the location of each whisker-object contact point in head-centered coordinates; this would be done in the manner just described for object location (whisking phase, timing, etc...). The contour of the object could then be determined by comparing these contact point locations – in head centered coordinates – across the array of whiskers. Although this scheme cannot be ruled out, it is computationally expensive and error prone, because the correct computation of object contour would depend on the correct computation of several object locations.

An alternative possibility is suggested by Figure 4.4CD, which indicates that after object contact, a new source of information becomes available to the animal: the contact forces and moments at the base of each whisker. The signals associated with contact mechanics tend to be much larger than the signals present during non-contact whisking (Boubenec et al., 2012; Campagner et al.,

2016; Khatri et al., 2009; Leiser et al., 2007; Quist et al., 2014; Szwed et al., 2003; Szwed et al., 2006b). Given the spatial invariance of a mechanoreceptor with respect to the follicle (Figure 4.3), the deformation of mechanoreceptors associated with contact is optimally expressed in whisker-centered coordinates. Two recent studies indicate that this mechanical information is indeed encoded by primary sensory neurons of the trigeminal ganglion (Bush et al., 2016a; Campagner et al., 2016).

We therefore propose that – just as during human exploration with fingertips (Tramper et al., 2013) – the rat exploits contact mechanics to determine object features such as contour. Although very few studies have examined whisker-object contact patterns, a few recent experiments provide clues as to how this computation is enabled by whisker motions.

First, several studies have indicated that as rats perform haptic exploration tasks, they gradually increase contact durations with the object (Deutsch et al., 2012; Grant et al., 2009; Saraf-Sinik et al., 2015). Mechanically, this would have the effect of damping out vibrations associated with object collision and ensuring that the whisker enters a quasistatic regime in which bending is the dominant effect (Boubenec et al., 2012; Quist et al., 2014; Yan et al., 2013). In 2D, the mechanical signals associated with bending have been shown to uniquely represent the whisker centered geometry $(r_{wobj}, \theta_{wobj})$ (Solomon et al., 2011). Moreover, recent work from our laboratory strongly indicates that a subset of forces and moments at the whisker base will also be sufficient to represent $(r_{wobj}, \theta_{wobj}, \phi_{wobj})$.

Second, studies on orienting behavior have shown that rats tend to position their heads so as to maximize the number of whiskers in contact with a surface, given the expected orientation of the

surface (Hobbs et al., 2015; Mitchinson et al., 2007). The tendency to maximize the number of whisker-object contacts suggests that the integration of information across multiple whiskers will play an important role during contour extraction.

Finally, a recent study employed a light sheet to directly visualize whisker-object contact patterns as naïve rats freely explored a flat, vertical surface (Hobbs et al., 2016). Results showed that every whisker exhibited brief windows during which many whiskers collectively made sustained (25 – 60 ms) contact with the surface. The number of whiskers in contact depended strongly on the pose of the head, but averaged around 15 to 20. Furthermore, during this contact window (termed the “sustained collective contact interval,” or SCCI), all whiskers converged and moved more slowly on the surface.

Taken together, we interpret these studies to suggest that the rat employs a strategy of “windowed sampling” during object exploration. As opposed to relying primarily on inter-vibrissal phase or timing cues to extract object spatial features (e.g., contour), the rat spatially integrates across whiskers the mechanical signals acquired during the SCCI. These mechanical signals can thus provide information about object identity through an integrative computation that does not depend on the object’s location in head-centered coordinates.

4.7 Conclusions

Three-dimensional investigation of vibrissotactile exploratory behavior is experimentally challenging, and simulations of 3D vibrissal geometry and mechanics are complex. Yet a 3D approach is critical if we are to begin understanding the input signals that drive activity at more central levels of the trigeminal system (Huet et al., 2016; Huet et al., 2015; Jones et al., 2004b; Lichtenstein et al., 1990; Yang et al., 2016). As the field progresses in its understanding of 3D

mechanics, geometry, and vibrissal-object contact patterns, it will be essential to ensure a systematic notation for each of the reference frames relevant to quantifying input variables.

In particular, the head-centered and resting-whisker reference frames naturally lend themselves to a description of object location, while the whisker-centered reference frame provides a natural description of mechanics. We further suggest that by exploiting contact mechanics, the animal could obtain estimates of contact point location within the whisker-centered reference frame; object contours can then be determined by integrating mechanical information across vibrissae during a brief (25 to 60 ms) window of quasi-static deflection that lasts only a fraction of the whisk. We posit that rats perform a “haptic enclosure” (Klatzky et al., 1995; Lederman et al., 2009) with their whiskers, similar to a grasping motion of the human hand.

Although this article has implicitly raised a host of interesting questions about the neural representations of these coordinate systems, we can only offer speculative ideas as to how and where those neural representations would emerge. By analogy to reaching and grasping (Graziano, 2001), we suggest that rodents may employ a variety of reference frames (head-centered, unilateral-array centered, whisker-centered) depending on their behavioral goals. Some evidence for task-specific coordination of head and whisker movements has recently emerged in freely behaving mice. We suggest that a careful consideration of whisking motions may make the rodent system an excellent model for the study of neural transformations between reference frames, a choice that would complement work in primates.

Chapter 5: Continuous, multidimensional coding of complex tactile stimuli by primary sensory neurons of the vibrissal system

5.1 Abstract

To uncover the full representational capabilities of sensory neurons, it is crucial to observe neural responses to a variety of complex and naturalistic stimuli. In the rodent whisker system, mechanical information at the base of the follicle is known to drive the firing of primary sensory neurons of the trigeminal ganglion (Vg). Until now, studies of the encoding properties of these neurons have been primarily limited to 2D analyses, and often employ restricted stimulus sets. Here we quantify the full 3D shape and mechanics of whiskers during complex and naturalistic stimulation while recording from Vg neurons. The data is used to fit generalized linear models that predict with high accuracy the firing of these neurons in response to 3D mechanical information. Our results show that individual Vg neurons simultaneously represent multiple mechanical features of a given stimulus, and that the binary distinction between rapidly and slowly adapting populations does not hold during complex stimulation. A comparison of tuning properties across recorded neurons reveals that feature representations vary continuously and tile all available mechanical information without segregating into feature specific functional streams.

5.2 Introduction

The overarching goal of sensory neuroscience is to quantify how neurons encode and process fundamental physical stimuli: photons, pressure waves, chemicals, and mechanical forces. A common experimental approach is to use a highly controlled, reduced, and repeatable stimulus set to elicit consistent neural responses that can be averaged to reduce trial-to-trial variability (Jones et al., 2004b; Lottem et al., 2011; Shoykhet et al., 2000; Storchi et al., 2012; Stuttgen et al., 2008;

Szwed et al., 2006b). This method lends itself to a description of neural coding in which units are tuned to a small number of stimulus features in a manner well described by low-dimensional tuning curves (Bale et al., 2013), and to a categorization of units into functional classes (Zeng et al., 2017) based on differential responses to the stimuli presented (Kwegyir-Afful et al., 2008; Lichtenstein et al., 1990; Lottem et al., 2011; Shoykhet et al., 2000; Stuttgen et al., 2008; Stuttgen et al., 2006; Zucker et al., 1969). A problem with this approach is that the results are constrained by the stimuli, which are generally categorical themselves. The presented stimuli significantly underrepresent the stimulus space to which the neurons respond, the space of natural stimuli being larger in both extent and dimensionality. It is thus almost inevitable that the neurons will, in turn, exhibit simple tuning curves and categorical response types. Descriptions of neural representations of stimuli therefore remain incomplete.

The rodent whisker system is one of the premier models for studying tactile processing and cortical function (Ramirez et al., 2014; Woolsey et al., 1970); however, most descriptions of the sensory inputs to this system —the responses of primary sensory neurons in the trigeminal ganglion (Vg) — are based on experiments that use reduced stimulus sets. Variations in the presented stimuli are discrete, involving only a few features or limited spatial directions, small in dynamic range, or presented only along the neuron's preferred tuning. More recent work in awake preparations — both head-fixed and freely moving — has allowed for continuous variability in the stimulus due to the behavioral control of whisking (Campagner et al., 2016; Khatri et al., 2009; Leiser et al., 2007; Severson et al., 2017). However, these studies have been restricted to analyzing a 2D projection of the whisker. Although together these studies have led to a better understanding of crucial aspects

of Vg coding properties, such as directional selectivity and temporal precision, an integrated view of stimulus encoding remains elusive.

During natural exploration, rodents whisk in stereotyped but non-repeatable 3D trajectories (Birdwell et al., 2007; Deutsch et al., 2012; Knutsen et al., 2008; Ritt et al., 2008). The whiskers contact objects actively via a combination of whisker, head, and body movements, and passively via extrinsic movement of the objects themselves. The result is a complex, 3D, and continuously varying pattern of physical stimuli that impinges on the whisker. The many components of these stimuli are often constrained to covary, calling into question the validity of categorical neural responses and traditional low dimensional tuning curves.

In the present work we take inspiration from studies of the visual system in which stimulus sets are becoming increasingly natural and complex (Chichilnisky, 2001; Kayser et al., 2003; McIntosh et al., 2016; Touryan et al., 2005), and apply to the whiskers a manual, naturalistically varying stimulus set specifically designed for a rich exploration of tactile stimulus space. We introduce a stereo-vision 3D whisker imaging technique, apply a validated 3D model of whisker mechanics (Huet et al., 2015), and use state of the art statistical modeling techniques (Theis et al., 2013; Williamson et al., 2015) to characterize the full 3D input space available to the whisker system, and the subsequent response properties of Vg neurons to stimuli that covary along many dimensions.

5.3 Results

5.3.1 Acquisition of 3D stimulus information

We recorded from 78 whisker-responsive neurons in the Vg of 22 anesthetized rats during manual tactile stimulation of single whiskers. During stimulation, high-speed video (300 or 500 fps) of

whisker motion was recorded in two views (Fig. 5.1A). Tactile stimulation methods were similar to those described previously (Bush et al., 2016a). Briefly, a graphite probe was used to repeatedly deflect the whisker at 2 or 3 different distances along the whisker length (Fig. 5.1C) in 8 cardinal directions (Fig. 5.1D). Stimulation speed varied across trials, but care was taken to ensure that two approximately distinct speeds (“fast” and “slow”) were used at each stimulation location. We recorded video and neural data for an average of ~500 seconds per neuron, with an average of 684 individual whisker deflections across all conditions. Whiskers were tracked in both camera views (Clack et al., 2012), and the shape of the whisker was reconstructed in 3D (Fig. 5.1B), along with estimates of the 3D stimulus contact point. Established mechanical models (Huet et al., 2015) were then used to compute the quasistatic forces and moments at the whisker base in each video frame (Fig. 5.1E).

In the anesthetized animal, exerting a force on the whisker not only causes the whisker to bend, but also causes the follicle to rotate within the mystacial pad (Bagdasarian et al., 2013; Bush et al., 2016c). This rotation generates a force between the follicle and the surrounding tissue, which may excite mechanoreceptors and contribute to the Vg response. Follicle rotation within the tissue is especially pronounced for proximal stimulations. Because the mechanical properties of the follicle-cheek interface are unknown, we used the angular rotation of the whisker as it emerged from the cheek (Fig. 5.1E, Suppl. Fig. 5.1) as a proxy for the force of the mystacial pad on the follicle. All signals, including spike times, were interpolated and binned to a sampling rate of 1 kHz.

A notable feature of the stimulation procedure used here is that although the deflections differ from each other in detail, they all have a similar temporal evolution. Since the manual stimulation

method does not permit repeated delivery of an identical stimulation, time-locked responses could not be compared across trials. However, each deflection evolves similarly with time, as would naturally occur for a set of repeated whisks against an object. This temporal structure lends itself to analysis through “time-normalized” histograms created by normalizing the duration of all stimulations to be exactly equal to one, a procedure that resembles a temporal phase analysis (Leiser et al., 2007; Moore et al., 2015; Szwed et al., 2003), while retaining individual whisk dynamics and variability.

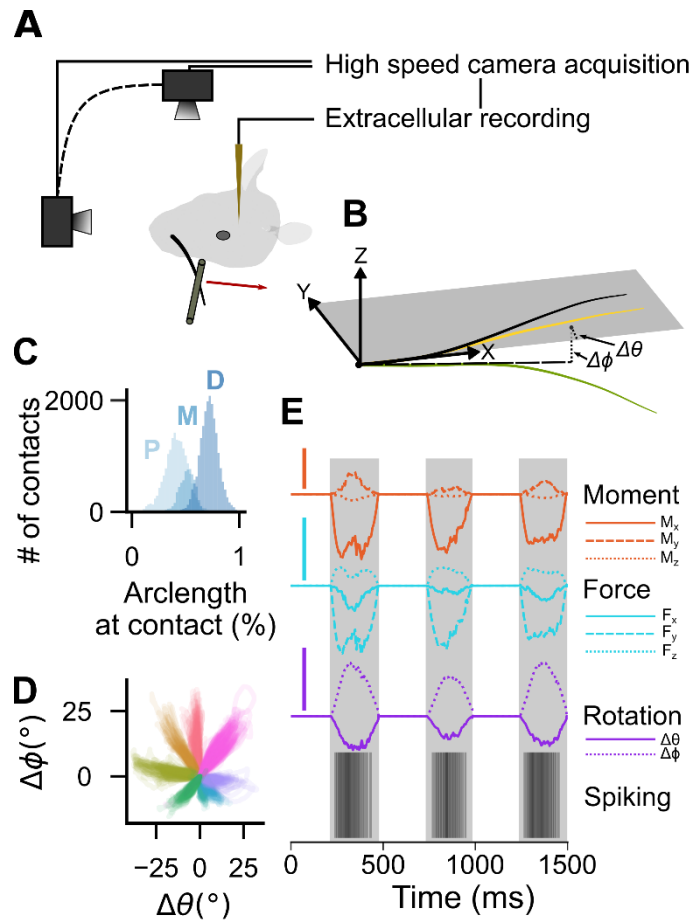


Figure 5.1: Acquisition of 3D stimulus information (A) Schematic of experimental setup. Two high-speed cameras are centered on the rat's whisker array. A tungsten electrode is lowered to record activity from a single Vg neuron during manual deflection of a single whisker. (B) Example 3D reconstructions of a whisker. Mechanics are calculated in whisker-centered coordinates based on the change in whisker shape (bending; yellow); rotational features are calculated based on the change in base segment emergence angles (green, $\Delta\theta$ on the x-y plane, $\Delta\phi$ on the x-z plane) compared to rest (black). See *Methods* for details. (C) Deflections were applied at 2 to 3 distances along the whisker arclength; whisker lengths were normalized to one. Unsupervised clustering algorithms grouped the contacts into three "distance groups": proximal (P), middle (M), and distal (D). A histogram of the number of contacts at a given fraction of the arclength is shown across all neurons. When only two distinct clusters were found for a given whisker, the middle group was omitted; the middle group is thus underrepresented. (D) Deflections were applied in approximately 8 directions in the plane perpendicular to the main axis of the whisker. Unsupervised clustering algorithms labeled each deflection as belonging to one of eight "direction groups". Trajectories described in terms of the two base angles are shown for all deflections of an example whisker; color indicates the assigned direction group. Qualitatively distinct groups are observed for this example and for all whiskers. (E) Traces of moments (orange; M_x, M_y, M_z), forces (cyan; F_x, F_y, F_z), rotation angles (magenta; $\Delta\theta, \Delta\phi$), and observed spikes for three successive deflections are shown for an example whisker/neuron pair. Scale bars are $0.1 \mu Nm$, $0.5 \mu N$, and 5° respectively.

5.3.2 Most neurons are jointly tuned to direction and location of stimulation along the whisker arclength

Multiple previous studies have demonstrated that Vg firing rate is strongly influenced by the direction of deflection (Gibson et al., 1983b; Jones et al., 2004a; Jones et al., 2004b; Lichtenstein et al., 1990; Woolston et al., 1983; Zucker et al., 1969) as well as the location at which the stimulus makes contact along the whisker length (Szwed et al., 2003; Szwed et al., 2006b). However, these studies have not quantitatively examined the joint effect of direction and stimulus contact location on firing rate.

Here, we quantify the effects of changes in both arclength of contact (two or three groups) and direction (eight groups) simultaneously; when incorporating trial-to-trial variability, this set of stimuli covers a large region of the possible stimulus space. For each neuron, we computed the average firing rate across many deflections for each arclength/direction combination, and used it

to compute a Directional Selectivity Index (DSI) defined as $(1 - \sigma^2)$, where σ^2 is the directional circular variance (Mazurek et al., 2014) (see *Methods*). Results of this analysis are shown in Figures 5.2A-D for one example neuron. This neuron's firing rate increased as stimulation became increasingly proximal (Fig. 5.2A,C). The neuron had a best direction near 225° (Fig. 5.2B,C), and exhibited a moderately strong DSI of 0.54 for proximal stimulation and of 0.64 for distal stimulation (Fig. 5.2D). Notice that multiple combinations of arclength and direction can result in the same firing rate (Fig. 5.2C). Additionally, the directional tuning curve is broader for more proximal stimulation, indicating that this neuron's directional tuning is weaker for more proximal deflections (Fig. 5.2C).

These results are generalized over all neurons in Figures 5.2E,F. Of the 78 recorded neurons, 75 had distinguishable arclength and direction groups. Although all 75 exhibited significant direction tuning, the DSI was found to be continuously and uniformly distributed across all neurons (Fig. 5.2E; Kolmogorov-Smirnov test $p=0.88$). In other words, there is a continuum of directional tuning strength across the population. Nearly all neurons (72/75) were tuned for arclength, with stronger responses primarily occurring for more proximal stimulations. Importantly, the firing rate of most neurons (68/75) was modulated by both direction and arclength. Figure 5.2G shows the change in DSI for distal compared to proximal stimulations for all cells. Interestingly, approximately equal numbers of neurons become more/less directionally tuned as the stimulation is increasingly distal. Cells with $(DSI_{\text{distal}} - DSI_{\text{proximal}})$ greater than zero were more directionally tuned for distal contacts (28/68 neurons).

The results of Figure 5.2 indicate that naturalistic and complex stimulation can recapitulate the classical Vg responses observed during tightly controlled ramp and hold stimulation (Kwegyir-

Afful et al., 2008; Lichtenstein et al., 1990; Shoykhet et al., 2000). In addition, these results also reveal an underappreciated feature of the response: when direction and arlength covary continuously and simultaneously, as they would during natural whisking, the firing rate is governed jointly by both stimulus features. These results suggest that it is not possible for the response of a single neuron to encode unambiguously a stimulus feature (e.g., arlength of contact), and that a population readout is required to accurately estimate these behaviorally relevant quantities.

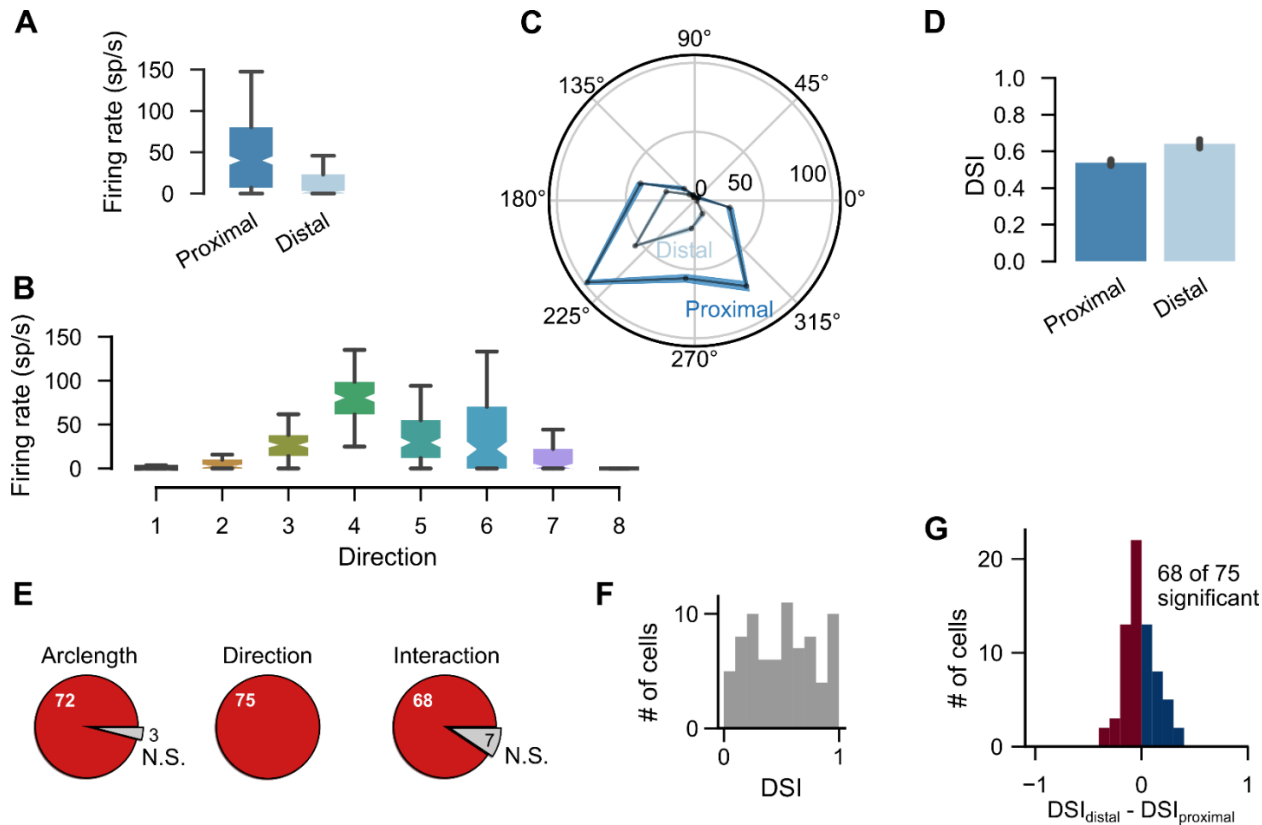


Figure 5.2: Most neurons have firing rates that correlate both with arlength of contact and deflection direction: (A-D) An example neuron whose firing rate is modulated by both arlength and direction. **(A)** Firing rate increases as stimulation becomes more proximal. **(B)** Firing rate modulation by direction group. The DSI for this neuron is 0.72. **(C)** Average firing rate and directional selectivity can depend on the arlength of contact. Average firing rate of

the example cell is shown as a function of deflection direction, for both proximal and distal arclength of contact. The lines indicate average firing rate for all deflections in each group, with line thickness indicating \pm S.E.M. **(D)** Quantification of the DSI for the example cell. **(E)** Number of cells with significant effects of arclength, direction, and their interaction on firing rate (one-way ANOVA). Red indicates significant effects. **(F)** Vg neurons range from not at all directionally modulated (DSI=0), to very strongly modulated (DSI=1). **(G)** Directional tuning strength is modulated by arclength of contact for most cells.

5.3.3 Temporal patterns of spikes during contact are complex and direction dependent

The previous analyses characterized how direction and arclength of contact affect the average firing rate. However, it is well known that detailed temporal features of the Vg response are important in shaping responses in more central structures (Hires et al., 2015). We exploited the variability across individual deflections to quantify the variety of complex dependencies between temporal firing pattern and direction of deflection across the population of recorded cells (Supplemental Videos 5.1-5.3). Two examples are shown in the time-normalized histograms of Figure 5.3A. Cell 1 exhibits no change in temporal firing pattern, but does exhibit strong changes in average firing rate with direction. In contrast, Cell 2 exhibits strong alterations in firing pattern based on stimulation direction; some directions show a strong onset response, others a strong offset response, and yet others show neither.

For both Cells 1 and 2, we found the time of maximal firing rate (“peak time”) for each direction. The center plots in the two examples of Figure 5.3A show time-varying firing rates as grayscale heatmaps for each direction, with peak times indicated as yellow asterisks to allow comparison across directions. The peak times for all cells and directions are shown in Figure 5.3B. Each cell has eight peak times, one per direction. Cells are ordered by peak time variance; cells with little directional modulation of peak time are at the top and those with strong modulation at the bottom.

Figure 5.3C aggregates data across neurons and directions; peak times are most likely to occur at onset, less likely at offset, and least likely in the middle of the deflection.

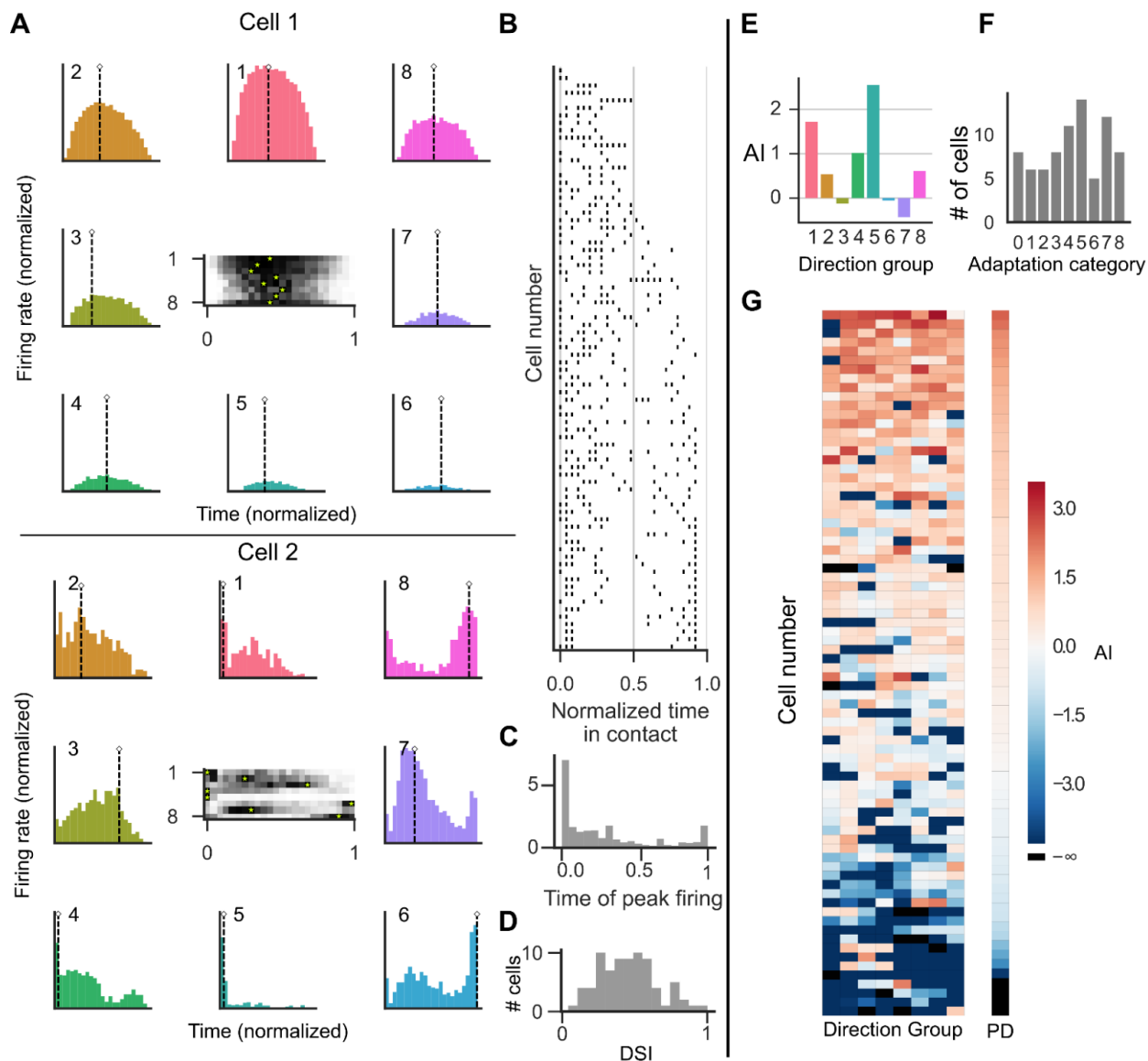


Figure 5.3: The temporal structure of the Vg responses can be complex and direction dependent. (A) Normalized peristimulus time histograms (PSTHs) grouped by deflection direction are shown for two example neurons. The horizontal axis of each histogram has been linearly normalized to a contact duration between 0 and 1, and each vertical axis is scaled to the maximum firing rate observed for that neuron. In each of the eight color panels surrounding the center, the color, position, and numerical label denote the direction group of the

corresponding PSTH. The central plot shows the same eight histograms, but firing rate is now represented as grayscale intensity and the y-axis indicates directions 1 – 8. Times of maximal firing rates (peak times) are indicated as yellow asterisks superposed on the grayscale plot for each deflection direction. A peak time of 0 indicates maximal spiking at onset of contact, while a peak time of 1 indicates maximal spiking at offset of contact. Cell 1 shows little change in temporal pattern with deflection direction, while Cell 2 shows significant modulation of temporal pattern with deflection direction. **(B)** Time of peak firing rate(s) for all neurons in all directions. Each row represents a neuron; each row has eight points, one for the normalized time of peak firing rate for each direction group. Identical peak times for several directions appear as superimposed points, so fewer than 8 points may appear in a row. Cells are ordered by variance of peak time of firing. **(C)** Histogram of time of peak firing collapsed across neurons and directions (eight counts per neuron). **(D)** DSI of the time of peak firing rate as a function of direction for all neurons. If the time of peak firing rate is heavily modulated by direction, $DSI \cong 1$. **(E)** Example of adaptation index AI as a function of direction group for Cell 2. Positive adaptation indicates that firing rate during the first 10 ms of contact is higher than the mean firing rate; negative values indicate that firing rate during the first 10 ms is lower than the mean firing rate. **(F)** Number of cells in each adaptation category. Category number indicates the number of directions in which a neuron exhibited RA-like responses (positive AI). **(G)** Adaptation index is shown in color for all neurons and direction groups. Negative infinity is represented as the darkest blue; directions in which no spikes were observed appear black. Cells are ordered by the mean adaptation index across all directions. Right column (PD) isolates the adaptation index for each neuron's preferred direction; neurons are ordered by decreasing adaptation index.

We quantified how strongly the direction of stimulation influences the peak time by calculating the DSI of the peak time. The DSI for the example cells are given in the inset of the central plots in Figure 5.3A. Across all neurons, the DSI of peak time is normally distributed (Shapiro Test $p=0.47$), as shown in Figure 5.3D. The dependency of the temporal pattern of spiking on deflection direction is moderate, with few neurons being very strongly ($DSI \cong 1$) or very weakly ($DSI \cong 0$) modulated.

Vg neurons are frequently classified as rapidly adapting (RA) and slowly adapting (SA) based on their response to ramp and hold stimulation (Kwegyir-Afful et al., 2008; Lichtenstein et al., 1990; Shoykhet et al., 2000; Stuttgen et al., 2006; Woolston et al., 1983). To implement a similar analysis

with the present data set, in which there is no clear ramp or hold period, we introduce an “Adaptation Index” (AI) as the log ratio of the firing rate during the first 10 ms of contact to the average firing rate. An AI of 0 indicates that there is no difference between the onset firing rate and the overall mean firing rate; if there is no firing during onset, the adaptation index is negative infinity. We calculate the AI separately for each direction group. The AI for each deflection direction of Cell 2 is shown in Figure 5.3E, and aggregated for all neurons and directions as a heatmap in Figure 5.3G. Cells are ordered by the mean value of AI across all directions; of note is the smooth transition between cells that spike preferentially at onset (top, red cells), and those that spike less during onset than average (bottom, blue cells). The top cells could be considered as most RA-like, and the bottom cells as most SA-like. The smooth transition from positive to negative AI is maintained if one considers only the preferred direction (PD) for each neuron (Figure 5.3G, right column). Note that in this PD column neurons have been reordered by decreasing AI.

Consistent with previous studies (Jones et al., 2004a), we found that RA-SA like response patterns were often strongly dependent on deflection direction; some cells exhibit a positive AI for some deflection directions and a negative AI for others. To describe these variable adaptation properties, Jones and Keller used the term “mixed” to indicate that a neuron could exhibit RA-like or SA-like responses depending on deflection direction. They use an “adaptation category” that quantifies the number of directions to which a neuron responds in an RA-like manner. We employ an analogous measure, by defining a neuron to be RA-like for a given direction if the AI for that direction exceeds 0. The number of directions for which a neuron responds in this RA-like manner is termed its “adaptation category” (Fig. 5.3F).

5.3.4 Neural responses are correlated with many components of the stimulus, but many components of the stimulus are themselves tightly correlated

The stimulation protocol used here allows us to quantify the full 3D shape of the whisker, including both rotation and bending; this shape can then be used to model the mechanical signals at the whisker base. Decomposing the forces and moments into their x, y, and z components yields six quantities, while the two angular rotations, $\Delta\theta$ and $\Delta\phi$, are proxies for the forces associated with the follicle rotating within the tissue. These eight quantities and their derivatives form a total of 16 dimensions that completely describe the mechanical state of the whisker. A tuning map from this 16-dimensional input space onto the average firing rate of each neuron quantifies neural response during contact. The full tuning map for each neuron can be projected onto each individual input dimension; some of these one-dimensional tuning maps (tuning curves) are shown in Figure 5.4A for an example cell, and additional two-dimensional tuning maps are shown in Figure 5.4B. These tuning maps represent low-dimensional projections of the neuron's tuning in the full dimensional input space.

In general, tuning curves for all cells showed structure in most of the one-dimensional projections we observed, indicating that the firing rate of most Vg neurons correlates with most of the whisker's physical quantities when their effect on average firing rates is considered individually. However, this correlation in responses could easily result from intrinsic covariation between individual input components – for instance, M_y will covary with dF_z , where d is the distance from the base of the whisker to the point at which F_z is applied. To quantify these covariations, we performed PCA on the input space for each whisker, with and without derivatives. The cumulative percent variance explained is shown in Figure 5.4C for all neurons. Without the derivatives, three

components are required to explain 95% of the variance in the 8-dimensional space; with derivatives, eight components are required to account for 95% of the variance in the 16-dimensional space.

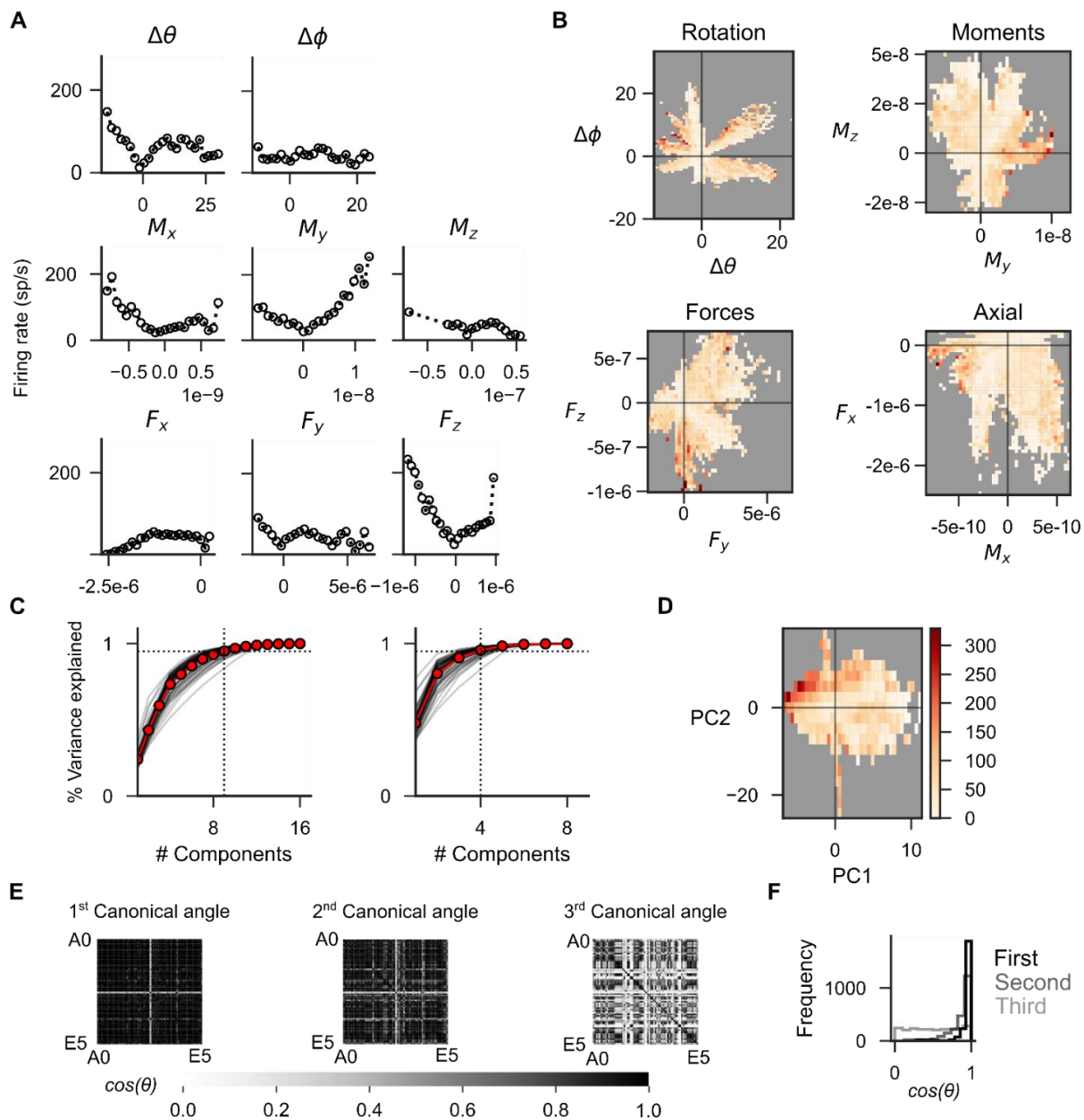


Figure 5.4: State spaces for each whisker fall in a lower dimensional subspace. (A) One-dimensional tuning maps: firing rate as a function of individual components of bending and rotation for an example cell. Units are degrees (top), Newton-meters (middle), and Newtons (bottom). (B) Two-dimensional tuning maps: firing rate as a function of pairs of components for the same neuron as in A. Color indicates firing rate, scale as in D; units as in A. (C) The cumulative percent variance explained by subsequent additions of ordered principal components for all whiskers (gray) and on average (red) when derivatives are included (left) and excluded (right). A 95 ms window LOESS smoothing was used before derivatives were computed. Dashed horizontal lines indicate 95% variance explained threshold; vertical lines indicate number of components needed to exceed the 95% threshold. (D) Two-dimensional tuning map of the neuron in B for the two first principal components of its input space, which includes derivatives. (E) Pairwise comparisons of the canonical angles between the 3-dimensional subspaces spanned by the first 3 PCs for all whiskers. Axes are ordered by whisker identity (A0(α)-E5). Shading is the value of $\cos(\theta_i)$, where θ_i is the i th canonical angle. (F) Histogram of the number of pairwise comparisons with a given value of $\cos(\theta_i)$.

Tuning maps can be obtained as a function of the principal components of the input space instead of the physical quantities. Example low-dimensional tuning maps for the two first principal components are shown in Figure 5.4D for the same neuron as in Figure 5.4B. Of note is that derivatives are included in the PCA decomposition, and that eigenvectors of the PCA tend to represent combinations of either physical quantities or their derivatives, but rarely both in a mixed manner (Suppl. Fig. 5.2).

Because all the physical quantities are measured independently of the head (Bush et al., 2016c), we can compare how similar the leading low-dimensional PC representations of the input spaces are for different whiskers. This analysis is equivalent to asking whether different whiskers constrain the physical input spaces in a similar way. The overlap between two PC subspaces can be quantified using the “canonical angles” between them (Bjorck et al., 1973) (see *Methods*). By performing a pairwise comparison between the subspaces spanned by the first three principal

components for every whisker, we quantified the similarity of input spaces across whiskers (Fig. 5.4E). The majority of the first two canonical angles are similar: $\cos(\theta) > 0.82 > 0.54 > 0.05$ for 95% of the three leading canonical angles. There is only a small amount of clustering, evidenced by the apparent groups in the third canonical angle. This result implies that the leading two-dimensional input space is similar across different whiskers.

5.3.5 GLMs reveal strong encoding of rotation and distributed tiling of explored stimulus space

The preceding sections have shown that Vg neurons encode multiple stimulus features, and that the stimulus features themselves are strongly correlated. The one- and two-dimensional tuning maps of Figure 5.4A,B provide some intuition as to the neural representation of select stimulus features, but they fall short of describing the full response of each neuron to the presented stimuli. A full description would require knowing the average firing rate in response to any arbitrary point in the stimulus space, and thus fitting a tuning histogram as those in Figure 5.4A to the full 16-dimensional stimulus space. This goal cannot be achieved by systematic and exhaustive exploration, and requires the use of a model.

To this end, we implemented a recent formulation of Generalized Linear Models (GLMs) (Williamson et al., 2015) that allows for multiple input filters to be discovered, and thus allows modeled neurons to be excited by inputs in multiple directions within the 16-dimensional stimulus space. As described in detail in *Methods*, all models were fit with 3 filters (see Supplemental Figure 5.4), each defined in the 16-dimensional input space. Only stimulus values at the current time bin are accessible to the models, which include no input history. A parametric nonlinearity (5

parameters) was fit for each filter, bringing the number of model parameters to $63 = [(16 + 5) * 3 \text{ filters}]$ per neuron; overfitting was minimized via 10-fold cross-validation. As illustrated for the example neuron in Figure 5.5A, we used the models to predict the spike rate with millisecond resolution, smoothed the observed spike train with a Gaussian kernel whose standard deviation σ was varied exponentially from 2 to 512 ms, and then compared the predicted rate to the smoothed rate for each value of σ . The Pearson Correlations comparing the observed rate and the predicted rate are shown in Figure 5.5B; correlations are calculated only during contact periods. On average, models best predicted the observed spike rate for $\sigma = 32$ ms, but high prediction accuracies are observed for many neurons for σ as short as 2 ms. The dependence shown in Figure 5.5B is nonmonotonic; as the value of σ increases the model performance drops, indicating that the models are accurately predicting temporal structure in the spike trains at a high temporal resolution rather than fitting the average spike rate. The median correlation value was 0.69 (IQR = [0.55, 0.81]) for $\sigma = 32$ ms, with a min of 0.08 and a max of 0.91.

We next asked how much information is gained by computing the full 3D whisker shape as opposed to a 2D projection (Fig. 5.5C,D). To answer this question, the 3D whisker shape was projected into the top camera view. The four mechanical variables associated with contact, $\{M, F_x, F_y, \Delta\theta\}$, were computed using a previously described 2D mechanical model (Huet et al., 2016; Huet et al., 2015). We considered tuning maps from an 8-dimensional input space (including derivatives) onto the average firing rate of each neuron, and as in the 3D case we modeled each map using a GLM with three filters. 70 neurons were fit with both a 2D and 3D model. We again found a non-monotonic dependence between the accuracy of firing rate predictions and the value of σ used to smooth the observed spike trains. For $\sigma = 32$ ms, the performance of 2D models was

significantly worse than that of 3D models (Wilcoxon rank-sum test $p < 0.001$; median=0.48, IQR = [0.37,0.60]). If we compare the 3D model for a given neuron with its 2D counterpart, we see most models (60/70) perform better with 3D information (Fig. 5.5D). The median performance increase from 2D to 3D was 29.8% (IQR = [13.0%,73.9%]).

In order to determine the relative contribution of each input component to firing rate prediction, we performed a dropout analysis in which models had access to progressively less information (Fig. 5.5E). For these analyses, we used only the $\sigma=32$ ms smoothed rate to compute correlations. Models without derivative information or rotation information perform significantly worse than the full model (Wilcoxon rank-sum test, $p < 0.001$; median=0.61, IQR = [0.52, 0.72]; median=0.55 IQR = [0.43, 0.69], respectively), indicating an important contribution of these physical quantities to firing rate prediction.

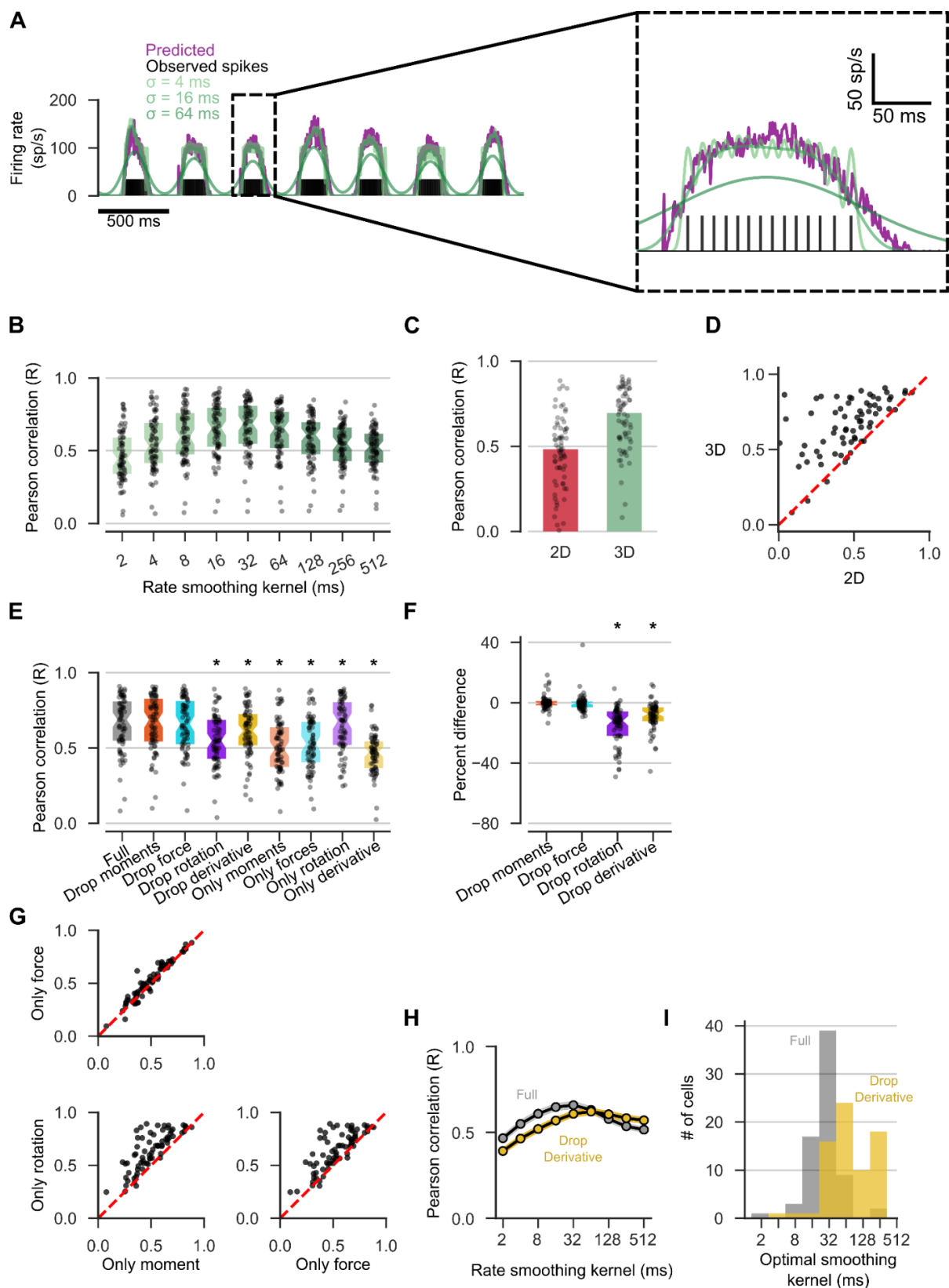


Figure 5.5: Statistical modeling of Vg neurons. Dots indicate individual models, bars are medians, boxes are median \pm IQR unless indicated. For all panels except **B**, Pearson Correlation values are used to compare predicted firing rate to observed rate smoothed with a Gaussian kernel with $\sigma = 32$ ms. **(A)** Observed spiking (black vertical lines) is converted to an estimated rate by smoothing with a Gaussian kernel (green traces, light to dark: $\sigma = [4, 16, 64]$ ms). Only three smoothing resolutions are shown, but nine are computed. Predicted rate is shown in purple. Inset shows an expanded plot of a single deflection. **(B)** Pearson Correlations for predicted rates based on a three-filter GLM model compared to the observed spiking smoothed with Gaussian kernels for different values of σ (coded by color intensity). Results shown for all recorded neurons. **(C)** Pearson Correlation measures the performance of models with access to either 2D or 3D physical information. **(D)** Pairwise comparisons of model performance given 2D or 3D physical information (Pearson Correlations). **(E)** Performance of models with access to subsets of the full input space. Asterisk indicates significant difference from full model (Wilcoxon rank-sum $p < 0.05$, Bonferroni corrected). **(F)** Percent difference between the performance of the full model and that of a model without access to a subset of input components, $(R_{full} - R_{subset}) / (R_{full})$. **(G)** Pearson Correlations are used to compare the performance of models with access only to input components of a given class. **(H)** Comparison of performance of models with and without access to input derivatives for different values of the σ of the smoothing kernel. Models with access to derivative information perform better than those without for $\sigma < 64$ ms. Shown are means \pm S.E.M. **(I)** For every neuron, the predicted firing rate is most correlated with the observed rate smoothed with a kernel using some optimal value of σ . The models with access to derivatives (grey) are more frequently optimal at lower values of σ than those without (yellow).

We then asked how well do models perform when given access to only one class of inputs: Moments, Forces, Rotations, or Derivatives (Fig. 5.5E). All models with access to only one class perform significantly worse than the full model (Wilcoxon rank-sum test $p < 0.001$). Models with only rotation components perform only slightly less accurately than the full models (median=0.68, IQR = [0.52,0.80]), indicating that a majority of the variance in firing rates is accounted for by the rotational components of the input. Models with access to only derivatives perform worst of all dropout models (median=0.47, IQR = [0.36,0.54]), while those with access to just moments or forces perform moderately well (median=0.49, IQR = [0.37,0.64]; median=0.53, IQR = [0.40,0.67]). The percent difference $(R_{full} - R_{subset}) / (R_{full})$ is used to quantify whether the loss of either rotation or derivative information is detrimental on a per neuron basis. As shown in Figure

5.5F, if we compare models with access to only one type of input, there is a strong correlation between the performance of models with access to different types of information, with the rotation only models performing better than either force-based or moment-based models. This result indicates that some neurons are more amenable to modelling than others, and that force and moment both carry important, but incomplete information about the response.

Lastly, we compared the temporal precision of the full model with that of the model without derivative information. Unsurprisingly, including derivative information increases the temporal precision of the models. If we compare the average performance of the models with and without derivative information across the different values of σ , we see that the models with derivatives perform better than those without them when their predictions are compared to spike rates smoothed with $\sigma < 64$ ms (Wilcoxon rank-sum test $p < 0.001$ Bonferroni corrected, Fig. 5.5H). Moreover, if we consider neuron specific models and identify the value of σ for which the firing rate of the neuron is best predicted, we find that most neurons are best predicted at shorter timescales when derivative information is accessible to the model (Wilcoxon rank-sum test $p < 0.001$, Fig. 5.5I).

Lastly, we analyzed the coefficients that characterize the GLM filters to ascertain whether this representation of neural tuning aligns with the PC decomposition of the stimulus space. Neurons could either encode the low dimensional subspace within the full input space that captures most of the stimulus variance, or neurons could respond to directions in input space that are independent of the low dimensional structure in the stimulus distribution.

The GLMs calculated here compute three linear combinations of the 16 input components in order to best predict the firing of each specific neuron. Thus, the response of each neuron is described

by three vectors within the full 16-dimensional input space, the *neural vectors*. Without reference to neural responses, PCA computes three orthogonal vectors in the 16-dimensional input space that best capture the variance of stimuli within that space, the *stimulus vectors*.

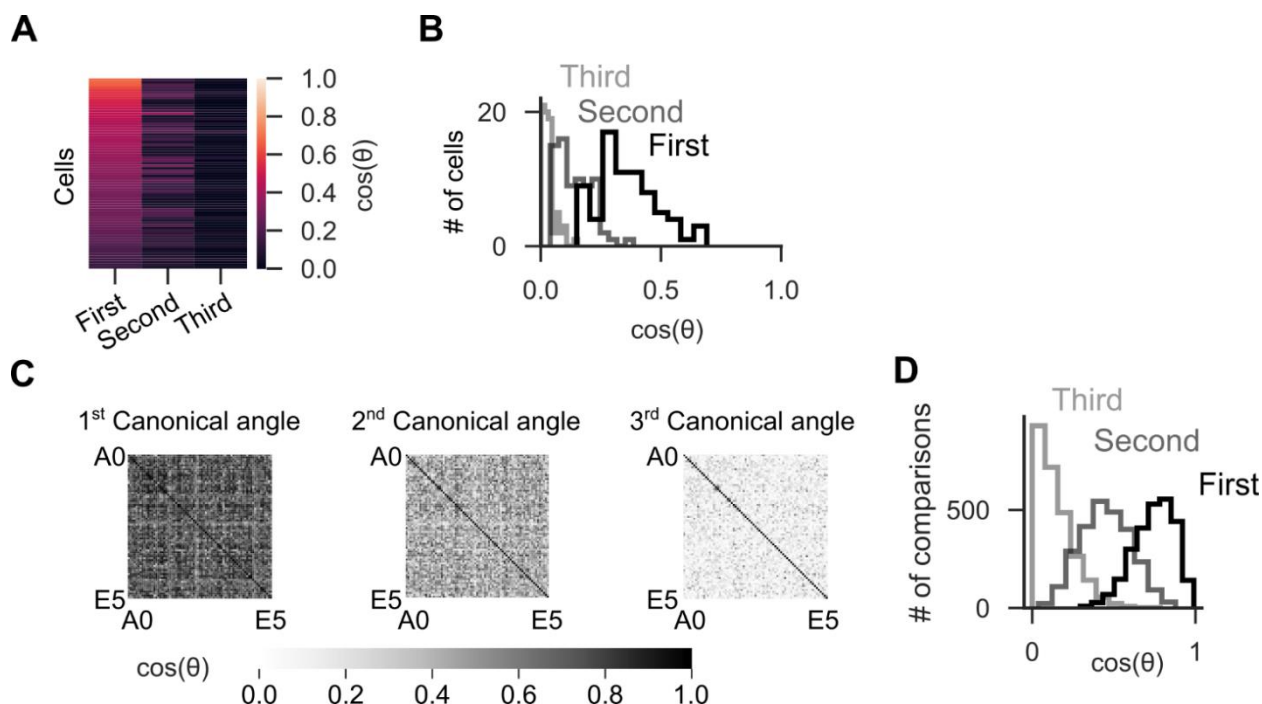


Figure 5.6: Neural tuning is well distributed across the population and covers the full input space. (A) Overlap between the 3-dimensional neural representation subspace and the 3-dimensional subspace spanned by the three leading stimulus principal components for each neuron. The value of $\cos(\theta_i)$ for the i th canonical angle between the PCA input subspace and the neural representation subspace is color coded. Each row is a neuron, ordered by the value of the first canonical angle. (B) Histograms of the values of $\cos(\theta_i)$ over all neurons for the three canonical angles. (C) Pairwise comparison of neural representation subspaces across all recorded neurons. Axes are ordered by innervated whisker - A0(α) to E5. Gray intensity indicates the value of $\cos(\theta_i)$, where θ_i is the i th canonical angle between neural representation subspaces for each pair of recorded neurons. (D) Histograms of the values of $\cos(\theta_i)$ across all pairwise comparisons of the neural representations.

For each cell, we calculated the canonical angles between the 3-dimensional subspace spanned by the stimulus vectors of the corresponding whisker and the 3-dimensional subspace spanned by the cell's neural vectors. The neural vectors are first orthogonalized, as required by the canonical angle

calculation; the stimulus vectors are orthogonal by construction. Figure 5.6A shows the first three canonical angles for all cells, ordered by decreasing value of the first canonical angle. The corresponding histograms are shown in Figure 5.6B. There is little overlap between the low dimensional input space and the neural representation space: $\cos(\theta) = [0.36 \pm 0.13, 0.14 \pm 0.07, 0.03 \pm 0.03]$, mean \pm S.D. for the three principal angles.

Neural representation subspaces can be compared across neurons by computing the canonical angles between the 3-dimensional subspaces spanned by the corresponding neural vectors. Pairwise comparisons are shown in Figure 5.6C and the resulting histograms in Figure 5.6D. The neural representation subspaces overlap moderately: $\cos(\theta) = [0.74 \pm 0.12, 0.45 \pm 0.15, 0.14 \pm 0.11]$, mean \pm S.D. for the three principal angles. Therefore, the neural representations of Vg neurons do not preferentially cover the low-dimensional representation of input space found by PCA, and their tuning spaces only moderately overlap, but do not cluster, suggesting a dense, uniform covering of the full input space (Suppl. Fig. 5.3).

5.4 Discussion

To fully characterize coding properties of a given Vg neuron, it is essential to quantify responses to complex stimuli that span the full extent of the stimulus space. The novel stereo-imaging and modelling techniques employed in the present work have allowed us to estimate the mechanical stimulus features present at the whisker base during complex, naturalistic, 3D passive whisker deflections. We have found that individual neurons simultaneously encode multiple features of the stimulus space, that rapidly adapting/slowly adapting properties fall in a continuum across neurons, and that neural representations of the stimulus overlap and thus provide a continuous tiling.

Together, these results suggest a view of Vg coding in which single stimulus features cannot unambiguously be determined by the activity of a single neuron; instead, features are represented across a population, and may be extracted by more central neurons that integrate across many Vg neurons. This view contrasts with proposed population codes that segregate behaviorally relevant quantities into separate streams (Knutsen et al., 2009; Lottem et al., 2015; Stuttgen et al., 2006; Szwed et al., 2003). During unrestricted exploration, the complexity of the stimuli encountered likely breaks structure that allows for simple feature readout. Continuous variation in mechanical tuning and adaptation properties emerges when the stimulus set is complex, suggesting a distributed representation of stimulus features.

5.4.1 Classical Vg tuning curves are “slices” of possible neural responses to complex stimuli

The present study has characterized the response of Vg neurons to complex, 3D, naturalistic stimulus. In contrast, previous studies have used categorical or restricted stimuli to characterize the response of Vg neurons through tuning curves that vary as a function of one or at most two stimulus dimensions, obtained while holding the many other mechanical covariates constant. The Vg responses shown in earlier studies (Bale et al., 2013; Chagas et al., 2013; Jones et al., 2004a; Kwegyir-Afful et al., 2008; Lichtenstein et al., 1990; Shoykhet et al., 2000; Stuttgen et al., 2008; Woolston et al., 1983) therefore correspond to slices through multidimensional tuning maps that describe the response of Vg neurons as a function of all relevant stimulus dimensions. Here we have shown how to use an extended GLM approach to characterize such tuning maps.

As an example, our results show that the average firing rate of Vg neurons is strongly influenced by both the arclength of contact and the deflection direction. This is in agreement with earlier work (Jones et al., 2004b; Kwegyir-Afful et al., 2008; Lichtenstein et al., 1990; Szwed et al., 2003).

However, our results go further, to show that Vg neurons are jointly tuned to both of these stimulus features, so that arc length and direction cannot be disambiguated based on average firing rate (Figure 5.2). Similarly, the predictive performance of our Vg model decreases when derivatives of mechanical features are not included as inputs (Figure 5.5E), indicating joint tuning to features that would correspond to stimulus “amplitude” and “velocity”, as described previously (Bale et al., 2013; Gibson et al., 1983b; Jones et al., 2004a; Shoykhet et al., 2000; Stuttgen et al., 2008; Woolston et al., 1983).

We argue that Vg coding properties previously identified in responses to simple or categorical stimuli can be seen as specific cases of the general coding capabilities of these neurons, and that low dimensional tuning curves represent a projection of a high dimensional tuning map onto the subspace spanned by the fewer stimulus features controlled in each specific experiment. Our results argue against models of Vg neurons that use single stimulus features to predict Vg firing; the firing of a Vg neuron can be well predicted from its stimulus, but individual features of the stimulus cannot be determined from an individual Vg response.

5.4.2 Vg neural responses tile the mechanical space

Several recent studies based on 2D analyses of whisker shape have shown that Vg responses are more accurately described in terms of mechanical rather than geometric variables (Bush et al., 2016a; Campagner et al., 2016; Severson et al., 2017). Note that rotations were considered in this work as mechanical variables because of their direct relation to the elasticity of the skin during passive deflections; rotations thus become a proxy for the force of the mystacial pad on the follicle. The Vg responses shown in these 2D studies fail to include some of the relevant mechanical variables, and can thus also be considered as “slices” of the tuning map that describes the Vg

activity observed in response to the 3D stimulation used here. The 3D analyses add crucial information about deflection direction, which strongly modulates the components of the applied forces.

Statistical models of V_g responses to 3D mechanical stimuli show tuning to multiple features of the stimulus space (Figure 5.5), and indicate that the main driver of neural activity is the rotation of the follicle in the skin rather than the bending of the whisker. The predictive performance of the model degrades if information about rotation is omitted, but does not degrade if information about bending is omitted. Remarkably, models that have access only to bending information still perform moderately well. That models still exhibit reasonable performance in the absence of the strongest predictor of neural firing (rotation) provides additional evidence for a broad, diffuse, and correlated tuning to mechanical features.

Since bending is strongly related to rotation (Supplemental Figure 5.1), it is possible that neurons respond to some latent mechanical feature that includes both bending and rotation. Principal components of the mechanical stimulus space would represent such latent features. However, Figure 5.6 shows that neural vectors that describe preferential firing do not align strongly with the principal components of the input space. Thus, neurons do not specifically encode linear combinations of stimulus features along high variance dimensions, but rather respond to combined aspects both rotation and bending. Preferential encoding along dimensions that differ from those that characterize the variance structure of the stimuli is consistent with a diffuse and tiled representation of mechanical information.

We expect the neural coverage of the input space to remain stable regardless of whether exploration is active or passive. The tuning map that characterizes the firing response of Vg neurons cannot depend on context, as the Vg neurons receive no context information. What is likely to change is the statistics of the stimuli, such as the relative importance of the physical quantities of rotation and bending. In the experimental protocol used here, neural responses are likely to be dominated by rotations of the whisker because the muscles holding the whiskers are relaxed. In contrast, during active whisking against an object, the muscles contract around the follicle and resist its passive rotation within the skin. In this scenario, the whisker will tend to bend rather than rotate (Campagner et al., 2016; Whiteley et al., 2015). The resulting changes in the configuration of forces and moments at the base of the whisker will correspondingly alter the effective stimulus space for the awake animal; we expect bending to be a more prominent mechanical feature. However, the neural representation of the mechanical space itself, that is to say the tuning map, ought to remain unchanged, with the caveat that follicle stiffness may itself change in the awake animal. The firing response of Vg neurons to stimuli characterized by the value of mechanical variables and their derivatives calculated at the base of the whisker are described in a whisker-centered reference frame that moves relative to the head as the animal whisks (Bush et al., 2016c). Neurons at more central levels must therefore extract relevant features of the stimulus from a tiled and distributed representation in the Vg population, while allowing for the invariance of the map from stimulus space to Vg neural activity across a change in context from passive to active.

5.4.3 Adaptation characteristics of Vg neurons lie along a continuum

Vg neurons are typically classified as rapidly and slowly adapting (RA/SA). This classification is conceptually intuitive, simplifies analysis, and is consistent with the presence of genetically and physiologically distinct mechanoreceptor types (Li et al., 2014; Maksimovic et al., 2014; Nakatani et al., 2015; Rutlin et al., 2014; Takatoh et al., 2018; Tonomura et al., 2015). A distinction between RA and SA classes appears to emerge when stimuli are themselves categorical (Chagas et al., 2013). However, the complexity of natural stimulation renders this distinction less meaningful. Specifically, the present work provides further evidence for a continuous distribution of adaptation properties at the level of the ganglion (Jones et al., 2004a; Woolston et al., 1983; Zucker et al., 1969), evident in part due to the complexity of the stimuli used.

Trigeminal ganglion neurons are responsive to a host of mechanical features and their temporal derivatives with differential weights, such that some neurons respond very little to derivatives (very SA-like) and some neurons respond almost exclusively to derivatives (very RA-like). The precise balance of these weights is likely affected by various aspects of follicle configuration: the physiological class of the mechanoreceptors, the arrangement and location of the mechanoreceptors in the follicle, and the tissue dynamics of the follicle/mustacial pad system (Ebara et al., 2002; Tonomura et al., 2015; Whiteley et al., 2015). The diversity within and across classes of mechanoreceptors is likely to be an important factor in creating a diversity of responses in the population of Vg neurons, so as to more completely tile the space of possible stimuli and thus provide a complete representation without gaps in the information conveyed to more central neurons. In further support of this integration of information across the Vg population, multiple anatomical studies have shown that single Vg neurons ramify to all subregions of the brainstem

trigeminal nuclei, suggesting a high dispersion and mixing of information (Hayashi, 1980; Jacquin et al., 1986; Shortland et al., 1996).

5.4.4 On the plausibility of a dense code

To fully describe the trigeminal population code would require simultaneous recording from a large number of Vg neurons. In this study, many Vg neurons were individually and sequentially recorded across different animals. Nonetheless, in the absence of a simultaneous characterization of the population code, several lines of reasoning suggest that the most parsimonious interpretation of the present results is that the population of Vg neurons represents the stimulus space via a dense coding scheme.

First, each Vg neuron responds to many different mechanical states of the whisker (Figure 5.5) and to many stimulus features (Figure 5.2), so that many Vg neurons are required to fully represent any given stimulus. Second, Vg coding properties are continuously distributed across all recorded neurons (Figures 5.3 and 5.6). Direction selectivity index, temporal adaptation patterns, alignment of the neural loadings with the stimulus principal components, and alignment between neural representations, all vary smoothly across the entire population of recorded neurons, indicating a smooth tiling of the representational space. Finally, Vg neurons exhibit a wide range of firing rates (Figure 5.2, (Leiser et al., 2007; Woolston et al., 1983; Zucker et al., 1969)), consistent with a dense coding scheme (D. J. Field, 1994).

Several characteristics of Vg neurons suggest an analogy to retinal photoreceptors, including their proximity to the periphery, the absence of lateral or top-down inputs, and their projection to cells with extensive recurrent filtering. Computational work that evaluates the density of population codes given different receptive field structures (Willmore et al., 2001) suggests that the population

of photoreceptors may implement a dense code. It would be intuitive for peripheral populations that must accommodate a large physical stimulus space to share computational properties such as implementing a dense code across sensory modalities. The analogy to peripheral vision could be extended to more central structures: neurons of the trigeminal brainstem nuclei may be more similar to retinal ganglion cells (RGCs), in which more extensive feature extraction has been shown to occur (Wienbar et al., 2018). Single Vg neurons ramify to target neurons in many brainstem nuclei (Hayashi, 1980; Jacquin et al., 1986; Shortland et al., 1996), where individual features may be extracted from the same full stimulus representation by way of complex spatiotemporal receptive fields, as well as lateral brainstem and top-down inputs (Chakrabarti et al., 2018; Furuta et al., 2006; Furuta et al., 2008; Furuta et al., 2010; Timofeeva et al., 2005). Similarly, approximately 180 RGCs sample from the same point on the mouse retina, with distinct feature selectivity arising as a result of cell type, and of processing through bipolar cell and amacrine cell circuits (Demb et al., 2015).

Neurons of the trigeminal ganglion must represent a large range of mechanical stimuli in multiple behavioral contexts, including active and passive touch, texture discrimination, abrupt collisions with objects, non-contact whisking, and airflow exploration (Jadhav et al., 2010; Moore et al., 2015; Severson et al., 2017; Wallach et al., 2016; Yu et al., 2016a). A dense coding scheme such as the one proposed here would offer several distinct advantages. It offers robustness against noise in individual neurons, and even their loss. It has a high representational capacity, a useful property given that there are only about 200 to 300 Vg neurons per whisker. A distributed, dense code would allow for individual Vg neurons to be informative of stimuli under many contexts, without filtering out information at this early stage. In this way, the Vg population could represent arbitrary

stimuli in the space of all possible stimuli, and allow more central neurons to extract those features that are relevant in the context of the animal's ongoing behavior and motor actions.

5.5 Methods

All procedures involving animals were approved by the Northwestern Animal Care and Use Committee. A total of 22 female Long Evans rats between 3 – 6 months were used.

5.5.1 Surgical procedures and electrophysiological recordings

Animals were anesthetized with a ketamine-xylazine-acepromazine cocktail administered intraperitoneally (60mg/kg ketamine, 3.0 mg/kg xylazine, 0.6 mg/kg acepromazine). After deep anesthesia was induced, the fur from the left whisker array was removed with depilatory cream (Nair) to increase contrast near the proximal region of the whisker close to the basepoint. Care was taken to minimize contact between Nair and the whiskers, and to wash off the Nair as soon as possible with saline. If the shape of a whisker was visibly altered by the fur removal procedures, it was removed from the array prior to recordings.

The head was immobilized with ear-bars to a custom stereotaxic device, and three stainless steel skull screws were inserted on the dorsal aspect of the cranium. Prior to the surgery, a non-insulated silver wire had been soldered to one of the skull screws to serve as a ground wire for electrophysiological recordings.

An approximately 1 mm diameter craniotomy was made over the left hemisphere, 2 mm caudal to bregma and 2 mm lateral to the midline. The skull was leveled to ensure that the bregma-lambda plane was horizontal, and a dental cement (methyl methacrylate) “bridge” was formed to connect the skull screws to the right side of the stereotaxic device. This procedure allowed for removal of the bite support and left ear bar while maintaining a level head position, giving free access to the

left whisker array for stimulation. Once the dental cement bridge had set, a single tungsten electrode (FHC 1-3 M Ω) was centered over the craniotomy and lowered to a depth of ~10 mm, until whisker responsive field potentials could be heard in audio monitoring of the amplified electrode signal during manual stimulation of the entire whisker array. We then waited ~5-10 minutes to allow the brain to relax after the initial penetration before advancing slowly to isolate a single whisker-responsive unit.

Once a single unit was isolated, the whisker associated with that neuron was visually isolated to ensure high contrast in both front and top camera views. A white paper background was placed behind the whisker to provide a uniform background for robust tracking in the front camera. Surrounding whiskers were either trimmed or placed carefully behind the paper background. Care was taken not to deform the whisker of interest or the surrounding mystacial pad.

A custom LED sheet with a transparent white plexiglass diffuser was used as the background lighting for the top camera. An adjustable Neewer CN-160 LED array was used as foreground lighting in the front camera field of view. High speed video from two identical top and front cameras was recorded directly at either 300 fps (Teledyne Dalsa HM640) or 500 fps (Mikrotron 4CXP) using StreamPix 7. Front and top cameras were synchronized by way of clocked 5V TTL to initiate exposure of each frame in both cameras from the same source. At the end of each experiment we recorded images of a checkerboard pattern with 2 mm squares in the field of view of both cameras; these images were later used for camera calibration and for calculation of the 3D whisker shape.

Neural signals were amplified using a A-M systems 4 channel amplifier, with a 10 Hz to 10 kHz hardware filter, at 1000x gain. Amplified signals were acquired via Measurements Computing

DT304 card using Datawave SciWorks v8. After acquisition, signals were digitally bandpass filtered at 300-6000 Hz before spike sorting with KlustaKwik (Rossant et al., 2016).

During recording, whiskers were manually deflected with a graphite probe (0.3 mm diameter) in 8 cardinal directions with respect to the emerging axis of the whisker. Deflections were applied at 2-3 distances along the whisker (arclengths), and at approximately 2 speeds, for a total of approximately 32-48 different categories of deflection. Each category of deflection was repeated ~20 times for each whisker. Care was taken to minimize slip along the length of the whisker during a deflection. Neural signals and subsequent stimulus quantifications were analyzed using custom python and Matlab code based on the neo and elephant python packages.

5.5.2 3D whisker reconstruction

Whiskers were first tracked in 2D automatically using the software “Whisk” (Clack et al., 2012). All tracked videos were manually inspected to verify that the desired whisker was adequately tracked in each frame and view. Videos in which the whisker was not adequately tracked (e.g., background edges were labeled as the whisker, manipulator was tracked as the whisker, tracking did not extend sufficiently to the tip or to the base) were omitted from further analyses. In order to reconstruct the 3D whisker, the basepoint position needed to be accurate in both front and top images. Since tracking of the basepoint location was occasionally noisy or unreliable, particularly in the front view, a mask outlining the rat head was manually created for each video and view (Pammer et al., 2013). Any part of the tracked whisker that fell within the mask was then removed. The distance between the edge of the mask and the basepoint was calculated, and the whisker was linearly extrapolated back to the basepoint. This gave an accurate and temporally smooth re-creation of the base segment and basepoint of the whisker in each view.

The two 2D tracked whisker shapes (one from each camera view) were cleaned by first removing and interpolating over mis-tracked basepoints via a median filter (window = 5 frames) and outlier deletion (Grubbs test $\alpha < 10^{-8}$). Next, the entire 2D whisker shape in each frame was smoothed with a spatial LOWESS filter (span = 15% of whisker length).

In order to create 3D reconstructions of the whisker, the two cameras had to be first calibrated. This involved computing the intrinsic properties of each camera (focal length, principal point, distortion, and skew), as well as the relationship of the cameras to each other (rotation and translation). These procedures were done with the Caltech Camera Calibration Toolbox, OpenCV, and custom Matlab and python code.

Once the cameras were calibrated, it became possible to calculate the location of an arbitrary 3D point in an external reference frame based only on two “corresponding” points in the two 2D camera views. In the case of the tracked whiskers, however, the only two available corresponding points are the base and the tip of the whisker, as there are no features on the whisker itself that can be identified as the same point in both camera views.

Therefore, in order to reconstruct the full shape of the whisker, we used an iterative optimization to find the best 3D whisker shape that minimized the back-projection error, where back-projection refers to the 2D projection of the estimated 3D whisker onto either camera. The back-projection error is simply the Euclidean distance between the back-projected whisker and the actual, imaged whisker, summed over all back-projected points. The basepoint is chosen as an initial corresponding point. We then randomly sample a 3D point at some distance s from the basepoint in a random direction, and compute the back-projection error for that point. We continued to sample random 3D points at the same distance s from the basepoint to find the point with the

minimal back-projection error. This optimal point became the next tracked point along the 3D whisker, and the origin for the next search over random 3D points at a distance s . Subsequent 3D points were added in the same manner, until either the cumulative back-projection error exceeded a preset threshold, or the whisker began to fold back on itself. The latter happened when the next optimal point was behind the previously fit point; this indicated that the whisker had been completely tracked and the folded point was then discarded. This process was carried out for each tracked frame for all videos. Quality of fits were inspected manually by observing the shape of the 3D whisker over time, viewing the overlap of the 2D back-projections with the original tracked 2D whiskers, and monitoring the temporal trajectories of the base and tip points for large deviations.

5.5.3 3D contact point estimation

We needed to calculate the 3D point of contact of between whisker and manipulandum, both to quantify the arclength at which contact occurred, and because the contact point is needed to compute the applied forces and moments in the 3D mechanical model (Huet et al., 2016; Huet et al., 2015). A difficulty was that the manipulator had no corresponding points, making the 3D reconstruction of the manipulator impossible. Instead, the manipulator was tracked as a 2D line in each frame via a custom written spatially and temporally constrained Hough line search. We then computed the intersection of that 2D manipulator line with the previously computed 2D back-projection of the 3D whisker for the corresponding frame and camera view. This resulted in a 2D point in the camera view. Since the 2D back-projected whisker consisted of the same number of tracked points as the 3D whisker, the node of the 2D back-projected whisker that was closest to

the intersection point was designated as the 2D contact point. This point corresponded to a point on the 3D tracked whisker, which was then deemed the 3D contact point.

This approach had the advantage that the manipulator needed to be tracked in only one camera view per frame, and that the 3D contact point was constrained to fall exactly on the reconstructed 3D whisker. The latter would not be guaranteed if the manipulator was reconstructed in 3D in the same way as the whisker. Moreover, it was likely that for any deflection in any given direction, the manipulator was relatively perpendicular to the field of view in one camera, and so line detection was robust. Accurate tracking of the manipulator in all frames was ensured in two ways: first the custom written tracking software would warn the user if large spatial or temporal changes were detected, which prevented errant tracking in almost all cases; second, tracking quality was monitored online in all videos during tracking and confirmed as acceptable by a second user offline.

5.5.4 Contact determination

Because stimulation was manually delivered, the actual time of contact onset was not known, and there was no temporally repeatable stimulus onset. To determine contact manually, the most accurate method would be to observe the recorded video and determine the first frame in which the tip of the whisker moved significantly. It was infeasible to do this for every contact and cell recorded, so we extracted the tip position of the whisker from the two camera views, resulting in a 4D temporal trace of tip position coordinates (Top (x,y), Front (x,y)). Naïve techniques in which contact was assumed to occur when these traces crossed a threshold were not robust enough to adequately distinguish contact from non-contact. Instead, we trained a temporal convolutional neural network to distinguish between contact and non-contact for every frame. We first whitened

the 4D tip position within a video to have zero mean and isotropic unit variance. We then labeled a random selection of ~1 million frames (amounting to approximately 10% of all data) across all experiments as either contact or non-contact. Labeling was achieved by viewing the randomly sampled segments of the 4D temporal trace of the tip position. A user visually determined the onset and offset of a contact period, marked by a significant deviation in the tip position. Frames between onset and offset were labeled as contact, and the remaining frames in the segment were labeled as non-contact. We split the labeled data into a training and a test set, and chose the architecture of the network to be able to correctly classify 97.7% of the training set and 97.4% of the test set. We then applied the trained neural network to the remaining ~9 million frames to get a contact/non-contact label for every frame, and manually verified the contact predictions by observing the labeled 4D temporal traces for all frames and correcting the predicted time of contact as needed. Ultimately, every contact was inspected manually based on the 4D temporal traces of the whisker tip, but the neural network drastically reduced the effort that would have been needed to manually label every one of the ~10 million recorded frames.

5.5.5 3D mechanical models

The mechanical models used here to calculate the three components of force and three components of moment at the base of the whisker have been described previously (Huet et al., 2017). All calculations were done in whisker-centered coordinates, in which the whisker basepoint is centered at the origin, and the whisker is rotated such that the approximately linear portion of the base segment of the whisker is colinear with the x-axis and the initial curvature of the whisker lies in the x-y plane. Mechanical models take the 3D shape of the whisker in the frame prior to each contact onset as the reference whisker for that contact. In each subsequent contact frame during

which the whisker is deformed, we estimated the forces and moments required to deform the reference whisker into the whisker shape observed during contact.

As described in previous studies (Huet et al., 2016; Huet et al., 2017; Huet et al., 2015), the mechanical model approximates the whisker as a tapered, truncated beam. The three components of force and three components of moment $\{F_x, F_y, F_z, M_x, M_y, M_z\}$ (Supplemental figure 5.1) were computed at the base of each whisker. Importantly, these computations were performed in whisker-centered coordinates for each frame, so that the applied force takes into account only the change in shape of the whisker (i.e., bending). To calculate the rotational component during whisker deflection, we computed the rotation (θ, ϕ) required to move the whisker from the camera-centered reference frame to the whisker-centered reference frame at every point in time. The rotation magnitude in each frame was then computed as the change in these angles $(\Delta\theta, \Delta\phi)$ from the position of the whisker in the frame prior to contact.

In some cases, we used two additional scalar physical mechanical quantities: the magnitudes of the bending moment M_B and of the rotation moment M_R , given by

$$M_B = \sqrt{M_y^2 + M_z^2}, \text{ (Equation 5.1)}$$

$$M_R = \sqrt{\Delta\theta^2 + \Delta\phi^2}, \text{ (Equation 5.2)}$$

5.5.6 2D mechanical models

In order to assess the amount of information gain when moving from 2D to 3D, we calculated the mechanics due to the bending and rotation of the whisker as if we only had information from the

top camera. Since the reconstruction of the 3D whisker is an estimation of the 3D shape, it was inappropriate to simply compare the 3D information with the information obtained from direct 2D tracking from the top camera, as the latter is likely more accurate. Instead, we back-projected the estimated 3D whisker onto the top camera, to get a 2D image of the whisker of comparable quality to that of the 3D reconstruction. The contact point was the same node along the whisker as identified during the 3D analysis and did not need to be recomputed. We used the back-projected 2D whisker shape to calculate the angular rotation $\Delta\theta$ as for the 3D models, but now restricted to the 2D projection. We then applied a previously described 2D mechanical model (Quist et al., 2012b; Quist et al., 2014), analogous to the 3D model already discussed, to calculate the bending magnitude M , the axial force F_x directed into the follicle, and the lateral force F_y . The derivatives of these physical quantities were calculated as described for the 3D mechanical quantities. The resulting 8-dimensional stimulus space included $\{M, F_x, F_y, \Delta\theta\}$ and their respective derivatives.

5.5.7 Smoothing, alignment, and upsampling

Errors inevitably occurred at various points in the data analysis: when tracking the 2D whisker shape, when reconstructing the 3D whisker, when calculating the 3D contact point or the force applied to the whisker. These errors caused fluctuations in the calculation of the quantities that characterize the stimulus space. Of particular difficulty were temporal outliers in which data from a given single frame differed greatly from data from the surrounding frames. These outliers added erroneous temporal structure to the various quantities. To deal with this problem, we applied mean absolute deviation (MAD) filtering to remove points that deviated from the mean by more than 10 times the mean deviation, and then applied a Hampel filter, a thresholded median filter with a window size of 5 frames and a threshold of 3 standard deviations (Liu et al., 2004). Lastly, we

performed Savitzky-Golay filtering on the data, with a span of 7 frames and degree 2, to smooth over high-frequency noise.

Neural data was recorded at 40 kHz, and high-speed video was recorded at either 300 or 500 frames per second. In addition to the voltage from the extracellular electrode, the neural data acquisition system recorded a 5V signal from the top camera that was high for 100 μ s at the start of the exposure for that frame. This allowed us to match each video frame to a sample in the neural data. Variables associated with the video images and tracked whiskers (e.g., mechanics, rotation) were linearly interpolated so as to be up-sampled to 1 kHz; spike times were rounded up to the nearest millisecond.

5.5.8 Contact removal

Due to occasional errors in tracking of the 3D whisker or contact point, there were sometimes entire contact periods that did not meet quality control and had to be removed. To deal with this problem we used the 3 components of moment to detect unacceptable contacts. First, gaps in moment information shorter than 10 consecutive frames were linearly interpolated, and a median filter with a window size of three consecutive frames was then applied to smooth over temporal outliers. Each contact interval was then given a score:

$$E = \sum_{t=1}^T \|\mathbf{M}_t - \mathbf{M}_{t-1}\|^2, \text{ (Equation 5.3)}$$

where \mathbf{M} is the 3D moment vector, and T is the duration of the contact. If a contact interval had an E value greater than 100 times the median value of E across all contacts for that given whisker, then the entire contact interval was discarded. We then manually inspected the moment versus

time traces for each video and discarded contacts in which the moment signal was dominated by noise.

5.5.9 Derivative calculations

Temporal derivative information has been shown previously to be of importance to Vg neurons (Bale et al., 2013; Jones et al., 2004a; Shoykhet et al., 2000). In order to calculate the temporal derivative of a physical quantity such as M_x , it is customary to temporally smooth the quantity to reduce the effects of sampling noise or small fluctuations in the calculation of the derivative. This procedure is analogous to performing a low pass filter on the quantity whose derivative is to be calculated. Since these quantities were defined to be exactly zero during non-contact, standard smoothing techniques such as Butterworth filters were inappropriate, in that they would have significantly altered the onset/offset boundaries and resulted in non-zero values during non-contact. Instead, we performed a local linear regression (LOESS) smoothing operation on the physical quantities with a window size of 95 ms. After LOESS smoothing, we performed discrete derivative calculations on each of the smoothed quantities.

5.5.10 Identification of direction and arclength groups

Although the naturalistic stimulation employed here does not allow for repeatability of trials, the applied stimuli could be categorized. Stimulations were applied in 8 cardinal directions relative to the whisker axis, and at 2 to 3 distances from the base (arclengths). In order to average across similar deflections, we labeled each deflection as belonging to a particular direction group and a particular arclength group. To categorize deflections into direction groups, we used $\Delta\theta$ and $\Delta\phi$ to represent the angular trajectory of the base segment during a deflection. Since deflections had variable durations, we subsampled the trajectories down to 10 time points per trajectory, and

represented the trajectory as a point in a 20-dimensional space of coordinates $\{\Delta\theta_i, \Delta\phi_i\}$, $1 \leq i \leq 10$. We then applied PCA to the set of 20-dimensional points that corresponded to all deflections of a given whisker, and reduced the dimensionality of this space from 20 to 2 by keeping only the two leading principal components. In this 2-dimensional space, each point provided an abstract representation of one specific whisker deflection. Each of these 2-dimensional vectors was then normalized to unit length, to eliminate the influence of deflection amplitude in the angular grouping. We then clustered all these normalized 2-dimensional vectors into 8 groups using a Gaussian Mixture Model unsupervised clustering algorithm (Windham, 1988). The procedure was implemented separately for each whisker, and the outcome was visually inspected by color coding all angular trajectories for a given whisker according to cluster label, as shown in Figure 5.1D. Although little overlap among clusters was observed, different direction groups were not always evenly spaced in angular separation, due to the manual nature of the stimulation. To characterize each deflection direction group, we calculated $\Delta\theta$ and $\Delta\phi$ at the apex of the deflection for each deflection in the group, and took the mean of these two maximal values to define the characteristic angular direction of that group.

In each contact frame, we calculated the arclength of contact to be the distance along the whisker from its base to the point where contact was made. We observed only minimal slip of the point of contact along the whisker during a deflection (average slip along whisker during contact was $\pm 0.47\text{mm}$). Given these small fluctuations in the arclength of contact, we used its median value during a deflection to characterize the whole deflection. We then used Gaussian mixture models to cluster the median arclengths into either 2 or 3 groups. Model selection between clustering into 2 or 3 distinct arclength groups was based on the minimization of the corresponding Akaike

Information Criterion (AIC) (Akaike, 1974). If three clusters were found, the deflections were labeled as proximal, medial, or distal; if only two were found, the deflections were labeled as proximal or distal.

5.5.11 Direction Selectivity Index (DSI)

Several analyses in the present work involve modulation by an angular covariate. In order to quantify this angular influence, we calculated the Direction Selectivity Index (DSI) (Mazurek et al., 2014), defined as:

$$\text{DSI} = \left| \frac{\sum_j r(\theta_j) \exp(i\theta_j)}{\sum_j r(\theta_j)} \right|, \text{ (Equation 5.4)}$$

Here $r(\theta)$ is the response variable, typically a firing rate, and θ_j is the value of the angular covariate for the j th direction. The DSI is equivalent to $1 - \sigma^2$, where σ^2 is the circular variance of the quantity in question.

5.5.12 Adaptation Index (AI)

The Adaptation Index (AI) was used to quantify how the firing rate of a given neuron changed over the course of a deflection. We defined the AI as the log of the ratio of the firing rate during the first 10 ms following deflection onset to the average firing rate during the entire deflection:

$$\text{AI} = \log \left(\frac{1}{10K} \sum_{k=1}^K N_{10}(k) \right) - \log \left(\frac{1}{TK} \sum_{k=1}^K N_T(k) \right). \text{ (Equation 5.5)}$$

Here K is the number of deflections, $N_{10}(k)$ is the number of spikes during the 10 ms following deflection onset for the k th deflection, $N_T(k)$ is the number of spikes during the entire k th deflection, and T ms is the mean deflection duration, averaged over all deflections of the neuron being characterized by the AI.

5.5.13 Low-dimensional tuning maps

Similar methods were used to calculate tuning maps in one and two dimensions. In one dimension, the stimulus variable was binned into 25 equal bins; in two dimensions, each of the two stimulus variables was binned into 50 equal bins. The resulting histograms sample the prior probability distribution of the stimulus, marginalized to the corresponding one or two dimensions within the 16-dimensional stimulus space. Bins for which the corresponding stimulus value was observed less than five times were considered empty. For occupied bins, normalized counts were used to estimate the prior probability distribution of the stimuli.

The evoked firing rate of the neuron being mapped was then computed for all occupied bins. The time-dependent spike rate was estimated by convolving the binary spike train with a Gaussian kernel with $\sigma = 2$ ms. For such small σ , conversion to a rate provided smoothing without greatly altering the temporal information. These rates were used to create a new histogram that estimated the expectation value of the firing rate given the stimulus. To this end, an average spike rate for each stimulus bin was computed over all the times a stimulus value within that bin was observed.

5.5.14 Generalized linear models (GLMs)

The input space available to a model for predicting the firing response of a specific neuron was the 16-dimensional space consisting of $\{M_x, M_y, M_z, F_x, F_y, F_z, \Delta\theta, \Delta\phi\}$ and the temporal derivatives of these quantities. Each input variable was sampled at 1 ms resolution. The target output for training each neuron specific model was the corresponding binary spike train recorded during the experiment: either a spike was observed (1) or not (0) in each 1 ms bin.

The input $X(t)$ consists of the values of the 16 stimulus variables at the time t of prediction. Since Vg neurons are known to respond to stimulus on fast time scales, sometimes less than 1 ms, and

since the temporal resolution of the stimulus is the same as the temporal scale of the Vg response, the model does not need to incorporate a time lag between inputs and outputs or a stimulus history, as has been the case in previous applications (Bush et al., 2016a; Pillow et al., 2008). The models implemented here were constructed using cylindrical basis functions (Williamson et al., 2015):

$$\hat{r}(t) = g \left(f_1(K_1^T X(t)) + f_2(K_2^T X(t)) + f_3(K_3^T X(t)) \right) . \text{ (Equation 5.6)}$$

Here $X(t)$, the stimulus input at time t , is projected onto filters K_i , $1 \leq i \leq 3$. Each filter is a 16-dimensional vector of weights assigned to each component of X ; each f_i is a nonlinearity that maps the corresponding projected stimulus into a firing rate. The function g is an overall sigmoidal nonlinearity. The functions $f_i(x_i(t))$, $1 \leq i \leq 3$, each a function of a single scalar $x_i(t) = K_i^T X(t)$, were parametrized as the linear combination of 5 cylindrical basis functions (Williamson et al., 2015):

$$f_i(x_i) = \sum_{j=1}^5 \alpha_{ij} \phi_j(x_i), \quad \text{with} \quad \phi_j(x_i) = \exp \left\{ - \frac{(x_i - \mu_{ij})^2}{2 \sigma^2} \right\} . \text{ (Equation 5.7)}$$

The coefficients $\{\alpha_{ij}\}$, $1 \leq i \leq 3$, $1 \leq j \leq 5$, that control the linear combinations of cylindrical basis functions, as well as the additional model parameters $\{K_i\}$, $1 \leq i \leq 3$, that specify the neural filters, were fit to minimize the negative log-likelihood of the observed spike train given the observed stimulus. All models were 10-fold cross-validated; 90% of the data was used for parameter fitting, and the resulting model was used to predict \hat{r} for the remaining 10% of the data. This was repeated 10 times, so that every 1 ms bin for which \hat{r} is predicted was at some point not part of the training data used to specify the parameters of the predictive model. Subsequent

analyses of the filter weights $\{K_i\}, 1 \leq i \leq 3$, for each neuron were performed on mean values obtained by averaging across the 10 cross-validation instances.

For the dropout analysis to establish the relevance of the various input components, we fitted the corresponding predictive models as described above after removing some classes of input components. We found no evidence of overfitting due to too large a parameter space; for instance, the model with the fewest number of parameters (the rotation only model, with only four input components) performed as well as the full model, while other reduced models showed poorer performance than the full model. Models for the 2D whisker description were constructed in the same manner, but based on an 8-dimensional input space that included $\{M, F_x, F_y, \Delta\theta\}$ and their temporal derivatives.

We also investigated an alternative approach to modeling the input-output relation of individual neurons, the “spike-triggered mixture model” (Theis et al., 2013), based on similar input spaces and employing similar parameters. Results were both qualitatively and quantitatively similar; details about these models and their corresponding results are available on request.

5.5.15 Pearson Correlations

All models computed a probability of firing $\hat{r}(t)$ in a given 1 ms bin based on the fitted parameters $\{K_i\}, 1 \leq i \leq 3$ for the linear filters and the mixing coefficients $\{\alpha_{ij}\}, 1 \leq i \leq 3, 1 \leq j \leq 5$ for constructing the fitted nonlinearities f_i . This expected rate or firing probability within a 1 ms bin is a continuous variable with values between 0 and 1. The observed spiking $y(t)$ can be considered as a single observation of the response given an underlying rate $r(t)$. We computed the underlying rate r by smoothing the observed spike train y with a Gaussian kernel with standard deviation σ . The value of σ was varied to investigate the temporal precision of the models. We used $\sigma =$

[2,4,8,16,32,64,128,256,512] ms; this resulted in nine different estimates of r , one for each level of smoothing. The Pearson Correlation was then computed between each smoothed $r(t)$ and the model prediction $\hat{r}(t)$. The calculation of correlations was restricted to periods of contact, to avoid overestimation due to silent non-contact periods.

5.5.16 Canonical angles

The input space considered in the neural response analyses reported here was a 16-dimensional space consisting of the physical quantities $\{M_x, M_y, M_z, F_x, F_y, F_z, \Delta\theta, \Delta\phi\}$ and their temporal derivatives. At any 1 ms time bin during whisker deflection, the stimulus can be represented as a point in this space. For each whisker, the principal components decomposition of the cloud of such points accumulated over many deflections provides eigenvectors and eigenvalues that characterize the stimuli for that whisker, regardless of the response of a Vg neuron associated with that whisker. The eigenvectors are sorted in decreasing order of the eigenvalues, which measure the variance in the corresponding eigenvector direction. Dimensionality reduction to the subspace spanned by the leading eigenvectors maximizes the amount of variance accounted for. Since each whisker has different physical properties (arclength, intrinsic curvature, diameter), the pattern of covariation of the input components will be different for different whiskers, and so will be the resulting eigenvectors. We have kept the three leading eigenvectors for each whisker, effectively reducing the 16-dimensional input space to a 3-dimensional subspace that is whisker specific. We then asked how similarly oriented were the subspaces associated with different whiskers. The canonical angles (Bjorck et al., 1973) between two subspaces quantify this similarity. Given two 3-dimensional subspaces A and B embedded in the full 16-dimensional input space, we considered their spanning vectors $A = [a_1, a_2, a_3], B = [b_1, b_2, b_3]$. Here $\{a_i\}$ and $\{b_i\}$ are the three leading

eigenvectors that span each subspace; each of them a 16-dimensional column vector. The canonical angles $\{\theta_i\}$, $1 \leq i \leq 3$, follow from

$$U\Sigma V^T = \text{SVD}(A^T B), \text{ (Equation 5.8)}$$

where the diagonal elements of the matrix Σ are the cosines of the canonical angles,

$$\Sigma = \begin{bmatrix} \cos(\theta_1) & 0 & 0 \\ 0 & \cos(\theta_2) & 0 \\ 0 & 0 & \cos(\theta_3) \end{bmatrix}, \text{ (Equation 5.9)}$$

with $\cos(\theta_1) \geq \cos(\theta_2) \geq \cos(\theta_3)$, or $\theta_1 \leq \theta_2 \leq \theta_3$.

In addition to comparing input subspaces across whiskers, we used principal angles to relate the 3-dimensional input subspace associated with a given whisker to the 3-dimensional subspace that best predicted the response of a Vg neuron associated with that whisker. The GLM model for each neuron identified three vectors $\{K_i\}$, $1 \leq i \leq 3$, each of them a vector in the 16-dimensional input space, and each associated with a preferred input direction for maximal neural response. The orthonormalization of these three vectors provided a basis for a 3-dimensional input subspace that accounted for preferred neural responses. Canonical angles allowed us to compare this 3-dimensional subspace of neural responses to the 3-dimensional subspace that accounted for most of the input variance to the corresponding whiskers.

5.5.17 Participation ratios

The participation ratio quantifies how evenly distributed the components of a vector are. Given a d -dimensional vector $A = [a_1, a_2 \dots a_d]$, the participation ratio is defined as:

$$Q = \frac{\sum_i a_i^4}{(\sum_i a_i^2)^2}. \text{ (Equation 5.10)}$$

When all the components of A are equal, $a_i = a$ for all $1 \leq i \leq d$, Q attains a minimum value of $1/d$. When only one component of A is non-zero, $a_j = a$ and $a_i = 0$ for all $i \neq j$, Q attains a maximum value of 1. Intermediate values of Q quantify the degree of inhomogeneity among the components of the vector A .

Chapter 6: Discussion

6.1 Toward a more complete description of primary sensory representations

Physical interactions between the whiskers and the tactile environment result in a rich, but complex, kaleidoscope of mechanosensory information. The work in this thesis leverages recent technical and computational advances in an attempt to generalize the field's understanding of how whisker-object interactions govern the tactile sensory representation of the external world. Ultimately, the forces resulting from contacts are amplified and filtered through the physical instantiation of the whisker itself. The whisker acts as a lever that deforms the tissue in the follicle in which the mechanoreceptors reside, creating high-dimensional representations of whisker-object interactions. The shape and material properties of the whisker also constrain the covariation between certain components of mechanical information.

The accepted descriptions for primary sensory neuron coding of tactile information focused on how Vg neuron activity relates to object properties or external parameters of motion (Ahissar et al., 2008; Gibson et al., 1983b; Jones et al., 2004a; Jones et al., 2004b; Leiser et al., 2007; Lichtenstein et al., 1990; Shoykhet et al., 2000; Szwed et al., 2003; Szwed et al., 2006b; Zucker et al., 1969). Here we attempt to shift the focus of primary sensory neuron encoding toward a view that describes interactions with the external environment as in terms that incorporate the whisker's physical properties. All representations of the external world are acquired through the whiskers themselves, as the transduction machinery in the mechanoreceptors is physically tied to the follicle. This change of focus is particularly important given that whisker motion is under active control by the animal which will fundamentally dictate the sensory information that is acquired (Carvell et al., 1990).

The perception of the environment must be robust to the contextual changes that occur during active sensation. It follows that Vg neurons must represent the world in a way allows downstream neurons to recreate or interpret a stimulus under a variety of contexts. While certain behaviors or contexts may lie within constrained regions of the stimulus space (e.g., rostrocaudal whisking primarily represents features in the rostrocaudal plane), Vg neurons must be able to represent the entire possible space of contexts with the same neural substrate.

The results of this thesis probe how the primary sensory neurons represents the full complexity of the available mechanical stimulus space. We show that these neurons are capable of carrying behaviorally relevant information about complex and non-canonical stimuli by describing systematic representation of features present during wind stimulation. This highlights the fact that reduced or artificial stimulus analyses can neglect important representational properties of Vg neurons that must simultaneously exist. In shifting the focus of stimulus quantification from an externally (or object) focused description, we show that Vg neurons represent the mechanical space of whisker states. We integrate this whisker-mechanical centric viewpoint with the need to address the shortcoming that whisker studies generally neglect motion in 3 dimensions (often due to technical limitations) by defining 3D coordinate systems and transformations from whisker-centered to head centered coordinate systems. Lastly, we show that it is critical to appreciate this full, 3D space of mechanical stimuli available to the whisker to understand a given neurons representation of physical stimuli. When the full representation capacity of these neurons is taken into account, a vastly different view of how the population solves the problem of representing natural stimuli appears. Rather than observing functional cell categories, categorical response properties, or segregated information streams (Gibson et al., 1983a; Stuttgen et al., 2006; Szwed

et al., 2003), we observe smooth coverage and tiling of the available stimulus space. This, combined with the knowledge that every Vg neuron sends collaterals to all whisker representative ascending processing pathways (Hayashi, 1980; Jacquin et al., 1986) suggests that Vg neurons form a complete and high dimensional representation of mechanical inputs that serve all whisker mediated behaviors. This result places more demanding decoding constraints on downstream processing centers.

One interesting aspect of this result is that the neural tuning does not seem to strongly align with the high-variance dimensions of the available stimulus space, suggesting that these neurons are not preferentially encoding what might seem to be “important” features of the stimulus space. Rather, the neurons are agnostic to the statistical distribution of the inputs. This may have the effect of enhancing flexibility of the stimulus representation in that mechanical features that are not frequently observed are not less important. In fact, they may indicate surprising or noteworthy interactions that ought to draw the attention of the animal

6.2 Natural, multidimensional stimuli are required for complete sensory representations

The work in this thesis places special emphasis not only on the representational capacity of Vg neurons, but also on appropriate stimulus choice and quantification. The animal’s nervous system did not evolve to perform the types of reduced tactile behavioral discrimination tasks frequently used to probe the capacity of the whisker system (Harvey et al., 2001; Knutsen et al., 2006; Mihailoff et al., 1989; Morita et al., 2011). Rather, through extensive training, the animal can be coerced to solve these artificial behaviors. These solutions likely reside within the natural capabilities of the system, but do not exploit the natural function of sensory processing.

During natural exploration, the mapping from raw stimuli to a behavior could be executed in an infinite number of ways. It is important to remember that when investigating a stimulus set, the neural processing that happens as a result of that stimulus set is not exhaustive—the same neural substrate must be capable of representing and acting on all possible sets of relevant stimuli in addition to the one probed.

The reductionist approach would argue that one can isolate a particular dimension of the entire feature space to discern how the neurons respond along that dimension (Chagas et al., 2013; Lichtenstein et al., 1990; Shoykhet et al., 2000; Stuttgen et al., 2008; Szwed et al., 2003; Szwed et al., 2006b). One could then survey all the relevant dimensions available to that neuron and be able to recapitulate the neuron's encoding properties by piecing together the tuning to these component dimensions. This approach is unsatisfying for the following reasons. First, the definition of “important” dimensions is determined by the researcher. As humans we have an intuition, guided for reasons that vary from known physics to our intuition, as to what might be important dimensions to survey. For concreteness, it is intuitive for us to consider the amplitude and velocity of a stimulus as being key features that Vg neurons might be responsive to. However, we cannot reject the possibility that these features, which to us are intuitive and have compelling mathematical or physical reasons to be complete descriptors of a space, are the ones that are driving the response of the neurons. There could be some driving latent feature that is related to our intuition, but is inaccessible to our imaginations. Our preponderance to try to map the responses of neurons onto simple, clean, and imaginable dimensions could possibly preclude us from being able to describe the responses of neurons.

Second, when one performs these reductionist studies and comes to some conclusion about how these neurons respond to a particular dimension, one often plays down the variability across neurons in favor of describing the function of a population. This minimizes the role individual neurons play in representing a space. What is lost however, is that the variability between neurons likely correlates to variability in other dimensions. Unless one allows multiple stimulus features to covary simultaneously, one misses structure in multiple dimensions. By analogy, one cannot recreate a multivariate joint distribution from two marginal distributions without knowing the covariance structure of those probabilities. Similarly, one does not fully understand the capabilities of sensory neurons to natural stimuli if we only know the marginal distributions. This idea is not novel in many systems (Pillow et al., 2008; Schwartz et al., 2002; Sharpee et al., 2003; Williamson et al., 2015), but has been largely ignored in the description of Vg neurons.

The inability of past work to satisfactorily uncover these joint, high-dimensional tuning curves is understandable, as the computational and technical tools for describing them in the whisker system were not available until recently. The tools now exist, but it may be difficult going forward to conceptually accept high-dimensional and non-linear response properties, as it becomes difficult to make generalizable statements about the coding properties of a population, and it is conceptually difficult to understand the capability of a single neuron.

6.3 Perceptual tasks may overlap during sensing

Often, works attempt to create models of how a population might decode particular features such as texture, shape, or object location (Ahissar et al., 2011; Jadhav et al., 2010; Knutsen et al., 2009; Szwed et al., 2006a). It seems likely to me that there are not “texture” neurons, nor are there “shape” neurons or object position neurons, or even functional subsets of neurons that serve the

dimensions of these different types of tactile stimuli. All of these types of distinctions are likely to be performed simultaneously during natural exploration. Given the observation of this thesis that Vg neurons smoothly cover the mechanical stimulus space, it seems likely that most neurons would be active during any interaction during natural stimulation, and the different features would combine to confound any single task decoding scheme (Moore et al., 2015).

No one to our knowledge has attempted to record from Vg neurons while quantifying responses to multiple stimulus set types. We think of texture, shape, and position as being very different categories of information, but they all have their basis in mechanical interactions with the whiskers. It seems therefore more reasonable that Vg neurons are mapping this more universal mechanical space, and texture, shape, and position live in different regions of that mechanical space.

This idea is underscored in our work in Chapter 3. Wind is a complex tactile stimulus that has not been considered in the Vg literature until now. We see robust responses to airspeed direction and velocity, but this is not to say there are “wind” neurons. Rather, the mechanical consequences of these features are present in the Vg code. At some point in sensory processing, these features can be extracted, animals use their whiskers to localize an airflow source (Yu et al., 2016a). What is important is that the natural tactile scene encompasses a wide variety of possible stimuli (Hobbs et al., 2016; Huet et al., 2016), that all exist somewhere in the space of forces and moments experienced in the follicle.

Certain “categories” of stimuli may live in low-dimensional manifolds of that space. It is likely that primary sensory neurons have the job of faithfully representing that mechanical space. More central regions have the benefit of complex circuits with top-down and lateral connectivity to be

able to infer where in that mechanical space the animal is sampling, and how to best interact with that situation.

6.4 A little slow; missing the temporal code

One major limitation of this work is the mismatch between the temporal precision of Vg neurons (on the order of 1ms) (Bale et al., 2015; Bale et al., 2013; Jones et al., 2004a; Jones et al., 2004b) compared with the temporal precision of the statistical models presented in chapters 2 and 5 (~16ms). The limitation is a technical one. The manual stimulation protocol introduced in these works imparts a variability in the stimulus parameters, but in doing so, precludes the possibility of repeated trials. The variability in spike trains across similar, but slightly different stimuli, is most likely the result of slight variations on the stimulus itself, to which the Vg neurons are sensitive. Although the stimulus quantification techniques developed in this work are precise, it is likely that the precision of the vibrissal system exceeds that of the image processing used here. As such, we are unable to account for some variation in the neuronal response. By their construction, the statistical models implemented in the work will tend to model an “average” response of the neuron to stimuli that are quantitatively similar. This will reduce the accuracy of the model in predicting spiking behavior, simply because the features which are being used to train the statistical model are inadequate.

In addition, the deterministic nature of these neurons prohibits us from implementing a probabilistic spiking model that can benefit from a “spike history” term (Pillow et al., 2008; Williamson et al., 2015). In practice, including these terms leads to a feedforward model in which presence of spiking in the previous time is predictive of spiking in later windows because the

autocorrelation present in the stimulus; once a neuron begins to fire, it does not cease to fire once the stimulus has disappeared (data not shown).

We are thus forced to interpret the model's prediction of a spiking probability that is then mapped to a rate function. It is not appropriate however, for us to draw spiking events from this probability because the uncertainty in knowing whether a spike occurs or not comes from the error in quantifying the stimulus, and not in some Poisson spike generation function that resembles biophysical mechanisms as it does in retinal or cortical systems (Pillow et al., 2008). In evaluating our models, we then compare the model's rate prediction (a continuous quantity), with the actual spiking activity of the neuron (a series of discrete events). Since we cannot adequately map the model predicted rate to a spike train, we must conversely map the observed spiking to a rate function. This involves a loss in temporal information of the actual spike train. Since the models themselves are trained on the discrete spike events, it seems reasonable that our limitations in temporal prediction are due to the smoothing of the observed rate being an inadequate estimate, more so than the models themselves being inaccurate.

Due to our inability to predict spike trains, we therefore cannot assess the information carried in the precise timing of spikes. It is likely that spike timing is important, but the rates that we predict only approximate that information. Undoubtedly, future work could benefit from the ability to investigate precise spike timing and how timing code information might be incorporated in the Vg representation.

6.5 What defines a cell class?

One major conclusion of this work is that Vg neurons are tuned to a wide set of mechanical components that are experienced at the base of the follicle. This includes the temporal derivatives

of these components. Many of the results of previous work which parse the Vg population into functional cell classes can be reframed as the neuron's tuning to these mechanical features.

The direction tuning shown in early work (Lichtenstein et al., 1990) can be interpreted as tuning to particular directional components of the 3D mechanics. The rapidly and slowly adapting results can (Gibson et al., 1983a; Zucker et al., 1969) be rephrased as being explained by sensitivity to the temporal derivative of a quantity (RA) or the quantity itself (SA). The fact the firing rate of neurons correlates with both amplitude and velocity (Shoykhet et al., 2000) can be explained by weighting on both derivatives and quantities. Putting this together, the complex adaptation properties observed in our work and previous work in that the threshold and adaptation properties can vary as a function of direction can be explained by the conjunction of these ideas; neurons are tuned to multiple derivative and quantity features, with a preference for particular directional components.

With the arguments in this work, we put forth the idea that there are no “functional cell classes” in the Vg representation of tactile stimuli. This claim must be carefully qualified in that we are not claiming that there do not exist cell classes of some sort. There are clearly distinct mechanoreceptor subtypes based on morphology, anatomical location in the follicle, and genetic markers (Abraira et al., 2013; Ebara et al., 2002; Maksimovic et al., 2014; Owens et al., 2014; Rice, 1993; Rice et al., 1986). In conjunction, the specificity with which Vg neurons innervate only one mechanoreceptor subtypes indicates some genetic distinction between Vg neurons (Rice, 1993; Rice et al., 1986; Tonomura et al., 2015).

Moreover, detailed studies of mechanoreceptor stimulus-response properties clearly delineate different functional types of mechanoreceptors, with different biophysical filtering characteristics (Li et al., 2014; Nakatani et al., 2015; Owens et al., 2014; Woo et al., 2015). For example, it has

been recently shown that the phasic portion of a step depression of a Merkel afferent is due to the Merkel cell proper, and the tonic response is due to the intrinsic mechanoreceptive capabilities of the Vg neuron axon (Woo et al., 2015).

The claim we make is somewhat different in that different genetic cell types will differ in the filtering properties they perform on the impinging mechanical stimuli, but the functional variability of Vg neurons of particular cell types is high enough that the between class variability is on the same scale. Therefore, the coding properties of the different subpopulations will overlap enough so as to make the classes indistinct when viewed with respect to naturalistic stimuli.

The data in this thesis are not strong enough to prove this claim; one would need to record from Vg neurons as they respond to natural or naturalistic stimuli and subsequently identify the mechanoreceptor subtype from which they receive information. The first steps approaching this experiment have been performed using an optogenetic tagging technique (Severson et al., 2017). In this experiment, mice were genetically engineered to express channel rhodopsin in Merkel afferents. The experimenters could then isolate a whisker responsive Vg neuron and stimulate the follicle with blue light. If the stimulation elicited a spike in the isolated neuron, the experimenters were confident the neuron recorded from was receiving information from Merkel afferents. This study did not, however, find conclusive differences in coding properties between Merkel afferents and other (unidentified) afferents recorded in the study. Unfortunately, genetic targets for the other known types of mechanoreceptors do not yet exist, precluding the possibility of an exhaustive survey of coding properties on a per-mechanoreceptor type basis.

An alternative approach involves recording from the neurons, backfilling with dye, and recreating the entire axon and mechanoreceptor. This technique is perhaps prohibitively difficult and low

yield, although the sparse data collected with this technique are quite powerful in mapping response type to mechanoreceptor (Tonomura et al., 2015).

6.6 3D whisker motion and mechanical response invariance: future directions

Much of the work in this thesis was performed on anesthetized animals, as this allowed for higher number of recordings per animal. In addition, the anesthetized approach offers the advantage of being able to systematically survey the entire space of possible inputs for system identification of these neurons response properties; during active exploration the prior distribution of stimulus inputs will be restricted by the common modes of the animal's behavior (Arkley et al., 2014; Grant et al., 2009; Hobbs et al., 2016; Mitchinson et al., 2007; Towal et al., 2008). Although the ultimate goal of this line of research would be to understand the responses of these neurons during active touch, it is important to consider that not all awake touch involves whisking. Passive deflections of the whiskers will occur when a moving object encounters the array, or when the animal moves its head with respect to the environment without subsequently moving the whiskers.

It is my opinion that the response of these neurons during an anesthetized state ought to be nearly identical to those during the awake state for the following reasons. First, since the Vg neurons are passive conductors of sensory information, it seems infeasible that conscious state should alter these neuron's response properties. Second, these neurons have been shown to be exceedingly precise and invariable given a known stimulation (Jones et al., 2004a). This indicates that that the mapping between the mechanical information and the spike trains of these neurons is stationary, at least in the anesthetized animal.

As such, one would expect the coding properties uncovered during passive stimulation would hold during awake exploration. The results from chapter X suggest that passive stimulation and awake

exploration fall in different regions of the mechanical stimulus space; that is, the mechanical implications of contact during active exploration may be different than passive stimulation. When the animal is awake, the intrinsic and extrinsic musculature will hold the whisker base rigid. This will incur more bending of the whisker, and less rotation of the follicle with respect to the cheek as seen in passive stimulation. An important caveat is that in the awake animal hydrostatic pressure in the blood sinus of the follicle may alter the tissue properties and fundamentally change the mechanical consequences of contacts (Ebara et al., 2002; Rice, 1993).

As part of the future directions of this project, we have begun recording from Vg neurons in head-fixed mice as they actively whisk into objects while simultaneously quantifying the 3D mechanics. We then acutely anesthetize the animal and repeat the stimulation protocol described in Chapter 5. In this experiment we aim to answer two main questions. First, we will perform similar statistical models as in Chapter 5 to model responses to the anesthetized stimulation protocol. We can then use those model parameters to predict the firing of Vg neurons during active contact. We expect the accuracy of these models to be similar to control models fit on data recorded from the awake contacts. Secondly, we can test the hypotheses put forth in Chapter 4 that the tuning properties of Vg neurons will rotate with the follicle as the whisker rolls during protraction. We would expect that the preferred direction of Vg neurons would change as a function of the protraction angle of the whisk.

6.7 Simulation of Vg populations

The work in this thesis have given us not only an appreciation for the fact that Vg neurons represent large regions of the available mechanical input space, but actual neural representations of that space in the form of model parameters. A future direction for this work would be to use the

knowledge of how real neurons represent the mechanical space to test hypotheses for encoding and decoding principles in artificial systems.

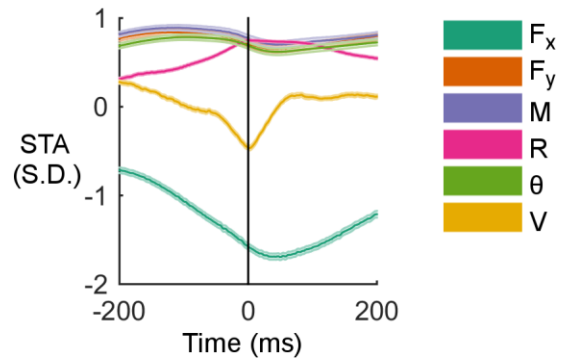
First, we can use the model parameters computed in chapter 6 to create a pseudopopulation of simulated Vg neurons. This population would be statistical models of neurons that are of the same form as those computed, but with parameters drawn from the distribution of real neurons. We could then simulate the responses of an entire population of Vg neurons for a given whisker to a vast variety of tactile stimuli. Not being restricted by the necessity of recording and isolating the cell *in vivo* affords an infinite number of stimulations. We could ask questions about how the population of neurons encodes different types of features. For example, how many neurons are needed for accurate estimation of object contours, or discrimination of textures, and are the populations needed for these discriminations distinct? Finding out where the models fail can direct future Vg neuron recordings or inform us as to why this particular model structure is inappropriate for a given type of stimulus. We could even vary the mechanical properties of the whisker to see what morphological computation advantages are afforded by the real rat whisker.

We can then simulate the Vg population for the entire bilateral array of 62 whiskers as simulated rat arrays investigate virtual environments. These simulations offer the ability to investigate possible mechanisms by which the whisker system may integrate information across whiskers during natural exploration. The simulation environments could vary from being very simple – perhaps a single vertical surface with a given texture – to very complex. We have recently used 3D depth cameras to collect surface maps of natural environments in which rats are found. Combining this with concurrent experiments in which we quantify head and body movements during natural exploration, we could ultimately simulate a virtual rat investigating real

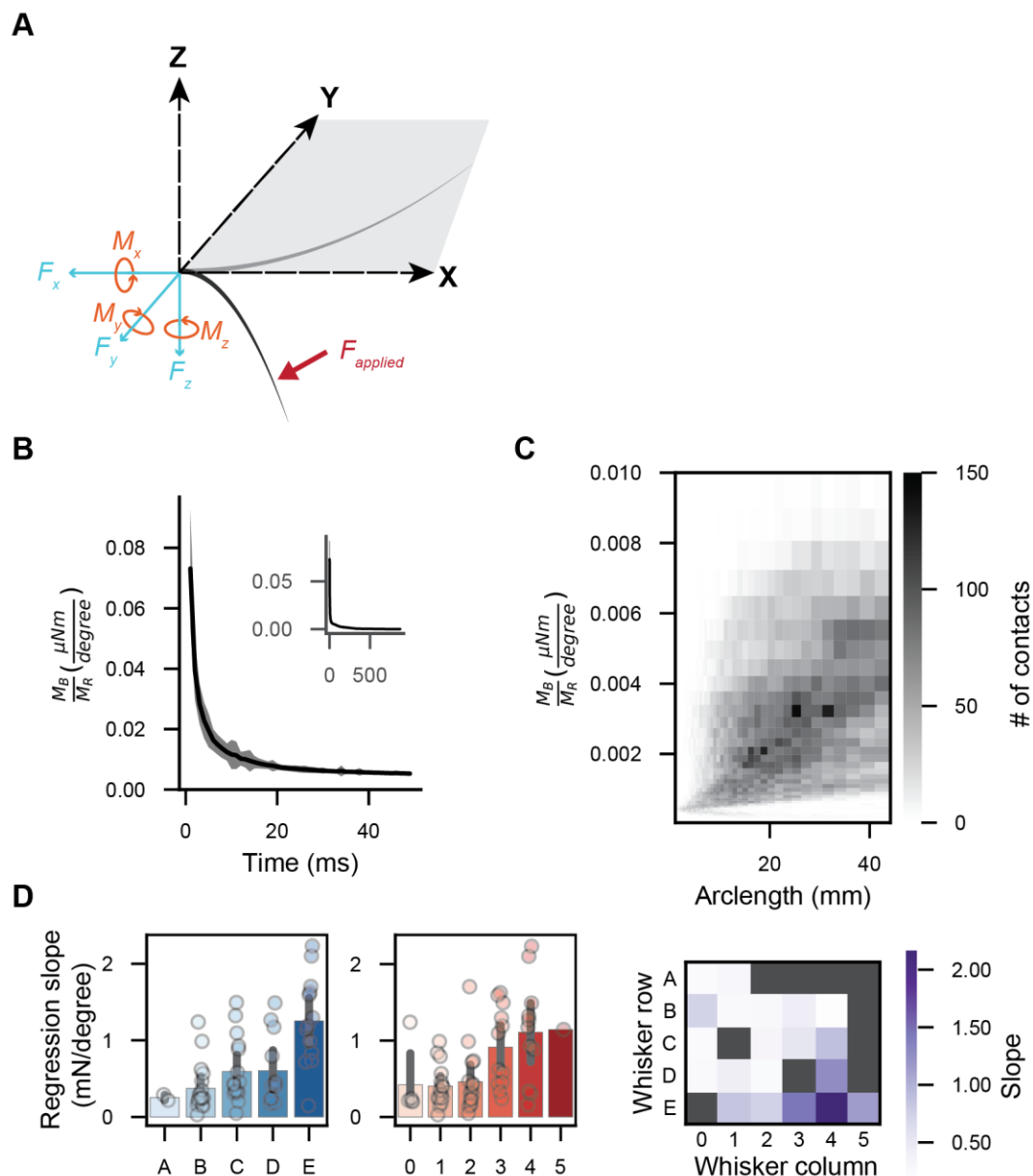
environments, while estimating the entire primary sensory neuron population response to tactile stimuli.

7: Supplemental Information

7.1 Supplemental Figures

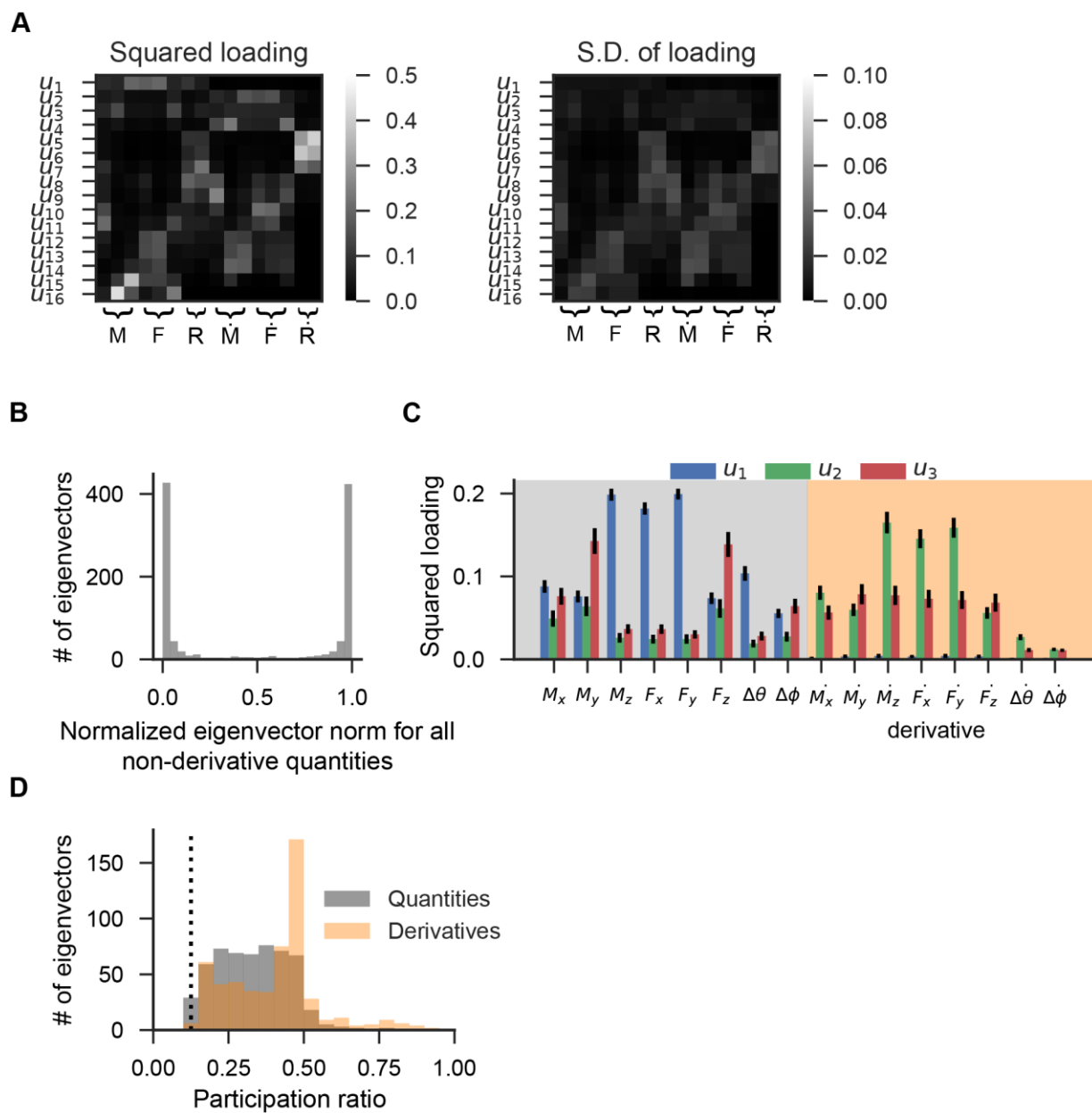


Supplemental Figure 2.1: Spike triggered averages. Examples of spike-triggered averages of the six input variables for the cell shown in Fig. 4C. Shaded regions are standard error of the mean, too small to be observed for most traces.

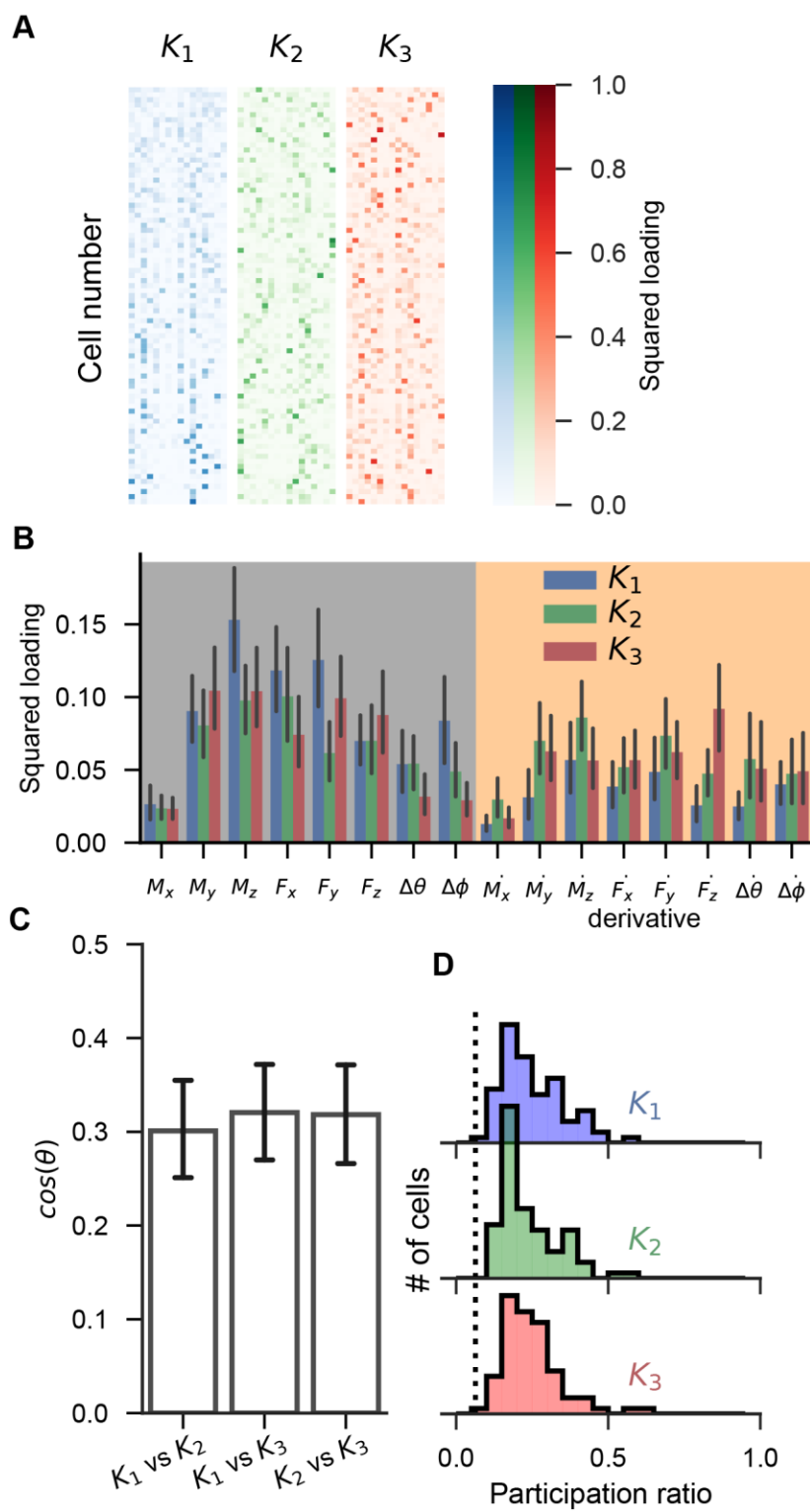


Supplemental Figure 5.1: Relationship between bending magnitude and rotation magnitude. (A) Schematic of the mechanical components of bending in whisker centered coordinates. The base of the whisker at rest (light grey) defines the origin. The x-axis is defined as colinear with the base segment of the whisker, the y-axis by the direction orthogonal to the x-axis into which the whisker curves due to its natural shape. The z-axis is orthogonal to the x-y plane. A force applied to the whisker (red) bends the whisker into a new shape (dark grey). The resulting x,y, and z components of both force (cyan) and moment (orange) are experienced at the base of the whisker, as determined by the mechanical properties and shape of the whisker, and the force applied. (B) Bending precedes rigid rotation of the whisker. The ratio of the

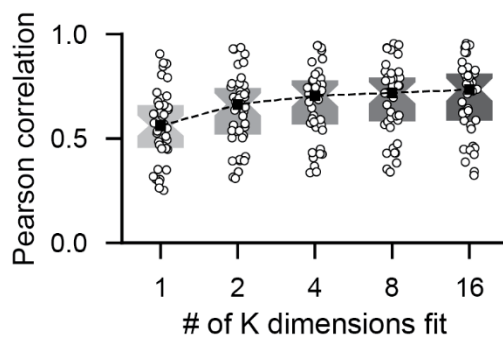
magnitude of the bending moment to the magnitude of rotation is shown as a function of time after onset of contact. Shaded region is 10 times the S.E.M. Inset shows the same relationship on a longer time scale. Data averaged across all contacts and across all whiskers. **(C)** Ratio between the magnitude of the bending moment to the magnitude of rotation as a function of arclength of contact, for every contact. Arclength is the median value of arclength during a contact; ratio here is the median value of the bending-rotation ratio during a contact, estimated from the steady state achieved in **(B)**. **(D)** Slope of the linear regression of bending-rotation ratio against the arclength of contact for all contacts for each whisker. As the mechanical properties of the whiskers change with row and column identity, the relationship between bending and rotation changes. The slope of the linear regression is shown as a function of row identity (left), column identity (middle), and the whisker identity (right). Only datapoints with significant linear regression are shown; two datapoints with large negative regression slopes were removed as outliers.



Supplemental Figure 5.2: PCA descriptions of the input space. PCA was applied to the observed mechanical features to obtain whisker specific low-dimensional representations of a 16-dimensional input space that incorporated components of moment, force, rotation, and their temporal derivatives (calculated as discrete difference after LOESS smoothing with a 95 ms window). **(A)** The squared loading of each mechanical component for the 16 PCs, shown as rows and ordered by variance accounted for. Shown left are averages across all reported whiskers; shown right are the standard deviations of the squared loadings across whiskers. **(B)** Histogram of the ratio of the L2 norm of the first half of each eigenvector, which comprises only the eight non-derivative quantities, to the L2 norm of the full eigenvector. The histogram includes all 16 eigenvectors for each measured whisker. The distribution peaks at 0 and 1, indicating that each eigenvector had significant loads on non-derivative or derivative quantities, but not on both **(C)** Squared loading of each input component for each of the three leading eigenvectors, averaged across whiskers and labeled by the corresponding mechanical input variable. **(D)** The participation ratio is computed for each eigenvector, 16 per whisker, and reported for all whiskers. Eigenvectors were categorized as representing physical quantities (non-derivative) or their derivatives based on whether the summed norm of the squared loadings over all non-derivative quantities exceeded 0.5. Dashed line indicates a lower bound to the participation ratio, realized when all input components are equally weighted.



Supplemental Figure 5.3: Neural representations of the input space. (A) Visualization of the GLM weights that characterize the response of all recorded Vg neurons. The response of each neuron is characterized by three vectors $\{K_i\}, 1 \leq i \leq 3$, each a 16-dimensional vector with components associated with each of the input components. Each row is a neuron, sorted by the participation ratio for the first vector, K_1 . Color represents each of the three vectors; color saturation represents the square of the corresponding component of the normalized K vector. (B) Squared loadings of each input component for each of the normalized neural vectors, averaged across neurons and labeled by the corresponding mechanical input variable. (C) Overlap between normalized neural vectors; the pairwise cosines are shown, averaged across neurons. A value of zero indicates that the neural vectors are orthogonal; a value of 1 indicates collinearity. (D) Histograms of the participation ratio for each neural vector, for all neurons. Dashed line indicates a lower bound to the participation ratio, realized when all components are equally weighted. A participation ratio of 1 indicates that only one component of the neural vector is nonzero, indicating that only one of the input variables affects the firing rate of that neuron. In contrast, these results indicate that Vg neurons fire in response to distributed combinations of input variables.



Supplemental Figure 5.4: Performance of the neural model as a function of the number of neural vectors. Increasing the number of neural vectors increases model performance, which saturates at about four neural vectors in the full 16-dimensional input space. The Pearson correlation R is measured between the spike rate predicted by the model and the observed spike train smoothed with a gaussian kernel with $\sigma = 32$ ms.

7.2 Supplementary Videos

Video 2.1: Comparison of active whisking with passive, manual deflection.

Two seconds of high speed video (A) as an awake, body restrained rat whisks against a peg, and (B) as the whisker is passively deflected using manual stimulation in the anesthetized animal. Videos are slowed by factors of ~16 and ~15, respectively.

Videos 2.2A – 2.2D: 3D visualization of mechanical and kinematic relationships in awake and anesthetized animals.

Each of the four videos shows a rotating view of the corresponding neuron from Figure 3, with radial distance represented along the third axis. (A) Neuron shown in Figure 3A, active exploration. (B) Neuron shown in Figure 3B, active exploration. (C) Neuron shown in Figure 3C, manual deflection. (D) Neuron shown in Figure 3D, manual deflection.

Video 2.3: Comparison of distal and proximal contact in the anesthetized rat.

High speed video of distal and proximal contacts (3 seconds per clip, slowed by a factor of ~5) highlights the movement of the follicle relative to the skin when contact is made close to the whisker base.

Video 5.1: Reconstruction of three-dimensional whisker motion with neural recording- Example Cell 1

Top: Raw high speed images of whisker motion (slowed ~16x) from front-on (left) and top down (right) cameras. The whisker and probe are visible, as well as a small portion of the mystacial pad. *Bottom left:* 3D reconstruction of whisker shape as tracked from the separate video frames above. Red dot is the emergence point at the follicle. Purple-white trail is the point of contact and

with 10-ms history. *Bottom right:* Mechanical components of applied force computed at the base of the follicle due to the observed whisker motion. Vertical gray lines are recorded action potentials.

**Video 5.2: Reconstruction of three-dimensional whisker motion with neural recording-
Example Cell 2**

Data as in 5.1, for example cell 2

**Video 5.3: Reconstruction of three-dimensional whisker motion with neural recording-
Example Cell 3**

Data as in 5.1, for example cell 3

References

- Abdelkefi, A. (2016). Aeroelastic energy harvesting: A review. *International Journal of Engineering Science*, *100*, 112-135.
- Abraira, V. E., & Ginty, D. D. (2013). The sensory neurons of touch. *Neuron*, *79*(4), 618-639. doi:10.1016/j.neuron.2013.07.051
- Ahissar, E., & Knutsen, P. M. (2008). Object localization with whiskers. *Biological Cybernetics*, *98*(6), 449-458. doi:10.1007/s00422-008-0214-4
- Ahissar, E., & Knutsen, P. M. (2011). Vibrissal location coding. *Scholarpedia*, *6*(10), 6639.
- Akaike, H. (1974). A new look at the statistical model identification. *IEEE Transactions on Automatic Control*, *19*(6), 716-723. doi:10.1109/tac.1974.1100705
- Albert, J., Friedrich, O., Dechant, H.-E., & Barth, F. (2001). Arthropod touch reception: spider hair sensilla as rapid touch detectors. *Journal of Comparative Physiology A*, *187*(4), 303-312.
- Andermann, M. L., Ritt, J., Neimark, M. a., & Moore, C. I. (2004). Neural correlates of vibrissa resonance: Band-pass and somatotopic representation of high-frequency stimuli. *Neuron*, *42*, 451-463. doi:10.1016/S0896-6273(04)00198-9
- Arabzadeh, E., Panzeri, S., & Diamond, M. E. (2006). Deciphering the spike train of a sensory neuron: Counts and temporal patterns in the rat whisker pathway. *Journal of Neuroscience*, *26*, 9216-9226. doi:10.1523/JNEUROSCI.1491-06.2006
- Arabzadeh, E., Zorzin, E., & Diamond, M. E. (2005). Neuronal encoding of texture in the whisker sensory pathway. *PLoS Biology*, *3*(1), e17. doi:10.1371/journal.pbio.0030017
- Arkley, K., Grant, R. A., Mitchinson, B., & Prescott, T. J. (2014). Strategy Change in Vibrissal Active Sensing during Rat Locomotion. *Current Biology*, *24*(13), 1507-1512. doi:10.1016/j.cub.2014.05.036
- Bagdasarian, K., Szwed, M., Knutsen, P. M., Deutsch, D., Derdikman, D., Pietr, M., . . . Ahissar, E. (2013). Pre-neuronal morphological processing of object location by individual whiskers. *Nature Neuroscience*, *16*(5), 622-631. doi:10.1038/nn.3378
- Bale, M. R., Campagner, D., Erskine, A., & Petersen, R. S. (2015). Microsecond-scale timing precision in rodent trigeminal primary afferents. *Journal of Neuroscience*, *35*(15), 5935-5940. doi:10.1523/jneurosci.3876-14.2015
- Bale, M. R., Davies, K., Freeman, O. J., Ince, R. A. A., & Petersen, R. S. (2013). Low-dimensional sensory feature representation by trigeminal primary afferents. *Journal of Neuroscience*, *33*(29), 12003-12012. doi:10.1523/jneurosci.0925-13.2013
- Barth, F., Németh, S., & Friedrich, O. (2004). Arthropod touch reception: structure and mechanics of the basal part of a spider tactile hair. *Journal of Comparative Physiology A*, *190*(7), 523-530.

- Beer, F., Johnston, E., DeWolf, J., & Mazurek, D. (2015). *Mechanics of materials, 7th Edition* (Vol. 1). New York: McGraw Hill.
- Belli, H. M., Bresee, C. S., Graff, M. M., & Hartmann, M. J. Z. (2018). Quantifying the three-dimensional facial morphology of the laboratory rat with a focus on the vibrissae. *PLoS One*, *13*(4), 31. doi:10.1371/journal.pone.0194981
- Belli, H. M., Yang, A. E., Bresee, C. S., & Hartmann, M. J. Z. (2017). Variations in vibrissal geometry across the rat mystacial pad: Base diameter, medulla, and taper. *Journal of Neurophysiology*, *117*(4), 1807-1820. doi:10.1152/jn.00054.2016
- Bermejo, R., Friedman, W., & Zeigler, H. P. (2005). Topography of whisking II: Interaction of whisker and pad. *Somatosensory and Motor Research*, *22*(3), 213-220. doi:10.1080/08990220500262505
- Bermejo, R., Vyas, A., & Zeigler, H. P. (2002). Topography of rodent whisking--i. Two-dimensional monitoring of whisker movements. *Somatosensory and Motor Research*, *19*(4), 341-346. doi:10.1080/0899022021000037809
- Bhattacharyya, U., & Bhalla, U. S. (2015). Robust and rapid air-borne odor tracking without casting. *eNeuro*, *2*(6), e0102. doi:10.1523/ENEURO.0102-15.2015
- Billah, K. Y., & Scanlan, R. H. (1991). Resonance, Tacoma Narrows bridge failure, and undergraduate physics textbooks. *American Journal of Physics*, *59*(2), 118-124.
- Birdwell, J. A., Solomon, J. H., Thajchayapong, M., Taylor, M. A., Cheely, M., Towal, R. B., . . . Hartmann, M. J. Z. (2007). Biomechanical models for radial distance determination by the rat vibrissal system. *Journal of Neurophysiology*, *98*(4), 2439-2455. doi:10.1152/jn.00707.2006
- Bjorck, A., & Golub, G. H. (1973). Numerical methods for computing angles between linear subspaces. *Mathematics of Computation*, *27*(123), 579-594. doi:10.2307/2005662
- Boubenec, Y., Shulz, D. E., & Debregeas, G. (2012). Whisker encoding of mechanical events during active tactile exploration. *Frontiers in Behavioral Neuroscience*, *6*. doi:10.3389/fnbeh.2012.00074
- Bush, N. E., Schroeder, C. L., Hobbs, J. A., Yang, A. E., Huet, L. A., Solla, S. A., & Hartmann, M. J. (2016a). Decoupling kinematics and mechanics reveals coding properties of trigeminal ganglion neurons in the rat vibrissal system. *Elife*, *5*, e13969. doi:10.7554/elife.13969
- Bush, N. E., Solla, S. A., & Hartmann, M. J. Z. (2016c). Whisking mechanics and active sensing. *Current Opinion in Neurobiology*, *40*, 178-186. doi:10.1016/j.conb.2016.08.001
- Campagner, D., Evans, M. H., Bale, M. R., Erskine, A., & Petersen, R. S. (2016). Prediction of primary somatosensory neuron activity during active tactile exploration. *Elife*, *5*, 18. doi:10.7554/eLife.10696
- Carvell, G. E., & Simons, D. J. (1990). Biometric analyses of vibrissal tactile discrimination in the rat. *Journal of Neuroscience*, *10*(8), 2638-2648.

- Casas, J., & Dangles, O. (2010). Physical ecology of fluid flow sensing in arthropods. *Annual Review of Entomology*, *55*, 505-520.
- Catania, K. C. (2013). Stereo and serial sniffing guide navigation to an odour source in a mammal. *Nature communications*, *4*, 1441.
- Celikel, T., & Sakmann, B. (2007). Sensory integration across space and in time for decision making in the somatosensory system of rodents. *Proceedings of the National Academy of Sciences*, *104*(4), 1395-1400. doi:10.1073/pnas.0610267104
- Chagas, A. M., Theis, L., Sengupta, B., Stuttgen, M. C., Bethge, M., & Schwarz, C. (2013). Functional analysis of ultra high information rates conveyed by rat vibrissal primary afferents. *Frontiers in Neural Circuits*, *7*, 17. doi:10.3389/fncir.2013.00190
- Chakrabarti, S., & Schwarz, C. (2018). Cortical modulation of sensory flow during active touch in the rat whisker system. *Nature communications*, *9*, 12. doi:10.1038/s41467-018-06200-6
- Chen, J. L., Margolis, D. J., Stankov, A., Sumanovski, L. T., Schneider, B. L., & Helmchen, F. (2015). Pathway-specific reorganization of projection neurons in somatosensory cortex during learning. *Nature Neuroscience*, *18*(8), 1101-1108. doi:10.1038/nn.4046
- Chichilnisky, E. J. (2001). A simple white noise analysis of neuronal light responses. *Network-Computation in Neural Systems*, *12*(2), 199-213. doi:10.1080/713663221
- Clack, N. G., O'Connor, D. H., Huber, D., Petreanu, L., Hires, A., Peron, S., . . . Myers, E. W. (2012). Automated tracking of whiskers in videos of head fixed rodents. *PLoS Computational Biology*, *8*(7), e1002591. doi:10.1371/journal.pcbi.1002591
- Clements, T. N., & Rahn, C. D. (2006). Three-dimensional contact imaging with an actuated whisker. *IEEE Transactions on Robotics*, *22*(4), 844-848. doi:10.1109/tro.2006.878950
- Curtis, J. C., & Kleinfeld, D. (2009). Phase-to-rate transformations encode touch in cortical neurons of a scanning sensorimotor system. *Nature Neuroscience*, *12*(4), 492-501. doi:10.1038/nn.2283
- Darian-Smith, I., Sugitani, M., Heywood, J., Karita, K., & Goodwin, A. (1982). Touching textured surfaces: cells in somatosensory cortex respond both to finger movement and to surface features. *Science*, *218*(4575), 906-909.
- Dehnhardt, G., Mauck, B., & Bleckmann, H. (1998). Seal whiskers detect water movements. *Nature*, *394*(6690), 235-236.
- Dehnhardt, G., Mauck, B., Hanke, W., & Bleckmann, H. (2001). Hydrodynamic trail-following in harbor seals (*phoca vitulina*). *Science*, *293*(5527), 102-104. doi:10.1126/science.1060514
- Demb, J. B., & Singer, J. H. (2015). Functional circuitry of the retina. *Annual Review of Vision Science*, *1*(1), 263-289. doi:10.1146/annurev-vision-082114-035334

- Deschenes, M., Haidarliu, S., Demers, M., Moore, J., Kleinfeld, D., & Ahissar, E. (2015). Muscles involved in naris dilation and nose motion in rat. *Anatomical Record-Advances in Integrative Anatomy and Evolutionary Biology*, 298(3), 546-553. doi:10.1002/ar.23053
- Desimone, R., Albright, T. D., Gross, C. G., & Bruce, C. (1984). Stimulus-selective properties of inferior temporal neurons in the macaque. *Journal of Neuroscience*, 4(8), 2051-2062.
- Deutsch, D., Pietr, M., Knutsen, P. M., Ahissar, E., & Schneidman, E. (2012). Fast feedback in active sensing: Touch-induced changes to whisker-object interaction. *PloS One*, 7(9). doi:10.1371/journal.pone.0044272
- Diamond, M. E., von Heimendahl, M., Knutsen, P. M., Kleinfeld, D., & Ahissar, E. (2008). 'Where' and 'what' in the whisker sensorimotor system. *Nature Reviews Neuroscience*, 9(8), 601-612. doi:10.1038/nrn2411
- DiCarlo, J. J., & Johnson, K. O. (2000). Spatial and temporal structure of receptive fields in primate somatosensory area 3b: effects of stimulus scanning direction and orientation. *The Journal of Neuroscience*, 20(1), 495-510.
- DiCarlo, J. J., Johnson, K. O., & Hsiao, S. S. (1998). Structure of receptive fields in area 3b of primary somatosensory cortex in the alert monkey. *The Journal of Neuroscience*, 18(7), 2626-2645.
- Dorfl, J. (1985). The innervation of the mystacial region of the white-mouse - a topographical study. *Journal of Anatomy*, 142(OCT), 173-184.
- Ebara, S., Kumamoto, K., Matsuura, T., Mazurkiewicz, J. E., & Rice, F. L. (2002). Similarities and differences in the innervation of mystacial vibrissal follicle-sinus complexes in the rat and cat: A confocal microscopic study. *Journal of Comparative Neurology*, 449(2), 103-119. doi:10.1002/cne.10277
- Enroth-Cugell, C., & Robson, J. G. (1966). The contrast sensitivity of retinal ganglion cells of the cat. *The Journal of physiology*, 187(3), 517-552.
- Erzurumlu, R. S., Bates, C. A., & Killackey, H. P. (1980). Differential organization of thalamic projection cells in the brain-stem trigeminal complex of the rat. *Brain Research*, 198(2), 427-433. doi:10.1016/0006-8993(80)90756-8
- Fee, M. S., Mitra, P. P., & Kleinfeld, D. (1997). Central versus peripheral determinants of patterned spike activity in rat vibrissa cortex during whisking. *Journal of Neurophysiology*, 78(2), 1144-1149.
- Field, D. J. (1994). What is the goal of sensory coding. *Neural Computation*, 6(4), 559-601. doi:10.1162/neco.1994.6.4.559
- Field, D. J. (1999). Wavelets, vision and the statistics of natural scenes. *Philosophical Transactions of the Royal Society of London. Series A: Mathematical, Physical Engineering Sciences*, 357(1760), 2527-2542.
- Flock, Å. (1971). Sensory transduction in hair cells. In *Principles of receptor physiology* (pp. 396-441): Springer.

- Fourcaud-Trocme, N., Hansel, D., van Vreeswijk, C., & Brunel, N. (2003). How spike generation mechanisms determine the neuronal response to fluctuating inputs. *Journal of Neuroscience*, *23*(37), 11628-11640.
- Furuta, T., Nakamura, K., & Deschenes, M. (2006). Angular tuning bias of vibrissa-responsive cells in the paralemniscal pathway. *Journal of Neuroscience*, *26*(41), 10548-10557. doi:10.1523/jneurosci.1746-06.2006
- Furuta, T., Timofeeva, E., Nakamura, K., Okamoto-Furuta, K., Togo, M., Kaneko, T., & Deschenes, M. (2008). Inhibitory gating of vibrissal inputs in the brainstem. *Journal of Neuroscience*, *28*(8), 1789-1797. doi:10.1523/jneurosci.4627-07.2008
- Furuta, T., Urbain, N., Kaneko, T., & Deschenes, M. (2010). Corticofugal control of vibrissa-sensitive neurons in the interpolaris nucleus of the trigeminal complex. *Journal of Neuroscience*, *30*(5), 1832-1838. doi:10.1523/jneurosci.4274-09.2010
- Geisler, W. S. (2008). Visual perception and the statistical properties of natural scenes. *Annual Reviews of Psychology*, *59*, 167-192.
- Georgian, J. (1965). Vibration frequencies of tapered bars and circular plates. *Journal of Applied Mechanics*, *32*(1), 234-235.
- Gibson, J. M., & Welker, W. I. (1983a). Quantitative studies of stimulus coding in 1st-order vibrissa afferents of rats .2. Adaptation and coding of stimulus parameters. *Somatosensory Research*, *1*(2), 95-117. doi:10.3109/07367228309144543
- Gibson, J. M., & Welker, W. I. (1983b). Quantitative studies of stimulus coding in 1st-order vibrissa afferents of rats. 1.Receptive-field properties and threshold distributions. *Somatosensory Research*, *1*(1), 51-67. doi:10.3109/07367228309144540
- Grant, R. A., Mitchinson, B., Fox, C. W., & Prescott, T. J. (2009). Active touch sensing in the rat: Anticipatory and regulatory control of whisker movements during surface exploration. *Journal of Neurophysiology*, *101*(2), 862-874. doi:10.1152/jn.90783.2008
- Graziano, M. S. A. (2001). Is reaching eye-centered, body-centered, hand-centered, or a combination? *Reviews in the Neurosciences*, *12*(2), 175-185.
- Haidarliu, S., Golomb, D., Kleinfeld, D., & Ahissar, E. (2012). Dorsorostral snout muscles in the rat subserve coordinated movement for whisking and sniffing. *Anatomical Record-Advances in Integrative Anatomy and Evolutionary Biology*, *295*(7), 1181-1191. doi:10.1002/ar.22501
- Haidarliu, S., Kleinfeld, D., Deschenes, M., & Ahissar, E. (2015). The musculature that drives active touch by vibrissae and nose in mice. *Anatomical Record-Advances in Integrative Anatomy and Evolutionary Biology*, *298*(7), 1347-1358. doi:10.1002/ar.23102
- Haidarliu, S., Simony, E., Golomb, D., & Ahissar, E. (2010). Muscle architecture in the mystacial pad of the rat. *Anatomical Record-Advances in Integrative Anatomy and Evolutionary Biology*, *293*(7), 1192-1206. doi:10.1002/ar.21156

- Hartmann, M. J., Johnson, N. J., Towal, R. B., & Assad, C. (2003). Mechanical characteristics of rat vibrissae: Resonant frequencies and damping in isolated whiskers and in the awake behaving animal. *Journal of Neuroscience*, *23*(16), 6510-6519.
- Hartmann, M. J. Z. (2009). Active touch, exploratory movements, and sensory prediction. *Integrative and Comparative Biology*, *49*(6), 681-690. doi:10.1093/icb/icp107
- Hartmann, M. J. Z. (2015). Vibrissal mechanical properties. *Scholarpedia*.
- Harvey, M. a., Bermejo, R., & Zeigler, H. P. (2001). Discriminative whisking in the head-fixed rat: Optoelectronic monitoring during tactile detection and discrimination tasks. *Somatosensory and Motor Research*, *18*, 211-222. doi:10.1080/01421590120072204
- Hayashi, H. (1980). Distributions of vibrissae afferent fiber collaterals in the trigeminal nuclei as revealed by intra-axonal injection of horseradish-peroxidase. *Brain Research*, *183*(2), 442-446. doi:10.1016/0006-8993(80)90478-3
- Hill, D. N., Bermejo, R., Zeigler, H. P., & Kleinfeld, D. (2008). Biomechanics of the Vibrissa Motor Plant in Rat: Rhythmic Whisking Consists of Triphasic Neuromuscular Activity. *The Journal of Neuroscience*, *28*(13), 3438-3455. doi:10.1523/jneurosci.5008-07.2008
- Hill, D. N., Curtis, J. C., Moore, J. D., & Kleinfeld, D. (2011). Primary motor cortex reports efferent control of vibrissa motion on multiple timescales. *Neuron*, *72*(2), 344-356. doi:10.1016/j.neuron.2011.09.020
- Hires, S. A., Gutnisky, D. A., Yu, J. N., O'Connor, D. H., & Svoboda, K. (2015). Low-noise encoding of active touch by layer 4 in the somatosensory cortex. *Elife*, *4*, 18. doi:10.7554/elife.06619
- Hires, S. A., Pammer, L., Svoboda, K., & Golomb, D. (2013). Tapered whiskers are required for active tactile sensation. *Elife*, *2*, 10.7554/eLife.01350. doi:10.7554/eLife.01350
- Hobbs, J. A., Towal, R. B., & Hartmann, M. J. Z. (2015). Probability distributions of whisker-surface contact: Quantifying elements of the rat vibrissotactile natural scene. *Journal of Experimental Biology*, *218*(16), 2551-2562. doi:10.1242/jeb.116186
- Hobbs, J. A., Towal, R. B., & Hartmann, M. J. Z. (2016). Spatiotemporal patterns of contact across the rat vibrissal array during exploratory behavior. *Frontiers in Behavioral Neuroscience*, *9*. doi:10.3389/fnbeh.2015.00356
- Hoffman, B. U., Baba, Y., Griffith, T. N., Mosharov, E. V., Woo, S. H., Roybal, D. D., . . . Lumpkin, E. A. (2018). Merkel Cells Activate Sensory Neural Pathways through Adrenergic Synapses. *Neuron*, *100*(6), 1401-+. doi:10.1016/j.neuron.2018.10.034
- Hubel, D. H., & Wiesel, T. N. (1962). Receptive fields, binocular interaction and functional architecture in the cat's visual cortex. *The Journal of physiology*, *160*(1), 106-154.
- Huet, L. A., & Hartmann, M. J. Z. (2014). The search space of the rat during whisking behavior. *Journal of Experimental Biology*, *217*(18), 3365-3376. doi:10.1242/jeb.105338

- Huet, L. A., & Hartmann, M. J. Z. (2016). Simulations of a vibrissa slipping along a straight edge and an analysis of frictional effects during whisking. *IEEE Transactions on Haptics*, *PP*(99). doi:10.1109/TOH.2016.2522432
- Huet, L. A., Rudnicki, J. W., & Hartmann, M. J. Z. (2017). Tactile sensing with whiskers of various shapes: Determining the three-dimensional location of object contact based on mechanical signals at the whisker base. *Soft Robotics*, *4*(2), 88-102. doi:10.1089/soro.2016.0028
- Huet, L. A., Schroeder, C. L., & Hartmann, M. J. (2015). Tactile signals transmitted by the vibrissa during active whisking behavior. *Journal of Neurophysiology*, *113*(10), 3511-3518. doi:10.1152/jn.00011.2015
- Humphrey, J. A., & Barth, F. G. (2007). Medium flow-sensing hairs: biomechanics and models. *Advances in Insect Physiology*, *34*, 1-80.
- Hutcheon, B., & Yarom, Y. (2000). Resonance, oscillation and the intrinsic frequency preferences of neurons. *Trends in Neurosciences*, *23*(5), 216-222.
- Isett, B. R., Feasel, S. H., Lane, M. A., & Feldman, D. E. (2018). Slip-based coding of local shape and texture in mouse S1. *Neuron*, *97*(2), 418-+. doi:10.1016/j.neuron.2017.12.021
- Jacobs, G. A. (1995). Detection and analysis of air currents by crickets. *Bioscience*, *45*(11), 776-785.
- Jacquin, M. F., Renehan, W. E., Mooney, R. D., & Rhoades, R. W. (1986). Structure-function-relationships in rat medullary and cervical dorsal horns .1. Trigeminal primary afferents. *Journal of Neurophysiology*, *55*(6), 1153-1186.
- Jadhav, S. P., & Feldman, D. E. (2010). Texture coding in the whisker system. *Current Opinion in Neurobiology*, *20*(3), 313-318. doi:10.1016/j.conb.2010.02.014
- Jadhav, S. P., Wolfe, J., & Feldman, D. E. (2009). Sparse temporal coding of elementary tactile features during active whisker sensation. *Nature Neuroscience*, *12*(6), 792.
- Johnson, K. O. (2001). The roles and functions of cutaneous mechanoreceptors. *Current Opinion in Neurobiology*, *11*(4), 455-461.
- Jones, L. M., Depireux, D. A., Simons, D. J., & Keller, A. (2004a). Robust temporal coding in the trigeminal system. *Science*, *304*(5679), 1986-1989. doi:10.1126/science.1097779
- Jones, L. M., Kwegyir-Afful, E. E., & Keller, A. (2006). Whisker primary afferents encode temporal frequency of moving gratings. *Somatosensory and Motor Research*, *23*(1-2), 45-54. doi:10.1080/08990220600702707
- Jones, L. M., Lee, S., Trageser, J. C., Simons, D. J., & Keller, A. (2004b). Precise temporal responses in whisker trigeminal neurons. *Journal of Neurophysiology*, *92*(1), 665-668. doi:10.1152/jn.00031.2004

- Kan, Q. H., Rajan, R., Fu, J., Kang, G. Z., & Yan, W. Y. (2013). Elastic modulus of rat whiskers—a key biomaterial in the rat whisker sensory system. *Materials Research Bulletin*, *48*(12), 5026-5032. doi:10.1016/j.materresbull.2013.04.070
- Kaneko, M., Kanayama, N., & Tsuji, T. (1998). Active antenna for contact sensing. *IEEE Transactions on Robotics and Automation*, *14*(2), 278-291.
- Kayser, C., Salazar, R. F., & Konig, P. (2003). Responses to natural scenes in cat V1. *Journal of Neurophysiology*, *90*(3), 1910-1920. doi:10.1152/jn.00195.2003
- Kerr, F. W. L., & Lysak, W. R. (1964). Somatotopic organization of trigeminal-ganglion neurones. *Archives of Neurology*, *11*(6), 593-&.
- Khan, A. G., Sarangi, M., & Bhalla, U. S. (2012). Rats track odour trails accurately using a multi-layered strategy with near-optimal sampling. *Nature communications*, *3*, 703.
- Khatri, V., Bermejo, R., Brumberg, J. C., Keller, A., & Zeigler, H. P. (2009). Whisking in air: Encoding of kinematics by trigeminal ganglion neurons in awake rats. *Journal of Neurophysiology*, *101*(4), 1836-1846. doi:10.1152/jn.90655.2008
- Kim, J.-N., Yoo, J.-Y., Lee, J.-Y., Koh, K.-S., & Song, W.-C. (2012). A mechanism of rat vibrissal movement based on actual morphology of the intrinsic muscle using three-dimensional reconstruction. *Cells Tissues Organs*, *196*(6), 565-569. doi:10.1159/000338332
- Klatzky, R. L., & Lederman, S. J. (1995). Identifying objects from a haptic glance. *Perception and Psychophysics*, *57*(8), 1111-1123. doi:10.3758/bf03208368
- Kleinfeld, D., Ahissar, E., & Diamond, M. E. (2006). Active sensation: Insights from the rodent vibrissa sensorimotor system. *Current Opinion in Neurobiology*, *16*(4), 435-444. doi:10.1016/j.conb.2006.06.009
- Kleinfeld, D., & Deschenes, M. (2011). Neuronal basis for object location in the vibrissa scanning sensorimotor system. *Neuron*, *72*(3), 455-468. doi:10.1016/j.neuron.2011.10.009
- Kleinfeld, D., Deschenes, M., Wang, F., & Moore, J. D. (2014). More than a rhythm of life: Breathing as a binder of orofacial sensation. *Nature Neuroscience*, *17*(5), 647-651.
- Knutsen, P. M. (2015). Whisking kinematics. *Scholarpedia*, *10*(3), 7280. doi:doi::10.4249/scholarpedia.7280
- Knutsen, P. M., & Ahissar, E. (2009). Orthogonal coding of object location. *Trends in Neurosciences*, *32*(2), 101-109. doi:10.1016/j.tins.2008.10.002
- Knutsen, P. M., Biess, A., & Ahissar, E. (2008). Vibrissal kinematics in 3D: Tight coupling of azimuth, elevation, and torsion across different whisking modes. *Neuron*, *59*(1), 35-42. doi:10.1016/j.neuron.2008.05.013

- Knutsen, P. M., Derdikman, D., & Ahissar, E. (2005). Tracking whisker and head movements in unrestrained behaving rodents. *Journal of Neurophysiology*, *93*(4), 2294-2301. doi:10.1152/jn.00718.2004
- Knutsen, P. M., Pietr, M., & Ahissar, E. (2006). Haptic object localization in the vibrissal system: Behavior and performance. *Journal of Neuroscience*, *26*(33), 8451-8464. doi:10.1523/JNEUROSCI.1516-06.2006
- Krupa, D. J., Matell, M. S., Brisben, A. J., Oliveira, L. M., & Nicolelis, M. A. L. (2001). Behavioral properties of the trigeminal somatosensory system in rats performing whisker-dependent tactile discriminations. *Journal of Neuroscience*, *21*(15), 5752-5763.
- Kwegyir-Afful, E. E., Marella, S., & Simons, D. J. (2008). Response properties of mouse trigeminal ganglion neurons. *Somatosensory and Motor Research*, *25*(4), 209-221. doi:10.1080/08990220802467612
- Land, P. W., Buffer Jr, S. A., & Yaskosky, J. D. (1995). Barreloids in adult rat thalamus: Three-dimensional architecture and relationship to somatosensory cortical barrels. *Journal of Comparative Neurology*, *355*(4), 573-588. doi:10.1002/cne.903550407
- Lederman, S. J., & Klatzky, R. L. (2009). Haptic perception: A tutorial. *Attention Perception & Psychophysics*, *71*(7), 1439-1459. doi:10.3758/app.71.7.1439
- Leiser, S. C., & Moxon, K. A. (2006). Relationship between physiological response type (ra and sa) and vibrissal receptive field of neurons within the rat trigeminal ganglion. *Journal of Neurophysiology*, *95*(5), 3129-3145. doi:10.1152/jn.00157.2005
- Leiser, S. C., & Moxon, K. A. (2007). Responses of trigeminal ganglion neurons during natural whisking behaviors in the awake rat. *Neuron*, *53*(1), 117-133. doi:10.1016/j.neuron.2006.10.036
- Li, L. S., & Ginty, D. D. (2014). The structure and organization of lanceolate mechanosensory complexes at mouse hair follicles. *Elife*, *3*, 24. doi:10.7554/elife.01901
- Lichtenstein, S. H., Carvell, G. E., & Simons, D. J. (1990). Responses of rat trigeminal ganglion neurons to movements of vibrissae in different directions. *Somatosensory and Motor Research*, *7*, 47-65. doi:10.3109/08990229009144697
- Liddell, E. G. T., & Sherrington, C. S. (1924). Reflexes in response to stretch (myotatic reflexes). *Proceedings of the Royal Society of London. Series B, Containing Papers of a Biological Character*, *96*(675), 212-242.
- Liu, H. C., Shah, S., & Jiang, W. (2004). On-line outlier detection and data cleaning. *Computers & Chemical Engineering*, *28*(9), 1635-1647. doi:10.1016/j.compchemeng.2004.01.009
- Lottem, E., & Azouz, R. (2009). Mechanisms of tactile information transmission through whisker vibrations. *Journal of Neuroscience*, *29*(37), 11686-11697. doi:10.1523/JNEUROSCI.0705-09.2009

- Lottem, E., & Azouz, R. (2011). A unifying framework underlying mechanotransduction in the somatosensory system. *Journal of Neuroscience*, *31*(23), 8520-8532. doi:10.1523/jneurosci.6695-10.2011
- Lottem, E., Gugig, E., & Azouz, R. (2015). Parallel coding schemes of whisker velocity in the rat's somatosensory system. *Journal of Neurophysiology*, *113*(6), 1784-1799. doi:10.1152/jn.00485.2014
- Lumpkin, E. A., & Caterina, M. J. (2007). Mechanisms of sensory transduction in the skin. *Nature*, *445*(7130), 858.
- Ma, P. M., & Woolsey, T. A. (1984). Cytoarchitectonic correlates of the vibrissae in the medullary trigeminal complex of the mouse. *Brain Research*, *306*(1-2), 374-379. doi:10.1016/0006-8993(84)90390-1
- Magal, C., Dangles, O., Caparroy, P., & Casas, J. (2006). Hair canopy of cricket sensory system tuned to predator signals. *Journal of Theoretical Biology*, *241*(3), 459-466.
- Maksimovic, S., Nakatani, M., Baba, Y., Nelson, A. M., Marshall, K. L., Wellnitz, S. A., . . . Lumpkin, E. A. (2014). Epidermal Merkel cells are mechanosensory cells that tune mammalian touch receptors. *Nature*, *509*(7502), 617-621. doi:10.1038/nature13250
- Mameli, O., Caria, M. A., Pellitteri, R., Russo, A., Saccone, S., & Stanzani, S. (2016). Evidence for a trigeminal mesencephalic-hypoglossal nuclei loop involved in controlling vibrissae movements in the rat. *Experimental Brain Research*, *234*(3), 753-761. doi:10.1007/s00221-015-4503-6
- Mameli, O., Stanzani, S., Mulliri, G., Pellitteri, R., Caria, M. A., Russo, A., & De Riu, P. (2010). Role of the trigeminal mesencephalic nucleus in rat whisker pad proprioception. *Behavioral and Brain Functions*, *6*. doi:10.1186/1744-9081-6-69
- Maravall, M., & Diamond, M. E. (2014). Algorithms of whisker-mediated touch perception. *Current Opinion in Neurobiology*, *25*, 176-186. doi:10.1016/j.conb.2014.01.014
- Mazurek, M., Kager, M., & Van Hooser, S. D. (2014). Robust quantification of orientation selectivity and direction selectivity. *Frontiers in Neural Circuits*, *8*, 17. doi:10.3389/fncir.2014.00092
- McCullagh, P., & Nelder, J. A. (1989). *Generalized linear models, second edition*: Taylor & Francis.
- McIntosh, L. T., Maheswaranathan, N., Nayebi, A., Ganguli, S., & Baccus, S. A. (2016). Deep learning models of the retinal response to natural scenes. *Advances in Neural Information Processing Systems*, *29*, 1369-1377.
- McKay, I. (2012). *A mm-scale aeroelastic oscillation-based anemometer*. Paper presented at the ASME 2012 International Mechanical Engineering Congress and Exposition.
- Mehta, S. B., Whitmer, D., Figueroa, R., Williams, B. a., & Kleinfeld, D. (2007). Active spatial perception in the vibrissa scanning sensorimotor system. *PLoS Biology*, *5*, 0309-0322. doi:10.1371/journal.pbio.0050015

- Mihailoff, G. A., Kosinski, R. J., Azizi, S. A., & Border, B. G. (1989). Survey of noncortical afferent-projections to the basilar pontine nuclei - a retrograde tracing study in the rat. *Journal of Comparative Neurology*, 282(4), 617-643. doi:10.1002/cne.902820411
- Minnery, B. S., Bruno, R. M., & Simons, D. J. (2003). Response transformation and receptive-field synthesis in the lemniscal trigeminothalamic circuit. *Journal of Neurophysiology*, 90(3), 1556-1570. doi:10.1152/jn.00111.2003
- Mitchinson, B., Martin, C. J., Grant, R. A., & Prescott, T. J. (2007). Feedback control in active sensing: Rat exploratory whisking is modulated by environmental contact. *Proceedings of the Royal Society B-Biological Sciences*, 274(1613), 1035-1041. doi:10.1098/rspb.2006.0347
- Monahan, A. H., He, Y., McFarlane, N., & Dai, A. (2011). The probability distribution of land surface wind speeds. *Journal of climate*, 24(15), 3892-3909.
- Moore, J. D., Deschenes, M., Furuta, T., Huber, D., Smear, M. C., Demers, M., & Kleinfeld, D. (2013). Hierarchy of orofacial rhythms revealed through whisking and breathing. *Nature*, 497(7448), 205-+. doi:10.1038/nature12076
- Moore, J. D., Lindsay, N. M., Deschenes, M., & Kleinfeld, D. (2015). Vibrissa self-motion and touch are reliably encoded along the same somatosensory pathway from brainstem through thalamus. *PLoS Biology*, 13(9). doi:10.1371/journal.pbio.1002253
- Morita, T., Kang, H., Wolfe, J., Jadhav, S. P., & Feldman, D. E. (2011). Psychometric Curve and Behavioral Strategies for Whisker-Based Texture Discrimination in Rats. *PloS One*, 6(6), 10. doi:10.1371/journal.pone.0020437
- Muchlinski, M. N. (2010). A comparative analysis of vibrissa count and infraorbital foramen area in primates and other mammals. *Journal of Human Evolution*, 58(6), 447-473. doi:https://doi.org/10.1016/j.jhevol.2010.01.012
- Nakatani, M., Maksimovic, S., Baba, Y., & Lumpkin, E. A. (2015). Mechanotransduction in epidermal Merkel cells. *Pflugers Archiv: European Journal of Physiology*, 467(1), 101-108. doi:10.1007/s00424-014-1569-0
- Neimark, M. A., Andermann, M. L., Hopfield, J. J., & Moore, C. I. (2003). Vibrissa resonance as a transduction mechanism for tactile encoding. *Journal of Neuroscience*, 23(16), 6499-6509.
- Newsome, W. T., & Pare, E. B. (1988). A selective impairment of motion perception following lesions of the middle temporal visual area (MT). *Journal of Neuroscience*, 8(6), 2201-2211.
- O'Connor, D. H., Clack, N. G., Huber, D., Komiyama, T., Myers, E. W., & Svoboda, K. (2010). Vibrissa-based object localization in head-fixed mice. *Journal of Neuroscience*, 30(5), 1947-1967. doi:10.1523/jneurosci.3762-09.2010
- O'Connor, D. H., Hires, S. A., Guo, Z. C. V., Li, N., Yu, J. N., Sun, Q. Q., . . . Svoboda, K. (2013). Neural coding during active somatosensation revealed using illusory touch. *Nature Neuroscience*, 16(7), 958-U238. doi:10.1038/nn.3419

- Oladazimi, M., Brendel, W., & Schwarz, C. (2018). Biomechanical Texture Coding in Rat Whiskers. *Scientific Reports*, 8(1), 11139. doi:10.1038/s41598-018-29225-9
- Owens, D. M., & Lumpkin, E. A. (2014). Diversification and specialization of touch receptors in skin. *Cold Spring Harbor Perspectives in Medicine*, 4(6). doi:10.1101/cshperspect.a013656
- Pammer, L., O'Connor, D. H., Hires, S. A., Clack, N. G., Huber, D., Myers, E. W., & Svoboda, K. (2013). The mechanical variables underlying object localization along the axis of the whisker. *Journal of Neuroscience*, 33(16), 6726-6741. doi:10.1523/JNEUROSCI.4316-12.2013
- Pillow, J. W., Shlens, J., Paninski, L., Sher, A., Litke, A. M., Chichilnisky, E. J., & Simoncelli, E. P. (2008). Spatio-temporal correlations and visual signalling in a complete neuronal population. *Nature*, 454(7207), 995-999. doi:10.1038/nature07140
- Prescott, S. A., De Koninck, Y., & Sejnowski, T. J. (2008). Biophysical basis for three distinct dynamical mechanisms of action potential initiation. *PLoS Computational Biology*, 4(10), e1000198. doi:10.1371/journal.pcbi.1000198
- Quist, B. W., Faruqi, R. A., & Hartmann, M. J. Z. (2011). Variation in young's modulus along the length of a rat vibrissa. *Journal of Biomechanics*, 44(16), 2775-2781. doi:10.1016/j.jbiomech.2011.08.027
- Quist, B. W., & Hartmann, M. J. (2012a). Mechanical signals at the base of a rat vibrissa: The effect of intrinsic vibrissa curvature and implications for tactile exploration. *Journal of Neurophysiology*, 107(9), 2298-2312. doi:10.1152/jn.00372.2011
- Quist, B. W., & Hartmann, M. J. Z. (2012b). Mechanical signals at the base of a rat vibrissa: The effect of intrinsic vibrissa curvature and implications for tactile exploration. *Journal of Neurophysiology*, 107(9), 2298-2312. doi:10.1152/jn.00372.2011
- Quist, B. W., Seghete, V., Huet, L. A., Murphey, T. D., & Hartmann, M. J. (2014). Modeling forces and moments at the base of a rat vibrissa during noncontact whisking and whisking against an object. *Journal of Neuroscience*, 34(30), 9828-9844.
- Ramirez, A., Pnevmatikakis, E. A., Merel, J., Paninski, L., Miller, K. D., & Bruno, R. M. (2014). Spatiotemporal receptive fields of barrel cortex revealed by reverse correlation of synaptic input. *Nature Neuroscience*, 17(6), 866-875. doi:10.1038/nn.3720
- Ranade, S., Hangya, B., & Kepecs, A. (2013). Multiple modes of phase locking between sniffing and whisking during active exploration. *Journal of Neuroscience*, 33(19), 8250-8256. doi:10.1523/jneurosci.3874-12.2013
- Rao, R. P., Mielke, F., Bobrov, E., & Brecht, M. (2014). Vocalization-whisking coordination and multisensory integration of social signals in rat auditory cortex. *Elife*, 3, 20. doi:10.7554/eLife.03185
- Rice, F. L. (1993). Structure, vascularization, and innervation of the mystacial pad of the rat as revealed by the lectin griffonia-simplicifolia. *Journal of Comparative Neurology*, 337(3), 386-399. doi:10.1002/cne.903370304

- Rice, F. L., Mance, A., & Munger, B. L. (1986). A comparative light microscopic analysis of the sensory innervation of the mystacial pad .1. Innervation of vibrissal follicle-sinus complexes. *Journal of Comparative Neurology*, 252(2), 154-174. doi:10.1002/cne.902520203
- Richardson, F. E. (1909). A study of sensory control in the rat. *Psychological Monographs*, 12(1), 1-124.
- Ritt, J. T., Andermann, M. L., & Moore, C. I. (2008). Embodied information processing: Vibrissa mechanics and texture features shape micromotions in actively sensing rats. *Neuron*, 57(4), 599-613. doi:10.1016/j.neuron.2007.12.024
- Rossant, C., Kadir, S. N., Goodman, D. F. M., Schulman, J., Hunter, M. L. D., Saleem, A. B., . . . Harris, K. D. (2016). Spike sorting for large, dense electrode arrays. *Nature Neuroscience*, 19(4), 634-641. doi:10.1038/nn.4268
- Rutlin, M., Ho, C. Y., Abaira, V. E., Cassidy, C., Bai, L., Woodbury, C. J., & Ginty, D. D. (2014). The cellular and molecular basis of direction selectivity of adelta-ltmrs. *Cell*, 159(7), 1640-1651. doi:10.1016/j.cell.2014.11.038
- Salinas, E., Hernandez, A., Zainos, A., & Romo, R. (2000). Periodicity and firing rate as candidate neural codes for the frequency of vibrotactile stimuli. *Journal of Neuroscience*, 20(14), 5503-5515.
- Saraf-Sinik, I., Assa, E., & Ahissar, E. (2015). Motion makes sense: An adaptive motor-sensory strategy underlies the perception of object location in rats. *Journal of Neuroscience*, 35(23), 8777-8789. doi:10.1523/jneurosci.4149-14.2015
- Scholz, G. R., & Rahn, C. D. (2004). Profile sensing with an actuated whisker. *IEEE Transactions on Robotics and Automation*, 20(1), 124-127.
- Schroeder, J. B., & Ritt, J. T. (2016). Selection of head and whisker coordination strategies during goal-oriented active touch. *Journal of Neurophysiology*, 115(4), 1797-1809.
- Schwartz, O., Chichilnisky, E., & Simoncelli, E. P. (2002). *Characterizing neural gain control using spike-triggered covariance*. Paper presented at the Advances in Neural Information Processing Systems.
- Sellien, H., Eshenroder, D. S., & Ebner, F. F. (2005). Comparison of bilateral whisker movement in freely exploring and head-fixed adult rats. *Somatosensory and Motor Research*, 22(3), 97-114.
- Severson, K. S., Xu, D., Van de Loo, M., Bai, L., Ginty, D. D., & O'Connor, D. H. (2017). Active touch and self-motion encoding by merkel cell-associated afferents. *Neuron*, 94(3), 666-676. doi:10.1016/j.neuron.2017.03.045
- Sharpee, T., Rust, N. C., & Bialek, W. (2003). *Maximally informative dimensions: analyzing neural responses to natural signals*. Paper presented at the Advances in Neural Information Processing Systems.
- Shortland, P. J., Demaro, J. A., Shang, F., Waite, P. M. E., & Jacquin, M. F. (1996). Peripheral and central predictors of whisker afferent morphology in the rat brainstem. *Journal of Comparative Neurology*, 375(3), 481-501.

- Shoykhet, M., Doherty, D., & Simons, D. J. (2000). Coding of deflection velocity and amplitude by whisker primary afferent neurons: Implications for higher level processing. *Somatosensory and Motor Research*, *17*, 171-180. doi:10.1080/08990220050020580
- Shoykhet, M., Shetty, P., Minnery, B. S., & Simons, D. J. (2003). Protracted development of responses to whisker deflection in rat trigeminal ganglion neurons. *Journal of Neurophysiology*, *90*, 1432-1437. doi:10.1152/jn.00419.2003
- Simons, D. J. (1978). Response properties of vibrissa units in rat S1 somatosensory neocortex. *Journal of Neurophysiology*, *41*, 798-820.
- Simony, E., Bagdasarian, K., Herfst, L., Brecht, M., Ahissar, E., & Golomb, D. (2010). Temporal and spatial characteristics of vibrissa responses to motor commands. *Journal of Neuroscience*, *30*(26), 8935-8952. doi:10.1523/jneurosci.0172-10.2010
- Sinclair, R. J., & Burton, H. (1991). Neuronal activity in the primary somatosensory cortex in monkeys (*Macaca mulatta*) during active touch of textured surface gratings: responses to groove width, applied force, and velocity of motion. *Journal of Neurophysiology*, *66*(1), 153-169.
- Smear, M., Shusterman, R., O'Connor, R., Bozza, T., & Rinberg, D. (2011). Perception of sniff phase in mouse olfaction. *Nature*, *479*(7373), 397-400. doi:10.1038/nature10521
- Solomon, J. H., & Hartmann, M. J. (2006). Robotic whiskers used to sense features. *Nature*, *443*(7111), 525-525. doi:10.1038/443525a
- Solomon, J. H., & Hartmann, M. J. Z. (2008). Artificial whiskers suitable for array implementation: Accounting for lateral slip and surface friction. *IEEE Transactions on Robotics*, *24*(5), 1157-1167. doi:10.1109/tro.2008.2002562
- Solomon, J. H., & Hartmann, M. J. Z. (2010). Extracting object contours with the sweep of a robotic whisker using torque information. *International Journal of Robotics Research*, *29*(9), 1233-1245. doi:10.1177/0278364908104468
- Solomon, J. H., & Hartmann, M. J. Z. (2011). Radial distance determination in the rat vibrissal system and the effects of weber's law. *Philosophical Transactions of the Royal Society B-Biological Sciences*, *366*(1581), 3049-3057. doi:10.1098/rstb.2011.0166
- Storchi, R., Bale, M. R., Biella, G. E., & Petersen, R. S. (2012). Comparison of latency and rate coding for the direction of whisker deflection in the subcortical somatosensory pathway. *Journal of Neurophysiology*, *108*(7), 1810-1821. doi:10.1152/jn.00921.2011
- Stuttgen, M. C., Kullmann, S., & Schwarz, C. (2008). Responses of rat trigeminal ganglion neurons to longitudinal whisker stimulation. *Journal of Neurophysiology*, *100*(4), 1879-1884. doi:10.1152/jn.90511.2008
- Stuttgen, M. C., Ruter, J., & Schwarz, C. (2006). Two psychophysical channels of whisker deflection in rats align with two neuronal classes of primary afferents. *Journal of Neuroscience*, *26*(30), 7933-7941. doi:10.1523/JNEUROSCI.1864-06.2006

- Szwed, M., & Ahissar, E. (2006a). Mapping the gates. Focus on "relationship between physiological response type (ra and sa) and vibrissal receptive field of neurons within the rat trigeminal ganglion". *Journal of Neurophysiology*, *95*(5), 2729-2730. doi:10.1152/jn.00147.2006
- Szwed, M., Bagdasarian, K., & Ahissar, E. (2003). Encoding of vibrissal active touch. *Neuron*, *40*(3), 621-630. doi:10.1016/s0896-6273(03)00671-8
- Szwed, M., Bagdasarian, K., Blumenfeld, B., Barak, O., Derdikman, D., & Ahissar, E. (2006b). Responses of trigeminal ganglion neurons to the radial distance of contact during active vibrissal touch. *Journal of Neurophysiology*, *95*(2), 791-802. doi:10.1152/jn.00571.2005
- Takatoh, J., Prevosto, V., & Wang, F. (2018). Vibrissa sensory neurons: Linking distinct morphology to specific physiology and function. *Journal of Neuroscience*, *368*, 109-114. doi:10.1016/j.neuroscience.2017.06.033
- Taneda, S. (1956). Experimental investigation of the wake behind a sphere at low Reynolds numbers. *Journal of the Physical Society of Japan*, *11*(10), 1104-1108.
- Theis, L., Chagas, A. M., Arnstein, D., Schwarz, C., & Bethge, M. (2013). Beyond glms: A generative mixture modeling approach to neural system identification. *PLoS Computational Biology*, *9*(11), 9. doi:10.1371/journal.pcbi.1003356
- Timofeeva, E., Dufresne, C., Sik, A., Zhang, Z. W., & Deschenes, M. (2005). Cholinergic modulation of vibrissal receptive fields in trigeminal nuclei. *Journal of Neuroscience*, *25*(40), 9135-9143. doi:10.1523/jneurosci.3073-05.2005
- Tonomura, S., Ebara, S., Bagdasarian, K., Uta, D., Ahissar, E., Meir, I., . . . Kumamoto, K. (2015). Structure-function correlations of rat trigeminal primary neurons: Emphasis on club-like endings, a vibrissal mechanoreceptor. *Proceedings of the Japan Academy Series B-Physical and Biological Sciences*, *91*(10), 560-576. doi:10.2183/pjab.91.560
- Touryan, J., Felsen, G., & Dan, Y. (2005). Spatial structure of complex cell receptive fields measured with natural images. *Neuron*, *45*(5), 781-791. doi:10.1016/j.neuron.2005.01.029
- Towal, R. B., & Hartmann, M. J. Z. (2008). Variability in velocity profiles during free-air whisking behavior of unrestrained rats. *Journal of Neurophysiology*, *100*(2), 740-752. doi:10.1152/jn.01295.2007
- Towal, R. B., Quist, B. W., Gopal, V., Solomon, J. H., & Hartmann, M. J. Z. (2011). The morphology of the rat vibrissal array: A model for quantifying spatiotemporal patterns of whisker-object contact. *PLoS Computational Biology*, *7*(4), 17. doi:10.1371/journal.pcbi.1001120
- Tramper, J. J., & Flanders, M. (2013). Predictive mechanisms in the control of contour following. *Experimental Brain Research*, *227*(4), 535-546. doi:10.1007/s00221-013-3529-x
- van der Loos, H., & Woolsey, T. A. (1973). Somatosensory cortex: Structural alterations following early injury to sense organs. *Science*, *179*(4071), 395-398.

- Vaxenburg, R., Wyche, I., Svoboda, K., Efros, A. L., & Hires, S. A. (2018). Dynamic cues for whisker-based object localization: An analytical solution to vibration during active whisker touch. *PLoS Computational Biology*, *14*(3), e1006032. doi:10.1371/journal.pcbi.1006032
- Veinante, P., Jacquin, M. F., & Deschenes, M. (2000). Thalamic projections from the whisker-sensitive regions of the spinal trigeminal complex in the rat. *Journal of Comparative Neurology*, *420*(2), 233-243. doi:10.1002/(sici)1096-9861(20000501)420:2<233::aid-cne6>3.0.co;2-t
- Vincent, S. B. (1912). The functions of the vibrissae in the behavior of the white rat. *Behavioral Monographs*, *1*, 1 - 81.
- Vinje, W. E., & Gallant, J. L. (2000). Sparse coding and decorrelation in primary visual cortex during natural vision. *Science*, *287*(5456), 1273-1276.
- Voges, D., Carl, K., Klauer, G. J., Uhlig, R., Schilling, C., Behn, C., & Witte, H. (2012). Structural characterization of the whisker system of the rat. *IEEE Sensors Journal*, *12*(2), 332-339. doi:10.1109/jsen.2011.2161464
- Voigts, J., Herman, D. H., & Celikel, T. (2015). Tactile object localization by anticipatory whisker motion. *Journal of Neurophysiology*, *113*(2), 620-632.
- Wallach, A., Bagdasarian, K., & Ahissar, E. (2016). On-going computation of whisking phase by mechanoreceptors. *Nature Neuroscience*, *19*(3), 487-493. doi:10.1038/nn.4221
- Welker, C. (1971). Microelectrode delineation of fine grain somatotopic organization of SmI cerebral neocortex in albino rat. *Brain Research*, *26*(2), 259-275. doi:https://doi.org/10.1016/S0006-8993(71)80004-5
- Welker, C., & Woolsey, T. A. (1974). Structure of layer IV in the somatosensory neocortex of the rat: Description and comparison with the mouse. *Journal of Comparative Neurology*, *158*(4), 437-453. doi:10.1002/cne.901580405
- Welker, W. I. (1964). Analysis of sniffing of the albino rat. *Behaviour*, *22*, 223-244.
- Whiteley, S. J., Knutsen, P. M., Matthews, D. W., & Kleinfeld, D. (2015). Deflection of a vibrissa leads to a gradient of strain across mechanoreceptors in a mystacial follicle. *Journal of Neurophysiology*, *114*(1), 138-145. doi:10.1152/jn.00179.2015
- Wienbar, S., & Schwartz, G. W. (2018). The dynamic receptive fields of retinal ganglion cells. *Progress in Retinal and Eye Research*, *67*, 102-117. doi:10.1016/j.preteyeres.2018.06.003
- Williams, C. M., & Kramer, E. M. (2010). The advantages of a tapered whisker. *PloS One*, *5*(1), 8. doi:10.1371/journal.pone.0008806
- Williams, M. N., Zahm, D. S., & Jacquin, M. F. (1994). Differential foci and synaptic organization of the principal and spinal trigeminal projections to the thalamus in the rat. *European Journal of Neuroscience*, *6*(3), 429-453. doi:10.1111/j.1460-9568.1994.tb00286.x

- Williamson, C., & Govardhan, R. (2004). Vortex-induced vibrations. *Annu. Rev. Fluid Mech.*, *36*, 413-455.
- Williamson, R. S., Sahani, M., & Pillow, J. W. (2015). The equivalence of information-theoretic and likelihood-based methods for neural dimensionality reduction. *PLoS Computational Biology*, *11*(4). doi:10.1371/journal.pcbi.1004141
- Willmore, B., & Tolhurst, D. J. (2001). Characterizing the sparseness of neural codes. *Network-Computation in Neural Systems*, *12*(3), 255-270. doi:10.1080/713663277
- Windham, M. P. (1988). Mixture-models - inference and applications to clustering - mclachlan,gj, basford,ke. *Journal of Classification*, *5*(1), 105-107. doi:10.1007/bf01901678
- Wineski, L. E. (1985). Facial morphology and vibrissal movement in the golden hamster. *Journal of Morphology*, *183*(2), 199-217.
- Wolfe, J., Hill, D. N., Pahlavan, S., Drew, P. J., Kleinfeld, D., & Feldman, D. E. (2008). Texture coding in the rat whisker system: Slip-stick versus differential resonance. *PLoS Biology*, *6*(8), 1161-1177. doi:10.1371/journal.pbio.0060215
- Woo, S. H., Lumpkin, E. A., & Patapoutian, A. (2015). Merkel cells and neurons keep in touch. *Trends in Cell Biology*, *25*(2), 74-81. doi:10.1016/j.tcb.2014.10.003
- Woo, S. H., Ranade, S., Weyer, A. D., Dubin, A. E., Baba, Y., Qiu, Z. Z., . . . Patapoutian, A. (2014). Piezo2 is required for Merkel-cell mechanotransduction. *Nature*, *509*(7502), 622-626. doi:10.1038/nature13251
- Woolsey, T. A., & Van der Loos, H. (1970). The structural organization of layer IV in the somatosensory region (si) of mouse cerebral cortex. The description of a cortical field composed of discrete cytoarchitectonic units. *Brain Research*, *17*(2), 205-242. doi:10.1016/0006-8993(70)90079-x
- Woolston, D. C., Lalonde, J. R., & Gibson, J. M. (1983). Corticofugal influences in the rat on responses of neurons in the trigeminal nucleus interpolaris to mechanical stimulation. *Neuroscience Letters*, *36*(1), 43-48. doi:10.1016/0304-3940(83)90483-4
- Xu, N.-l., Harnett, M. T., Williams, S. R., Huber, D., O'connor, D. H., Svoboda, K., & Magee, J. C. (2012). Nonlinear dendritic integration of sensory and motor input during an active sensing task. *Nature*, *492*(7428), 247.
- Yan, W., Kan, Q., Kergrene, K., Kang, G., Feng, X.-Q., & Rajan, R. (2013). A truncated conical beam model for analysis of the vibration of rat whiskers. *Journal of Biomechanics*, *46*(12), 1987-1995. doi:10.1016/j.jbiomech.2013.06.015
- Yang, A., & Hartmann, M. (2016). Whisking kinematics enables object localization in head-centered coordinates based on tactile information from a single vibrissa *Frontiers in Behavioral Neuroscience*, in review.
- Yu, C., Horev, G., Rubin, N., Derdikman, D., Haidarliu, S., & Ahissar, E. (2013). Coding of object location in the vibrissal thalamocortical system. *Cerebral Cortex*, *25*, 563-577.

- Yu, C. X., Derdikman, D., Haidarliu, S., & Ahissar, E. (2006). Parallel thalamic pathways for whisking and touch signals in the rat. *PLoS Biology*, *4*(5), 819-825. doi:10.1371/journal.pbio.0040124
- Yu, Y. S. W., Graff, M. M., Breese, C. S., Man, Y. B., & Hartmann, M. J. Z. (2016a). Whiskers aid anemotaxis in rats. *Science Advances*, *2*(8), 7. doi:10.1126/sciadv.1600716
- Yu, Y. S. W., Graff, M. M., & Hartmann, M. J. Z. (2016b). Mechanical responses of rat vibrissae to airflow. *Journal of Experimental Biology*, *219*(7), 937-948. doi:10.1242/jeb.126896
- Zeng, H., & Sanes, J. R. (2017). Neuronal cell-type classification: Challenges, opportunities and the path forward. *Nature Reviews Neuroscience*, *18*(9), 530-546. doi:10.1038/nrn.2017.85s
- Zucker, E., & Welker, W. I. (1969). Coding of somatic sensory input by vibrissae neurons in rats trigeminal ganglion. *Brain Research*, *12*(1), 138-&. doi:10.1016/0006-8993(69)90061-4